DEVELOPMENT OF MODIFIED TITANIA NANO PHOTOCATALYSTS TO SYNERGISE VISIBLE LIGHT UTILISATION FOR ENHANCED PHOTOCATALYSIS

LEONG KAH HON

THESIS SUBMITTED IN FULFILMENT OF THE REQUIREMENTS FOR THE DEGREE OF DOCTOR OF PHILOSOPHY

FACULTY OF ENGINEERING
UNIVERSITY OF MALAYA
KUALA LUMPUR

2015

UNIVERSITI MALAYA

ORIGINAL LITERARY WORK DECLARATION

Name of Candidate: LEONG KAH HON (I.C/Passport No: 850102-08-6169)

Registration/Matric No: KHA 120005

Name of Degree: DOCTOR OF PHILOSOPHY

Title of Project Paper/Research Report/Dissertation/Thesis (“this Work”): DEVELOPMENT OF MODIFIED TITANIA NANO PHOTOCATALYSTS TO SYNERGISE VISIBLE LIGHT UTILISATION FOR ENHANCED PHOTOCATALYSIS

Field of Study: WATER RESOURCES ENGINEERING (CIVIL ENGINEERING)

I do solemnly and sincerely declare that:

(1) I am the sole author/writer of this Work;
(2) This Work is original;
(3) Any use of any work in which copyright exists was done by way of fair dealing and for permitted purposes and any excerpt or extract from, or reference to or reproduction of any copyright work has been disclosed expressly and sufficiently and the title of the Work and its authorship have been acknowledged in this Work;
(4) I do not have any actual knowledge nor do I ought reasonably to know that the making of this work constitutes an infringement of any copyright work;
(5) I hereby assign all and every rights in the copyright to this Work to the University of Malaya (“UM”), who henceforth shall be owner of the copyright in this Work and that any reproduction or use in any form or by any means whatsoever is prohibited without the written consent of UM having been first had and obtained;
(6) I am fully aware that if in the course of making this Work I have infringed any copyright whether intentionally or otherwise, I may be subject to legal action or any other action as may be determined by UM.

Candidate’s Signature Date

Subscribed and solemnly declared before,

Witness’s Signature Date

Name:
Designation:

ABSTRACT

The present thesis focused on the development of modified titania nano photocatalysts to synergise enhanced visible light photocatalysis that niched for the destruction of lethal aquatic pollutants. In preliminary phase template TiO_2 was successfully synthesised through a facile non-hydrolitic sol-gel technique. The materials chemistry revealed the pristine anatase phase and crystallinity of TiO_2. It also demonstrated the influence of crystallinity over photocatalysis efficiency. This was well reflected in photocatalysis evaluation studies under solar irradiation where good crystallinity shown a better photodegradation performance over the non-crystalline. The inherent photocatalytic characteristics of the synthesised TiO_2 was modified and enhanced by incorporating the noble characteristic derived from palladium (Pd) and silver (Ag). This was achieved through a smart, ease and sustainable method. The adopted novel method explicitly revealed the capability of sunlight for anchoring the noble metal onto TiO_2 with controlled particle size of Pd NPs (17-29 nm) and laid pathway for the effective absorbance of visible matter triggered by the synergetic effect of LSPR. Similarly, a collective oscillation of conduction electrons that were induced by the deposited Ag NPs onto the TiO_2, drastically enhanced the light absorption of the composite. Moreover these noble NPs also contributed for extending the lifetime of electrons and holes pairs. The study also expressed the variation of these noble metal loading and its influence on the photocatalysis irradiated under artificial visible light. The photocatalysis evaluation studies were performed with lethal and endocrine disrupting compounds (EDCs) of different classification. This includes Amoxicillin for antibiotics and 2, 4-dichlorophenol (2, 4-DCP) for pesticides. Both the composites exhibited an excellent photocatalysis under the artificial visible light with an efficiency of 97.5 % and 63.5 % for removing AMX by Pd/TiO_2 and Ag/TiO_2 respectively. In addition the Ag composite also demonstrated similar photocatalysis efficiency for 2, 4-DCP. However the optimal metal loading for an ideal photocatalysis was found to be 0.5wt% for Pd/TiO_2 and 3.0wt% for Ag/TiO_2. Furthermore in order to enhance the characteristics of the TiO_2 the conducting carbon materials were considered along with the noble metal. The reduced graphene oxide (RGO) a category of conducting carbon was considered for the ternary composite along with Ag. The ternary shown an increased visible light absorption characteristics over the binary composite. This was acknowledged to the intrinsic nature contributed by the RGO. The study also clarified the promotion of electron mobility and prolongation of the lifetime of the charge carriers. This was well correlated with the photocatalysis evaluation achieved through both good and poor photosensitizing pollutants namely Methylene Blue (MB), Reactive Blue 19 (RB19) and Bisphenol A (BPA). The objective was further extended with exploring the prospective Graphitic Carbon Nitride (g-C_3N_4) a semiconductor carbon compound as a visible light enhancer. The wrapping of g-C_3N_4 onto the surface of TiO_2 drastically increased the absorption intensity in-between 390-460 nm and shifted the absorption edge to 460 nm. Subsequently, it well correlated with the photocatalysis efficiency whereby (g-C_3N_4)-Ag/TiO_2 showed the highest photodegradation rate under artificial visible light. Hence, the present studies progressively presented the caliber of the synergisation of conventional photocatalyst to upbeat the limitations and developed a new category of composite photocatalyst. The synthesised photocatalysts well proved their candidature as an active visible light photocatalyst and laid a sustainable pathway for environmental cleanup as demanded by the planet.

ABSTRAK

Tujuan utama tesis ini adalah untuk mengkaji kesan modifikasi yang dibuat terhadap fotokatalis nano titania dalam meningkatkan keupayaan cahaya nampak yang akan digunakan untuk memusnahkan bahan toksik di dalam hidupan akuatik. Pada fasa permulaan, TiO_2 telah berjaya disintesis melalui teknik mudah iaitu “non-hydrolytic sol-gel”. Ciri-ciri kimia membuktikan kehadiran fasa anatase dan penghabluran pada TiO_2. Ia juga menunjukkan kesan penghabluran terhadap kecekapan fotokatalis. Ini dijelaskan lagi dalam kajian penilaian fotokatalis di bawah sinaran cahaya matahari di mana penghabluran yang tinggi menunjukkan prestasi yang lebih baik. Ciri-ciri yang wujud dalam fotokatalis TiO_2 yang telah disintesis diubahsuai dan ditambahbaikkan dengan menggabungkannya dengan logam yang lebih baik iaitu “palladium (Pd)” dan “silver (Ag)”. Pengubahsuaian dan penambahbaikkan telah dicapai melalui kaedah yang sesuai dan ringkas. Penggunaan kaedah baru ini jelas mendedahkan keupayaan cahaya matahari dalam penggabungan logam mulia dan TiO_2 pada saiz yang tertentu iaitu zarah Pd NP_S (17-29 nm) dan ia kemudiannya diletakkan untuk penyerapan cahaya nampak dan memberi kesan yang lebih disebabkan oleh kesan sinergi daripada LSPR. Ayunan kolektif elektron konduksi turut terhasil yang disebabkan oleh penggabungan Ag NPs dengan TiO_2, keadaan ini menyebabkan peningkatan penyerapan cahaya nampak secara drastik. Logam mulia juga melanjutkan hayat elektron dan lubang pasang. Kajian ini menunjukkan perubahan jumlah logam mulia dan kesannya terhadap fotokatalis yang diradiasi oleh cahaya nampak tiruan. Kajian penilaian terhadap fotokatalis telah dijalankan dengan bahan toksik dan sebatian endokrin (EDC) dengan klasifikasi yang berbeza. Ini termasuk “Amoxicillin” untuk antibiotik dan 2, 4-diklorofenol (2, 4-DCP) untuk racun makhluk perosak. Kedua-dua komposit mempamerkan fotokatalis yang baik di bawah cahaya nampak tiruan masing-masing dengan kecekapan 97.5% dan 63.5% bagi menghapuskan AMX oleh Pd/TiO_2 dan Ag/TiO_2. Selain itu, komposit Ag

juga membuktikan kecekapan fotokatalis yang sama bagi 2, 4-DCP. Walau bagaimanapun kapasiti logam yang optimum untuk fotokatalis didapati 0.5wt% untuk Pd/TiO_2 dan 3.0wt% untuk Ag/TiO_2. Selain itu, untuk meningkatkan ciri-ciri TiO_2, bahan-bahan karbon digabungkan bersama-sama dengan logam mulia. “Reduced Graphene Oxide (RGO)” iaitu salah satu jenis karbon telah dipertimbangkan untuk komposit pertigaan bersama-sama dengan Ag. Komposit pertigaan meningkatkan penyerapan cahaya nampak berbanding dengan komposit binari. Ini disebabkan oleh sifat intrinsik yang disumbangkan oleh RGO. Kajian ini juga menjelaskan penggalakan pergerakan elektron dan pemanjangan jangka hayat pembawa cas. Ia berkait rapat dengan penilaian fotokatalis yang dicapai menggunakan bahan pencemar photosensitizing iaitu “Methylene Blue (MB)”, “Reactive Blue 19 (RB19)” dan “Bisphenol A (BPA)”. Objektif kajian telah dikembangkan lagi dengan menerokai bakal “Graphitic Carbon Nitride (g-C_3N_4)” semikonduktor iaitu sebatian karbon sebagai penambah kepada cahaya nampak. Dengan menyaluti g-C_3N_4 pada permukaan TiO_2 secara drastik meningkatkan intensiti penyerapan di antara 390-460 nm dan mengalihkan daya penyerapan sehingga 460 nm. Selain itu, ia juga berkait rapat dengan kecekapan fotokatalis dimana (g-C_3N_4)-Ag/TiO_2 menunjukkan kadar pemfotorosotaan tertinggi di bawah cahaya nampak tiruan. Oleh itu, kajian ini berjaya meningkatkan kebolehan fotomangkin konvensional dan mengembangkan pertemuan baru dalam fotomangkin komposit. Fotokatalis yang disintesiskan juga membuktikan ianya sebagai fotomangkin cahaya nampak dan dapat digunakan dalam pembersihan alam sekitar.

ACKNOWLEDGEMENTS

During my PhD candidature at University of Malaya for the past three years, I have truly learned great things not just about my academic research but also about life. It is always not an easy riding especially at the beginning of my studies, but I have to mention that I have really enjoyed every single moment of the learning. These experiences painted another important learning chapter in my life that I would never forget. I believe this would not be possible without the help and guidance from each and everyone around me and I would like to take this great opportunity to acknowledge them.

Firstly, I would like to express my greatest gratitude to my supervisor, Dr. Saravanan Pichiah for his endless support and guidance. His positive attitude motivates me to achieve my greatest goal in my research. He gave me countless opportunities which frame and build up my academic career. He is very supportive in many of my new research ideas. I also like to convey my appreciation to my co-supervisor Prof. Dr. Shaliza Ibrahim for her advice and supervision. To my seniors, Dr. Azrina Abdul Aziz who supported me at the early stage of my candidature and Dr. Sim Lan Ching for her advice, discussion and research collaborations.

To all my colleagues, Yee Li, Anis, Chee Ching, Hong Ye, Bee Ling, Aziz, Ranjini, Kien Tek, Sharmini and Shanmuga, thank you for your help and encouragement. Thank you to all the lab assistants, Mdm Kalai, Mdm Rozita and Ms Alya for their supportive assistance and making sure the lab is always in perfect working conditions.

Last but not least to my beloved parents for their kind support and always pray for my success. To my brother and sister, thank you for their never ending words of encouragement. With their unfailing love and support, I could be able to go through all the hardships throughout my PhD candidature.

Thank you all.

TABLE OF CONTENTS

CHAPTER 1: INTRODUCTION

CHAPTER 2: LITERATURE REVIEW

CHAPTER 3: METHODOLOGY

CHAPTER 4: RESULTS AND DISCUSSION

CHAPTER 5: CONCLUSIONS AND RECOMMENDATIONS

LIST OF FIGURES

LIST OF TABLES

LIST OF SYMBOLS AND ABBREVIATIONS

Symbols/Abbreviations	**Meaning**
AOP	advanced oxidation process
CO_2	carbon dioxide
H_2O	water
O_2	oxygen
UV	ultraviolet
$^{\bullet}OH$	hydroxyl radical
$^{\bullet}O_2^-$	superoxide anion radical
OP	organic pollutant
TiO_2	titania
GO	graphene oxide
RGO	reduced graphene oxide
$g\text{-}C_3N_4$	graphitic carbon nitride
Ag	silver
Pd	palladium
Au	gold
Pt	platinum
NPs	nanoparticles
LSPR	localized surface plasmon resonance
EDC	endocrine disrupting compound
2, 4-DCP	2, 4-dichlorophenol
AMX	amoxicillin
BPA	bisphenol A
MB	methylene blue

RB19	reactive blue 19
E_g	band gap energy
E_f	fermi level
e^-	electron
h^+	hole
λ	wavelength
CB	conduction band
VB	valence band
hv	photon energy
NHE	normal hydrogen electrode
$AgNO_3$	silver nitrate
$KMnO_4$	potassium permanganate
H_2SO_4	sulphuric acid
H_2O_2	hydrogen peroxide
HCl	hydrogen chloride
$TiCl_4$	titanium (IV) chloride
Na_2PdCl_4	sodium tetrachloropalladate (II)
THF	tetrahydrofuran
I_D	intensity of D band
I_G	intensity of G band

CHAPTER 1

INTRODUCTION

1.1 Photocatalysis

Semiconductor photocatalysis has been established as one of the main stream techniques over the last few decades for promising environmental remediation and cleanup. Since 1972, the catalytic ability of Titania (TiO_2) stimulated through photons was first discovered by Fujishima and Honda on their endeavor for water splitting reaction (Fujishima & Honda, 1972). Their discovery has led to a remarkable breakthrough in Advanced Oxidation Process (AOP). This process has proven to be an effective tools in addressing variant environmental problems as compare to those conventional techniques such as adsorption, coagulation, reverse osmosis, ultrafiltration and etc. In recent years, research interest in heterogeneous photocatalysis has been the main focus in environmental applications such as water, wastewater treatment, air purification and etc. This is mainly due to the benefits of heterogeneous photocatalysis such as (i) final oxidation products that are non-hazardous and harmless to the environment (CO_2, H_2O and other inorganic species), (ii) less formation of secondary pollutants, (iii) uses greener oxidant (O_2), (iv) relatively excited under renewable energy source like natural sunlight in the form of irradiation energy, (v) almost complete degradation or mineralization of pollutants (Ding, Lu, & Greenfield, 2000).

Heterogeneous photocatalysis mainly involves the participation of semiconductor photocatalyst to generate active radicals such as superoxide anions and hydroxyl radicals with the presence of sufficient photon energy. Generally, it consists of two main steps. First, while the photon energy (hν) is absorbed by the semiconductor photocatalyst, electrons from the valence band (VB) are promoted to conduction band (CB) leaving behind an equal number of positive holes at the VB. Thus the photogenerated electrons and holes will then migrate to the surface of the semiconductor photocatalyst and react with the strong oxidation and reduction species forming active radicals for oxidation. In the midst most of the electrons and holes tend to recombine and dissipate the energy in the form of heat and light. A simplified mechanism for heterogeneous photocatalysis involving a semiconductor is illustrated in Figure 1.1.

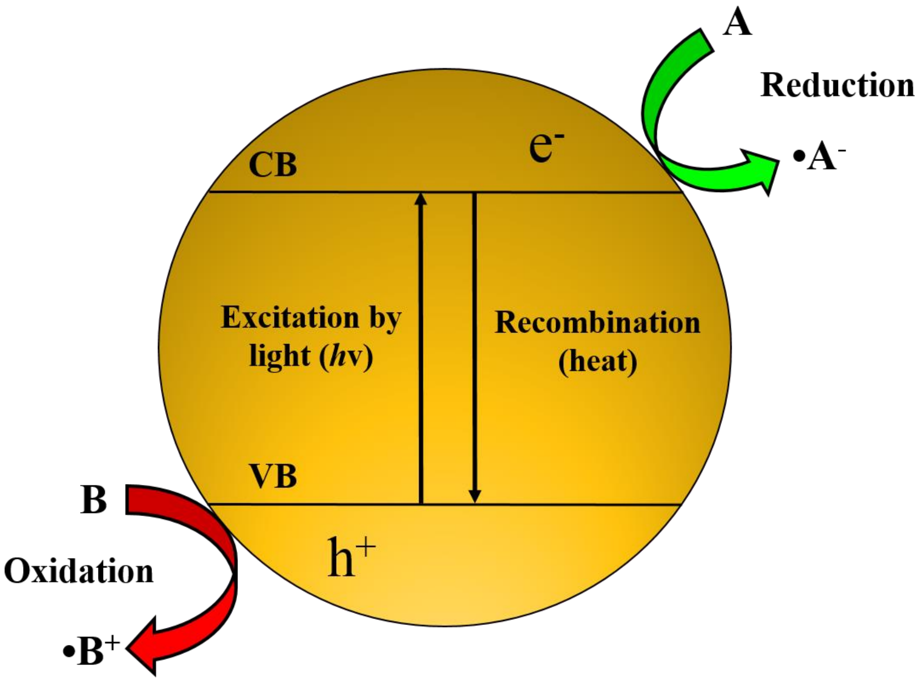

Figure 1.1: Simplified mechanism for photocatalysis involving a semiconductor

1.2 Titania Semiconductor Photocatalyst

In general various potential semiconductors were employed for heterogeneous photocatalysis depending on their band gap energy as illustrated in Figure 1.2. However in particular, TiO_2 has emerged as the most studied semiconductor in environmental applications with high efficiency removal of any organic molecules mainly due to its unconditional benefits. The benefits include; (i) non-toxicity, (ii) chemically and biologically inert, (iii) strong photooxidation power, (iv) natural abundance, (v) low cost and (vi) favourable optoelectronic properties over other equivalent photocatalysts like ZnO, SnO_2, CdS, ZnS and etc (Ding et al., 2000; Grabowska et al., 2013; R. Su et al., 2011; Yuxin Tang et al., 2012; Z. Wang et al., 2014; Yan et al., 2013; Zhou, Liu, Yu, & Fan, 2012).

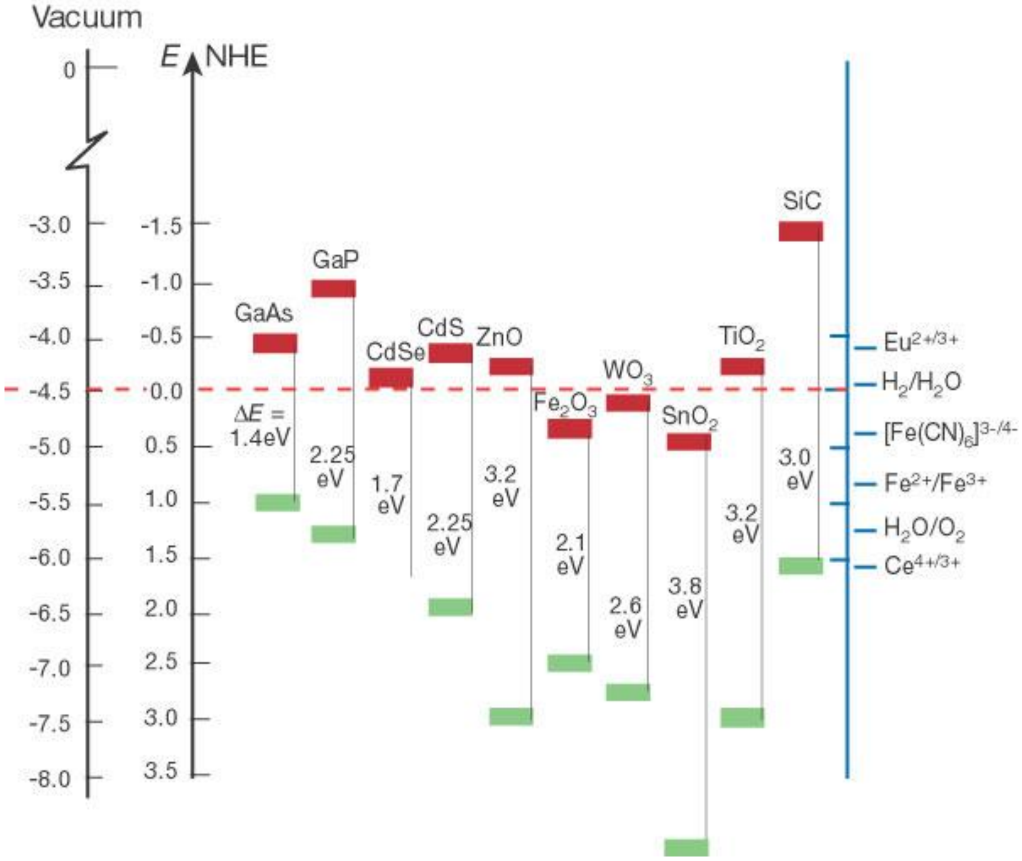

Figure 1.2: Band positions of various semiconductors (Gratzel, 2001)

TiO_2 exits in Anatase, Rutile and Brookite crystallographic phases. The difference in crystallographic phases has much influence on the photocatalysis characteristics. Among these phases, anatase and rutile with a tetragonal structure are the most commonly suitable for photocatalysis application (Yan et al., 2013). However, anatase phase upbeats the rutile and emerged as most capable and efficient photocatalyst due to its higher Fermi level and degree of hydroxylation (Carp, Huisman, & Reller, 2004).

1.3 Problem Statements

Although TiO_2 exhibits great photocatalysis by producing hydroxyl and superoxide anion radicals, it also possess several drawbacks that narrow down its applicability. This includes the wider band gap energy (E_g) of TiO_2 (3.21 eV) (Reyes-Coronado et al., 2008) that shrinks its candidature to ultraviolet (UV) region. It is well known that the availability of the UV source is restricted (< 5 %) in the sphere by the ozone layer than that of the visible and infrared (Das & Ghosh, 2013; S. G. Kumar & Devi, 2011; Tong et al., 2012; Z. Wang et al., 2014). In order to promote the environmental sustainability, endless renewable natural source of cleaner fuel, the contemporary Titania must be considered for greater modifications. Next coming back to its recombination characteristics of excited electron (e^-) and hole (h^+) it is always very rapid and suppress the generation of active radicals for photocatalysis reaction (Bumajdad & Madkour, 2014; Leung et al., 2010; Ong, Tan, Chai, Yong, & Mohamed, 2014). This recombination rate was found to be ~30 ns that leads to poor photocatalytic performance (J. Chen, Yao, & Wang, 2008; Chong, Jin, Chow, & Saint, 2010; S. Kim, Hwang, & Choi, 2005). Hence, it is vital to fabricate photocatalysts that possess enhanced visible light absorption along with prolonged lifetime duration of generated electrons (e^-) and holes (h^+).

Various modifications have been practiced to overcome the shortfalls of TiO_2 photocatalyst through doping with metals and non-metals (Pan, Yang, Fu, Zhang, & Xu, 2013; D.-H. Wang, Jia, Wu, Lu, & Xu, 2012; Xiang, Yu, & Jaroniec, 2011), mashing with other semiconductors (Karunakaran & Gomathisankar, 2013; G. Li, Zhang, & Jimmy, 2009; M. Li et al., 2013; Yajun Wang et al., 2013b), incorporation of carbonaceous materials like graphene, activated carbon and carbon nanotubes (Ong, Gui, Chai, & Mohamed, 2013; L. Sun, Zhao, Zhou, & Liu, 2012; Y. Zhang, Tang, Fu, & Xu, 2011). However, recent innovation on improvisation to TiO_2 photocatalyst had benefited to overcome its limitations.

Noble metals, recognized as a new category of efficient agent or dopant to stimulate the visible light utilization due to their higher optical absorption in visible spectrum. They demonstrates a localized surface plasmon resonance (LSPR) phenomenon that allows their interaction, promotes and maximize light absorption in the visible region. Besides that, the formation of Schottky junction between the noble metal and semiconductor prolong the lifetime of the generated charge carriers. On top of it, they can function as effective co-catalysts to reduce the over potential for surface electrochemical reactions (Qu & Duan, 2013).

On the other hand the recent development and domination of the carbonaceous elements attracted the photocatalysis researchers as well. The RGO finds a greater application owing to its unique characteristics that facilitates the bonding of Ti with C. (Tan, Ong, Chai, & Mohamed, 2013; Umrao et al., 2014). Apart from it the polymeric semiconductor graphitic carbon nitride (g-C_3N_4) also plays a vital role due to its exclusive properties of good physicochemical stability and an appealing electronic structure combined with a medium band gap (2.7 eV). Thus demonstrating their necessity as potential agent for enhancing and modifying the characteristics of conventional TiO_2 (Sridharan, Jang, & Park, 2013; L. Zhang et al., 2014).

1.4 Objectives and Scope of Research

The key scope of the present study is to top down the identified limitations of the conventional titania by incorporating the most active noble metals (Pd and Ag) to trigger the surface plasmon resonance characteristic and form a classification called *"plasmonic photocatalysts"*. In addition, conducting carbon materials such as reduced graphene oxide (RGO) was wrapped with TiO_2 together with noble metals to further enhance the visible light absorption and promote the charge carrier transportation. Apart, the photocatalytic ability is also examined by incorporating with a ternary metal free semiconductor (g-C_3N_4). The visible light photocatalysis ability of the synthesized nanocomposite photocatalysts were evaluated by degrading variant genera of pollutants that include Endocrine Disrupting Compounds (EDCs) and Dyes under solar and artificial visible light source. Overall the studies presented new insights in the modification of the TiO_2 that enhances the visible light absorption and lead to a better photocatalytic activity performance. The objectives of the work are as follows:

- **Synthesis of Template:** To synthesize highly pristine anatase TiO_2 nanoparticles (NPs) as template through a simple, facile and ease method.
- **Inclusion of Plasmonic Phenomenon:** To identify suitable noble metals from the periodic table along with a novel, smart, ease and sustainable method to incorporate them onto TiO_2 template for activating Localized Surface Plasmon Resonance (LSPR) Phenomenon and identifying the optimum loading of noble metals.

- **Electron Mobility Promoter:** To investigate the contribution of carbon materials for visibility, electron mobilizing and charge carriers' transportation by wrapping it onto the synthesized composite photocatalysts.
- **Dissection of Photocatalysts:** To characterize the prepared nanocomposite photocatalysts for its various intrinsic natures through crystalline phase analysis, morphology, elemental composition, surface area and pore size characteristics, chemical composition with electronic state, Raman scattering, optical and photoluminescence properties.
- **Assessment of Visible Light Performance:** To evaluate the visible light photocatalysis ability of the synthesized nanocomposite photocatalysts by adopting various categories of simulated EDC and Dye pollutants.

1.5 Report Overview

Chapter 1 presents the introductory note on photocatalysis process and semiconductor titania. This is followed by problem statement together with specific research hypotheses. The chapter ends with identified specific objectives for resolving the research hypothesis.

Chapter 2 outlines the comprehensive report on the literatures. It elaborates the clear background on heterogeneous and semiconductor photocatalyst (TiO_2). Besides that, it also elaborates on the synthesis method and modifications of TiO_2 which lead to enhance visible light absorption and suppress the recombination rate of electron and hole pairs. It also reviews the environmental applications of prepared photocatalyst in degradation of variant toxic and lethal liquid pollutants.

Chapter 3 discusses on the adopted precursor, solvents and synthesis method for obtaining synergized modified photocatalysts. The chapter also narrates on the various experimental conditions, analytical methods practiced for characterizing the synthesized photocatalysts and quantifying the studied pollutants.

Chapter 4 presents the results of the adopted research hypotheses. This chapter unveils the materials chemistry of the prepared photocatalysts and its versatility in utilizing the visible light with its mechanism. The chapter also substantially discusses on the photocatalysis excellence demonstrated by the prepared materials towards visible light driven environmental cleanup applications.

Chapter 5 summarizes the entire significant outcome of the thesis and recommendations for the continuation of the current studies.

CHAPTER 2

LITERATURE REVIEW

2.1 Heterogeneous Photocatalysis

Heterogeneous photocatalysis a classification of Advanced Oxidation Processes (AOPs) plays a major role in Environmental Nanotechnology and is recognized as one of the “foundation pillars” of green chemistry (Anastas, Kirchhoff, & Williamson, 2001). In general catalyst is defined *as a substance that can accelerates a chemical reaction without being consumed as a reactant*. Meanwhile, photocatalyst is defined *as the acceleration of a reaction by the presence of a catalyst through photon energy*. Over the past decades, the application of this photocatalysis concept has proven to be promising in solving many major environmental and energy concerns like toxic organics pollutants degradation, water split reaction for hydrogen production and CO_2 reduction.

The heterogeneous photocatalysis involves the presence of a semiconductor photocatalyst to initiate or accelerate specific redox reactions (reduction and oxidation). A schematic illustration of the principle of semiconductor photocatalysis is shown in Figure 2.1. When this semiconductor photocatalyst is illuminated with photon energy which is equal or greater than their band gap energy, electrons and holes are generated in the valence band (Figure 2.1(I)). Moreover, with sufficient energy, the electrons (e^-) are excited from valence band to conduction band leaving behind positive holes (h^+) (Hoffmann, Martin, Choi, & Bahnemann, 1995). Thus excited electrons and formed holes migrate to the surface and perform the redox reactions. The electrons from the conduction band possess chemical potential of +0.5 to -1.5 V versus the normal hydrogen electrode

(NHE) and reveal a strong reduction capacity (Figure 2.1(III)). Meanwhile, the holes in the valence band possess chemical potential of +1.0 to +3.5 V versus the NHE and exhibited a strong oxidative potential (Figure 2.1(IV)). Thus photogenerated electrons and holes felicitates the robust redox reaction. The electron donors or electron acceptors are adsorbed on the surface of semiconductor and produces active radical, responsible for the degradation of pollutants (Figure 2.1(V)) (H. Wang et al., 2014).

During the photocatalysis, recombination of excited electrons with the holes are forced and dissipates the input energy in the form of light or heat (Figure 2.1(II)). This recombination phenomena occurs due to the scavenger or crystalline defects and able to trap the electrons and holes. Based on the fundamental of semiconductors photocatalyst principles, this phenomenon heavily hinders the photocatalytic efficiency.

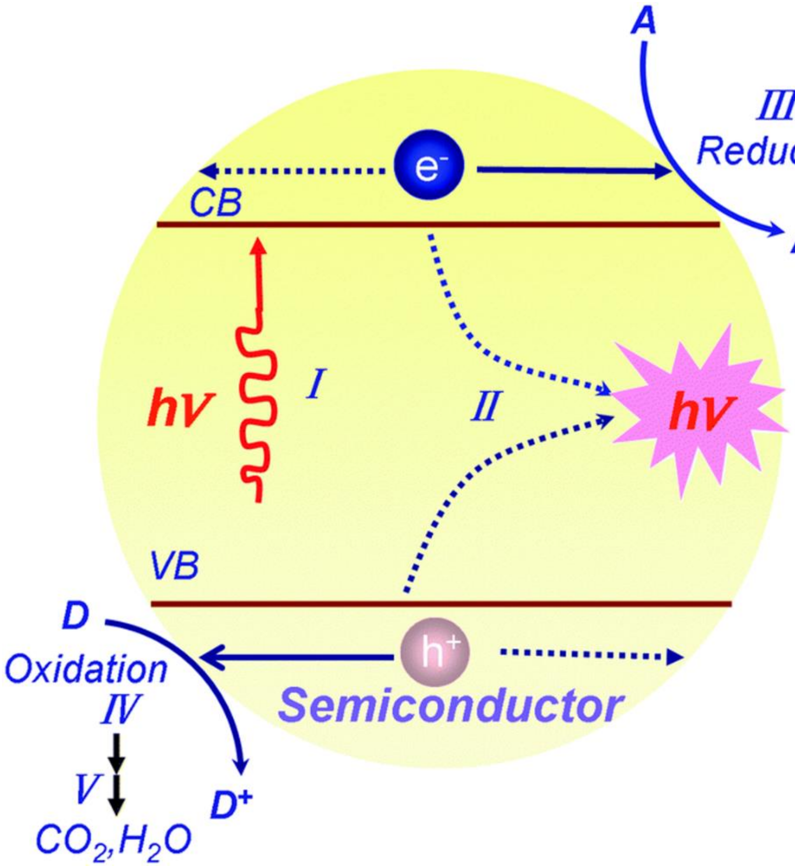

Figure 2.1: Schematic illustration of semiconductor photocatalysis principle (H. Wang et al., 2014)

Numerous advantages that heterogeneous photocatalysts can offer are such as (i) enrich the semiconductor light absorption ability by incorporating with metal/non-metal, other semiconductors and noble metal (ii) improving the charge separation efficiency by forming a Schottky junction (metal/semiconductor heterostructures) with build in electrical potential or p-n (semiconductor/semiconductor heterostructures) (iii) integration with a suitable cocatalyst can lower the redox over potential at the relevant active sites (Qu & Duan, 2013).

2.2 Semiconductor Photocatalyst (TiO_2)

Over the past years, interest in the application of semiconductor photocatalyst has grown tremendously attracted the environmental engineers for a full-fledged treatment of liquid and gaseous waste. These semiconductors (TiO_2, ZnO, Fe_2O_3, CdS and ZnS) embrace electronic structure of completely filled valence band and empty conduction band. The electronic structure endorses as sensitizers for light reduced redox processes (Hoffmann et al., 1995). Among the many semiconductors, TiO_2 turn out to be the most attractive and promising semiconductor as photocatalyst. This was owing to its superficies, versatile and unique characteristics that allow concurrent oxidation of water and reduction of protons. The innovative feature of TiO_2 was first identified by Honda and Fujishima in 1972 where they discovered a photosensitization effect of TiO_2 electrode for electrolysis of water into H_2 and O_2 upon applying an external bias (Fujishima & Honda, 1972). Further it also exhibits merits including non-toxicity, chemical and biological inert, photostability, high photoactivity and economical (Ding et al., 2000; Grabowska et al., 2013; R. Su et al., 2011; Yuxin Tang et al., 2012a; Z. Wang et al., 2014). Thus designate TiO_2 photocatalyst as potential candidate for various environmental and energy remediation.

It is well known that this photocatalyst exists in three crystalline phase i.e., anatase, rutile and brookite. The structures of these are depicted in Figure 2.2 and crystal data is tabulated in Table 2.1. Both the anatase and rutile exhibited tetragonal crystal structures and the distortion of cubic lattice is more significant for anatase resulting in a less orthorhombic symmetry than rutile (Nick Serpone & Pelizzetti, 1989; Thompson & Yates, 2006). It also possess higher Fermi level and degree of hydroxylation that makes its more active in driving photoreaction than the other phases (Carp et al., 2004; Hyun & Kang, 1996; Kermanpur, Ghassemali, & Salemizadeh, 2008; Samuneva, Kozhukharov, Trapalis, & Kranold, 1993). Besides rutile phase shows high recombination rate of electron-hole pairs and very low density of superficial hydroxyl groups that limits its photocatalytic reaction (Choi, Termin, & Hoffmann, 1994; Sclafani & Herrmann, 1996).

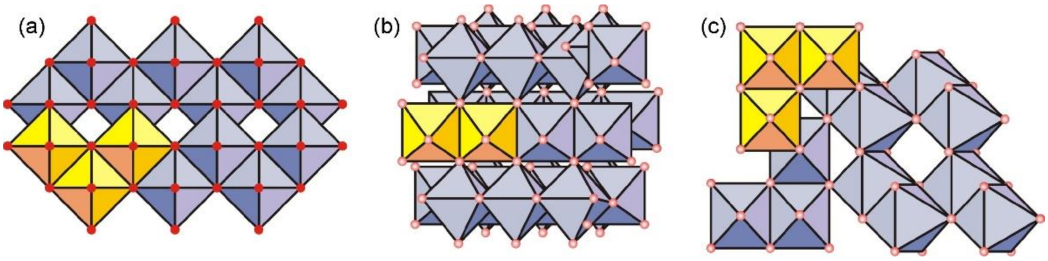

Figure 2.2: Crystalline structure of TiO_2 (a) Anatase, (b) Brookite and (c) Rutile (Khataee & Kasiri, 2010)

Table 2.1: Crystal structure data for various phase of TiO_2 (Baur, 1961; Cromer & Herrington, 1955)

	Anatase	**Rutile**	**Brookite**
Crystal structure	Tetragonal	Tetragonal	Orthorhombic
Lattice constants (Å)	$a = 3.784$	$a = 4.5936$	$a = 9.184$
	$c = 9.515$	$c = 2.9587$	$b = 5.447$
			$c = 5.145$
Space group	$I4_1/amd$	$P4_2/mnm$	*Pbca*
Molecule/cell	4	2	8
Volume/molecule (Å^3)	34.061	31.216	32.172
Density (g/cm^3)	3.79	4.13	3.99
Ti – O bond length (Å)	1.937 (4)	1.949 (4)	1.87 ~ 2.04
	1.965 (2)	1.980 (2)	
O – Ti – O bond angle	77.7°	81.2°	77.0° ~ 105°
	92.6°	90.0°	

The applications of semiconductor nanomaterial are much dependent on the preparation method and greatly influenced by the size and morphology also. Therefore various synthesis methods such as sol-gel process (Hench & West, 1990; Hou, Hung, et al., 2011; Rodríguez-González, Zanella, del Angel, & Gómez, 2008), hydrothermal and solvothermal process (Humin Cheng, Ma, Zhao, & Qi, 1995; Yoshimura & Byrappa, 2008; S. Zhu et al., 2012) and deposition methods (Lee & Tu, 2008, J.-J. Wu & Tseng, 2006) have been practised. Synthesis through sol-gel method has dominated over the rest due its facile nature in achieving TiO_2 with high purity and superior compositional homogeneity (Stoyanova et al., 2010).

2.3 Sol-Gel Synthesis

Sol-gel route is mostly considered in synthesis of pristine anatase TiO_2 because it provides compositional and microstructural modification through controlling the precursor and the governing synthesis parameters. It also delivers superior chemical homogeneity, unique metastable structures and high purity (Niederberger, Bartl, & Stucky, 2002; C.-C. Wang & Ying, 1999). However, most of the cases the chemical reactions rate are very fast especially with transition metal precursors, making it difficult to control the chemical process. This could be the major limitation of sol-gel method where a minor modification in the synthesis parameter could lead to a drastic change in structure and morphology of the nano photocatalyst (Stoyanova et al., 2010). In order to outwit this limitation and secure the benefits of sol-gel synthesis method, non-hydrolytic sol-gel method was developed (Djerdj, Arčon, Jagličić, & Niederberger, 2008; Vioux, 1997). This synthesis is performed in an organic solvents in the absence of water lead to a slower reaction rate and provides better control over the particle size and crystallinity (Niederberger & Garnweitner, 2006).

In synthesis of TiO_2 using non-hydrolytic sol-gel method, it usually involves the reaction of titanium chloride (or alkoxide) with different oxygen donor molecules such as alcohol, ether, aldehyde or ketone. The condensation between Ti – Cl and Ti – OR, results in the formation of Ti – O – Ti where the alkoxide functions can be provided by titanium alkoxides or can be formed in situ by reaction of titanium chloride with oxygen donors (Niederberger et al., 2002). Hence, this facile synthesis method results in the formation of pristine anatase TiO_2.

2.4 Modification of Titania

The candidature of TiO_2 has been studied extensively for three decades due to their incomparable qualities. However, they have few major drawbacks on its photoexcitation domain: (i) wide band gap energy 3.2 eV (ii) higher recombination rate of photogenerated electrons and holes and (iii) low absorption ability in the visible light region. All these limitations hinder its inherent photocatalytic characteristics especially in the visible light region. Therefore, remarkable effort has been dedicated to overcome all these limitations especially in utilizing the abundant renewable energy (solar energy), ~43.0% of visible light as compare to <5.0% of UV light. Hence, it is important to design a photocatalyst that can effectively extend the light absorption spectra to visible region in order to enhance the harvesting of solar energy. Besides that, further modification necessitates the minimisation of recombination rate of electrons and holes in order to enhance the redox reaction.

Tremendous modification methods through doping or composite with metal or non-metal (Xiang, Yu, & Jaroniec, 2011; Xiang, Yu, Wang, & Jaroniec, 2011; J. Yu, Xiang, & Zhou, 2009), coupling and construction of heterojunctions (Hefeng Cheng et al., 2013; K. Su, Ai, & Zhang, 2012; Zeyan Wang et al., 2009), integration with carbonaceous material (Ong et al., 2013; L. Sun et al., 2012) and plasmonic photocatalyst (Hou, Liu, Pavaskar, Hung, & Cronin, 2011; Lou et al., 2011; Peng Wang et al., 2011; F. Xiao, 2012b) had been executed by various researchers. Off these, plasmonic photocatalyst emerged as the best and overshoots the limitations of other modification methods. The notable drawbacks of these methods were listed below. The non-metal doping promotes production of oxygen vacancies that act as a recombination center for electrons and holes. Similarly, metal doping lead to the formation of defects inside TiO_2 which reduces the photoreactivity (Nagaveni, Hegde, & Madras, 2004; Xu, Gao, & Liu, 2002). Therefore, by decorating noble metal onto semiconductor spinal had proven to trigger the localized surface plasmon resonances phenomena (LSPR) for better visible light photocatalytic activities.

2.5 Plasmonic Photocatalyst

A combination of noble metal and semiconductor photocatalysts form a unique "*Plasmonic photocatalyst*" classification. Recently, plasmonic photocatalysts have been proven to yield high photocatalytic performance due to its inherent contributions to the semiconductor photocatalyst and results in enhanced wide range of light absorption, suppressed electron-hole recombination rates, increased photogenerated electron-hole pairs and improved the redox reactions rates (Z. Wang et al., 2014). The distinct characteristics features contributed by the plasmonic photocatalysis are illustrated in Figure 2.3.

Noble metals (i.e Ag, Au, Pd, Pt) in nanoparticles form acknowledge as new impurity agent for harvesting visible light energy due to their high optical absorption over a wide range of the solar spectrum (Cushing et al., 2012; Linic, Christopher, & Ingram, 2011). This strong absorption of light energy in visible region is due to its own characteristic of surface plasmon resonance (SPR) effect. The surface plasmon band is a robust and broad band in the visible spectrum of metallic nanoparticles possessing size > 2 nm (Shin et al., 2010). The intensity of the surface plasmon band is much dependent on the size, shape, monodispersity, dielectric constant of surrounding medium, electronic interactions between stabilizing ligands and nanoparticles (Moores & Goettmann, 2006).

Besides, when these nanoparticles interact with semiconductor it promotes Schottky junction a unique feature of noble metals. This Schottky formation contributes for reduction in recombination rates of electron-hole pairs (Zhichao Wang, Liu, & Chen, 2012).

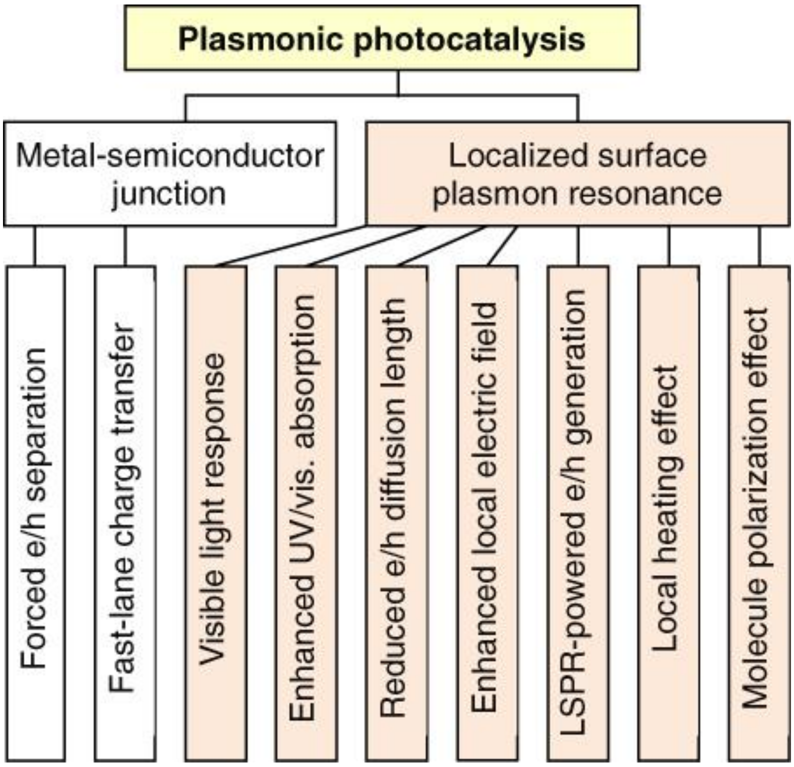

Figure 2.3: Major benefits of plasmonic photocatalysis (X. Zhang, Chen, Liu, & Tsai, 2013)

The Localized Surface Plasmon Resonance (LSPR) of a noble metal NPs arises when it’s being induced by the oscillating electric field of the imposing light. During the oscillation the photon frequency ties with the natural frequency of the noble metal leading to decline in electrons to one side of the noble metal NPs and surge on the other side of the surface. This phenomenon will cause the redistribution of the charge density and thus create an electric field inside and outside of the noble metal NPs in opposite direction.

Therefore a coulombic restoring force is then established and the conducting electrons of the noble metal NPs will then undergo a harmonic oscillation in phase with the incident light (Sarina, Waclawik, & Zhu, 2013; C. Wang & Astruc, 2014; Peng Wang, Huang, Dai, & Whangbo, 2012; Zhou et al., 2012). This oscillating charges excites electric field near the surface and once the frequency is adequate with the resonance of the noble metal, SPR is triggered, leading to the active absorption of visible light (Figure 2.4 (a)). This absorption visible spectrum promoted through SPR is attributed to the electric polarization effect. In addition, SPR on noble metal accelerates the electron transfer from the photoexcited noble metal to any polar semiconductor (P. Wang et al., 2012).

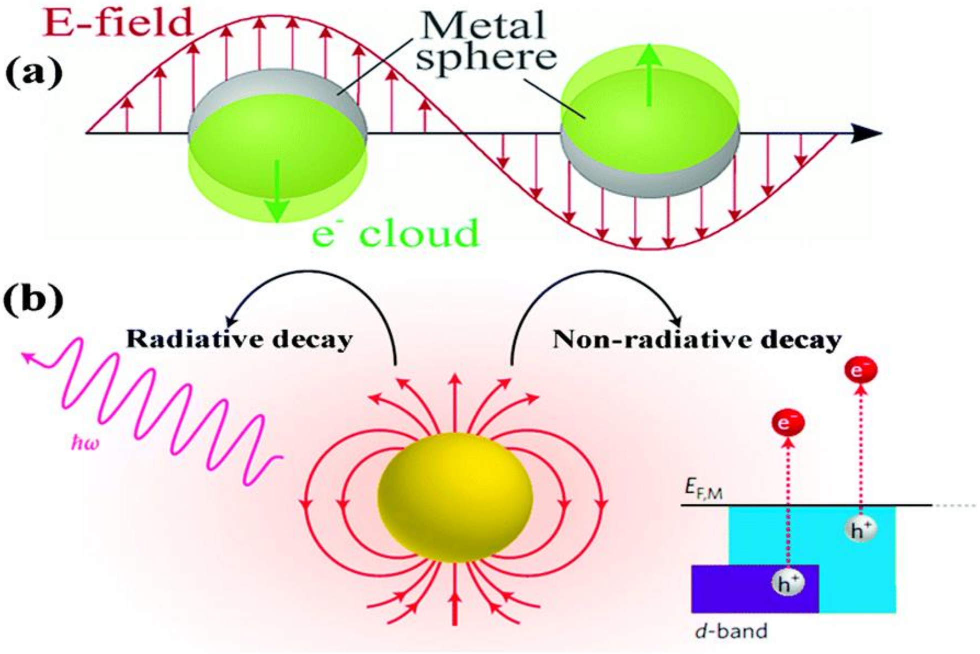

Figure 2.4: (a) Schematic of SPR in a noble metal particle that is illuminated by light (Kelly, Coronado, Zhao, & Schatz, 2003). (b) Surface plasmon decay processes (Clavero, 2014)

The plasmon excitation decaying processes play a crucial role and that determine the photocatalytic efficiency of plasmonic photocatalyst. It entails depositing energy into the absorbates through different pathways and transferring energy from the plasmonic metal NPs to any polar semiconductors (Kale, Avanesian, & Christopher, 2014). There are two major pathways for the occurrence of oscillation of electron decay either through radiative or non-radiative (Figure 2.4 (b)). The radiative process results in scattering of light effect and dominated by larger particle size (≥ 40 nm). Meanwhile the non-radiative decay process is mainly governed by smaller one and will enhance the absorption resulting in the excitation of energetic electrons and holes (C. Wang & Astruc, 2014). In noble metal this non-radiative decay occurs through intraband excitations within the conduction band or through interband excitations resulting from transitions between other bands and conduction band.

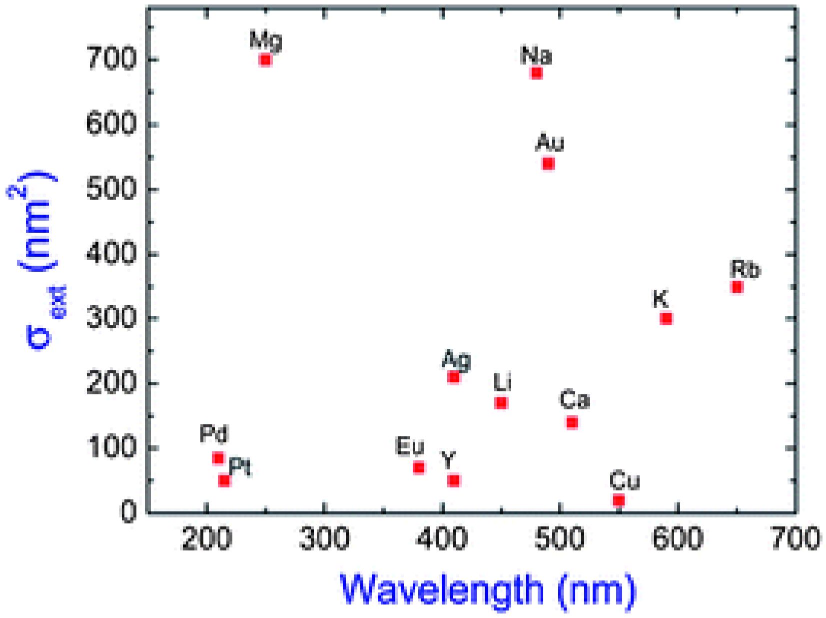

Figure 2.5: The corresponding resonant wavelength for metallic nanoparticles of 10 nm (Garcia, 2011)

The surface plasmon resonance frequency strongly influences various parameters of the noble metals and it includes particle size, shape, interparticle interactions and local dielectric environment (Galian & Perez-Prieto, 2010; Haruta, 2005; Palmisano et al., 2010; Stahl, 2005). It is also to be noted that not all noble metal with the particles size 10 nm are capable to absorb light in the visible region as shown in Figure 2.5. Most commonly, Ag and Au NPs are in favour to absorb photon energy with a relative strong excitation in the visible regime. Moreover, these two noble metals possess a characteristic of producing a stable high charge carrier density (Boltasseva & Atwater, 2011). However, cost of Ag makes it more appropriate to be used for wider applications. Hence, many studies had been reported by other researchers on using Ag as plasmonic materials (Choi, Shin & Jang, 2010; Xiang et al., 2010; Xie et al., 2011). Where else, palladium NPs with smaller size are restricted to UV spectrum. However, larger particle and clustered size overdrawn the restriction by well absorbing in the visible light regime. This was demonstrated by Mohapatra and coworkers where they successfully achieved the visible light enhancement for the Pd NPs in range of ~80 nm in diameter (Mohapatra, Kondamudi, Banerjee, & Misra, 2008). Similar findings were observed by Kwak et al by incorporating Pd NPs (~15 nm) onto TiO_2 leading to an increase absorption in visible spectrum (Kwak, Chae, Kim & Kang, 2009).

The mechanism of plasmon-assisted physics is of great interest in understanding the generation and injection of excited electrons. When photon energy is absorbed, free electrons of metal NP occupy higher energy level. Considering a single electron, the excitation will take place at lower Fermi level (E_f), producing a constant distribution of primarily excited electrons at energy level between E_f and $E_f + h\upsilon$ (Kale et al., 2014). This excited electron losses its energy readily right after the primary plasmon excitation through electron-electron relaxation within ~ 10 fs through non-equilibrium Fermi-Dirac electron distribution (Molina, Weinmann, & Jalabert, 2002). In this energy redistribution process, excited electron is transferred from the metal NPs to the semiconductor and it fully dissipates the electron in the semiconductor (Kochuveedu, Jang, & Kim, 2013). These phenomena of equilibration of the E_f will cause a bending of the semiconductor conduction band and form a Schottky barrier that prevents electron transfer from the metal to the semiconductor. The excited electrons with energies higher than the Schottky barrier are injected into the nearby semiconductor through the SPR decay effect (White & Catchpole, 2012). The plasmonic nanostructures will then leave positively charged holes due to electron depletion. Thus generates holes undergo electron-donor process or transporting generated holes to the counter electrode in order to prevent the recombination (Clavero, 2014). Figure 2.6 (a) shows the excitation of electron from the thermal equilibrium to higher energy state upon photons irradiation. While in Figure 2.6 (b) illustrates the collision prompted a formation of Fermi Dirac distribution at a high temperature Fermi level due to redistribution of electron energy. Figure 2.6 (c) portraits the excited electrons flow back to the standard distribution meanwhile in the semiconductor electrons and holes flow to different regions (Kochuveedu et al., 2013; X. Zhang et al., 2013).

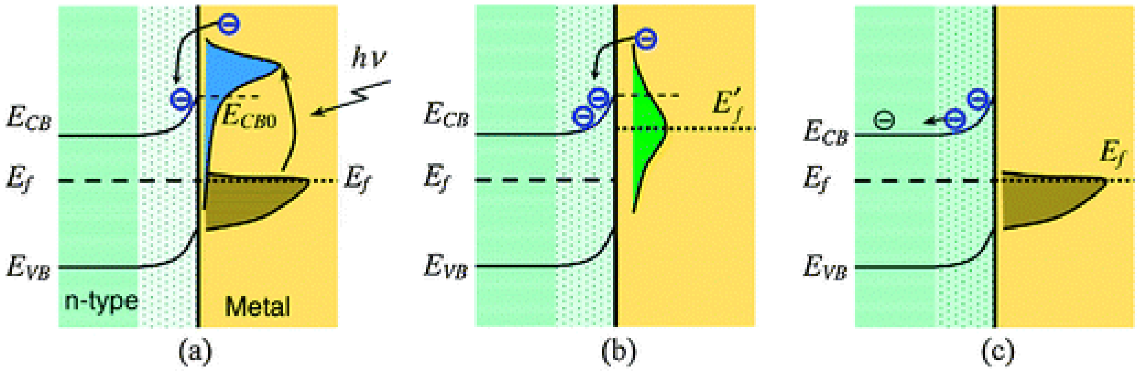

Figure 2.6: Illustration of Surface Plasmon Resonance principle (Kochuveedu et al., 2013; X. Zhang et al., 2013)

The formation of Schottky barrier is another unique characteristic of plasmonic photocatalysts. This formation is created when a metal and a semiconductor interact with each other (Figure 2.7). Electrons will flow from higher Fermi level to the lower in order to align the energy level at the interface of the metal and semiconductor. This equilibrium of Fermi level creates a build in electric field at the interface which will promote the charge separation of photogenerated electrons and holes by forcing the electrons and holes to move in different directions (Bumajdad & Madkour, 2014; Qu & Duan, 2013; Jian Tian, Zhao, Kumar, Boughton, & Liu, 2014; H. Wang et al., 2014).

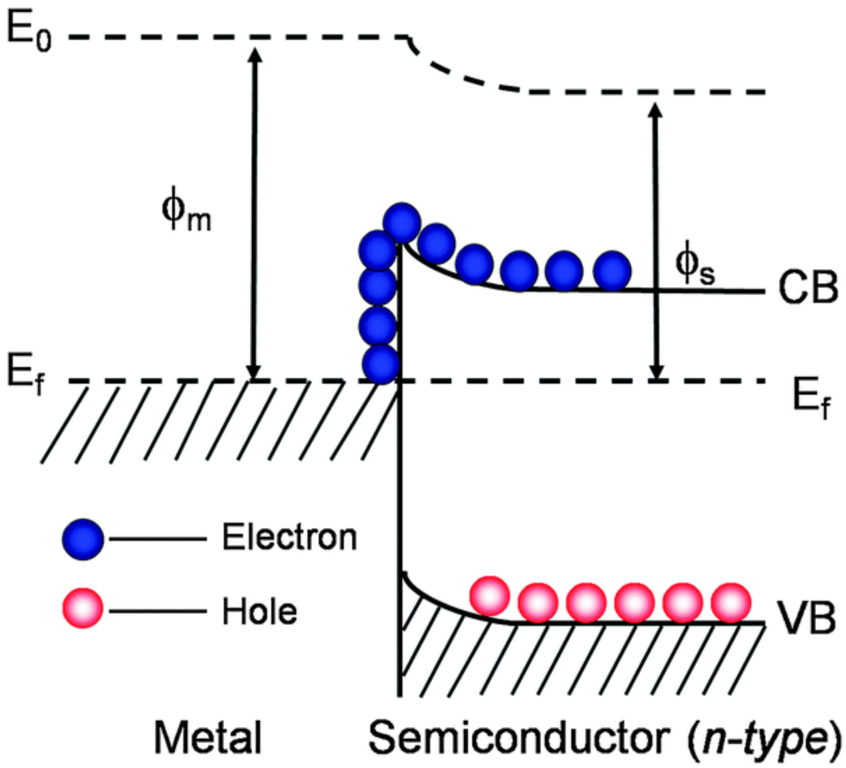

Figure 2.7: Schematic of the Schottky barrier (H. Wang et al., 2014)

2.6 Preparation of Plasmonic Photocatalysts

There are numerous synthesis method adopted or practiced to prepare plasmonic photocatalysts. Some of them are photoreduction (Kominami, Tanaka, & Hashimoto, 2010, 2011; Sung-Suh, Choi, Hah, Koo, & Bae, 2004; Xie, Kum, Zhao, & Cho, 2011), ion-exchange (Hefeng Cheng et al., 2011; Peng Wang, Huang, Lou, et al., 2010; Peng Wang, Huang, Zhang, et al., 2010), deposition-precipitation (Gomes Silva, Juárez, Marino, Molinari, & García, 2010; Peng, Hu, Hu, Zhou, & Qu, 2012; Hui Zhang, Fan, Quan, Chen, & Yu, 2011), chemical reduction (Christopher, Xin, & Linic, 2011; Ingram & Linic, 2011; Nair, Tripathi, & Samdarshi, 2011), hydrothermal (S. Sun, Wang, Zhang, Shang, & Wang, 2009; Xiang, Yu, Cheng, & Ong, 2010), physical vapour deposition (Hou, Liu, et al., 2011; Z. Liu, Hou, Pavaskar, Aykol, & Cronin, 2011), impregnation (H. Yu, Liu, Wang, Wang, & Yu, 2012; Zheng et al., 2011) and encapsulation (Thomann et al., 2011; Torimoto et al., 2011). The various preparation methods of plasmonic photocatalysts along with its photocatalysis performance are tabulated in Table 2.2.

Table 2.2: Photocatalysis performance of various plasmonic photocatalysts along with its preparation method

Composite photocatalyst	Preparation method	Photocatalytic experiment & Photocatalysis performance	Reference
TiO_2-Ag	Polyol process	Photodegradation of Methylene Blue (0.65 mM) under UV light irradiation. Ag cubes TiO_2 exhibited a better photo degradation as compare to other shapes such as wires and spheres.	Christopher, Ingram & Linic, 2010

Table 2.2, continued

Composite photocatalyst	Preparation method	Photocatalytic experiment & Photocatalysis performance	Reference
TiO_2-Ag	Polyol process	Photodegradation of Methylene Blue (0.65 mM) under UV light irradiation. Ag cubes TiO_2 exhibited a better photo degradation as compare to other shapes such as wires and spheres.	Christopher, Ingram & Linic, 2010
Ag-TiO_2	Microwave hydrothermal	Photodegradation of RhB under $\lambda > 420$nm. The prepared Ag-TiO_2 nanocomposite hollow spheres exhibited highest photocatalytic activity by a factor of more than 2 compare to pure TiO_2 and commercial Degussa (P25).	Xiang et al., 2010
Ag-TiO_2	Photo deposition	Degrading Rhodamine B under visible light with an initial concentration of 10^{-5} M. Ag-TiO_2 with 2% Ag content was found to be the optimum loading and achieved highest efficiency with ~30% increase in photo degradation as compare to TiO_2.	Sung-Suh et al., 2004
Ag/TiO_2	Electrochemical deposition	Photocatalytic degradation of Methyl Blue (2×10^{-5} M) illuminated with light intensity > 420 nm. Ag/TiO_2 achieved about 80% removal in 2.5 h as compare to pure TiO_2.	Z. Chen et al., 2014
Ag-TiO_2	Sol-gel process	Photodegradation of Indigo carmine under visible light with an initial concentration of 2.5×10^{-5} M. Ag modified TiO_2 showed great photocatalysis performance where it achieved a complete removal after 3 h as compare to pure TiO_2.	Suwanchawalit, Wongnawa, Sriprang, & Meanha, 2012

Table 2.2, continued

Composite photocatalyst	Preparation method	Photocatalytic experiment & Photocatalysis performance	Reference
Ag@TiO_2	Photo reduction by artificial UV light	Photodegradation of Rhodamine B irradiated under visible light. Ag@TiO_2 with an optimal catalyst loading of 1% of Ag shown a complete degradation in 30 min with an initial dye concentration of 10 mgL^{-1}.	D. Chen et al., 2013
Ag/AgCl	In situ oxidation process	Photodegradation of Methyl Orange and 2, 4 dichlorophenol under visible light irradiation. AgCl with the ratio of 85% revealed the best photocatalytic performance in degrading both the pollutants where an efficiency of 65% (Methyl Orange) and 78% (2, 4-dichlorophenol) was achieved	Jia, Yang, & Huang, 2014
Ag-AgCl	Hydrothermal	Decomposition of Methyl Orange under visible light with an initial concentration of 10 mg/L. It achieved almost a complete removal in 18 min.	Han, Wang, Zhu, Zhai & Dong, 2011
Ag-AgCl	Precipitation of AgCl followed by reduction	Photodegradation of Methyl Blue under visible light and sunlight with an initial concentration of 20 mg/L. It shows a great enhancement under sunlight with a complete removal in 30 min.	An, Peng & Sun, 2010
Ag-AgBr	Light induced chemical reduction	Degrading Methyl Orange (20 mg/L) under visible light illumination. A complete degradation was obtained after irradiation for 10 min.	Wang et al., 2009
Au-TiO_2	Electrochemical-evaporation	Water splitting under visible light irradiation. After the addition of Au nanoparticles, it observed a drastic enhancement in the photocatalytic splitting of water	Liu et al., 2011

Table 2.2, continued

Composite photocatalyst	Preparation method	Photocatalytic experiment & Photocatalysis performance	Reference
TiO_2-Au	Deposition – precipitation	Photocatalysed reduction of nitrobenzene (1×10^{-3} M) and photooxidation of alcohols (5×10^{-4} M) under UV and visible light respectively. TiO_2-Au/anatase showed a higher UV light activity for the reduction of nitrobenzene than TiO_2-Au/rutile. Meanwhile TiO_2-Au/rutile showed an increase in visible light activity for the oxidation of alcohols.	Kimura, Naya, Jin-nouchi & Tada, 2012
Au@TiO_2	Deposition-precipitation-photoreduction	Oxidation of benzene (0.07 mL) under visible light irradiation. Au@TiO_2 yielded about 61% of benzene was oxidized to phenol after 3 h of irradiation.	Zheng et al., 2011
Pd/TiO_2	Incipient wetness	Photo degradation of azo dyes under visible light with an initial dyes concentration of 0.024 mM. A complete removal was attained in 150 min (Methyl Red) and 270 min (Methyl orange) by Pd/TiO_2.	Mohapatra et al., 2008
Pt-TiO_2	Deposition-precipitation	Oxidation of benzyl alcohols (100 mg/L) to aldehydes under visible light source. After 3 h of visible light irradiation, Pt-TiO_2 shows about 90% conversion of alcohols as compared to pure TiO_2.	Zhai, Xue, Zhu, Luo & Tian, 2011

2.6.1 Photoreduction

Among the synthesis methods, photoreduction method had defeated the rest due to its relatively high deposition ratio and low aggregation (Zhou et al., 2012). This preparation method is simple and eases where it delivers high quality plasmonic photocatalysts. This process involves the efficient anchoring of noble metal onto the semiconductor with the presence of photon energy. Semiconductors like TiO_2, ZnO and etc possess a unique electronic structure where it composes of filled valence band (VB) and empty conduction band (CB). When the semiconductor is irradiated with adequate photon energy (photon energy that exceeded its band gap energy), it generates electrons and holes at the valence band. This further excites the electrons from the valance band to the conduction band leaving behind the positive charge holes. The generated photoexcited electrons can interrelate with any ionic metal species to produce metallic NPs onto the support materials where else the holes at the valence band reacts with sacrificial scavenger. The schematic representation of photoreduction method is illustrated in Figure 2.8

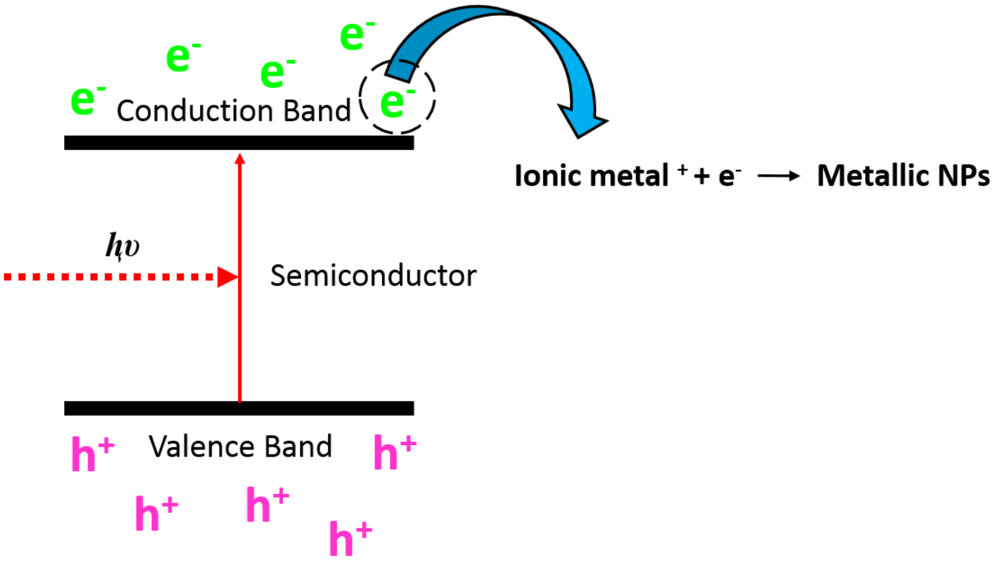

Figure 2.8: Schematic illustration of photoreduction synthesis method

The foremost advantage is that it possesses a high deposition ratio of noble metal onto the semiconductor surface. Kowalska et al., successfully deposited Au onto TiO_2 surface to form Au/TiO_2 under UV irradiation (Kowalska, Abe, & Ohtani, 2009). Meanwhile, Tanaka et al., also successfully synthesized Au/CeO with a large deposition ratio (> 99.9%) under UV light illumination (Tanaka, Hashimoto, & Kominami, 2011). The last one is it never requires further calcination as expected in other synthesis methods. The elimination of this calcination step reduces the aggregation of particles leading to high yield and homogenously deposition of noble metal onto the semiconductor.

In most cases an artificial UV light is being used as the source of photon energy for photoreduction method. But the high demand on sustainable and green approach in today context had driven us to look into a more renewable source of energy to replace the artificial UV light. Natural sunlight is an agent of sustainable choice for “green” chemical synthesis due to its abundance availability, environmentally friendly and economical. Therefore, utilizing the photon energy delivered by the natural sunlight could be a best replacement for artificial UV light. The supplied photon energy drives many photoreactions and encourages the reduction and deposition of noble metal onto any polar semiconductor to form plasmonic photocatalysts and support the sustainable route. This approach was successfully adopted in the presented study.

2.7 Carbon Material

Carbon nanomaterials applications in catalysis are well known and continue to grow for the past years. This type of nanomaterials is most commonly used either as support for immobilizing active species or as metal-free catalysis (Machado & Serp, 2012). There are few types of carbon nanomaterials like fullerenes, carbon nanotubes and graphene. Graphene a recent innovation had attracted great attention due to its versatile and diversified applications. It is a flat single layer of sp^2-bonded carbon atoms firmly packed into a two-dimensional honeycomb lattice (Jingqi Tian et al., 2012). It possesses distinctive electronic, optical, thermal and mechanical characteristics that had great influence in photocatalysis. Their numerous unique characteristics include: large specific surface area, outstanding thermal conductivity, high hydrophobicity, great adsorption capacity, high mobility of charge carriers and high optical transmittance (J. Liu, Tang, & Gooding, 2012; Machado & Serp, 2012; Yanhong Tang et al., 2012b; Jingqi Tian et al., 2012; Xiang, Yu, & Jaroniec, 2012; N. Zhang, Zhang, & Xu, 2012).

There are wide ranges of synthesis techniques for producing this graphene and can be classified into two different method namely "bottom-up" and "top-down" method. In bottom-up methods, the graphene is synthesized by chemical reaction through atoms or molecules (Xiang et al., 2012). The notable examples will be the growth on a single crystal SiC and chemical vapor deposition on metal foil surfaces (Juang et al., 2010; K. S. Kim et al., 2009; Wei et al., 2009). However these synthesis methods are not widely practiced due to its own complexity, limited scaling-up and high cost of precious metal substrates (Xiang et al., 2012). Therefore top-down methods such as thermal exfoliation (McAllister et al., 2007), electrostatic deposition (Tung, Allen, Yang, & Kaner, 2008) and chemical exfoliation of graphite (Dan Li, Müller, Gilje, Kaner, & Wallace, 2008; Park et al., 2009) are adopted for obtaining superior graphene. These top-down methods give rise to low cost, facile preparation process and larger yield as compare to bottom-up methods.

2.7.1 Chemical Exfoliation of Graphite

This is one of the most commonly used techniques in preparing high quality graphene and usually adapting the Hummers' method (Hummers Jr & Offeman, 1958). The reduced graphene oxide (RGO) in this method was achieved by oxidation of nature graphite powder with strong chemical oxidants like $KMnO_4$, HNO_3 and H_2SO_4. The obtained graphene oxide (GO) is then washed and dialysed to eliminate unnecessary inorganic impurities (residual ions and acids) through centrifugation. During the exfoliation of GO sheets, it normally possesses a rich assortment of oxygen containing groups (carboxylic, hydroxyl, epoxide functional groups) that allows the interactions with cations and further produces a reactive site. This reactive site is responsible for the rapid growth and nucleation of nanoparticles to various graphene based composites. Furthermore GO can also be reduced with fractional restoration of the sp^2-hybridized by either sonochemical (Vinodgopal et al., 2010), microwave reduction (Jasuja, Linn, Melton, & Berry, 2010), electrochemical (Ramesha & Sampath, 2009), photo thermal (Abdelsayed et al., 2010) or chemical method (Gao, Jang, & Nagase, 2009). A schematic of typical preparation of reduced graphene oxide by chemical reduction (Hummers' method) is depicted in Figure 2.9.

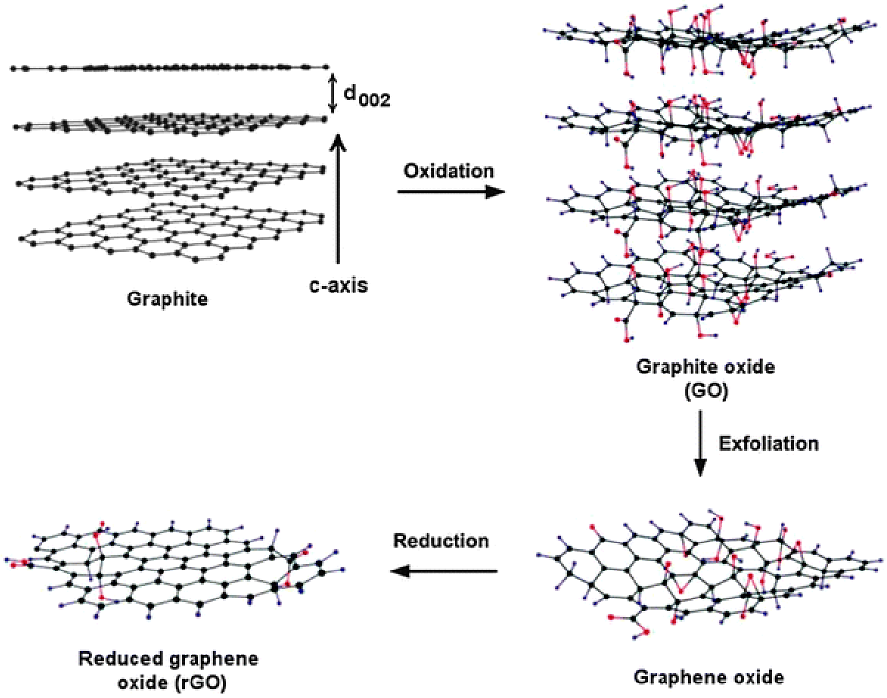

Figure 2.9: Schematic of preparation of reduced graphene oxide by chemical reduction (Hummers' method) (Bai, Li, & Shi, 2011)

2.7.2 Preparation of Graphene based Semiconductor Photocatalysts

The graphene based semiconductor photocatalysts are prominently obtained through in situ growth (Lambert et al., 2009), hydrothermal/solvothermal (Fu & Wang, 2011), solution mixing method (Akhavan & Ghaderi, 2009). Off them the hydrothermal technique is one of the traditional and an effective method for incorporating graphene into semiconductors. This simple process involves the incorporation of semiconductor composite onto the graphene sheets and reduces to graphene. During the hydrothermal reaction process, GO is reduced to graphene and simultaneously loaded onto the semiconductor composite. Table 2.3 detailed the various studies on RGO incorporating with TiO_2 and noble metal.

Table 2.3: Summary of literature studies of conducting carbon materials as composite for photocatalysts

Composite photocatalyst	Preparation method	Photocatalytic experiment	Reference
RGO-TiO_2	Hydrothermal	Photo degradation of Rhodamine B under UV and visible light irradiation. An improved photo degradation by RGO-TiO_2 as compare to P25 where almost 90% (UV light) and 70% (visible light) of removal was achieved in 120 min.	F. Wang & Zhang, 2011
TiO_2-RGO	Hydrothermal	Photo degradation of Methyl Orange (10 mg/L) under visible light irradiation. An optimum of TiO_2-2%RGO shows the highest removal rate of 87.4% as compared to only 7.6% by pure TiO_2 after 6 h of irradiation.	Y. Liu, 2014
RGO/P25	Hydrothermal	Photo degradation of Methyl Orange with an initial concentration of 32.73 ppm. The degradation ratio for the 0.75wt% RGO/P25 composite was the best with complete degradation after 120 min and 150 min of irradiation under UV and visible light, respectively.	Yueli Liu et al., 2014

Table 2.3, continued

Composite photocatalyst	Preparation method	Photocatalytic experiment	Reference
Ag-TiO_2-RGO	Solvothermal	Photo degradation of Rhodamine B under illumination of visible light. An initial concentration of 2×10^{-5} M was almost completely removed by 0.10 mol Ag-TiO_2-RGO in 60 min.	Shah et al., 2013
RGO/Ag-TiO_2	Electro - chemical deposition	Photo degradation of 2, 4-dichlorophenoxyacetic acid (10 mg/L) under simulated solar light. The ternary photocatalyst exhibited 93% removal efficiency as compare to 36.7% by TiO_2.	Y. Wang et al., 2013a
Ag/RGO-TiO_2	Electrodeposition and photoreduction process	Photocatalytic removal of 2, 4 dichlorophenoxyacetic acid under stimulated solar light irradiation. The ternary photocatalysts unveiled almost 100% removal efficiency with an initial concentration of 10 mg/L within a period of 160 min.	Yanhong Tang et al., 2012b
Ag/AgBr/RGO	Double jet precipitation, hydrothermal and UV light reduction	Photo degradation of Methyl Orange under visible light irradiation with an initial concentration of 20 mg/L. The prepared composite shows great photocatalytic activity by achieving ~90% removal with the optimum loading of 0.5wt% RGO.	Zeng, Guo, Tian, & Zhang, 2013
Ag/AgBr/TiO_2/RGO	Solvothermal-photo reduction	Photo degradation of penicillin (10 mg/L) was conducted under white light emitting diode irradiation. A degradation efficiency of 99% was achieved after 2h irradiation.	Penghua Wang, Tang, Dong, Chen & Lim, 2013

Table 2.3, continued

Composite photocatalyst	Preparation method	Photocatalytic experiment	Reference
Ag@AgCl(RGO)	Deposition-precipitation reaction followed by photo reduction	Photo degradation of Rhodamine B with a starting concentration of 10 mg/L was illuminated under visible light. The prepared photocatalysts shows a ~95% of dyes removal over the bare Ag@AgCl.	Hui Zhang et al., 2011

2.8 Graphitic Carbon Nitride

Apart from the RGO metal free polymeric semiconductor, graphitic carbon nitride (g-C_3N_4) had very recently attracted tremendous attention of researchers for a robust and stable visible light driven photocatalyst. As compared to other inorganic semiconductor, g-C_3N_4 consists mainly of carbon and nitrogen which are among the most abundant elements in our planet, making it a sustainable and environmentally organic semiconductor. The heptazine ring structure and the high condensation degree enable this metal free semiconductor to have various notable advantages such as good physicochemical stability, harvesting visible light with a band gap of 2.7 eV, suitable redox potential to efficiently catalyze reactions, abundant, and inexpensive. These unique properties make g-C_3N_4 a promising candidate for visible light enhancement. Nevertheless, pure g-C_3N_4 suffers from shortcomings such as rapid recombination rate of photo-generated electron-hole pairs and a small specific surface area. However, its 2-dimensional layered structure enables it for hybridizing with other component to overcome its shortcomings.

Most commonly g-C_3N_4 is prepared by simple route by adopting nitrogen rich organic molecules as single source precursors under thermal treatment. Zou *et al.*, reported a direct heating of melamine to g-C_3N_4 in a semi-closed system (Yan, Li, & Zou, 2009). J. Zhang *et al*., uses the thermal polycondensation of cyanamide or dicyandiamide into g-C_3N_4 with a continuous flow of N_2 gas (J. Zhang et al., 2010). Meanwhile, Lotsch and Schnick employed the thermal transformation of guanylurea dicyanamide to g-C_3N_4 that enable it to render more oxygen containing organic compound (Lotsch & Schnick, 2005). However, some of these precursors are toxic and harmful to human and environment, and some are unstable and difficult to synthesize on a large scale basis. Therefore, by choosing urea as the starting material had become an alternative (Jinghai Liu, Zhang, Wang, Dawson, & Chen, 2011).

2.8.1 Synthesis of Graphitic Carbon Nitride

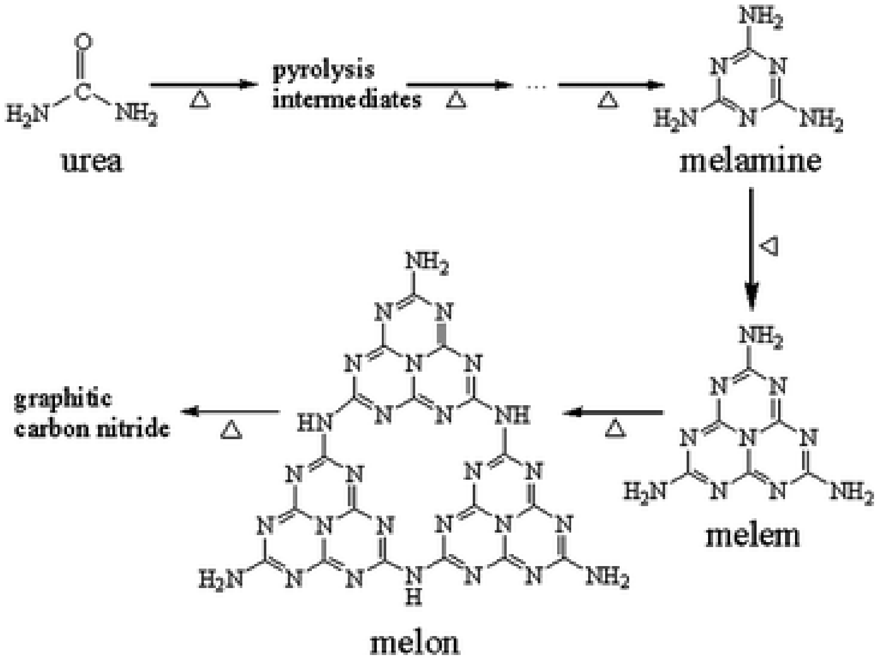

Figure 2.10: The formation mechanism of g-C_3N_4 by pyrolysis of urea (Xu, Li, Peng, Lu, & Li, 2013)

Urea being a common, non-toxicity and low cost raw material in chemical industry had turn out to be the promising precursor for synthesizing g-C_3N_4. (J. Liu et al., 2011; Xu et al., 2013). Furthermore, it is an active molecular precursor for thermal treatment. A simple thermal process utilizing it as the starting material in order to synthesis g-C_3N_4 in a large scale had overcome many other synthesis method. First upon heating under a closed air atmosphere, the urea decomposes into ammonia and isocyanic acid. Then it is converted into other intermediates like cyanuric acid, ammelide and ammeline. The formed cyanuric acid further turn into melamine which then condense to form melem. The formation of g-C_3N_4 was formed after the polymerization of melem into melon. The schematic formation mechanism of g-C_3N_4 by pyrolysis of urea is illustrated in Figure 2.10. Liu *et al*, had proven in their studies where they employed a simple pyrolysis of urea under ambient pressure and pyrolysis generated in self-supporting atmosphere produced large scale of g-C_3N_4 (J. Liu et al., 2011). Hence, this simple synthesis processes eliminates the needs of additional additive assistance and higher reaction pressure and atmosphere. The summary of the literature on g-C_3N_4 incorporating with TiO_2 and noble metal is presented in Table 2.4.

Table 2.4: Summary of literature on g-C_3N_4 incorporating with TiO_2 and noble metal

Composite photocatalyst	**Preparation method**	**Photocatalytic experiment**	**Reference**
TiO_2/g-C_3N_4	Thermal transformation	Decomposing methylene blue with concentration of 1.5 x 10^{-5} M under visible light irradiation. The prepared binary photocatalyst shown a 93% removal in 100 min.	Sridharan et al., 2013

Table 2.4, continued

Composite photocatalyst	Preparation method	Photocatalytic experiment	Reference
g-C_3N_4/TiO_2	Hydrolysis	Decomposing of phenol (5 mg/L) under UV illumination, an effective 96.6% degradation efficiency was achieved in 60 min for a weight ratio of 2. Meanwhile, 67.7% degradation was obtained in 180 min under the illumination of visible light with the same weight ratio.	Zhao, Chen, Yu & Quan, 2012
g-C_3N_4/TiO_2	Facile calcination process	The photocatalytic activity efficiencies were tested by degradation of Acid Orange 7 (20 mg/L) under visible light irradiation. The photocatalyst exhibited 99% degradation after 5 h of illumination.	Lei et al., 2015
(g-C_3N_4)-N-TiO_2	Facile Pyrolysis process	Photoreduction of CO_2 to CO in the presence of water vapor at room temperature. A highest amount of CO with 14.73 μmol was achieved after 12 h of light irradiation.	Zhou et al., 2014
g-C_3N_4/Ag/TiO_2	Ag NPs were photodeposited as the interlayer between g-C_3N_4 and surface of TiO_2	Photo Degradation of Methyl Orange (13.5 mg/L) and Phenol (16.6 mg/L) under visible light illumination. The g-C_3N_4 (4%)/Ag/TiO_2 showed significant enhancement in photocatalytic activity (94%) toward degradation of methyl orange. Similar trend was also observed for phenol.	Y. Chen, Huang, He, Situ & Huang, 2014
Ag/g-C_3N_4	Polymerization-photodeposition	Decomposed Methyl Orange (10 mg/L) under visible light irradiation. It shows great enhancement in photocatalytic degradation where 92% was achieved by an optimum with Ag loading of 5g in 120 min. Where else 56% and 70% was obtained by P25 and g-C_3N_4 respectively.	Yang et al., 2013

Table 2.4, continued

Composite photocatalyst	Preparation method	Photocatalytic experiment	Reference
Au/g-C_3N_4	Green photodeposition of Au onto g-C_3N_4	Photo degradation of Methyl Orange (10 mg/L) under visible light irradiation. The Au/g-C_3N_4 exhibited maximum of 92.6% as compared to g-C_3N_4 (21.5%) in 150 min.	N. Cheng et al., 2013
Ag/g-C_3N_4/RGO	Hydrothermal	Photo degradation of Methyl Orange with an initial concentration of 10 mg/L under the illumination of visible light. The obtained degradation rate on Ag/g-C_3N_4/RGO was 12.3, 7.2, 5.1 and 3.7 times than that on g-C_3N_4, Ag/RGO, g-C_3N_4/RGO and Ag/g-C_3N_4 respectively.	Lu, Shen, Wang, Cui, & Xie, 2015

2.9 Application of Modified Titania Photocatalyst

2.9.1 Photocatalytic Degradation Mechanism of Environment Pollutants

Semiconductor TiO_2 being a well-known photocatalyst for addressing numerous environmental concerns. It was greatly considered by the researchers over the past decades for its improvisation in order to maximize the usage of this notable semiconductor. The primary principles and mechanisms are illustrated in Figure 2.11. When TiO_2 is illuminated with a photon energy (< 390 nm), it will generate and excite an electron from the valence band to the conduction band leaving behind a positively charge hole. This excited electron where it promoted to the conduction band will then undergo oxidation with oxygen molecule to form superoxide anion radicals ($^\bullet O_2^-$) and followed by protonation that yields $^\bullet HO_2$ radicals. Then, this radicals combines easily with the trapped electrons to form H_2O_2 and finally to $^\bullet OH$ an active species radicals. Meanwhile, the positively charge hole at the valence band is positive enough to generate $^{\bullet}OH$ radicals at the surface of TiO_2 as shown in the following equations (Khataee & Kasiri, 2010):

$$TiO_2 + h\upsilon\ (\lambda < 390\ \text{nm}) \rightarrow e^- + h^+ \qquad (2.1)$$

$$e^- + O_2 \rightarrow \bullet O_2^- \qquad (2.2)$$

$$h^+ + H_2O \rightarrow H^+ + \bullet OH \qquad (2.3)$$

The $^{\bullet}OH$ radical is an active oxidizing agent which is responsible to attack the organic pollutant (OP) present at or near the surface of TiO_2. It has greater potential to oxidise any form of toxic and bio resistant OP into harmless species such as CO_2, H_2O and etc. The decomposition can be elucidated through the following reactions (Behnajady & Modirshahla, 2006):

$$h^+ + OP \rightarrow \bullet OP^+ \rightarrow \text{oxidation of OP} \qquad (2.4)$$

$$\bullet OH + OP \rightarrow \text{degradation of OP} \qquad (2.5)$$

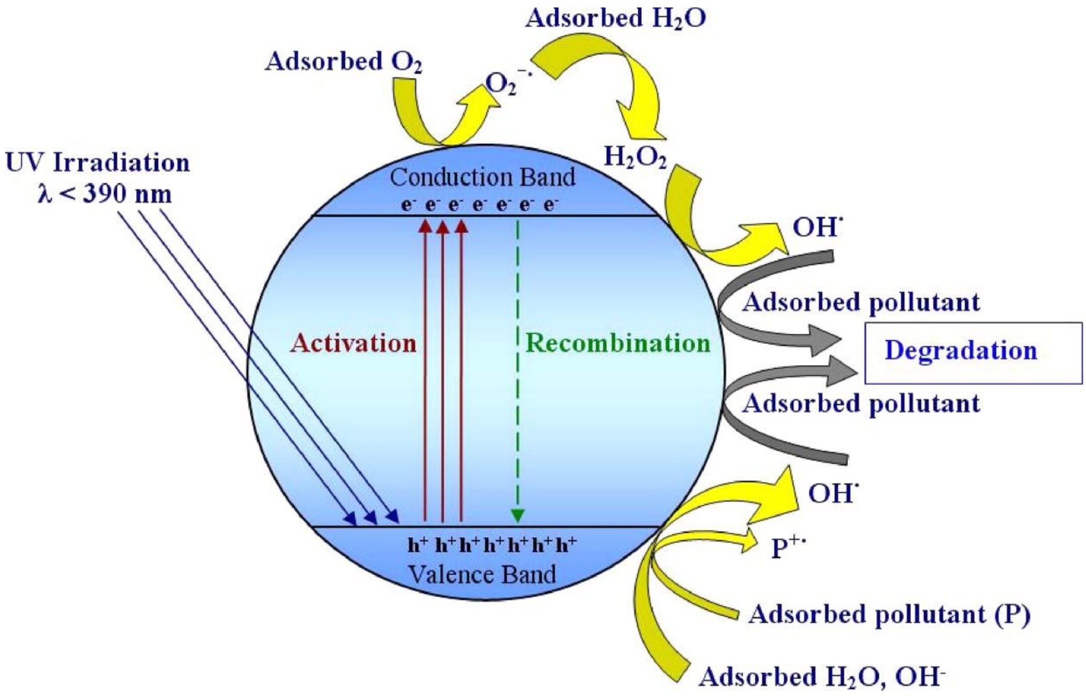

Figure 2.11: General mechanism of photocatalysis on TiO_2 nanomaterials (Khataee & Kasiri, 2010)

Modifications of titania with different noble metals and conducting carbon materials are required to address all its limitations. Hence, it leads to photocatalytic removal of genera organic pollutants. From the literature survey, it is evident that these modifications resulted in varied photocatalysis mechanism. The studies pertaining to it is reviewed and summarized in Table 2.5.

Table 2.5: Literature studies on photocatalysis mechanism of modified titania

Photocatalyst	Pollutants	Proposed reaction mechanism	Reference
Ag@TiO_2	Rhodamine B (RhB)	The Ag NPs attach on the surfaces of TiO_2 forming non-centrosymmetric nano structures due to the different in dielectric environment surrounding the plasmonic Ag. During visible light illumination, the localized surface plasmon resonance effect will then excite electrons to the conduction band of TiO_2 and leaving behind the holes. The separated electrons and holes then form active radicals.	D. Chen et al., 2013
Ag-TiO_2	Indigo carmine (IC)	Ag NPs deposited on TiO_2 surface acted as electron-hole separation center. The electrons are capable to transfer from the TiO_2 to Ag NPs due to the higher Fermi level of TiO_2. This favours the formation of Schottky barrier at the interface. During the light irradiation, (IC) injected electrons to the conduction band of TiO_2 reacts with O_2 to form active radicals. Ag NPs acted as the electron traps resulted in prolong the life time of the charge carrier.	Suwanchawalit et al., 2012
Ag/TiO_2	Methyl Orange and Phenol	During the visible light irradiation, the generated electrons near TiO_2 surface is mainly due to the resonant surface plasmon induced local electric fields in Ag. They are readily separated from each other and easily migrate to titania. Thus, it suppresses the recombination rate of electron and hole pairs.	Ramchiary & Samdarshi, 2014

Table 2.5, continued

Photocatalyst	Pollutants	Proposed reaction mechanism	Reference
Ag-TiO_2	Methyl Blue	Under the visible light illumination, electrons in Ag NPs are photoexcited and Ag^+ ions are formed due to the LSPR effect. Moreover, the formations of Schottky barrier at the interface due to the larger work function of Ag. The electric field enables the excited electrons to be promoted from the Ag NPs to the TiO_2 and enhanced the charge separation. Transferred electrons are then react with oxygen to form active radicals. In addition, the Ag^+ ions are also reactive radical species. They are able to directly oxidize MB.	Z. Chen et al., 2014
Au/TiO_2	Acetic acid	Modification of titania with expensive gold had enhanced the separation of charge carriers (e^-/h^+). This is attributed to the characteristic of noble metal serving as an electron sink. Hence, more electrons can be participated in the photo degradation of acetic acid and increase the photocatalysis efficiency.	Kowalska, Rau, & Ohtani, 2012
Pd-TiO_2	Water Splitting	The introduction of Pd onto the TiO_2 had enable Pd ions to capture the excited electron from titania. Thus, it depresses the recombination rate between the excited electrons and holes. Moreover, the Pd-TiO_2 has the strong ability of the oxidation - reduction than pure TiO_2.	Kwak et al., 2009

Table 2.5, continued

Photocatalyst	Pollutants	Proposed reaction mechanism	Reference
TiO_2-RGO	Methylene Blue	After irradiation with visible light, photo excitation in TiO_2 occurs and generated holes at the valence band. Thus the $^{\bullet}OH$ radicals are produced from water, having the potential to degrade the organic pollutants. The photo generated electrons then easily migrate to the surface and react with adsorbed O_2 in forming $^{\bullet}O_2^-$, thereby increasing the overall efficiency.	Umrao et al., 2014
RGO-Ag	Phenol, Bisphenol A and atrazine	Ag NPs acted as the antennae for visible light and RGO acted for efficient electron-hole separation. Visible light excite the Ag surface plasmon and this coherent oscillation generate energetic electrons on its surface. Then, the RGO quickly transports those electrons via its extended π-conjugation structure and lead to suppress the recombination of electron and hole pairs. This electron transfer was feasible due to the work functions of Ag (4.2 eV) and RGO (4.48 eV).	Bhunia & Jana, 2014
Ag-TiO_2-RGO	Rhodamine B	Titania with different oxides and consists of many defects give rise to the ability to absorb visible light. It then promotes the electron from the VB to the CB. These electrons then migrate to the Ag NPs and subsequently to RGO. As a result, the electron and holes pairs can be efficiently separated. Eventually, these electrons reduce the dissolved oxygen leading to the formation of $^{\bullet}O_2^-$ radicals.	Shah et al., 2013

Table 2.5, continued

Photocatalyst	Pollutants	Proposed reaction mechanism	Reference
g-C_3N_4-TiO_2	Acid Orange 7	When catalyst is irradiated by UV light, the photogenerated electrons from g-C_3N_4 readily transfer to the CB of TiO_2. Where by the holes at the VB of TiO_2 transfer to VB of g-C_3N_4. Thus, it suppresses the recombination rate of electron-holes leaving more electrons at the CB of TiO_2 and more holes in the VB of g-C_3N_4. In contrast, when it is illuminated by visible light, only g-C_3N_4 is excited because TiO_2 could not absorb visible light. Therefore the generated electrons in the CB of g-C_3N_4 migrate to CB of TiO_2.	Lei et al., 2015
Au/g-C_3N_4	Methyl Orange	Visible light irradiated the catalyst to generate CB electrons and VB holes. These electrons react with oxygen to form superoxide radical anions while the holes react with water to form active $^{\bullet}OH$ radicals. The presence of Au NPs acted as the electron traps to prolong the lifetime of the charge carriers. Furthermore, the plasmonic excitation resulted in additional generation of electrical surface charge.	Cheng et al., 2013
g-C_3N_4/Ag/TiO_2	Methyl Orange and Phenol	Under the visible light irradiation, only g-C_3N_4 absorbed visible light. The generated electron is then transferred to the CB of TiO_2 due to more negativity of g-C_3N_4. Meanwhile, the presence of Ag NPs acted as the electron-conduction bridge where it enhanced the separation of electron and hole pairs. Moreover, with the formation of Schottky barrier it provided an efficient path for the electron to be transferred from g-C_3N_4 toward TiO_2. Ag NPs owning to its surface plasmon resonance further enhance the visible light absorption.	N. Chen, Huang, He, Situ & Huang, 2014

Although some works have been carried out in this field, several insights are yet to be explored to fill the gaps of previous research. This includes developing sustainable synthesis method with high quality photocatalyst for enriching their unique inherent characteristics. Demonstrating the visible light photocatalysis ability of the prepared modified synergized photocatalysts in a more appropriate and meaningful way by adopting poor photosensitizing compounds.

CHAPTER 3

METHODOLOGY

This chapter elaborates the comprehensive synthesis methods, characterisations techniques and all the experiments adopted for achieving the adopted objectives.

3.1 Preparation of TiO_2 Template

3.1.1 Materials

Titanium (IV) chloride ($TiCl_4$, 99.9%) and benzyl alcohol (99.8%, anhydrous) were procured from Sigma Aldrich and tetrahydrofuran (THF) from Fluka. All chemicals were analytical grade and used as received without any further purification.

3.1.2 Synthesis of TiO_2 Template

Synthesis of anatase nanocrystalline TiO_2 in a room temperature by non-hydrolitic polycondensation between titanium (IV) chloride and anhydrous benzyl alcohol was performed in a glass beaker mediated through controlled inert gas (nitrogen) atmosphere. One mL of $TiCl_4$ was added drop wise into 20 mL of anhydrous benzyl alcohol under vigorous stirring. The reaction is vigorous in nature; the solution initially turns to dark red and then to orange. Further a complete addition of $TiCl_4$ with continuous stirring yields yellowish solution. The stirring was continued for 24 h and the solution was aged for 21 days at room temperature. The adopted experimental setup up is shown in Figure 3.1. The slow ageing process facilitated through room temperature ensured the formation of more uniform TiO_2 nanoparticles of smaller size rather than heating at higher temperature. Furthermore aging also dissolved any fluffy white precipitate. The resulting white precipitate after aging was recovered by centrifugation at 3000 rpm for 30 min. The precipitate was thoroughly washed with 20 mL of ethanol and followed by 20 mL of tetrahydrofuran (THF). The washing step was repeated for 3 times and after every washing, the solvent was removed by centrifugation. The practised washing steps ensure the complete removal of excess Cl^- anions. After washing, the obtained TiO_2 white powder was dried at room temperature and the sample is designated as TiO_2 as-synthesized. On the other hand, the as-synthesized sample was calcined at 450°C for 5 h and is designated as calcined TiO_2. The prepared sample is displayed in Figure 3.2.

Figure 3.1: Experiment setup for synthesis of nanocrystalline anatase TiO_2

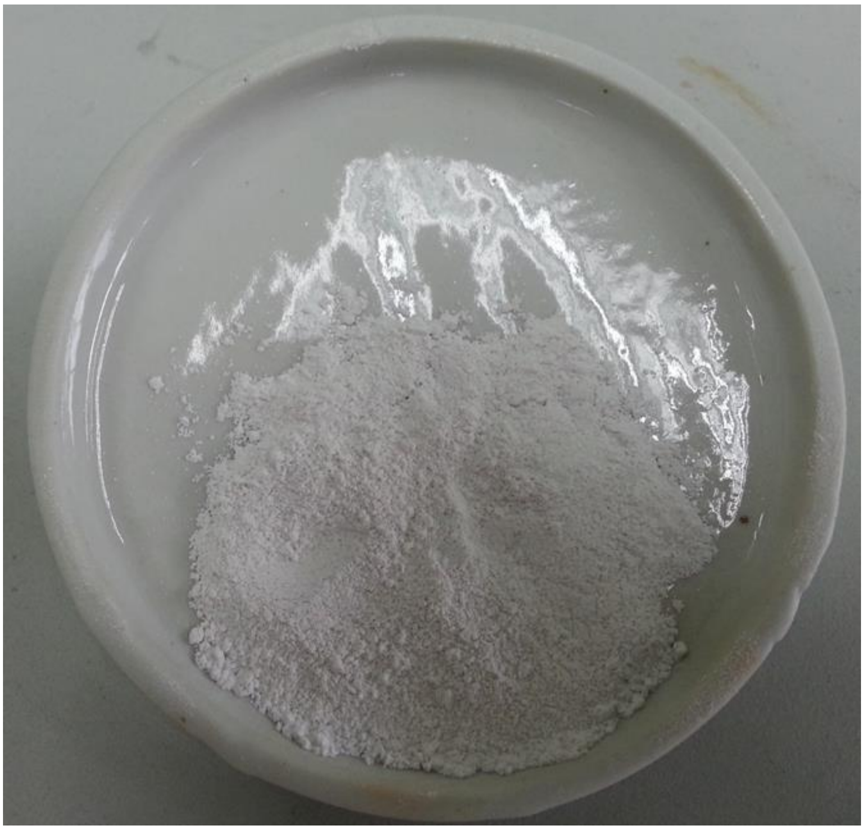

Figure 3.2: Photograph of synthesised TiO_2 powders

3.2 Preparation of Plasmonic Photocatalysts Pd/TiO_2 and Ag/TiO_2

3.2.1 Materials

Titanium (IV) chloride ($TiCl_4$, 99.9%, Merck), Silver Nitrate ($AgNO_3$, 99.9%, Sigma Aldrich), Sodium tetrachloropalladate (II) (Na_2PdCl_4, 99.998%, Sigma Aldrich), tetrahydrofuran (THF, Fluka), ethylene glycol and benzyl alcohol (99.8% anhydrous, R&M Chemicals) and Milli-Q water (18.2 MΩ·cm). All chemicals were analytical grade and used without any further purification.

3.2.2 Synthesis of Pd/TiO_2 and Ag/TiO_2

The synthesis of pristine anatase TiO_2 was adopted from the above synthesis procedure. The Pd/TiO_2 NPs were synthesized by adding 12 mL of ethylene glycol with

0.4 g of the prepared anatase TiO_2 with a designated amount of Na_2PdCl_4 i.e., 0.5 wt%, 1.0 wt% and 3.0 wt% respectively) for obtaining Pd of similar wt% as stated above. Likewise, the designed amount of $AgNO_3$ was chosen as Ag precursor for obtaining varied Ag/TiO_2 NPs with varied Ag loading (0.5 wt%, 1.0 wt%, 3.0 wt% and 5.0 wt%). The solution was then exposed under sunlight with continuous stirring for 30 min to promote sustainable photoreduction (~150 and 180 Wm^{-2}). The sunlight intensity was measured by using a Lux meter. The obtained precipitate was then centrifuged at 2000 rpm for 5 min. The produced Pd/TiO_2 and Ag/TiO_2 were finally washed with ethanol and deionized water, respectively and followed by overnight drying at 90°C. The amount of Pd and Ag deposited onto TiO_2 is tabulated in Table 3.1.

Table 3.1: The various loading of noble metal Ag and Pd on TiO_2

Weight Percentage (wt %)	Loading amount of Ag (g)	Loading amount of Pd (g)
0.5	0.062	0.062
1.0	0.124	0.124
3.0	0.372	0.372
5.0	0.620	-

3.3 Preparation of Reduced Graphene Oxide and Ag Wrapped TiO_2

3.3.1 Materials

Graphite flakes was purchased from Sigma-Aldrich, potassium permanganate ($KMnO_4$, 99.9%), sulphuric acid (H_2SO_4, 98%), hydrogen peroxide (H_2O_2, 30%), hydrogen chloride (HCl, 37%) and denatured ethanol (99.7%) were purchased from R&M chemical and Milli-Q water (18.2 MΩ·cm). All chemicals were analytical grade and used as received without any further purification.

3.3.2 Synthesis of Graphene Oxide (GO)

Simplified Hummers method was adopted in synthesis graphite oxide (Hummers Jr & Offeman, 1958). In a typical preparation nature graphite powder (3 g) was oxidized by a mixture of 400 mL of H_2SO_4 and 18 g of $KMnO_4$. The mixture was then stirred continuously for three days to ensure complete oxidation of the graphite. Once oxidation process was completed, H_2O_2 solution was added drop wise to terminate the oxidation process. The obtained graphite oxide was constantly washed with 1 M of HCl and Milli-Q water (18.2 MΩ·cm) until it reached pH in between 4−5. This washing process led to the exfoliation of graphite oxide to form GO gel. The solution was then dried overnight at 60°C under vacuum to obtain GO powders and it is depicted in Figure 3.3.

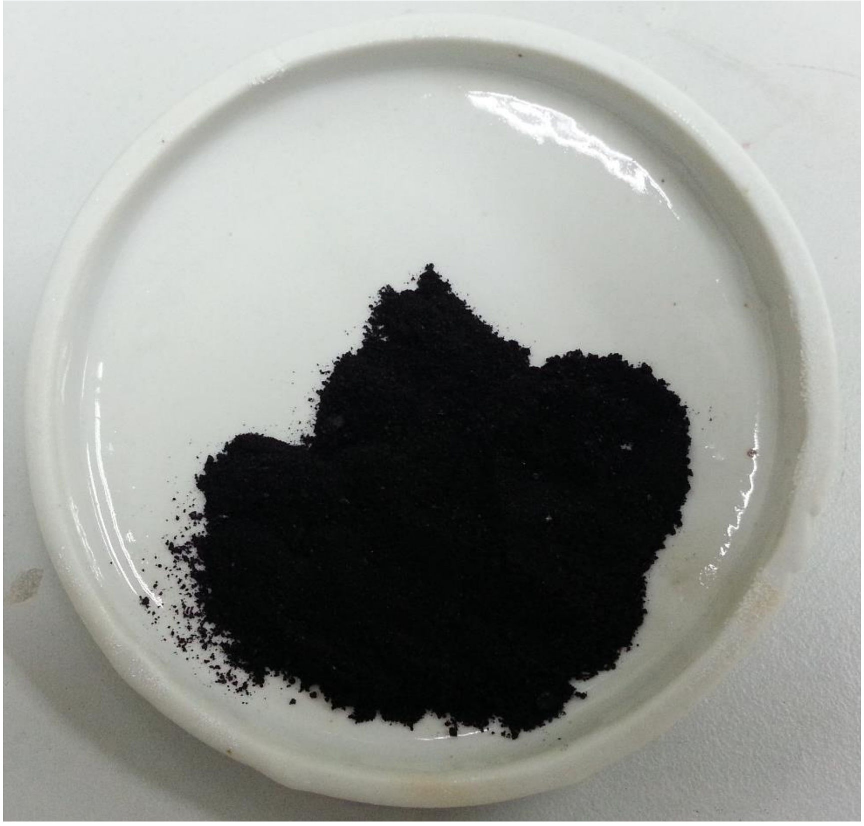

Figure 3.3: Photograph of synthesised GO powders

3.3.3 Synthesis of RGO-Ag/TiO_2

Similar synthesis method for preparation of anatase TiO_2 and Ag/TiO_2 was adopted in preparation of RGO-Ag/TiO_2. 0.2 g of the prepared GO was first dissolved in Milli-Q (18.2 MΩ·cm) water by ultrasonic treatment for an hour to yield a yellow-brown solution. This was followed by the addition of 1 g of the freshly prepared Ag/TiO_2 into the yellow-brown solution and stirred for 1 h until homogeneity was achieved. The solution was then transferred into a Teflon-lined autoclave and was subjected to hydrothermal treatment at 180°C for 6 h. The applied hydrothermal treatment reduced GO to RGO. The resulted suspension was retrieved by centrifugation and washed thoroughly with Milli-Q water (18.2 MΩ·cm) and air dried at room temperature. The schematic of the preparation is illustrated in Figure 3.4.

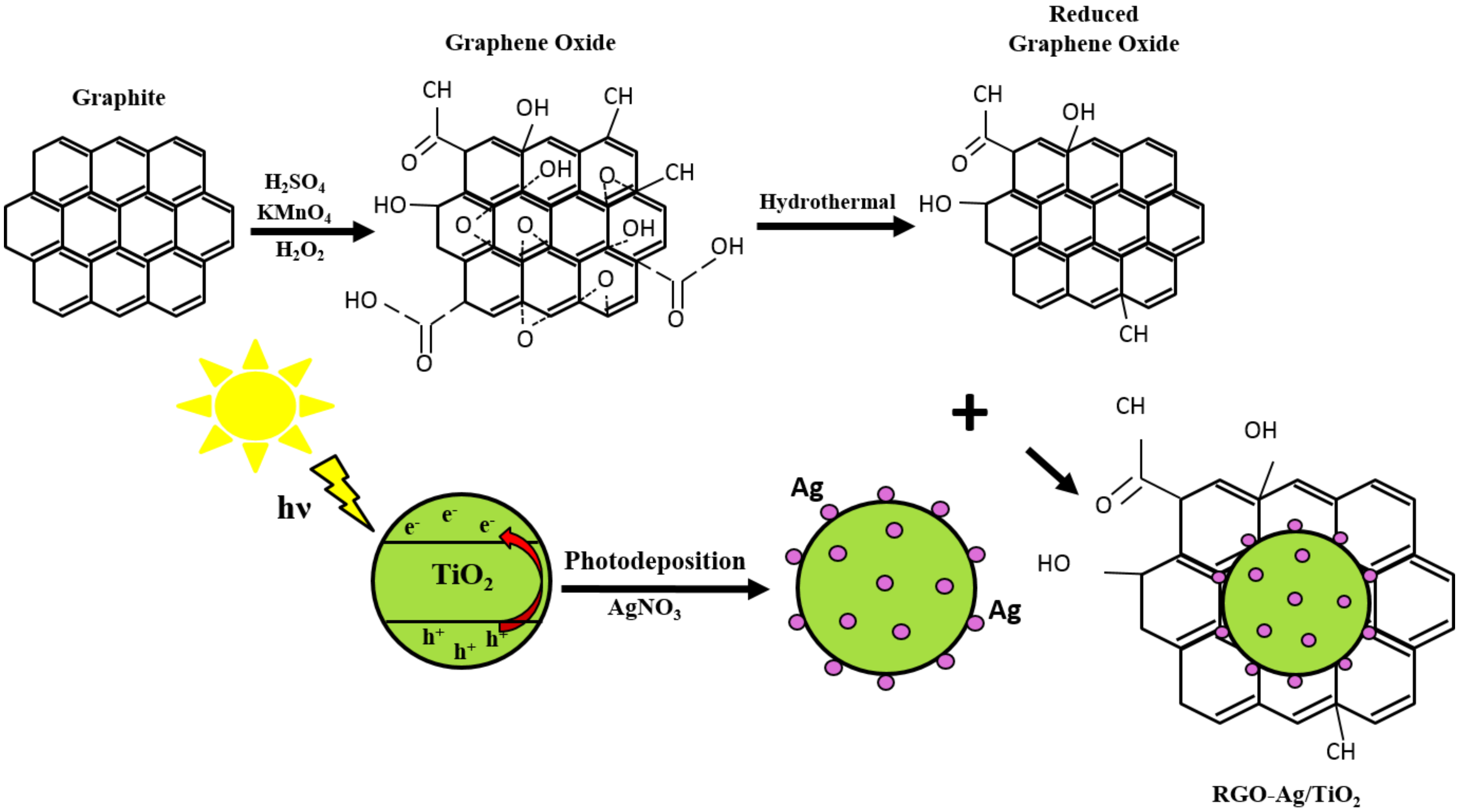

Figure 3.4: Schematic of synthesis route for RGO-Ag/TiO_2

3.4 Preparation of Graphitic Carbon Nitride and Ag with TiO_2

3.4.1 Materials

Urea and nitric acid were purchased from R&M chemical and Milli-Q water (18.2 MΩ·cm). All chemicals were analytical grade and used as received without any further purification.

3.4.2 Synthesis of g-C_3N_4

A facile thermal heating method was adopted for synthesizing g-C_3N_4. This was achieved by drying the weighted 10 g of urea in an oven at 80°C for 24 h. The dried sample was then pyrolysed at 550°C for 3 h in a Muffle Furnace. The obtained yellow coloured product was then washed with 0.1 M nitric acid and Milli-Q (18.2 MΩ·cm) water for few times in order to remove any residual alkaline species that was absorbed on the sample surface. The washed derivative was finally dried overnight in an oven at 80°C and illustrated in Figure 3.5 (J. Liu et al., 2011).

Figure 3.5: Photograph of synthesised g-C_3N_4 powders

3.4.3 Synthesis of (g-C_3N_4)-Ag/TiO_2

From the prepared g-C_3N_4 sheets a sample weighing 0.012 g was well dispersed in Milli-Q water (18.2 MΩ·cm) ultrasonically. 0.4 g of the as prepared Ag/TiO_2 was then added into the solution and subjected to a reaction at 70°C for 1 h in an open beaker. The resulting suspension was then centrifuged and washed with Milli-Q water (18.2 MΩ·cm) for few times and dried overnight at 60°C. Figure 3.6 depicts the schematic synthesis of (g-C_3N_4)-Ag/TiO_2.

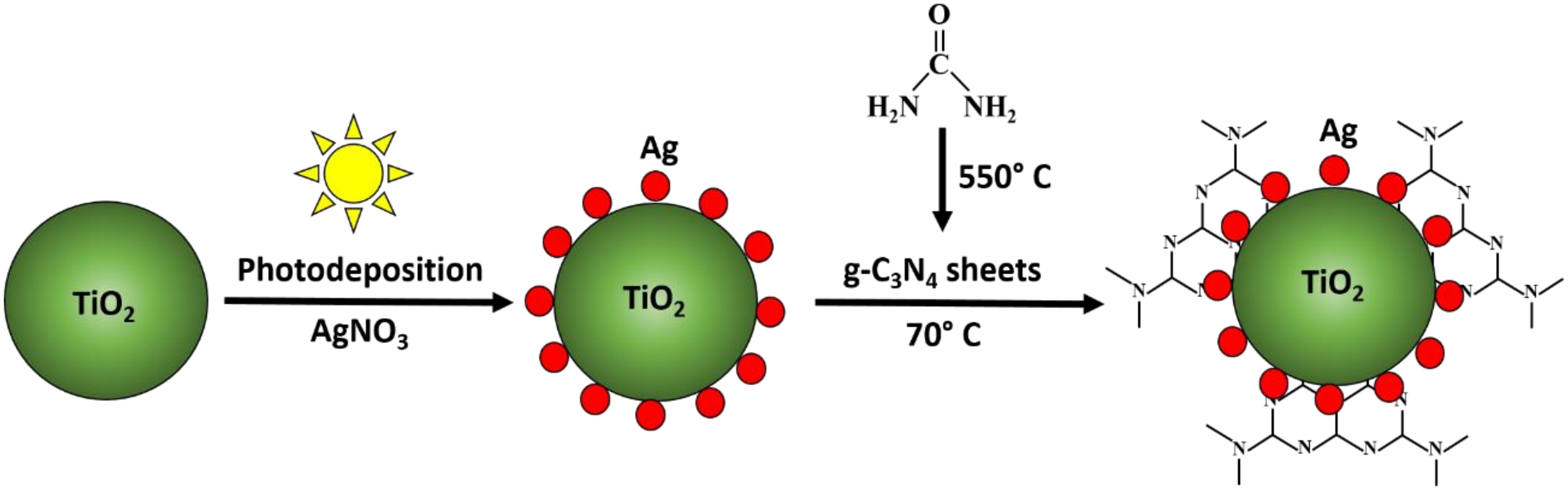

Figure 3.6: Schematic of synthesis route for (g-C_3N_4)-Ag/TiO_2

3.5 Characterization

The morphology of the samples were investigated by field emission scanning electron microscope (FESEM, Hitachi SU-8000) equipped with an energy dispersive X-ray spectroscopy (EDS, Zeiss Auriga). The images were recorded at an accelerating voltage of 20 kV. Transmission electron microscope (TEM) (Philips CM-12) and high resolution transmission electron microscope (HRTEM, JEM-2100F, Jeol) images were obtained at 200 kV. The phase composition were analysed by X-ray diffraction (XRD, Bruker D8 advance X-ray powder diffractometer with Cu Kα radiation λ=0.154 nm). A micro-PL/Raman spectroscope with the excitation wavelength at 514 nm and 325 nm (Renishaw, inVia Raman Microscope) was used to acquire the Raman and photoluminescence (PL) spectra. A Fourier transform infrared (FTIR) spectrum was obtained by Perkin Elmer Spectrum 400 spectrophotometer with scan range of 4000 – 450 cm^{-1}. Brunauer-Emmett-Teller (BET) surface area, pore volume, and Barret-Joyner-Halenda (BJH) pore size distribution based on nitrogen adsorption-desorption isotherms with TriStar II 3020 (Micrometrics®, USA). Prior to the analysis, the samples were degassed at 150°C for 5 h under nitrogen atmosphere. X-ray photoelectron spectra (XPS) were obtained with Axis Ultra DLD instrument of Kratos using monochromatic AlKα radiation (225 W, 15 mA, 15 kV). The C1s binding energy of adventitious carbon (284.9 eV) was used as reference. UV-Vis diffuse reflectance spectra (UV-DRS) were performed through Shimadzu UV-2600 spectrophotometer equipped with an integrating sphere attachment. The spectra were obtained with $BaSO_4$ as a reference.

3.6 Photocatalysis Experiments

3.6.1 Solar Photocatalysis

The solar photocatalytic performance of the prepared TiO_2 was evaluated by adopting a recalcitrant, non-photosensitising pesticide 2, 4-dichlorophenol (2, 4-DCP) as model pollutant. The experiments were carried out in a batch reactor of 500 mL capacity with a working volume of 250 mL (initial concentration of 2, 4-DCP = 50 mg/L) under stirring condition. The solar light was employed as the source of irradiation with the presence of 1 g of synthesized photocatalyst. The sunlight intensity during the experiments was fluctuated between 88 and 205 Wm^{-2}. A dark experiments were carried out prior to photocatalytic experiments to substantiate the possibility of parallel removal of contaminant molecule (2, 4-DCP) by adsorption and non-degradation of pollutant in the absence of light source. Additional control experiments were carried out with zero photocatalyst condition to ensure the degradation was only due to presence of photocatalyst. The samples were drawn out at regular intervals (30 min) and analysed for residual concentration of 2, 4-DCP using an ultra-performance liquid chromatography (Acquity UPLC H-Class, Waters). The parameters are tabulated in Table 3.2.

Table 3.2: LC analysis conditions for 2, 4-DCP

Pollutant	**2, 4-DCP**
Column	C18 (2.1 × 50 mm, 1.7 µm)
Mobile phase	Acetonitrile : Water (60:40)
Flow rate (mL/min)	0.4
Wavelength (nm)	285

The adopted calibration curve is illustrated in Figure 3.7. The degree of mineralization of 2, 4-DCP during photocatalytic experiment was estimated by Total Organic Carbon (TOC) analysis using O. I Analytical Aurora 1030W TOC Analyzer. Figure 3.8 shows the schematic experimental setup for solar photocatalysis of 2, 4-DCP.

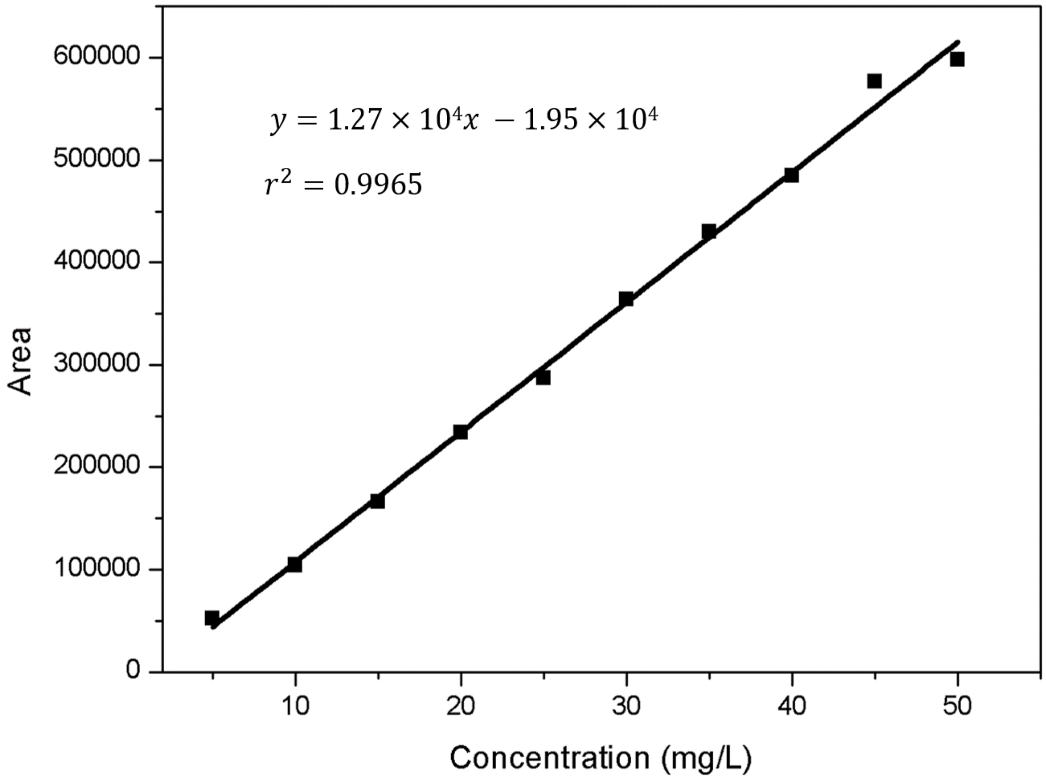

Figure 3.7: Calibration curve for 2, 4-DCP

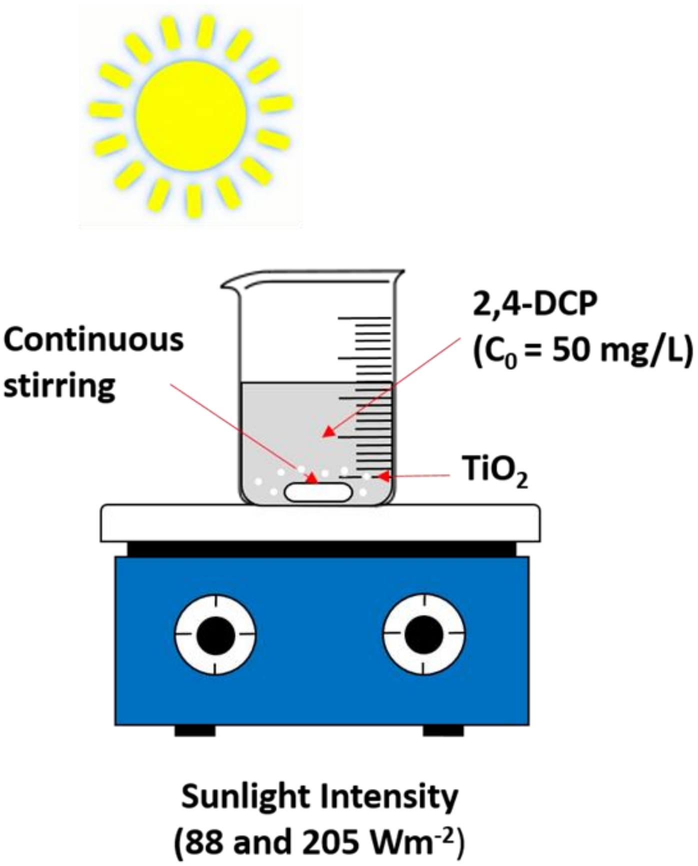

Figure 3.8: Experimental setup for solar photocatalysis experiment

3.6.2 Artificial Visible Light Photocatalysis

The photocatalytic performance of the prepared Ag/TiO_2 was evaluated by degrading two different types of pollutants namely, 2, 4-dichlorophenol (2, 4-DCP) and Amoxicillin (AMX). Then, Bisphenol A (BPA), Methylene Blue (MB) and Reactive Blue 19 (RB19) were chosen as pollutants to measure the photodegradation efficiency of (RGO-Ag/TiO_2). Meanwhile, the photocatalysis degradation efficiency of Pd/TiO_2 and (g-C_3N_4)-Ag/TiO_2 were studies by adopting AMX as pollutant. The pollutants 2, 4-DCP, AMX and BPA are classified as an Endocrine Disrupting Compounds (EDCs) with poor photosensitising ability. All the experiments were performed as batch process with a simple 500 mL borosilicate beaker with a working volume of 250 mL. The initial concentrations of all pollutants in these studies were set at 20 mg/L with 1 g photocatalyst loading under stirring conditions. The artificial photons were generated by 500 W tungsten-halogen lamps with high-pass UV filter (FSQ-GG400, Newport Corp). All experiments were performed under identical condition for a specific period of time. Respective control experiments were carried out with zero photocatalyst condition to ensure the photocatalytic degradation. The samples were drawn out at regular intervals, analysed for residual concentration of the pollutants using Acquity UPLC H-Class, Waters. The analysis parameters are tabulated in Table 3.3.

Table 3.3: LC analysis conditions for studied pollutants

Pollutant	**Amoxicillin**	**Bisphenol A**
Column	C18 (2.1 × 50 mm, 1.7 µm)	
Mobile phase	KH_2PO_4 (pH1.8) : Methanol (80:20)	Water : ACN (60:40)
Flow rate (mL/min)	0.4	
Column Temperature (°C)	40	
Sample Temperature (°C)	Room Temperature	10
Wavelength (nm)	228	226

The dyes MB and RB19 concentration was analysed by using visible spectrometer (Spectroquant® Pharo 100, Merck) at λmax = 664 nm and 596 nm respectively. The degree of mineralization of all pollutants was expressed as TOC using O.I Analytical Aurora 1030W TOC Analyzer. Figure 3.9-3.12 portrait the calibration curve for AMX, BPA, MB and RB19 respectively. The schematic of the experimental setup is displayed in Figure 3.13.

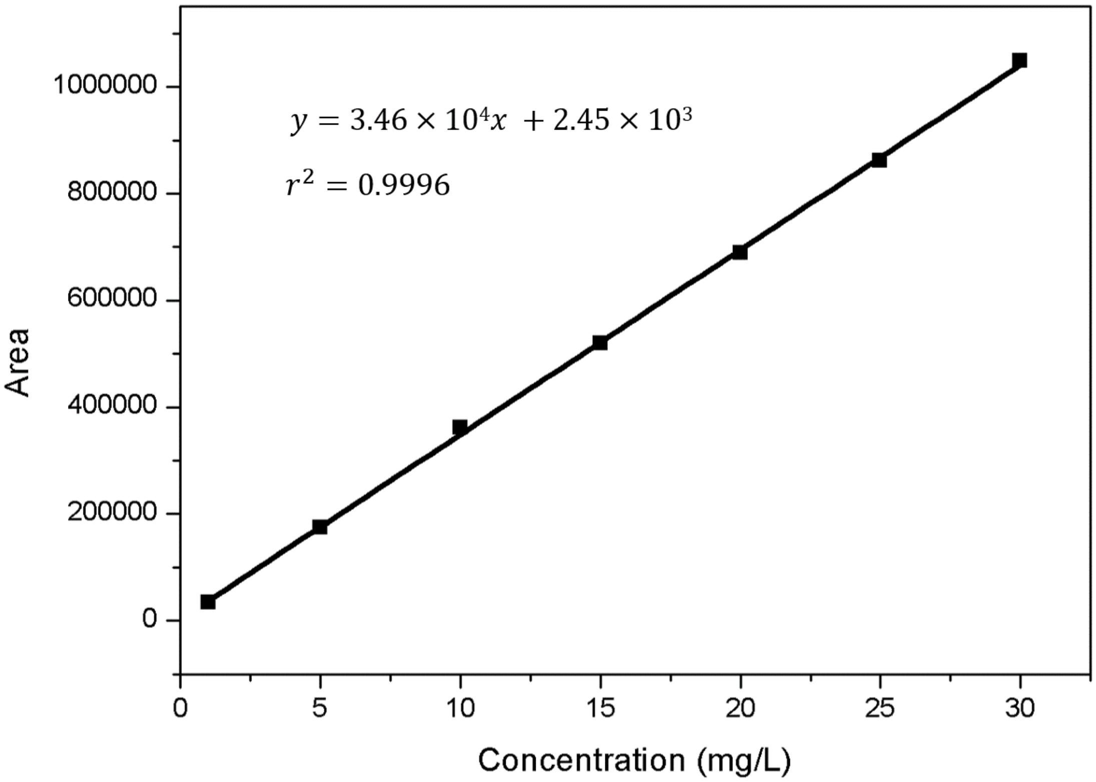

Figure 3.9: Calibration curve for AMX

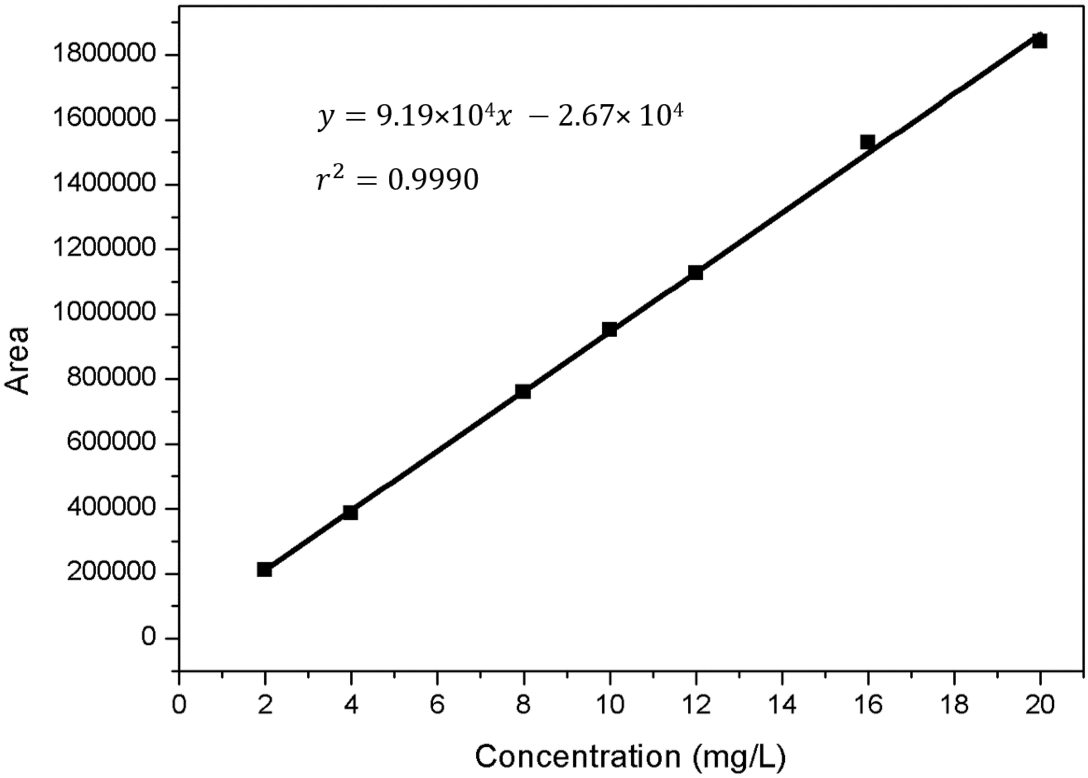

Figure 3.10: Calibration curve for BPA

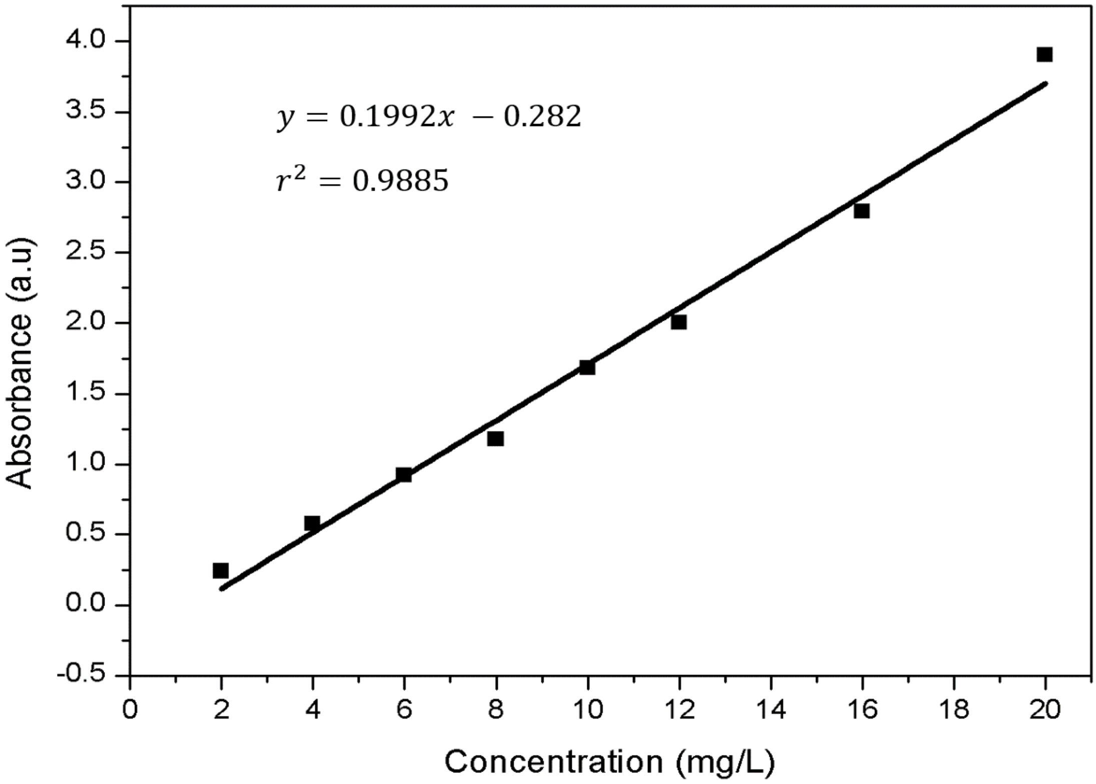

Figure 3.11: Calibration curve for MB

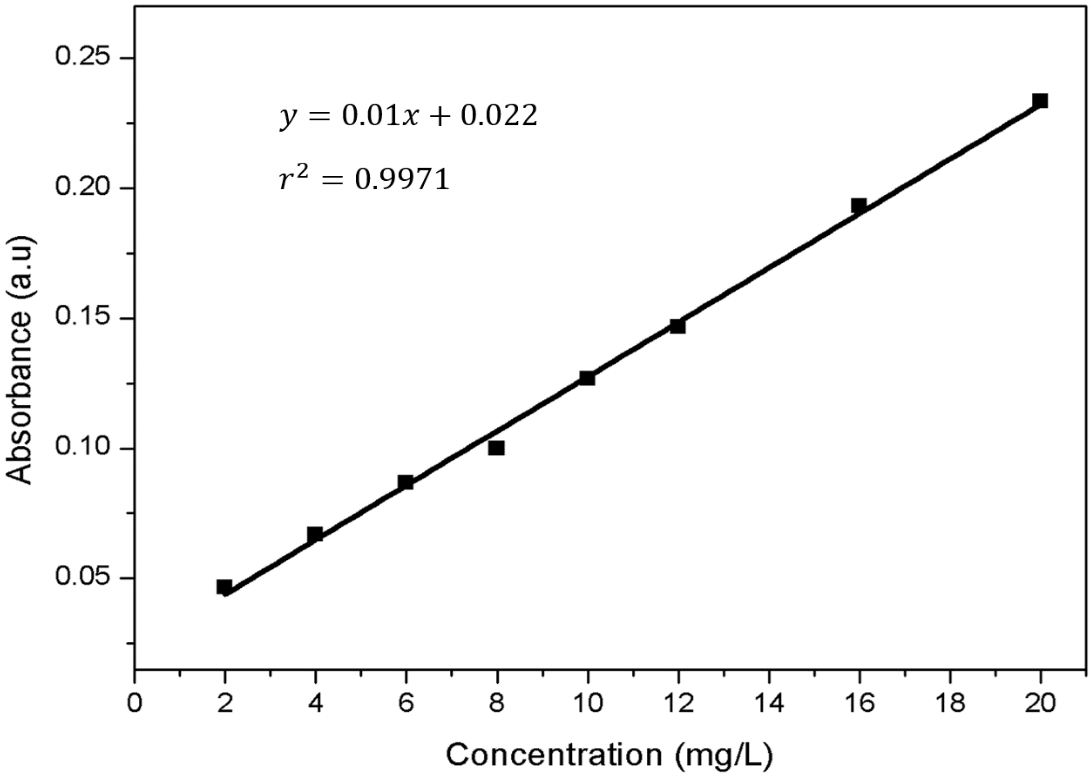

Figure 3.12: Calibration curve for RB19

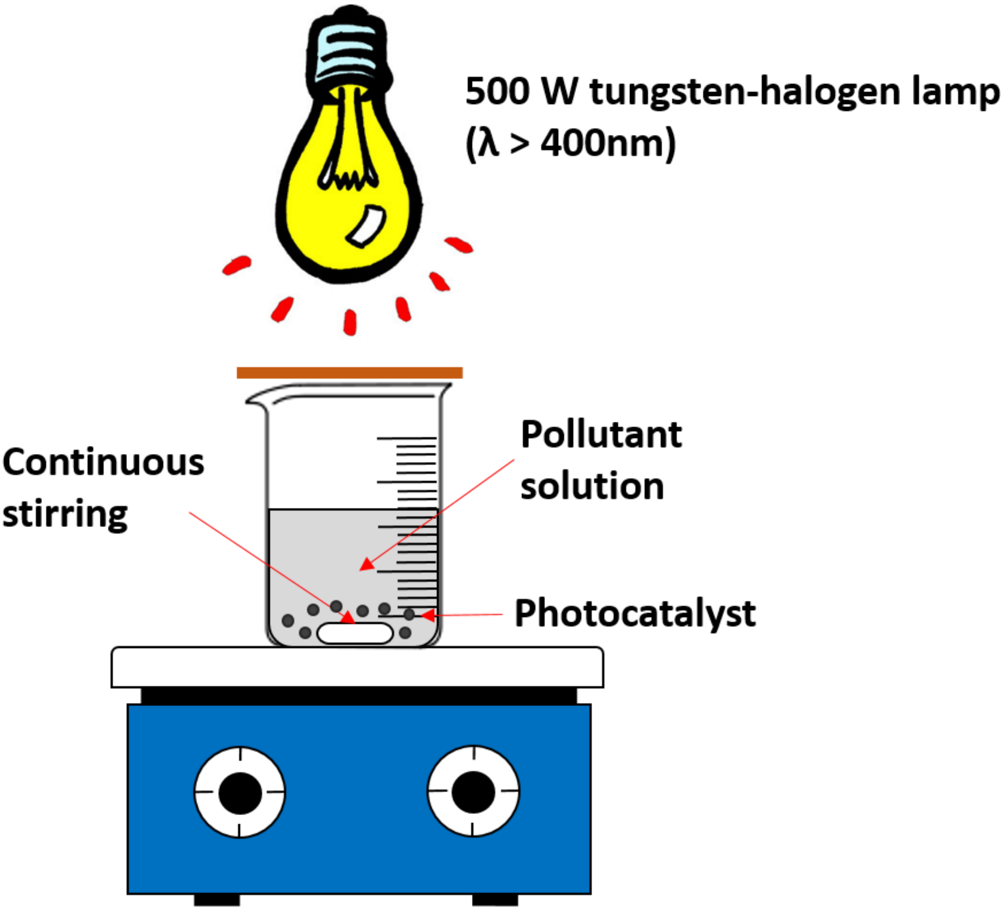

Figure 3.13: Schematic of the experimental setup adopted for artificial visible light photocatalysis experiments

CHAPTER 4

RESULTS AND DISCUSSION

This chapter presents the obtained results along with the analysis, inferences and science behind those observations. The preliminary section of the chapter discusses on the characteristics of the synthesized template TiO_2. The later sections present the evolution of synergised Titania achieved with the support of noble metals, conducting carbon material through sustainable approach for enhancement of visible light photocatalysis.

4.1 Anatase Template TiO_2

The present work is aimed to investigate the photocatalytic activity of anatase template TiO_2 synthesized through modified non-hydrolytic route using $TiCl_4$ as a precursor. The technique delivered two samples of varied characteristics and are designated as-synthesized and calcined. Thus obtained were characterized with various analytical characterization techniques for understanding the materials chemistry. Furthermore, their photocatalytic performance was evaluated by degrading 2, 4-DCP under solar light irradiation.

Figure 4.1 depicts the XRD patterns of the titania nanoparticles. The obtained diffraction peaks were synchronised well with the JCPDS card No: 21-1272 indicating the body-centered tetragonal anatase phase of TiO_2. The diffraction peaks at $2\theta = 25.25°$ (101), 47.98° (200), 53.59° (105), 37.82° (004) and 62.36° (215) were all corresponds to the lattice plane of complete anatase phase. The peaks at $2\theta = 27.5°$ (110) and 30.8° (121)

signifies the absence of rutile and brookite and further confirms both the synthesized TiO_2 bear complete anatase phase. The as-synthesized one showed a wide peak (25.25°) with more background disturbances indicating the amorphous nature. A sharp and more intense peak (Figure 4.1 (b)) was obtained for the calcined and was attributed to improved crystallinity and crystallite size achieved through heat treatment (W. Li & Zeng, 2011). Crystallite grain sizes were calculated using Scherer's formula.

$$D = \frac{k\lambda}{\beta cos\theta} \tag{4.1}$$

where, D is the crystallite size (nm), k is the shape constant (0.9), λ is the wave length of Cukα radiation (0.154 nm), θ is the diffraction angle (degree) and β is the full width at half maximum. The crystallite sizes were calculated to be 4.65 and 14.8 nm for as-synthesized and calcined samples respectively.

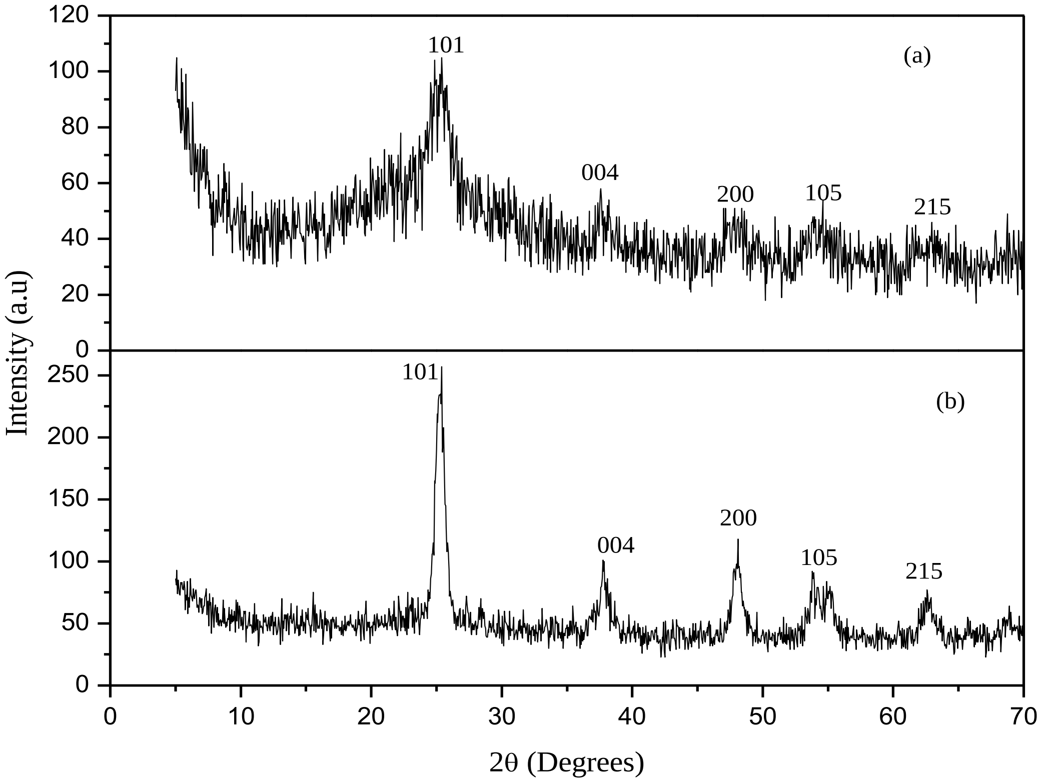

Figure 4.1: XRD diffraction pattern of (a) as-synthesized TiO_2 (b) calcined TiO_2

The Raman spectra of the prepared samples are presented in Figure 4.2. Two notable broad bands at 425 and 609 cm^{-1} was observed for the as-synthesized TiO_2 confirming the presence of amorphous phase. On the other hand calcined exhibited two minor bands at 399, 515 and a prominent band at 639 cm^{-1} correspond to the unique characteristic of crystalline anatase TiO_2. The obtained Raman shift after calcination well clarified the increase in the crystallinity and crystallite size. While the non-occurrence of bands at 445 and 612 cm^{-1} indicates the complete absence of rutile phases. Thus Raman spectrum of samples also confirms the presence of complete anatase phase (W. Li & Zeng, 2011; Tompsett et al., 1995; T. Zeng, Qiu, Chen, & Song, 1998).

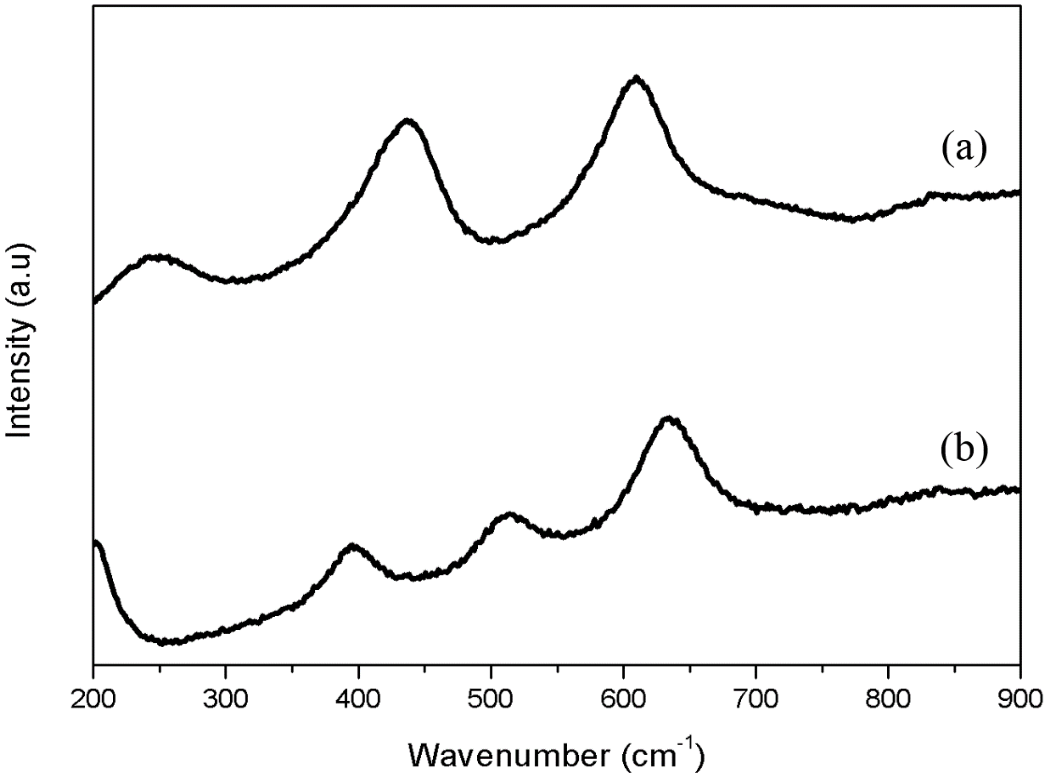

Figure 4.2: Raman Spectra of titania nanoparticles (a) as-synthesized TiO_2 (b) calcined TiO_2

The morphological images of the achieved anatase titania nanoparticles were depicted in Figure 4.3 (a-f). Figure 4.3 (a-c) signifies the amorphous nature of as-synthesized TiO_2 with a clear observation of uniform spherical shape and agglomeration. Where else Figure 4.3 (d-e) denotes the spheroid shaped with uniform size particles distributed homogeneously for the calcined. Higher magnification images clearly illustrate the amorphous nature of as-synthesized (Figure 4.3 (c)) and crystalline nature of calcined sample (Figure 4.3 (f)). The obtained images showed a higher particle size due to agglomeration of the nanoparticles. Further the images also revealed the more uniformity nature for the as-synthesised over calcined.

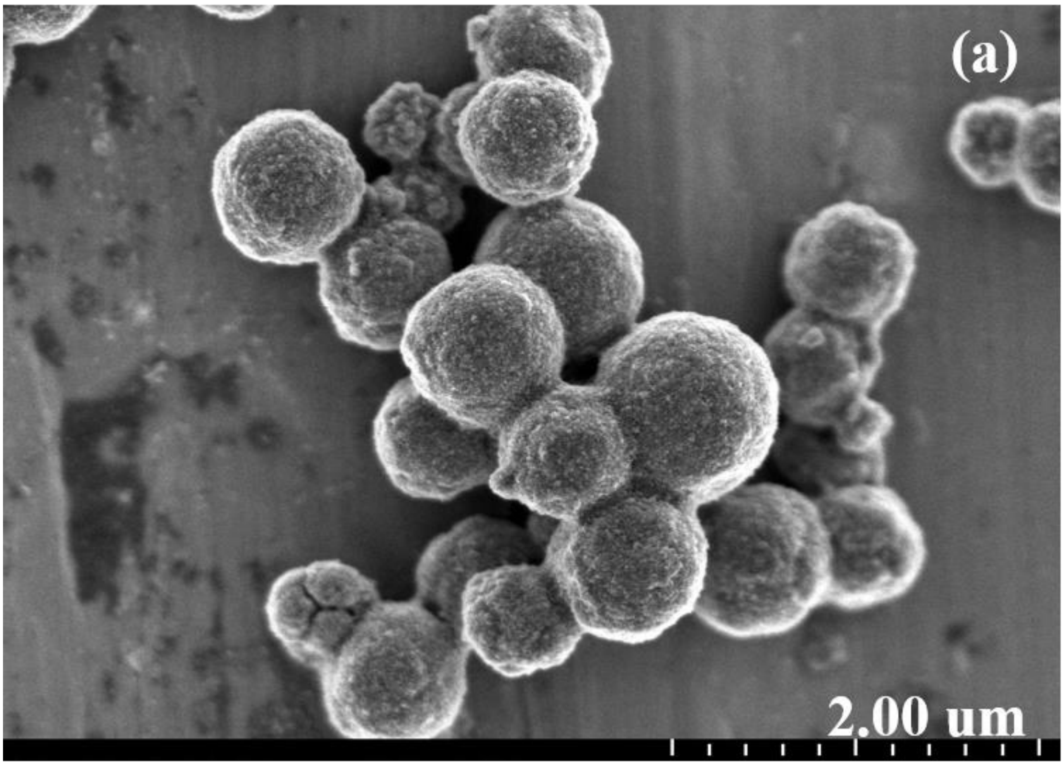

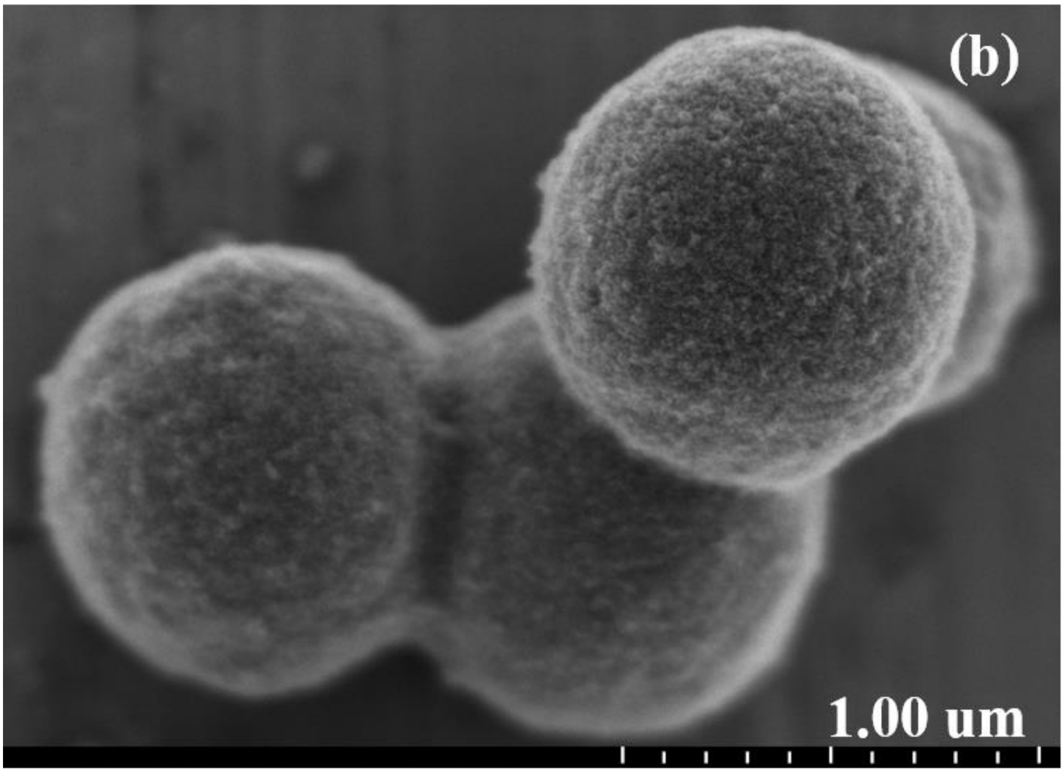
(b)
1.00 um

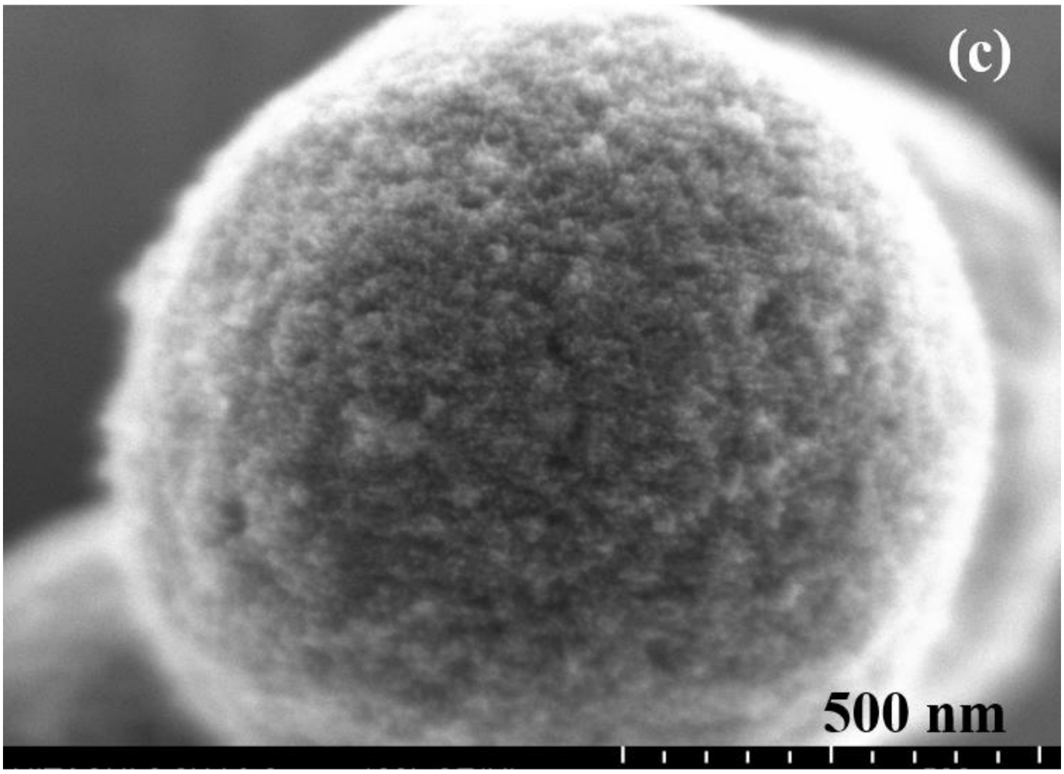
(c)
500 nm

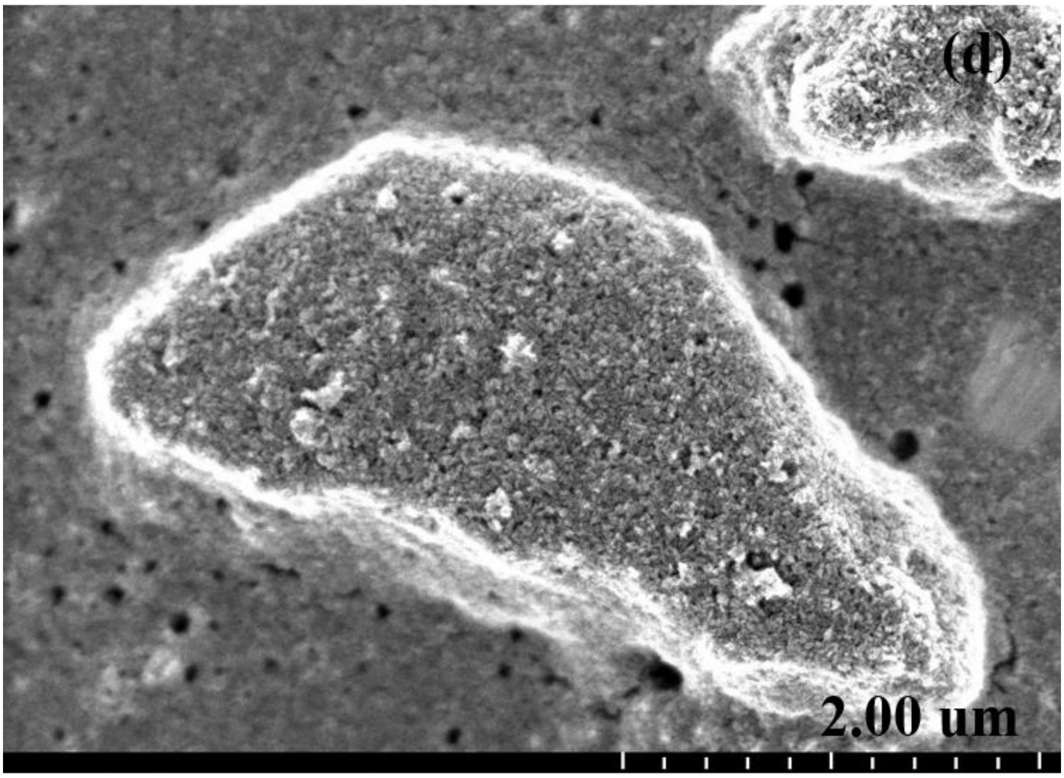
(d)
2.00 um

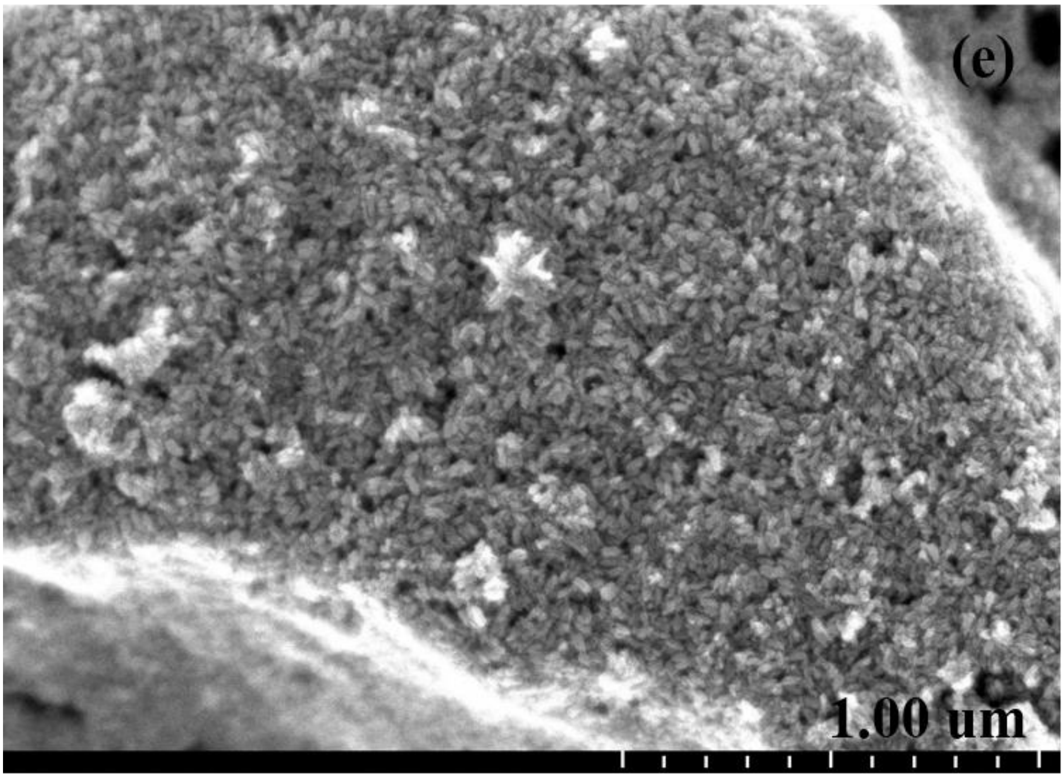
(e)
1.00 um

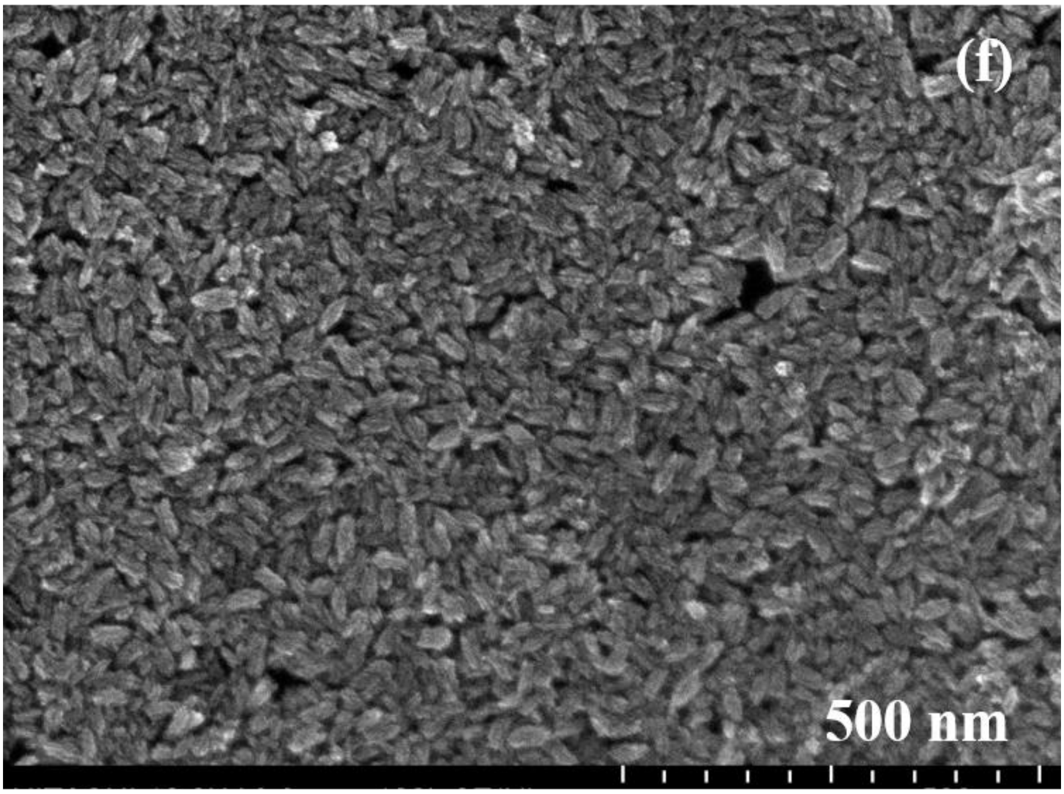

Figure 4.3: FESEM images of (a-c) as-synthesized TiO_2 (d-f) calcined TiO_2

The particle size of the titania was measured using TEM and presented in Figure 4.4 (a) and (b). The diameter of the as-synthesized TiO_2 was ranged between 3 and 6 nm (Figure 4.4 (a)). Similarly the diameter of the calcined TiO_2 was between 11 and 15 nm. The increase in particle size was attributed to the temperature effect and the obtained results were very well correlated with the crystallite size measured by XRD analysis. Although there is a morphological variation of the as-synthesized and calcined TiO_2 but the particles were more uniform in nature. The EDX spectra of the anatase TiO_2 were analyzed and the spectra showed the presence of Ti and O elements (Figure 4.5). The absence of the Cl^- ion confirms the effectiveness of the adopted washing procedure was in removing the unwanted anion (Cl^-).

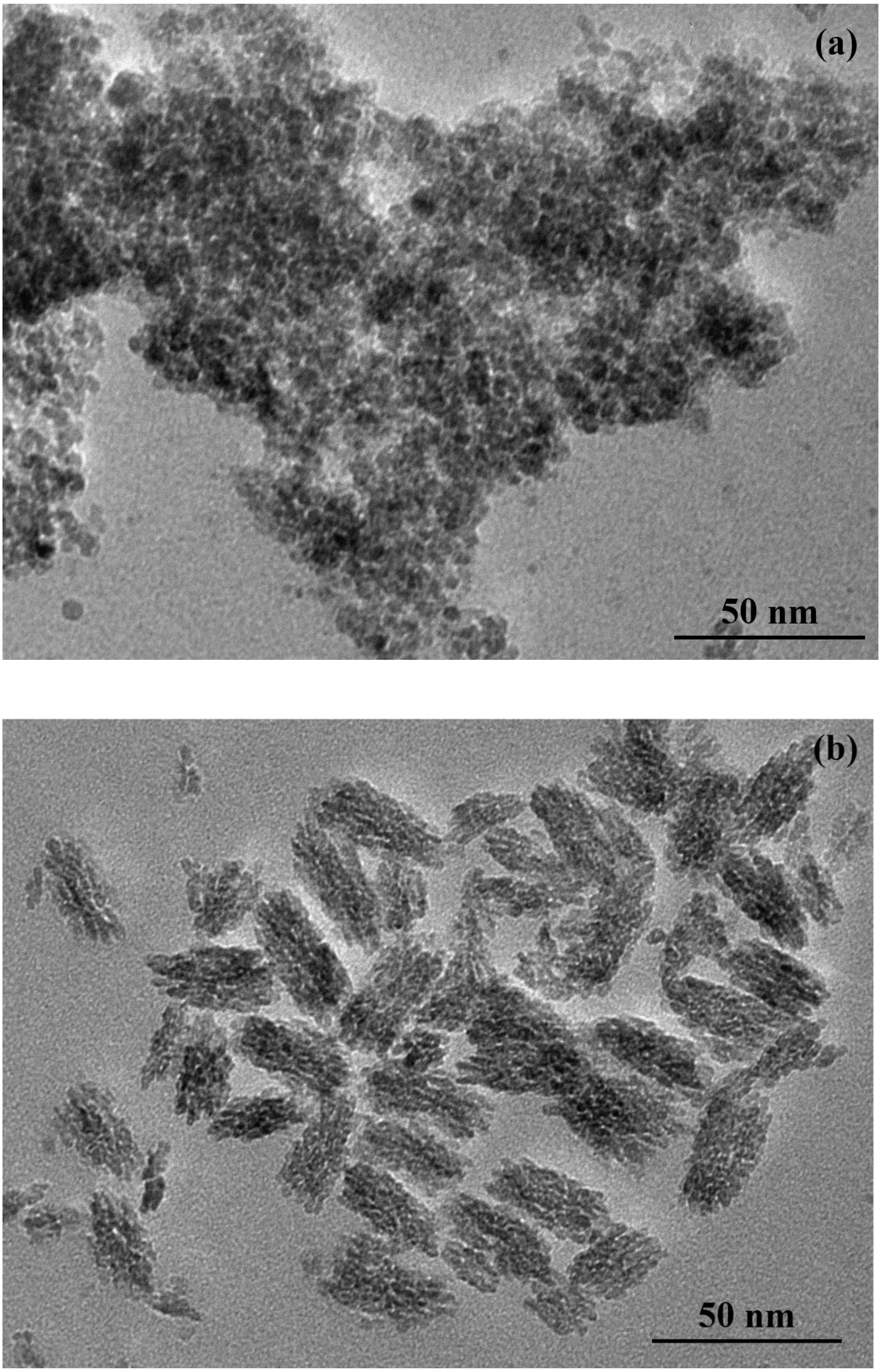

Figure 4.4: TEM images of (a) as-synthesized TiO_2 (b) calcined TiO_2

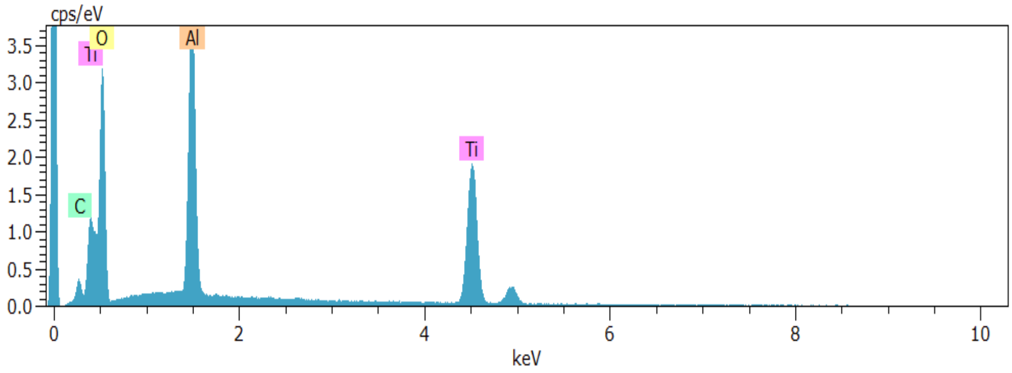

Figure 4.5: EDX spectra of anatase TiO_2

Nitrogen adsorption-desorption isotherms and corresponding pore size distribution of both as-synthesized and calcined TiO_2 was depicted in Figure 4.6 (a) and (b). Both the samples revealed a stepwise adsorption-desorption represented by type IV isotherms according to the IUPAC classification. The hysteresis loops indicates the slit-shaped pores for as-synthesized TiO_2 and cylindrical shaped pores for calcined TiO_2. The BET surface area of the as-synthesized and calcined TiO_2 was found to be 147.34 and 64.92 m^2/g, respectively. A sharp decrease in the BET surface area of the calcined TiO_2 was ascribed to the gradual increase in grain size during calcination. In addition, the average pore diameter, determined by Barrett–Joyner–Halenda (BJH) method (inset of Figure 4.6 (a) and (b)) increased after calcination. The pore size distribution indicates that the as-synthesized TiO_2 had a smaller pore size (3.46 nm) than calcined TiO_2 (9.24 nm). Bimodal pore size distributions observed for calcined TiO_2 and were attributed to the uncontrollable pore collapse during calcination and also reflect the detrimental effect in photocatalytic performance. It is know that the mesoporous anatase TiO_2 possessing both high surface area and crystallinity bear good photocatalytic properties (Q. Zhang et al., 2011). Although the surface area of the calcined TiO_2 was low compared to as-synthesized, the increased crystallinity of calcined showed a salutary effect in photocatalytic activity. In addition, solar energy conversion efficiency may vary based on the particle size and pore size distribution (Parmar, Ramasamy, Lee, & Lee, 2010). At times, very small average pore size of anatase TiO_2 would hinder the access of organic pollutants resulting in poor degradation. Hence both the anatase TiO_2 nanoparticles were experimented for their photocatalytic activity under sunlight irradiation.

High resolution XPS spectra of both the anatase nanoparticles were shown in Figure 4.7 (a) and (b). Both the TiO_2 nanoparticles exhibited similar pattern with existence of Ti 2p shell element. In general, the Ti 2p peak is varied between 456 and 464 eV. The obtained broad peak at 463 eV and a sharp narrow peak at around 458 eV for both the as-synthesized and calcined indicate the presence of Ti and Ti^{4+} species. These peaks are attributed to an active site which improves the photocatalytic activity, especially under the solar light irradiation (Aziz, Puma, Ibrahim, & Saravanan, 2013).

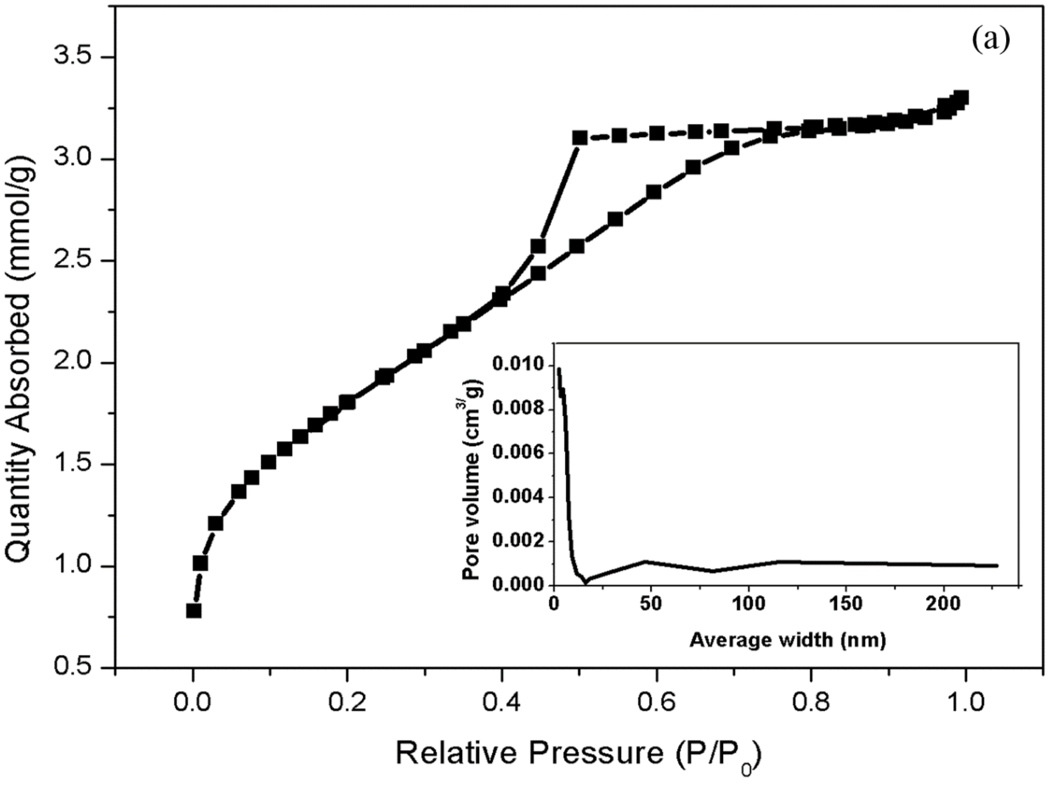

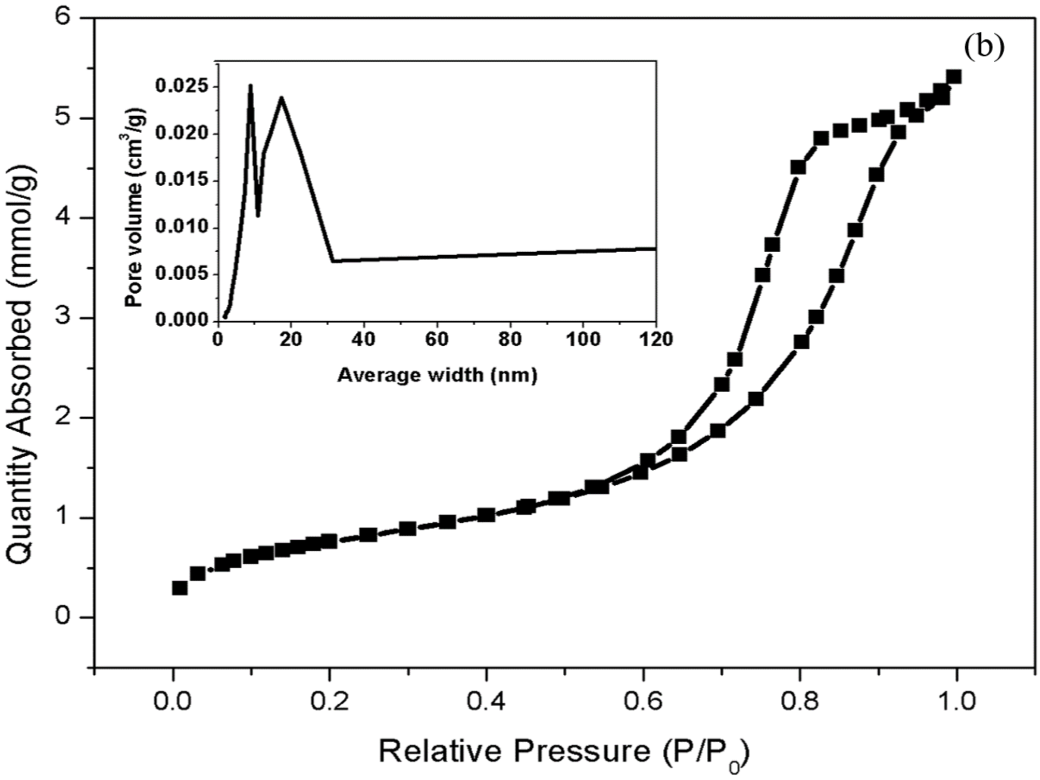

Figure 4.6: Adsorption-desorption isotherm of (a) as-synthesized TiO_2 (b) calcined TiO_2 along with the pore size distribution

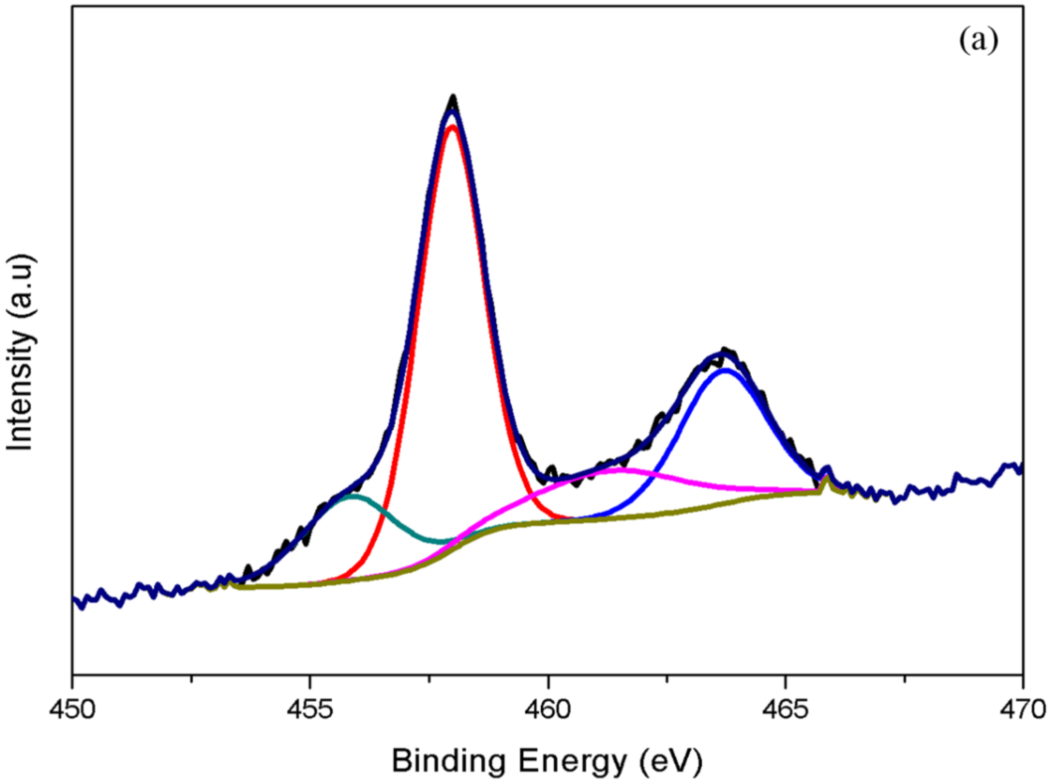

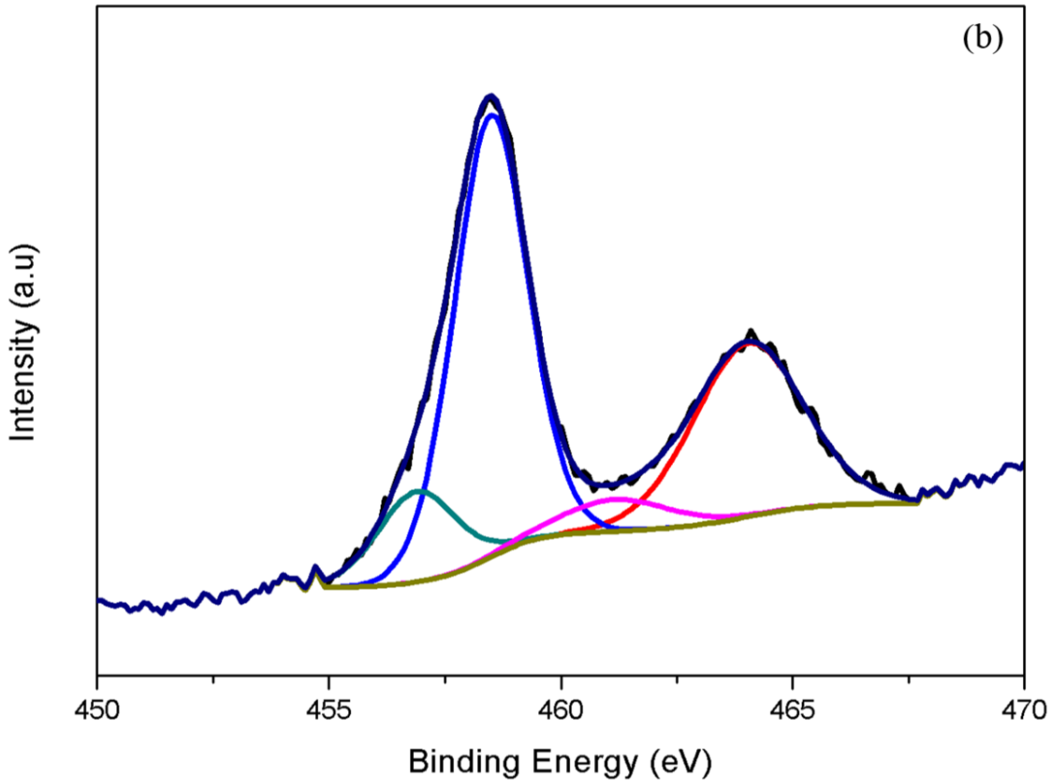

Figure 4.7: XPS spectra of Ti (a) as-synthesized TiO_2 (b) calcined TiO_2

The UV-Vis absorption spectra of the anatase TiO_2 samples were shown in Figure 4.8. The obtained spectrum depicts the response of the prepared TiO_2 in both UV and visible light spectrum. From the spectrum an evident strong increase in absorption at 425 nm was observed and is attributed to the excitations of electrons from the valence band to the conduction band of titania. Kulbeka-Munk equation was used to obtain the band gap energy of TiO_2 nanoparticles. The reflectance data was translated to the absorption coefficient F (R∞) values and is shown in Figure 4.9 (Burgeth & Kisch, 2002; Lin et al., 2006; Valencia, Marín, & Restrepo, 2010):

$$F(R\infty) = \frac{(1 - R\infty)^2}{2R\infty} \tag{4.2}$$

where, R∞ is the diffused reflectance of at the given wavelength

$$E(eV) = \frac{hC}{\lambda} \tag{4.3}$$

where, h is the Planck's constant (6.626×10^{-34} Js), C is the speed of light (3.0×10^{8} ms^{-1}) and λ is the wavelength (nm). From the Kulbeka-Munk analysis, the band gap energy of the as-synthesized and calcined TiO_2 was found to be 3.1 and 3.25 eV respectively. The increase in band gap energy for calcined TiO_2 was signified to the increase in crystallinity of calcined than the as-synthesized.

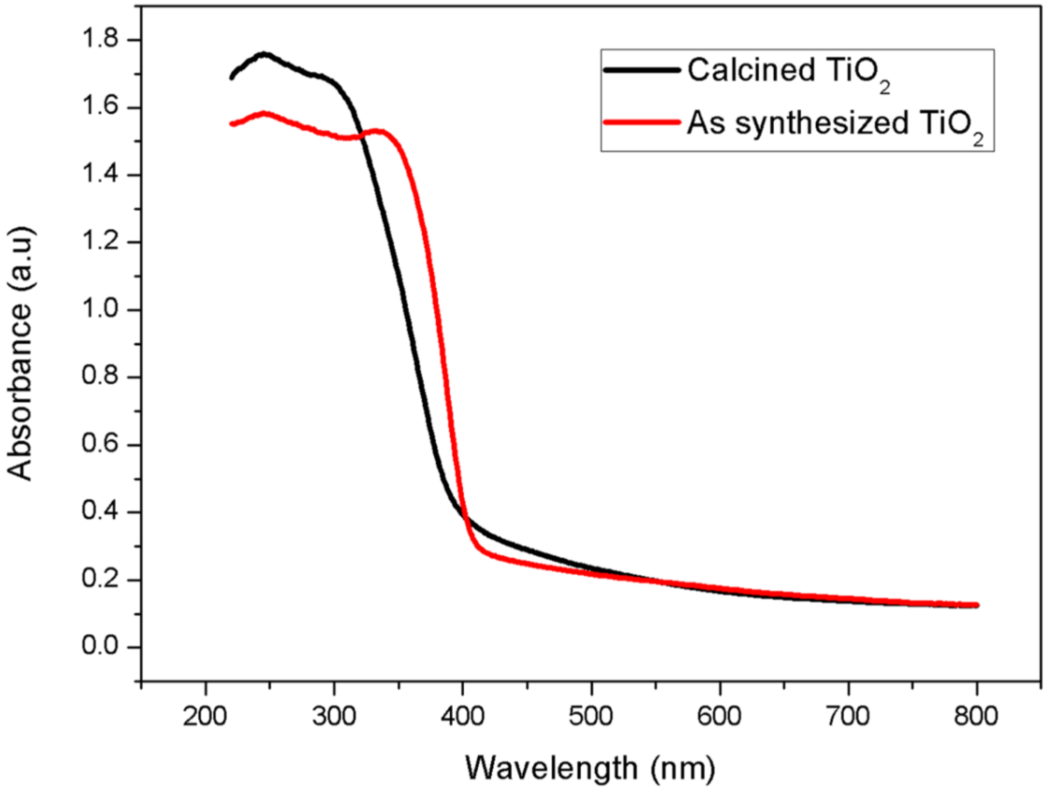

Figure 4.8: UV-Vis absorption spectra of prepared TiO_2 photocatalysts

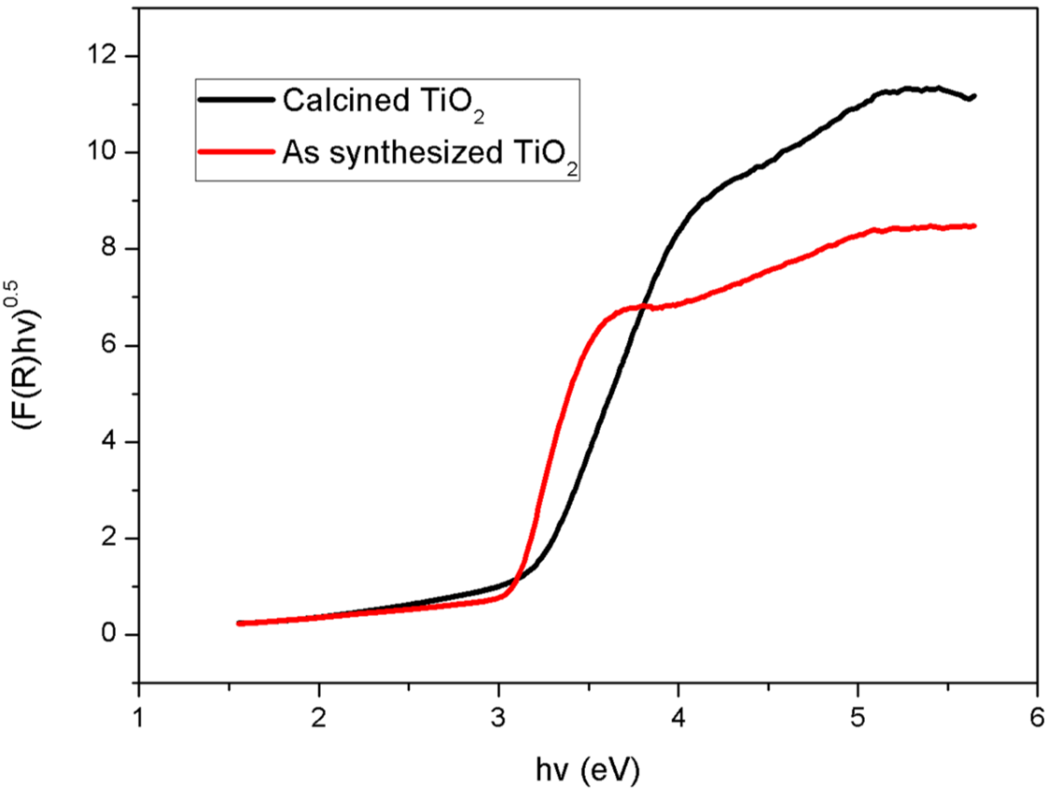

Figure 4.9: Calculated band gap energy of prepared TiO_2 photocatalysts

The results of control experiments and photocatalytic degradation experiments of 50 mg/L (250 ml solution) of 2, 4-DCP on as-synthesized and calcined TiO_2 under the solar light irradiation were depicted in Figure 4.10. The obtained results suggests that a complete degradation of 2, 4-DCP was achieved using both the TiO_2 photocatalysts with variation in time duration. The control experiments confirms that only a limited amount of 2, 4-DCP was removed (<1%) in the absence of the TiO_2 photocatalysts by direct photolysis. From the dark reactions (Figure 4.10), it was clear that a modest removal of 2, 4-DCP was occurred due to adsorption (10-12% for as-synthesized TiO_2 and 18-20% for calcined TiO_2). Almost complete degradation (99-100%) was achieved for both the samples under solar light radiation; however, the as-synthesized TiO_2 took longer period of 3.5 h than calcined that took 2.5 h. According to the optical spectra and band gap energy value the as-synthesized TiO_2 was expected to possess better photocatalytic activity than the calcined TiO_2. However, the obtained upturned observance was attributed due to various reasons. The photocatalytic activity depends on the efficiency of utilization of the fraction of incident light absorbed by the catalyst (Ahn, Kim, Kim, & Hahn, 2003; Dolat, Quici, Kusiak-Nejman, Morawski, & Li Puma, 2012; Pupo Nogueira & Guimarães, 2000; Sério, Melo Jorge, Maneira, & Nunes, 2011). In an irradiated suspension of photocatalyst particles photons were absorbed and scattered. Owing to amorphous nature of the as-synthesized photocatalyst the scattering of incident solar light energy was more than the absorbed energy (results in decreased formation of electron and hole pairs) as compared to that of calcined, and resulted in deprived photocatalytic activity. In addition amorphous surface has many defects that act as an active recombination centers for the photo generated electrons and holes, which further decreased the photocatalytic activity. Furthermore, when particle size become extremely small (i.e. ≤ 5 nm in diameter), most of the generated electron and hole pairs may quickly reach the surface and undergo a rapid surface recombination that reduces the photocatalytic activity of the as-synthesized one (Hines & Guyot-Sionnest, 1996; N Serpone, Lawless, Khairutdinov, & Pelizzetti, 1995). The other possibility for deprived photocatalytic activity of as-synthesized might be due to overloading of the photocatalyst (excess of photocatalyst particles scatters the sunlight) and also due to agglomeration of particles that hinders the penetration of sunlight.

From the dark reactions, it is clear that the adsorption capacity of 2, 4-DCP is higher for calcined than as-synthesized. Although the as-synthesized has higher surface area than the calcined, the high adsorption capacity was attributed to the surface charge characteristics. The calcination step contributed for the increment of crystallinity and the surface charge and led to increased adsorption of 2, 4-DCP. Thus in the calcined sample the photogenerated electrons were readily trapped on Ti^{4+} sites and form Ti^{3+} that traps the electrons and readily scavenged by oxygen. Hence, the localized holes can be scavenged by either reacting with hydroxide ions or through electron transfer with water to form hydroxyl and super oxide radicals (Almquist & Biswas, 2002; Ilisz, Dombi, Mogyorósi, Farkas, & Dékány, 2002; Li Puma & Yue, 2002; Lin et al., 2006). In the case of as-synthesized a similar number or more electrons and hole pairs were generated. However smaller particle size and higher surface area favored the recombination of the generated electron and hole pair resulting a deprived photocatalytic activity over calcined. Thus the photocatalytic activity of as-synthesized declined in spite of lower band gap energy (3.1 eV). Photocatalytic degradation potential of the as-synthesized and calcined TiO_2 was compared with different phenolic compounds under various irradiation sources and listed in Table 4.1. It was clear from the Table 4.1, that the UV as a source of irradiation resulted in better photocatalytic performance than visible light irradiation attributed to the band gap energy of the TiO_2 photocatalysts that can utilize only the wavelength less than 380 nm. It was also evident from the Table 4.1 that the synthesized photocatalysts has the potential to utilize the solar energy emerged with higher photocatalytic activity to completely degrade the 2, 4-DCP in a reasonable time.

Table 4.1: Comparison of the photocatalytic efficiency TiO_2 photocatalyst prepared from various precursors on phenolic compounds degradation under various irradiation sources

TiO_2 Photocatalyst	Model Pollutant	Dosage (g)	Initial Concentration (mg/L)	Irradiation Source	Photocatalytic Efficiency (%)	References
Tetra butyl Titanate as Precursor	2, 4-DCP	0.01	50.00	UV (30 W Hg lamp at λ_{max} =254nm)	45.0% in 2h	Han, Li, & Jia, 2010
$Ti(OC_4H_9)_4$ as Precursor	2, 4-DCP	1.00	15.00	UV (20 W Germicidal lamp with main λ= 254nm)	100% in 3h	Lifen Liu, Chen, Yang, Chen, & Crittenden, 2012
$Ti(OC_4H_9)_4$ as Precursor	2, 4-DCP	1.00	50.00	Visible light (diffused light)	90.0% in 5h	Aziz, Cheng, Ibrahim, Matheswaran, & Saravanan, 2012
$Ti(OC_4H_9)_4$ as Precursor	2, 4-DCP	1.00	50.00	Visible light (diffused light)	100% in 3h	Aziz, Yong, Ibrahim, & Pichiah, 2012
$TiCl_3$ as Precursor	phenol	0.20	50.00	UV (Philips 125 W high-pressure mercury lamp)	100% in 3h	Lu Liu et al., 2008
Degussa P25	2, 4-DCP	0.10	100.00	Visible Light (1000 W Iodine tungsten lamp with a glass filter)	39.3% in 4h	F. Chen, Zou, Qu, & Zhang, 2009

Table 4.1, continued

TiO_2 Photocatalyst	Model Pollutant	Dosage (g)	Initial Concentration (mg/L)	Irradiation Source	Photocatalytic Efficiency (%)	References
Degussa P25	2, 4-DCP	2.00	125.00	Solar Energy (Philips 1500 W xenon lamp)	99.0% in 6h	Bayarri, Gimenez, Curco, & Esplugas, 2005
Degussa P25	2-CP	1.00	100.00	Visible Light (100 W medium pressure mercury lamp)	50.0% in 2.5h	Doong, Chen, Maithreepala, & Chang, 2001
Degussa P25	phenol	0.20	100.00	Visible Light (200 W medium pressure mercury vapor quartz lamp with pyrex filter $<\lambda=320$nm)	60.0% in 3h	B. Sun, Vorontsov, & Smirniotis, 2003
$TiCl_4$ as Precursor	2-CP	0.01	75.00	UV (100 W mercury lamp)	78.0% in 3h	Barakat, Schaeffer, Hayes, & Ismat-Shah, 2005
$TiCl_4$ as Precursor	2, 4-DCP	1.00	50	Solar Energy	100% in 2.5h	Present study

Note: 2, 4-DCP: 2, 4-dichlorophenol, 2-CP: 2-chlorophenol

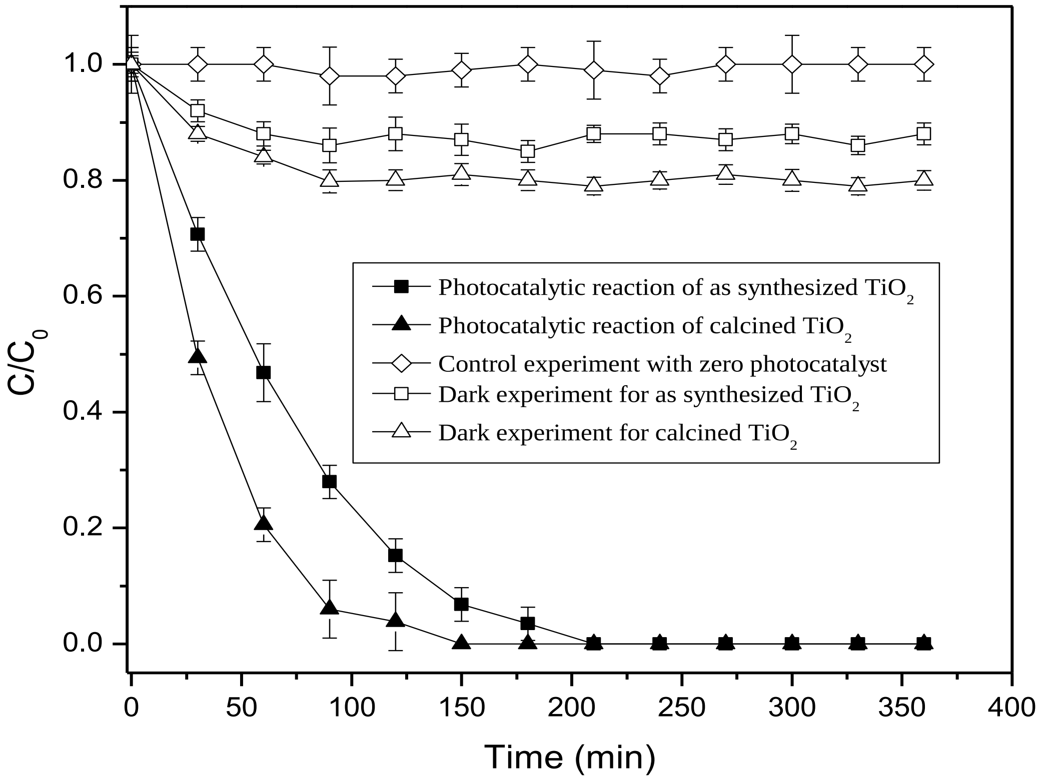

Figure 4.10: Photocatalytic evaluation of 2, 4-DCP by prepared TiO_2 photocatalysts under solar irradiation

The degree of mineralization of 2, 4-DCP during the photocatalysis was analysed as a function of TOC and depicted in Figure 4.11. An efficiency of 73.5% was achieved for as-synthesized TiO_2 while 61.5% for calcined one, respectively. A higher degree of mineralization was achieved for as-synthesized (73.5%) compared to that of calcined TiO_2 (61.5%) was again attributed to its smaller crystallite size and larger surface area. Only a significant mineralization occurred during dark experiment (< 9.0%) and control experiment (<1.0%) confirms that the mineralization was due to photocatalysis.

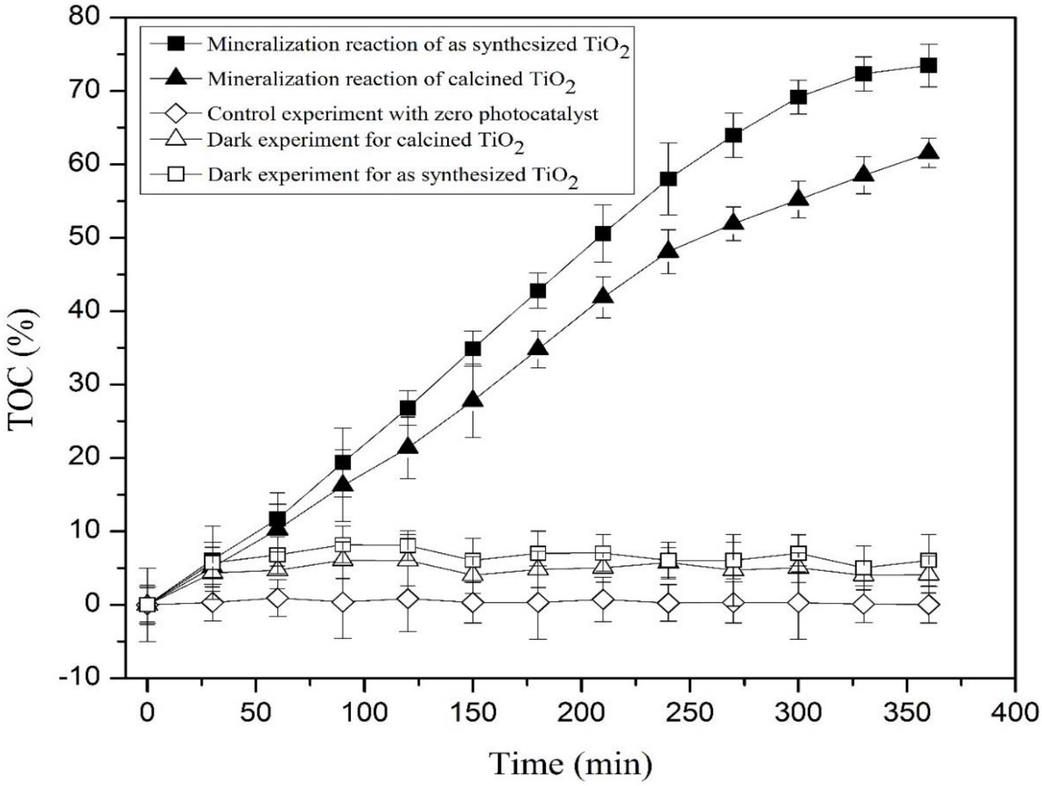

Figure 4.11: Percentage mineralization of 2, 4-DCP based on TOC analysis

The degradation kinetics of 2, 4-DCP on as-synthesized and calcined TiO_2 heterogeneous catalysts is explained by the first-order kinetics (K. V. Kumar, Porkodi, & Rocha, 2008). The first-order expression is given below.

$$-ln\frac{C}{C_0} = k_1 t \tag{4.4}$$

where, C_0 is the initial concentration of 2, 4-DCP (mg/L) and C is the concentration 2, 4-DCP at time t and k_1 represents the rate constant of first order reaction (min^{-1}). The obtained experimental data were fitted with first order kinetics and presented in Figure 4.12. Higher correlation coefficients ($r^2 > 0.97$) obtained for both the TiO_2 photocatalysts indicates that the degradation of 2, 4-DCP followed first-order kinetics. The first order reaction rate constants (k_1) were found to be 0.017 and 0.028 min^{-1} for as-synthesized and calcined TiO_2, respectively. Higher rate constant value of calcined TiO_2 indicates its potential for higher photocatalytic activity over as-synthesized.

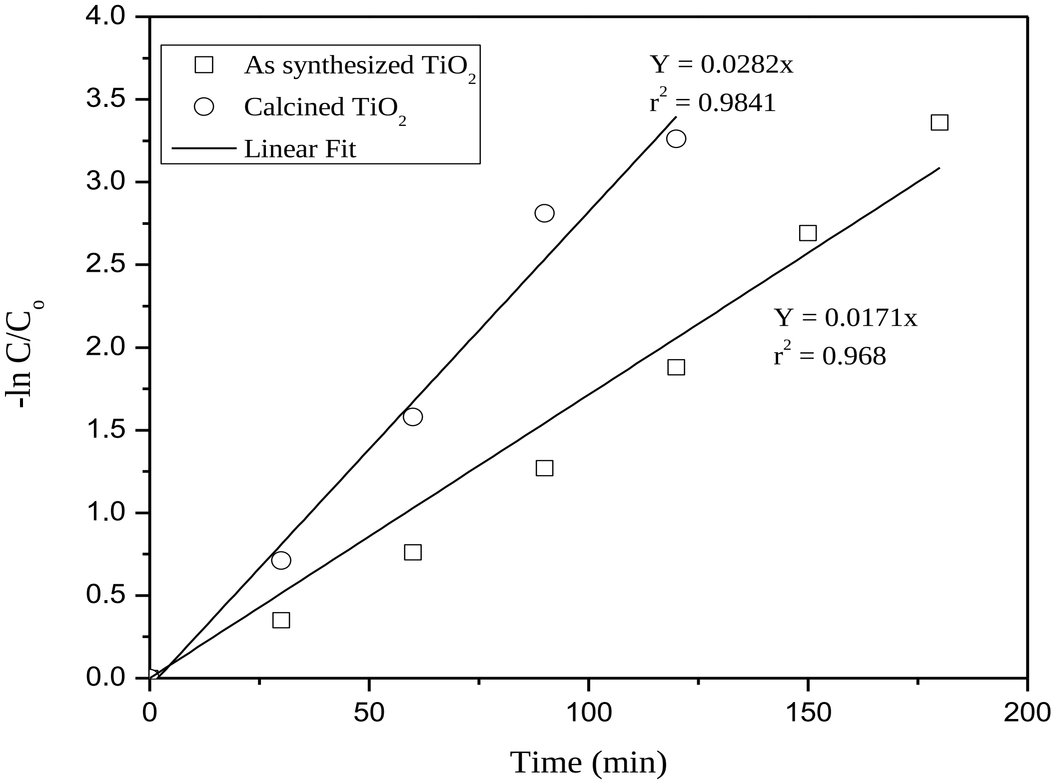

Figure 4.12: The kinetics of 2, 4-DCP degradation

Though an appreciable achievement was exhibited by the template TiO_2, but it still trail as an active visible light photocatalyst. Hence the necessary modifications were adopted for its successfulness as a visible light photocatalyst.

4.2 Palladium Modified TiO_2 for Synergised Visible Light Activity

The modification was approached by adopting a facile, ease and sustainable method with the support of noble metal (Pd) onto TiO_2. The Palladium NPs was chosen as a potential supporting candidate due to its high reactivity towards photocatalytic activity and reluctant toward surface oxidation. To the best of our knowledge, this is the first report on utilizing sustainable approach for the deposition of the Pd NPs onto TiO_2.

4.2.1 Deposition of Pd onto TiO_2 through Sustainable Route

The Pd/TiO_2 nanoparticles were synthesized via photodeposition with the aid of solar energy. The energy obtained from the exposed solar energy was adequate for the reduction and deposition of palladium onto TiO_2 surface. This was achieved by exciting TiO_2 under natural sunlight for the formation of electrons and holes. The generated electrons being excited to the conduction band (CB) which served as an electron source for reduction of palladium cations. The photoelectrons generated by TiO_2 reduced the Pd^{2+} to palladium nanoparticle and the holes from the valence band (VB) react with ethylene glycol to form aldehyde. The complete mechanism is illustrated in Figure 4.13.

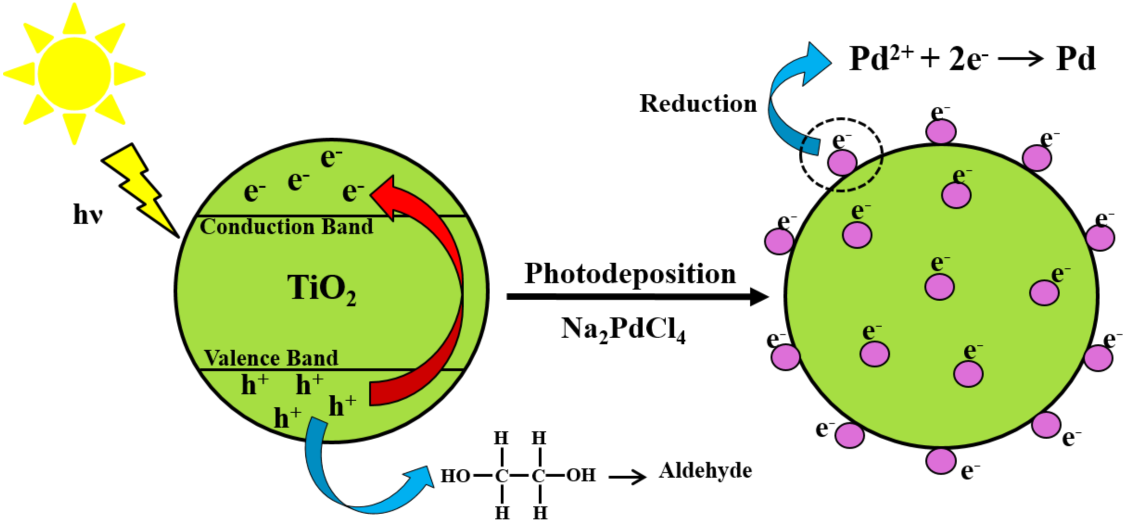

Figure 4.13: Schematic diagram for synthesis of Pd/TiO_2 via solar assisted photodeposition

4.2.2 Characterization

The synthesized modified photocatalyst was thoroughly investigated for its intrinsic nature. Figure 4.14 (a-c) depicts the morphological images of Pd/TiO_2 photocatalyst. It is evident from the obtained images that the synthesized palladium NPs is uniformly deposited onto the surface of TiO_2. It could be clearly seen from the Figure 4.14 (b) and (c) that TiO_2 particles are in spheroid shape with homogenous distribution. Where else, the Pd NPs exhibited spherical morphology with particles size ranging from 17-29 nm. The inset in Figure 4.14 (c) shows the corresponding EDX spectrum, confirming the presence elements in the synthesized photocatalysts. The HRTEM images (Figure 4.14 (d) and (e)) further confirmed the better formation of Pd/TiO_2 without changing the original morphology of TiO_2. It also further confirms the particles size of palladium. The presence of lattice fringes 0.22 nm and 0.35 nm spacing as seen in Figure 4.14 (f) clearly attributed to the face centered cubic (FCC) Pd (1 1 1) and anatase TiO_2 (1 0 1) planes, respectively (X. Chen et al., 2011; Mohapatra et al., 2008; Pan & Xu, 2013a; Xiong, Chen, et al., 2005). This also signifies the heterojunction formation between Pd and TiO_2, a mean for visible light absorption.

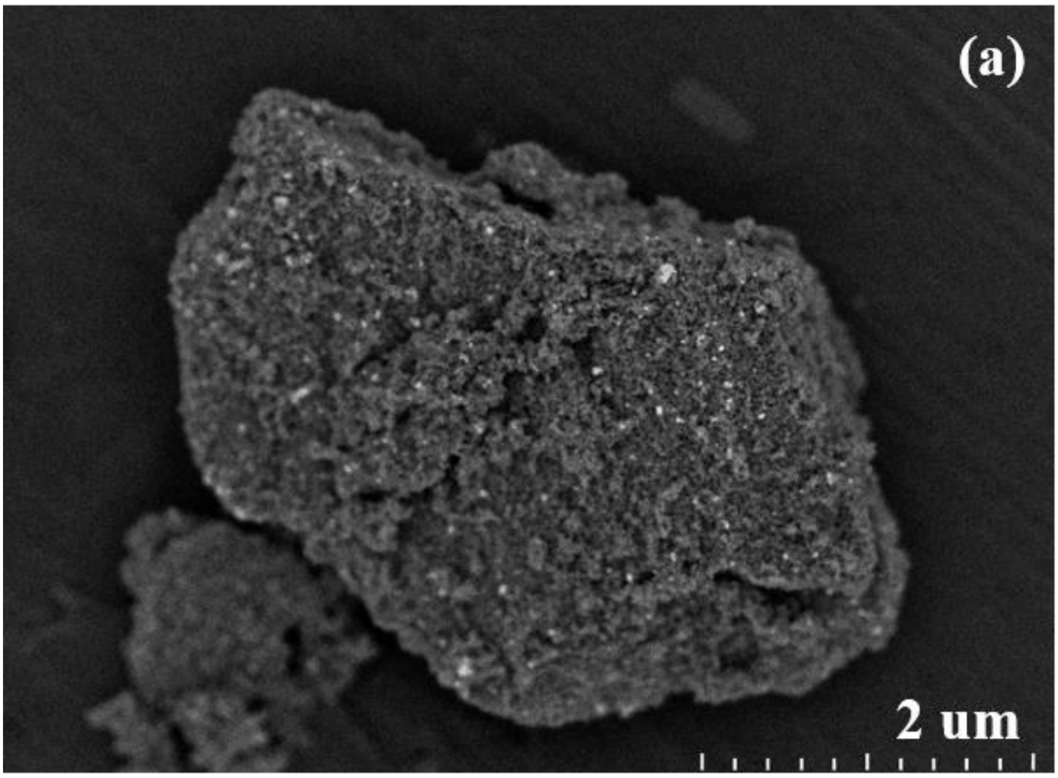
(a)
2 um

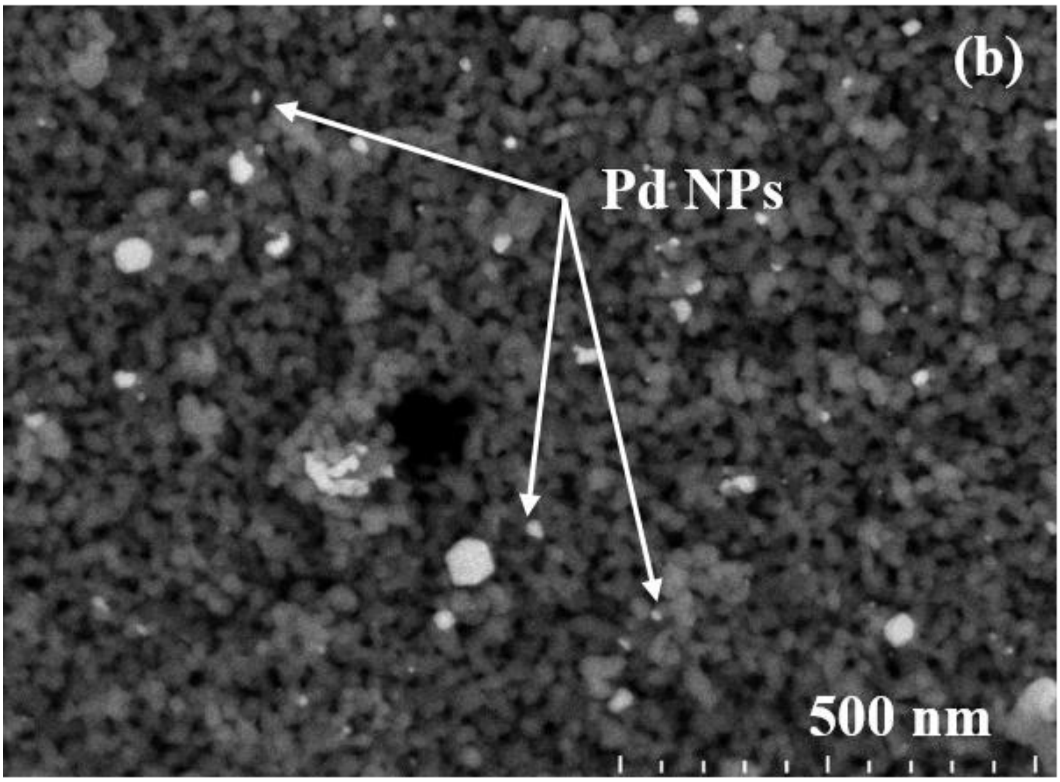
(b)
Pd NPs
500 nm

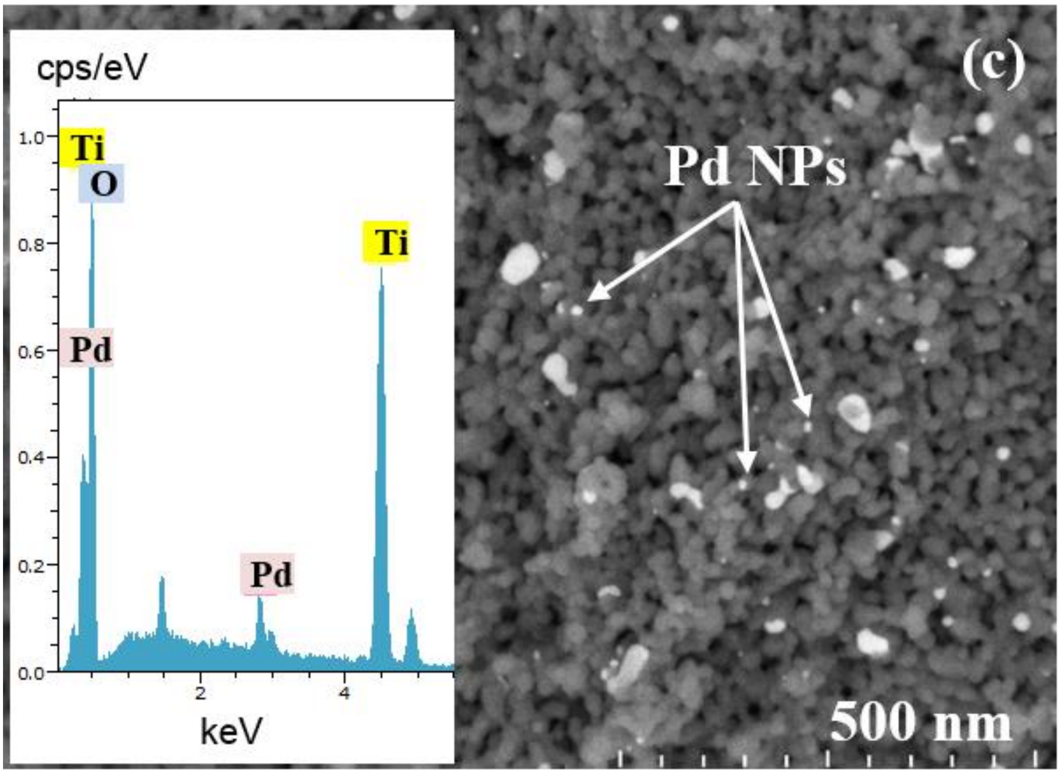
cps/eV
1.0
0.8
0.6
0.4
0.2
0.0
Ti
O
Pd
Pd
Ti
2
4
keV
(c)
Pd NPs
500 nm

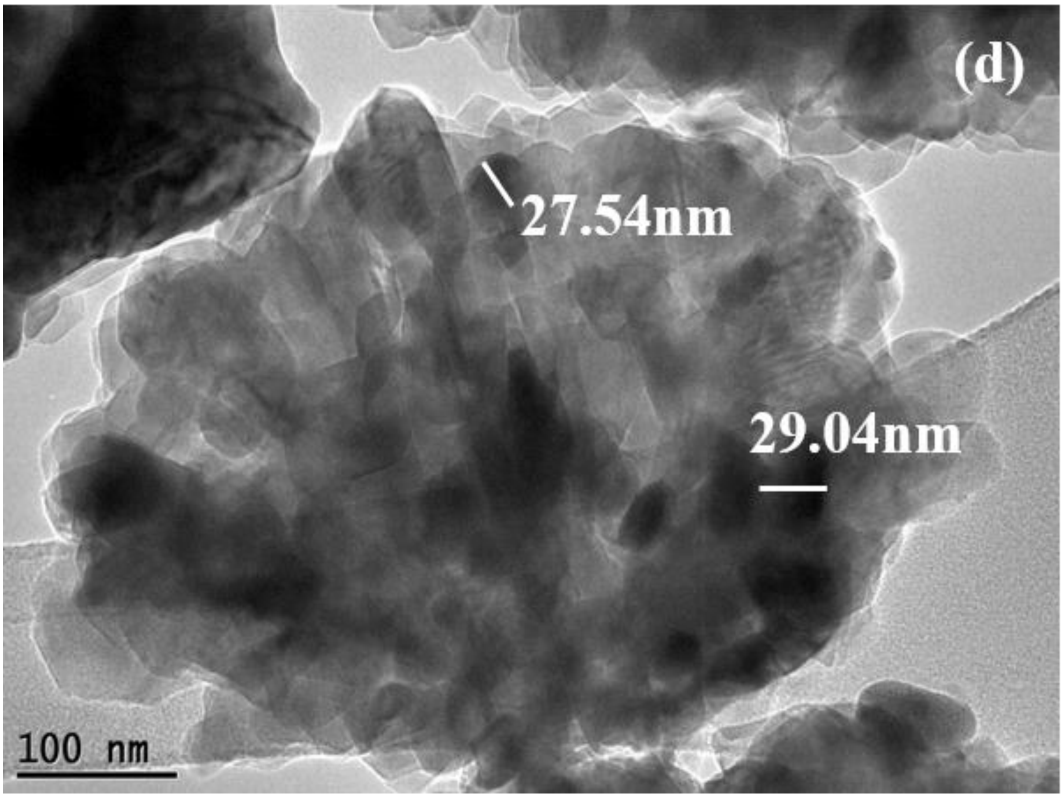
(d)
27.54nm
29.04nm
100 nm

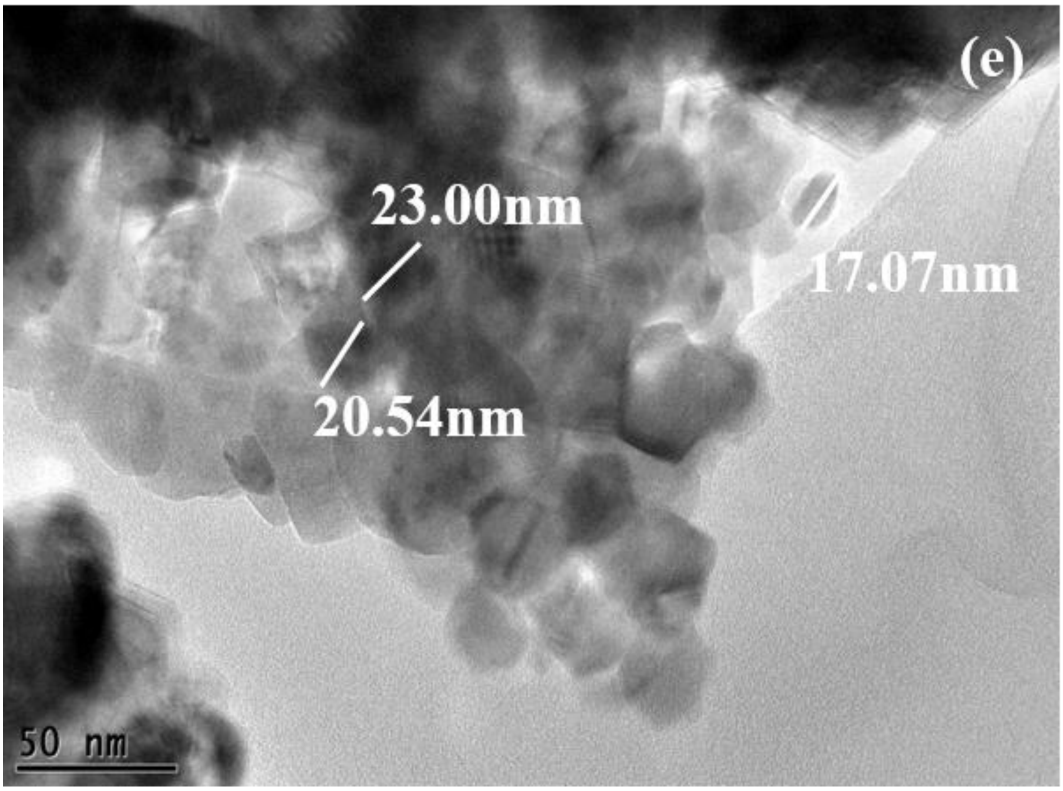

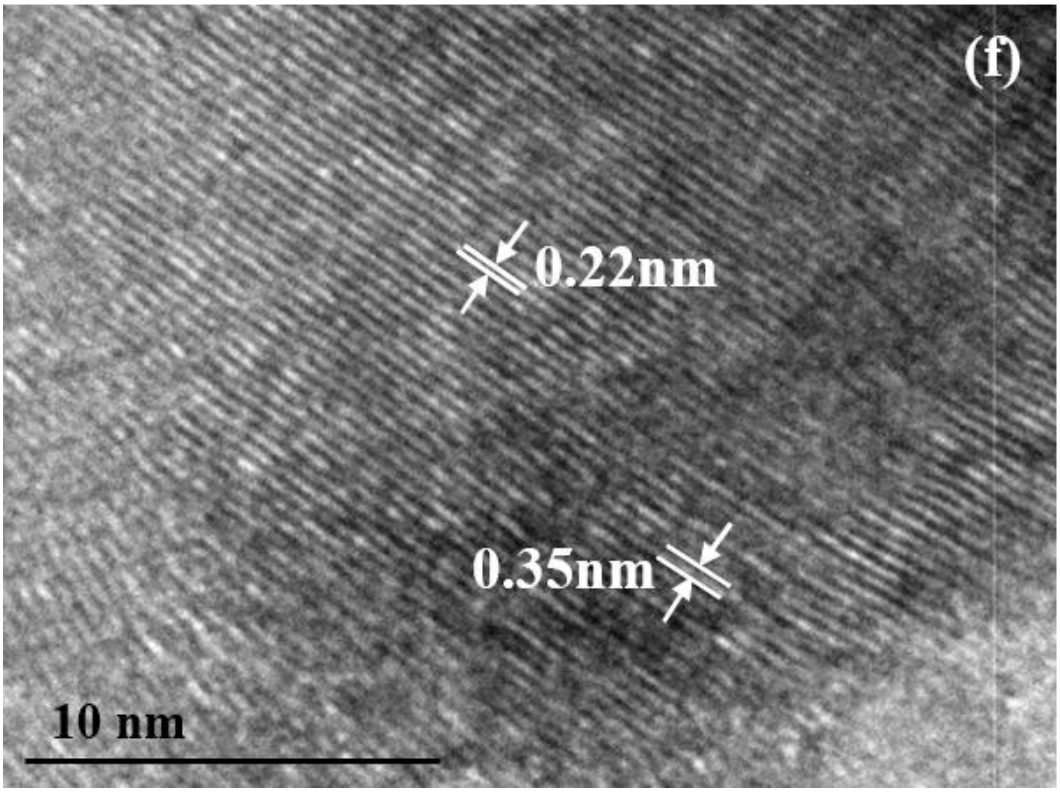

Figure 4.14: FESEM images of the (a) low magnification, (b-c) high magnification of 0.5wt% Pd/TiO$_2$. The inset of (c) is the EDX of 0.5wt% Pd/TiO$_2$ and (d-f) HRTEM images of 0.5wt% Pd/TiO$_2$

Figure 4.15 shows the X-ray diffraction patterns of anatase TiO_2 and Pd/TiO_2 with different Pd loading (0.5wt%, 1.0wt% and 3.0wt %). Pure anatase TiO_2 is observed in all samples indicating that its crystallinity and the phase is not distorted by the solar assisted photodeposition. The diffraction patterns of the prepared anatase TiO_2 well correlated with the standard peaks (JCPDS no. 21-1272). The presence of Pd NPs are signified by a diffraction peaks appeared at $2\theta = 40.1°$ and 46.7°. They are assigned to (1 1 1) and (2 0 0) crystal plane of face centered cubic (FCC) Pd (JCPDS no 46-1043) respectively. From the diffraction patterns only two peaks instead of three that designates Pd was observed. This was due to the peak overlap with the anatase TiO_2 at $2\theta = 68.1°$ (2 2 0) and pretends to be two peaks. Thus these three diffraction peaks further signifies the metallic state of the loaded Pd NPs. The peaks also confirm the stability of the synthesized palladium crystals that has a notable contribution to promising visible light performance (Chan, Chang, Hsu, Wang, & Lin, 2009). Overall, the prepared samples showed higher crystallinity that is ascertained by the sharp peaks. The average crystalline sizes of anatase TiO_2 and Pd particles were calculated using well know Scherrer equation. The crystalline size of the Pd particles was found to be 21.22 nm, 22.41 nm and 28.10 nm for 0.5wt% Pd/TiO_2, 1.0wt% Pd/TiO_2 and 3.0wt% Pd/TiO_2 respectively. No significant changes in crystalline size of anatase TiO_2 (19.75 nm) was observed after depositing Pd (19.57 nm). This very well clarified that Pd was deposited onto the TiO_2 surface and not incorporated into the TiO_2 lattice.

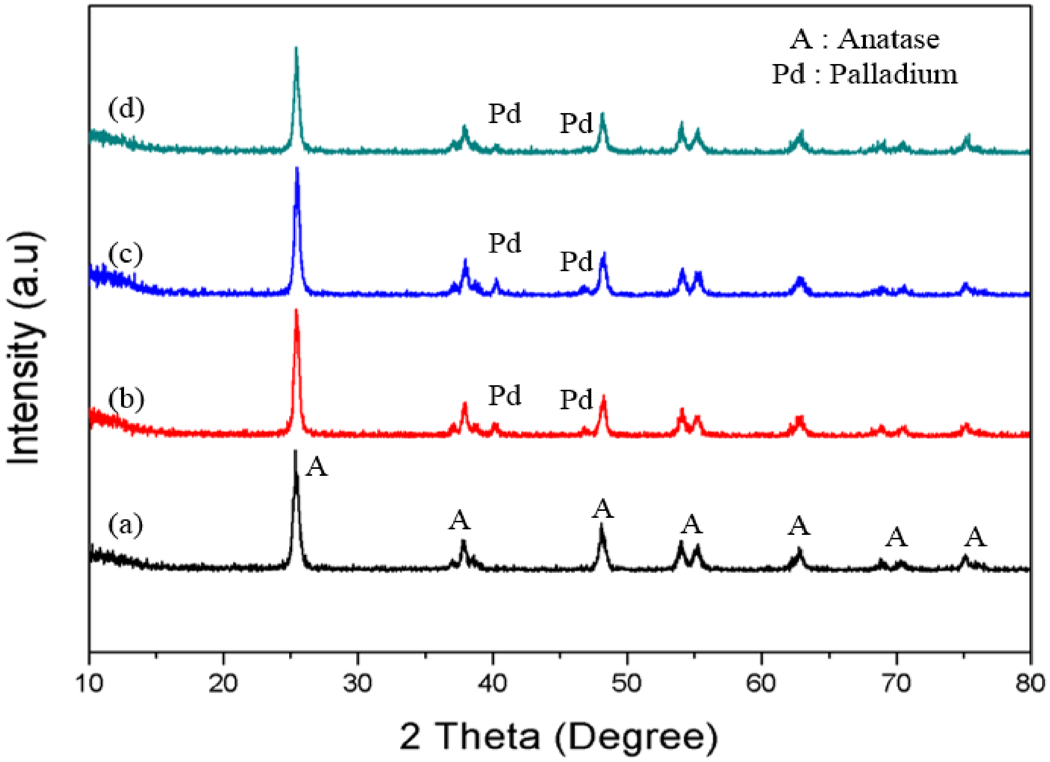

Figure 4.15: X-ray diffraction patterns of (a) TiO_2, (b) 0.5wt% Pd/TiO_2, (c) 1.0wt% Pd/TiO_2 and (d) 3.0wt% Pd/TiO_2

The Raman spectrum of the synthesized samples was shown in Figure 4.16. As usual four distinct peaks were detected at 145 (E_g), 399 (B_{1g}), 519 (A_{1g} + B_{1g}) and 639 cm^{-1} (E_g) that attributes to the pristine anatase phase of the synthesized TiO_2. It was evident that the deposition never distorted the phase of the TiO_2. These well matched with XRD analysis where the prepared samples are purely in crystalline anatase with the absence of rutile phase bands at 445 and 612 cm^{-1} (W. Li & Zeng, 2011).

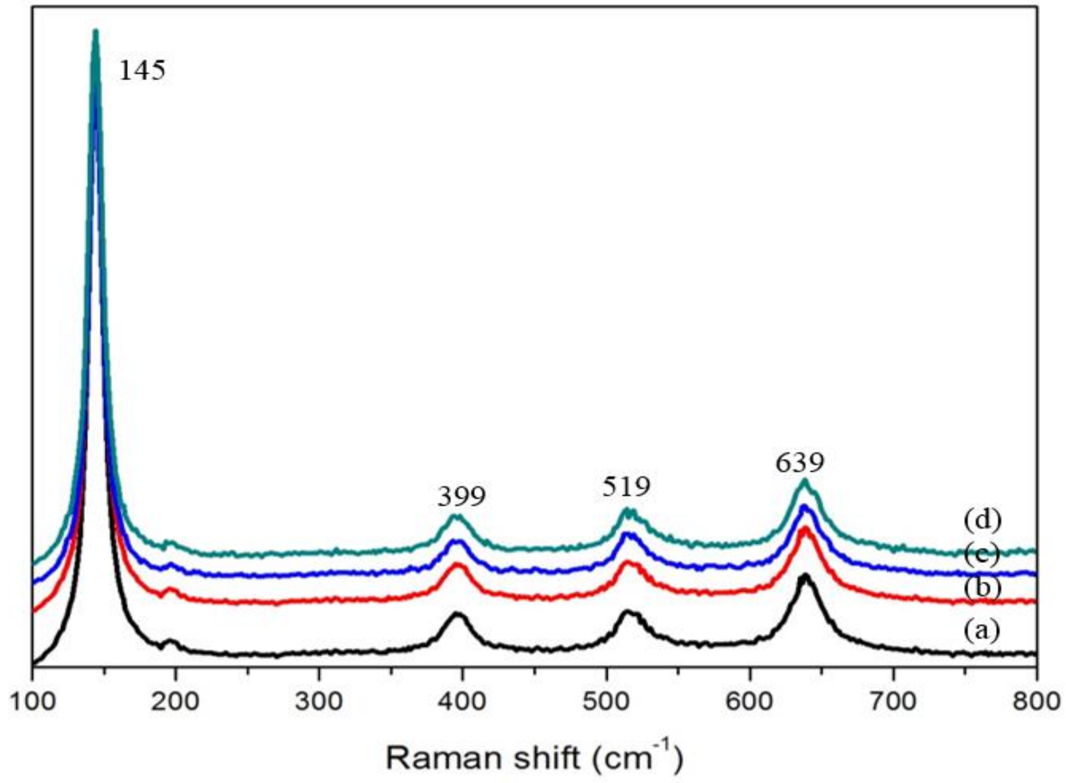

Figure 4.16: Raman spectra of (a) TiO_2, (b) 0.5wt% Pd/TiO_2, (c) 1.0wt% Pd/TiO_2 and (d) 3.0wt% Pd/TiO_2

The specific surface area and pore characteristics of the prepared samples are depicted in Figure 4.17 (a-d). All the samples demonstrated a stepwise adsorption - desorption hysteresis, well explained by type IV isotherms according to IUPAC classification with mesoporous characteristics (Pan & Xu, 2013b). The obtained BET surface area, average pore size and pore volume after Pd deposition is summarized in Table 4.2. In addition, the average pore diameter, determined by BJH method using the desorption isotherm was found to decrease after the deposition of Pd NPs (inset of Figure 4.17). The trivial decrease in BET surface area and average pore diameter was due to minor blockage of pores in anatase TiO_2 by the deposited Pd NPs (Pan & Xu, 2013a).

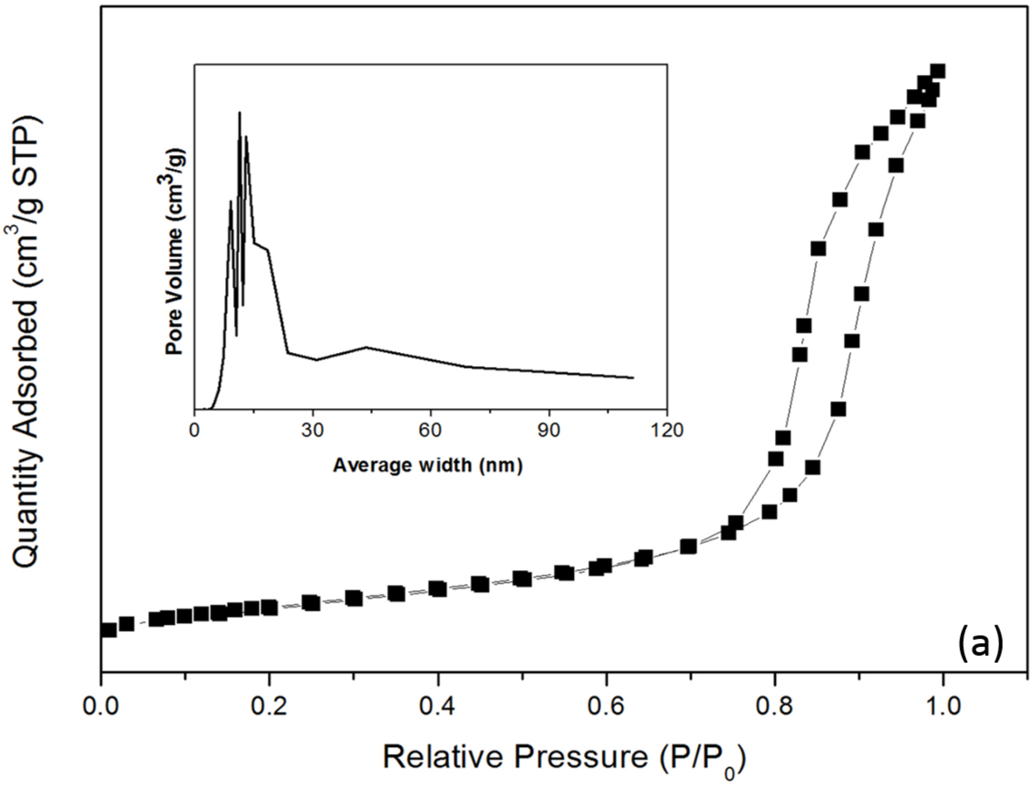
Quantity Adsorbed (cm^3/g STP)
Relative Pressure (P/P$_0$)
0.0
0.2
0.4
0.6
0.8
1.0
Pore Volume (cm^3/g)
Average width (nm)
0
30
60
90
120
(a)

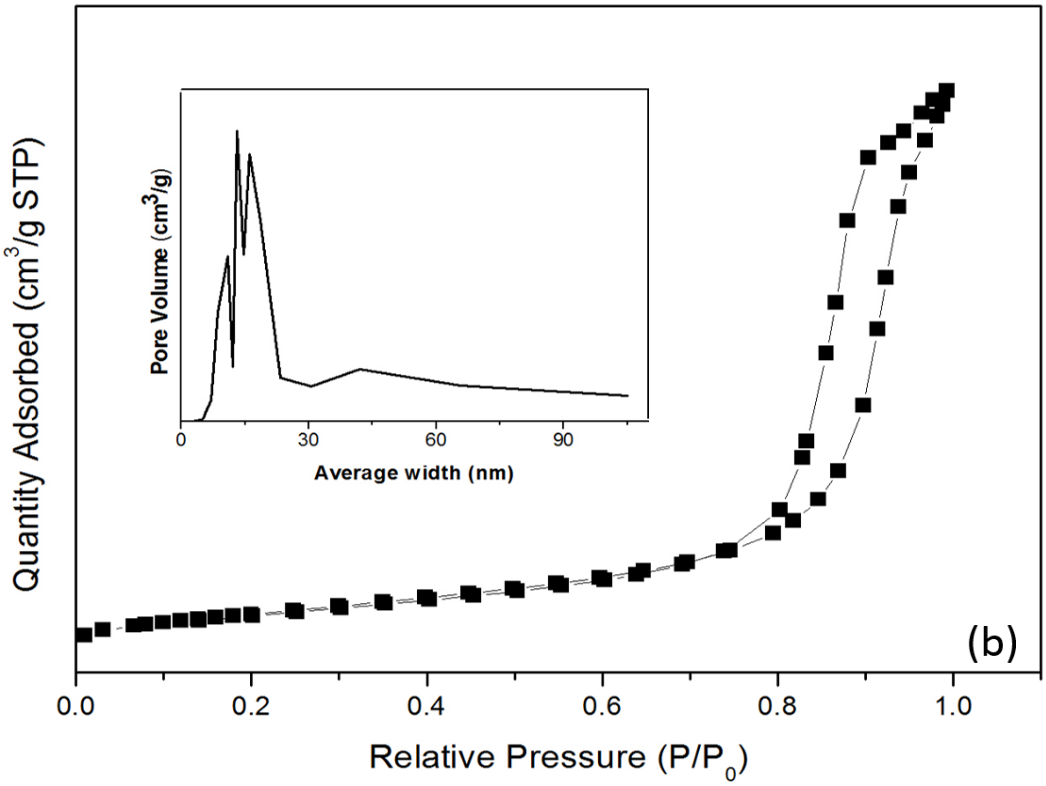
Quantity Adsorbed (cm^3/g STP)
Relative Pressure (P/P$_0$)
0.0
0.2
0.4
0.6
0.8
1.0
Pore Volume (cm^3/g)
Average width (nm)
0
30
60
90
(b)

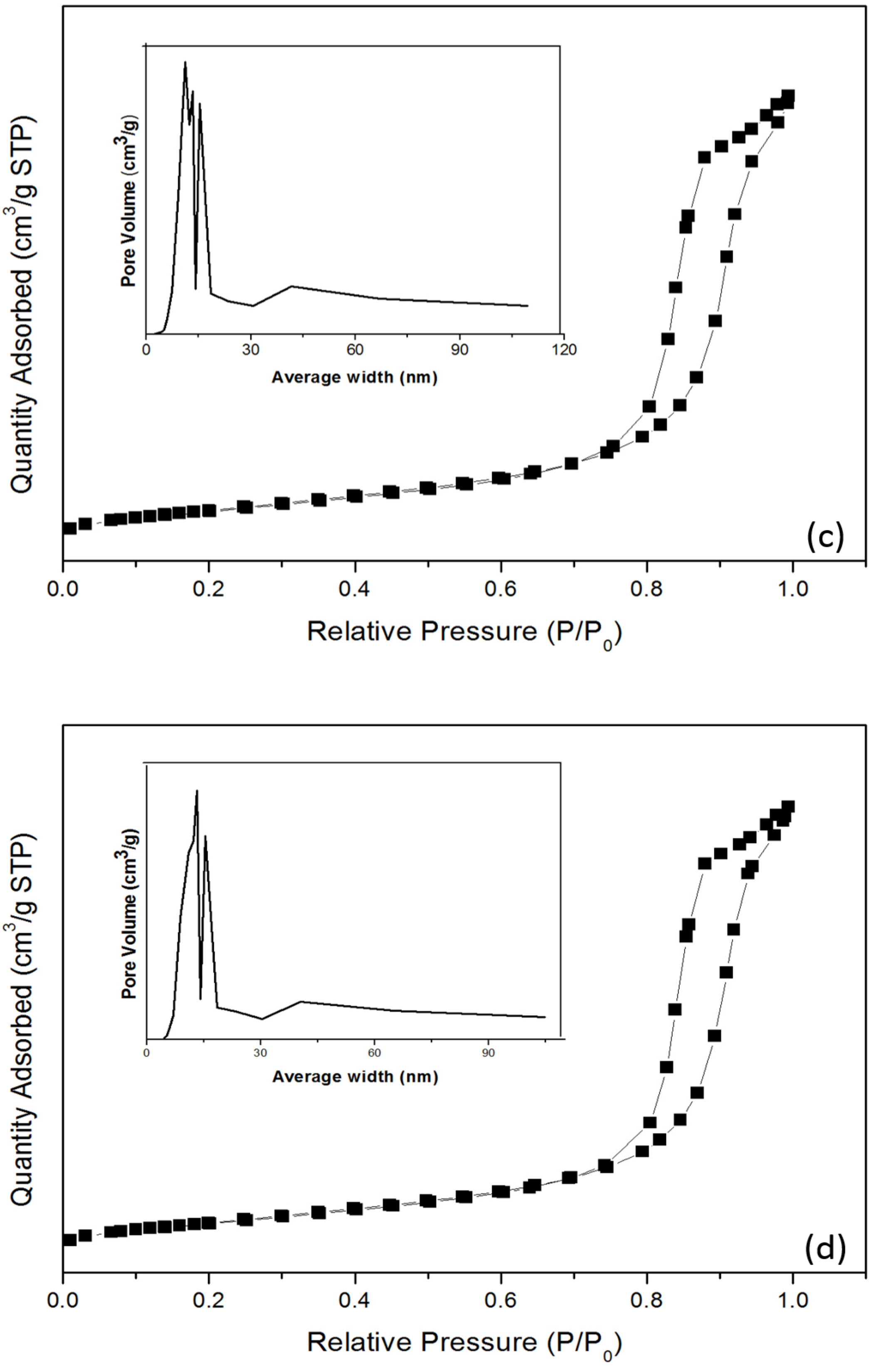

Figure 4.17: Adsorption-desorption isotherm of (a) TiO_2, (b) 0.5wt% Pd/TiO_2, (c) 1.0wt% Pd/TiO_2 and (d) 3.0wt% Pd/TiO_2 and the inset is the pore size distribution

Table 4.2: The surface characteristics of modified TiO_2 with varied Pd loading

Sample	BET surface area (m^2/g)	Average pore size (nm)	Pore volume (cm^3/g)
Anatase TiO_2	52.2374	12.9256	0.2098
0.5wt% Pd/TiO_2	46.6761	14.3101	0.2031
1.0wt% Pd/TiO_2	48.7703	12.9295	0.1949
3.0wt% Pd/TiO_2	48.6139	13.0052	0.1978

In order to determine the chemical composition and oxidation state for the prepared photocatalyst was subjected to X-ray photoelectron spectroscopy and the obtained spectrum are presented in Figure 4.18 (a). From the figure two peaks were observed at binding energies of 458.8 eV and 464.4 eV which corresponded to Ti $2p_{3/2}$ and Ti $2p_{1/2}$ spin-orbital splitting photoelectrons for anatase TiO_2 respectively (Kwak et al., 2009). These indicate the presence of typical Ti^{4+} in the synthesized samples. The presence of Pd NPs can be distinguished by two peaks centered at binding energies of 334.3 eV and 340.0 eV which is assigned to Pd $3d_{5/2}$ and Pd $3d_{3/2}$ respectively (Figure 4.18b) (Pan & Xu, 2013a). Thus confirming the predominant metallic form existence of the deposited noble metal.

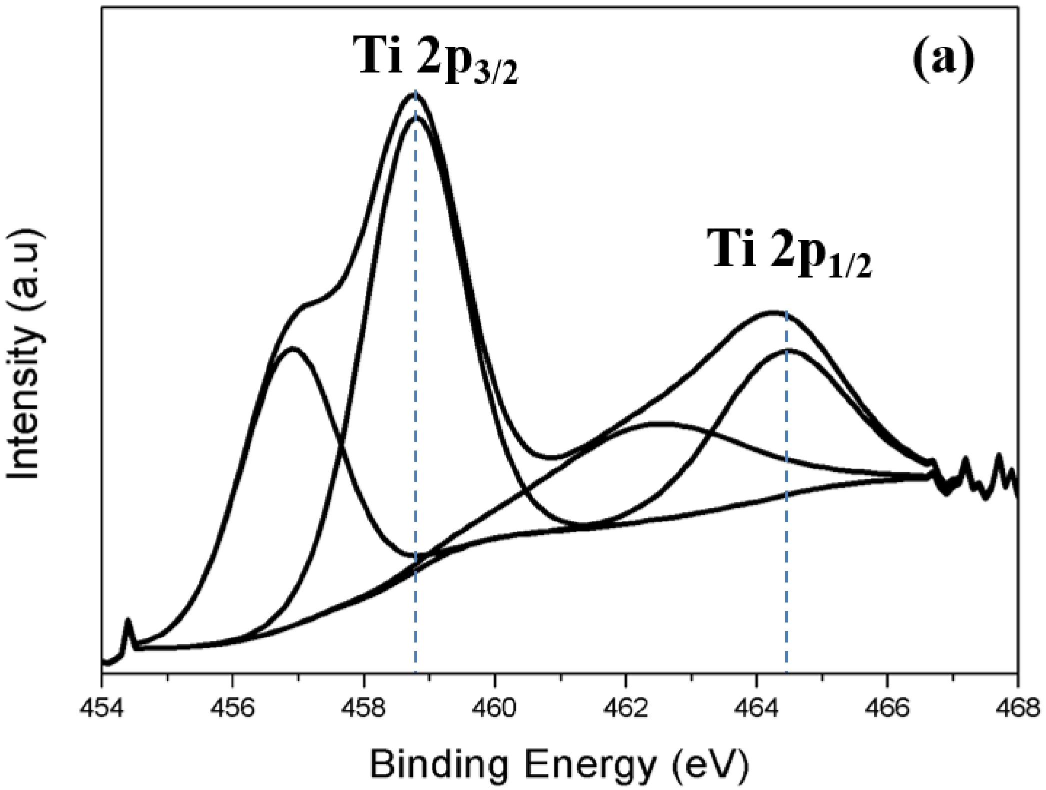

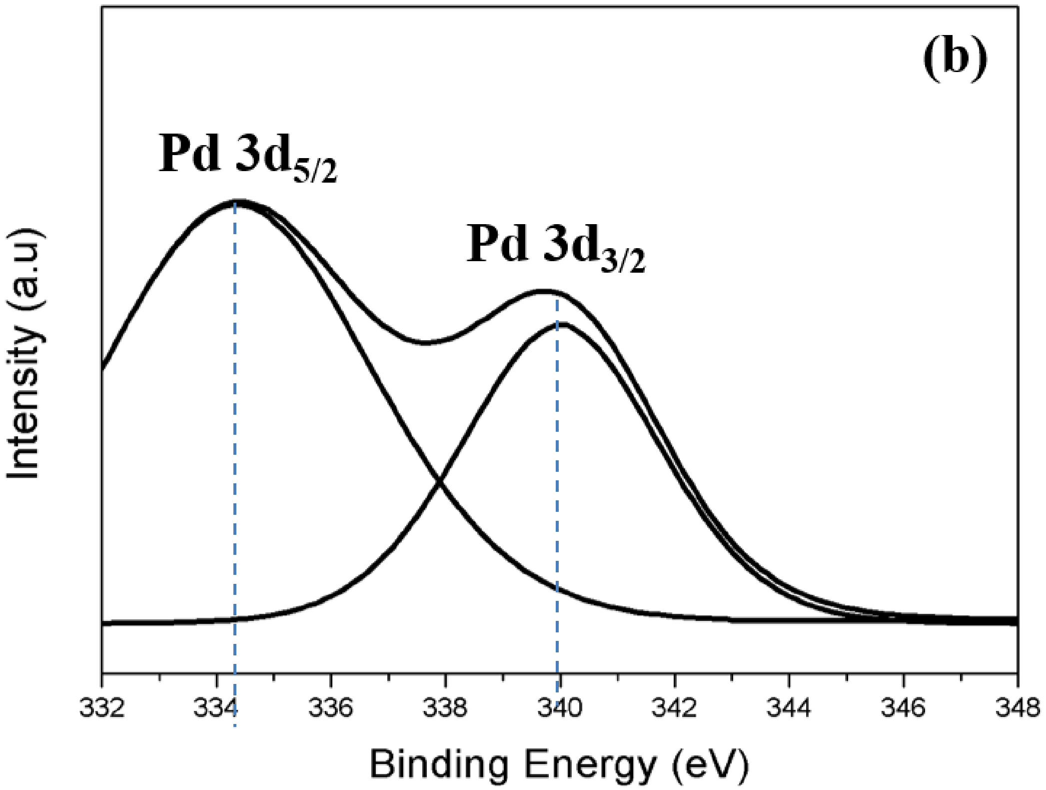

Figure 4.18: Core level XPS spectra of (a) Ti 2p and (b) Pd 3d of 0.5wt% Pd/TiO_2

The obtained optical absorbance spectrum is shown in Figure 4.19. The anatase TiO_2 showed almost zero absorption (~0.1 a.u) in the visible region. However, the deposition of Pd NPs caused a significant shift towards the visible region because of the surface plasmon absorption of palladium particles. The Pd particles <10 nm are capable to absorb the UV region, however particles >10 nm exhibits a red shift and enhances visible light absorption ability (Mohapatra et al., 2008; Xiong, Chen, et al., 2005). This ascends from the different polarization field induced through the surface charges affected by the amplitude and relative phase of the scattered and incident fields (Murray & Barnes, 2007). Thus it is well correlated with our present findings, where the average particles size of palladium was in the range of (17–29 nm). Therefore, with the broad absorption peak between 450-500 nm observed on Pd/TiO_2 with different palladium deposition, clearly showed the contribution of metallic Pd NPs. Although a small amount of Pd NPs enhanced the visible light absorption further surge in the Pd loading contributed for its excess presence. This induced dominant light scattering phenomena resulted in deprived performance (Kwak et al., 2009; W. Wang, Cheng, Yu, Liu, & Fan, 2012).

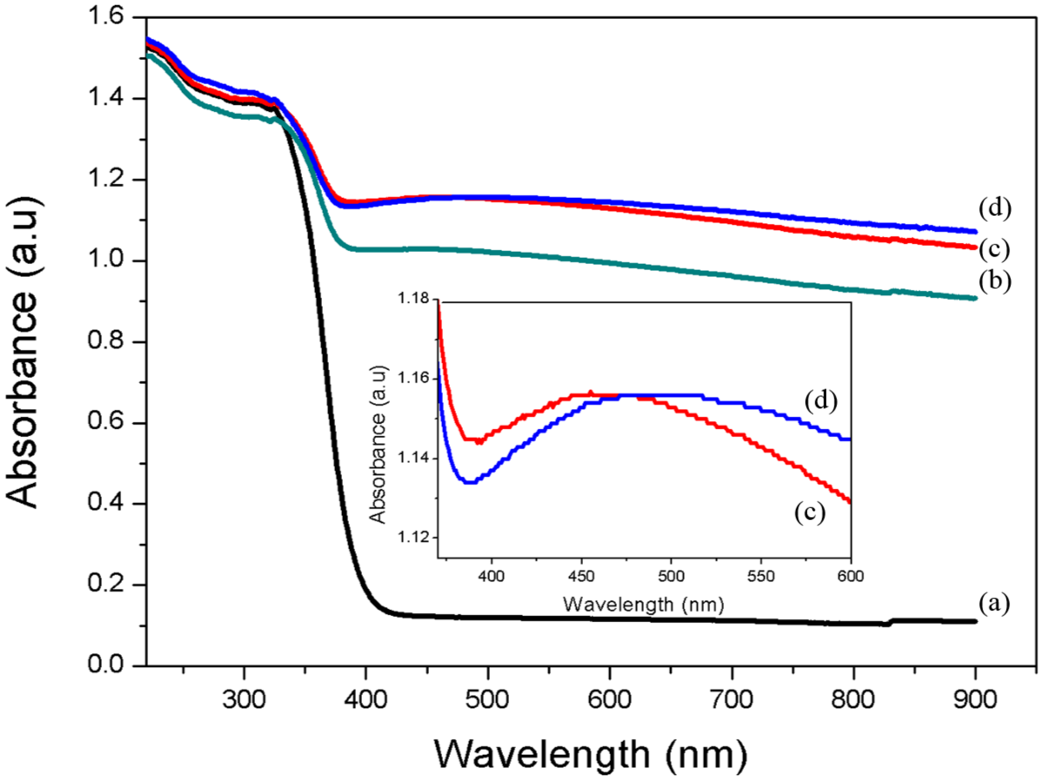

Figure 4.19: UV-visible absorption spectra of (a) TiO_2, (b) 3.0wt% Pd/TiO_2, (c) 0.5wt% Pd/TiO_2 and (d) 1.0wt% Pd/TiO_2

PL spectra are often employed to understand the surface processes involving the photogenerated electron-hole pairs (N. Zhang, Liu, Fu, & Xu, 2011). The obtained PL spectrum in Figure 4.20 shows the emission intensity that relates with the recombination rate of the excited electron and hole pairs. Lower PL intensity indicates that a lower recombination rate of electrons and holes due to more excited electrons are either transferred or trapped. The emission peak of Pd/TiO_2 is obviously quenched as compared to that of TiO_2. This further revealed that the deposition of Pd NPs has enhanced the trapping or transferring of electron and there by suppressing the electron-hole recombination. This high charge carrier separation efficiency extends the reactive electron-hole lifetime and hence leads to a better photocatalytic performance.

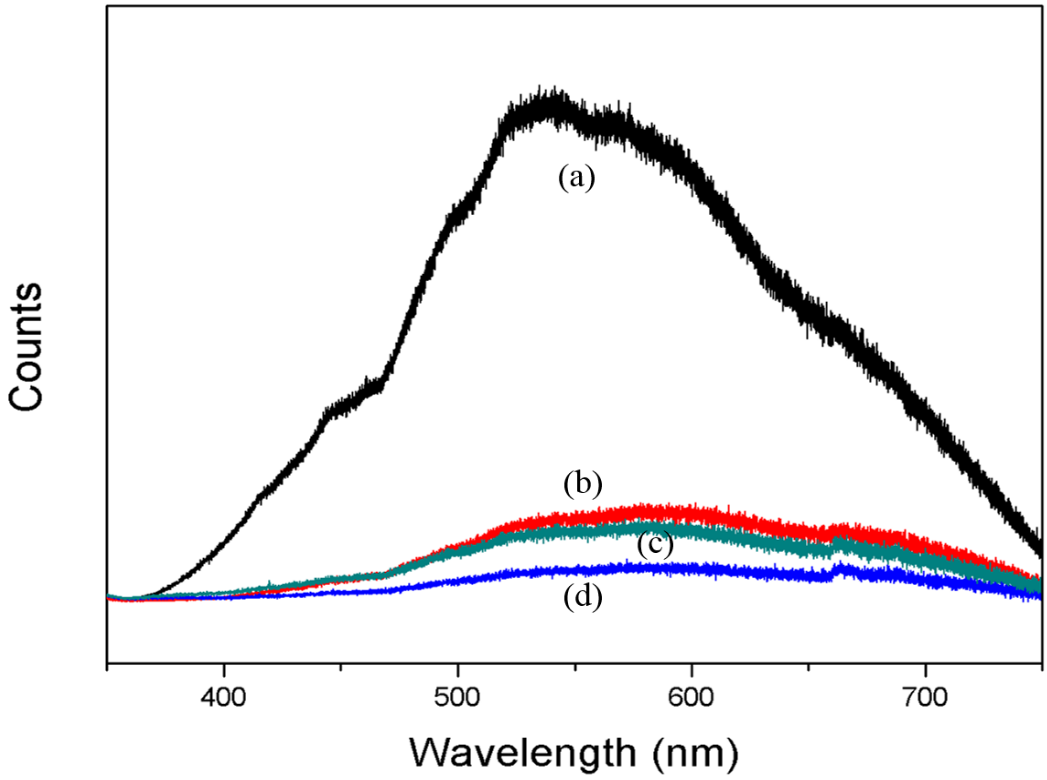

Figure 4.20: Photoluminescence spectra of (a) TiO_2, (b) 0.5wt% Pd/TiO_2, (c) 3.0wt% Pd/TiO_2 and (d) 1.0wt% Pd/TiO_2

Figure 4.21 shows the photocatalysis performance of the prepared samples (Pd/TiO_2) for the degradation of AMX under artificial visible light irradiation. The obtained results showed an excellent efficiency achieved irrespective of palladium loading with an initial AMX concentration of 20 mg/L. The degradation followed an order of 97.5% (0.5wt% Pd/TiO_2) > 83.4% (3.0wt% Pd/TiO_2) > 78.7% (1.0wt% Pd/TiO_2) > 27.5% (TiO_2) respectively. The control experiment with the absence of photocatalysts showed almost nil degradation and proved the poor photosensitizing ability of AMX. A significant enhancement in the degradation efficiency was achieved by depositing Pd NPs as compared to pure. This immense progress was attributed to the localized surface plasmon resonance and triggered Pd NPs to absorb visible light. This was further attributed to an optical excitation that produced a coherent oscillation of free electrons in the resonance with the electrical field component of incoming electromagnetic irradiation

(Kochuveedu et al., 2013; Lang et al., 2014; Qu & Duan, 2013). During the incidence of photons onto noble Pd NPs, the electron density of the metal was then polarized to one side and further oscillates within the resonance of light frequency (Bumajdad & Madkour, 2014). The absorption of visible light by Pd NPs is also a functionality of particle size and smaller Pd particles (<10 nm) are well received by the UV irradiation, where else the larger particles by visible light (Mohapatra et al., 2008; Xiong, Chen, et al., 2005; Xiong, Wiley, et al., 2005). The findings were observed in the present study where by a notable degradation was achieved for the Pd with particle size 17–29 nm. However, pure anatase TiO_2 showed a very poor degradation of AMX. This was attributed to its own characteristic of having large band gap energy which hinder the absorption in the visible region as shown in our optical absorbance spectrum. Therefore with the low absorption of energy, only minimum electrons can be excited from the VB to CB of TiO_2 and thus led to such inference.

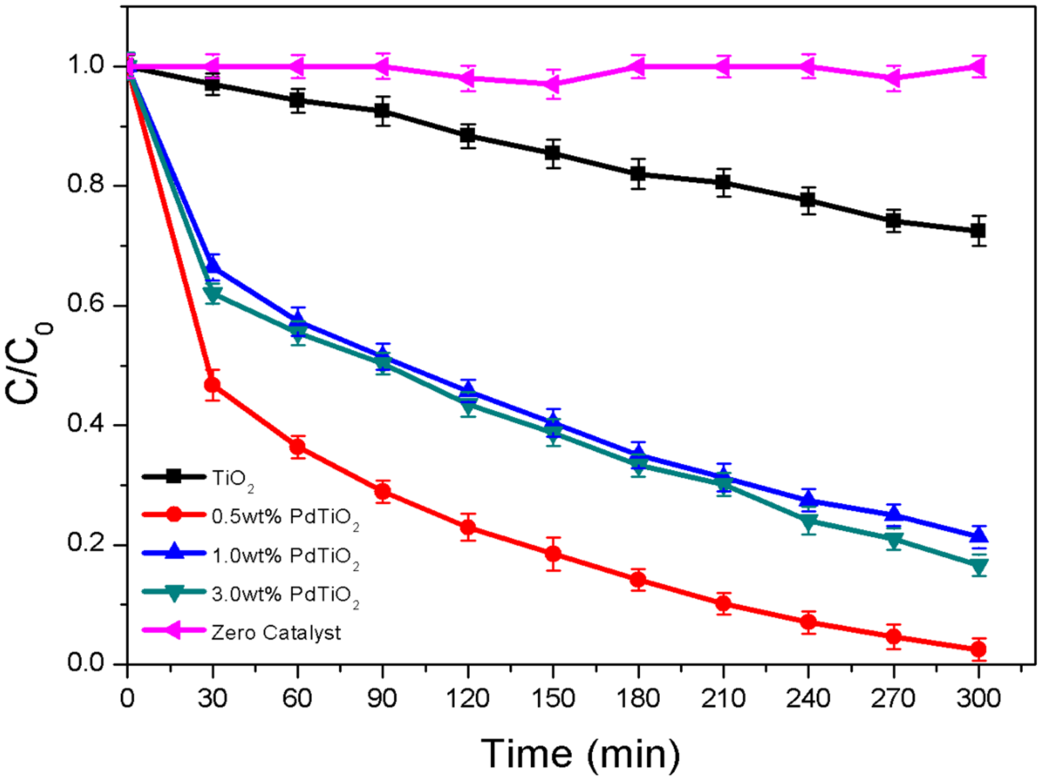

Figure 4.21: Photocatalytic degradation rates of AMX under artificial visible light irradiation

The degradation mechanism and electron transfer was explained in Figure 4.22. When Pd/TiO_2 is exposed to the visible light, the plasmon resonance excites the electrons below the Fermi level of the Pd NPs in the VB to be transferred to CB leaving behind the positive charges (h^+) at VB. Since the CB of TiO_2 is an electron acceptors, it readily accepts the electrons that are transferred from Pd NPs to form superoxide anion radicals ($^{\bullet}O_2^-$). This was followed by protonation reaction that results in $^{\bullet}HO_2$ radicals. Thus formed instable $^{\bullet}HO_2$ radicals further combines with trapped electron to form H_2O_2, and lead to the formation of hydroxyl radicals ($^{\bullet}OH$). They are the active species that are responsible for the degradation. Besides that, when Pd NPs interacts with TiO_2 Schottky junction is promoted and build an internal electric field close to the interface (Kochuveedu et al., 2013; Zhou et al., 2012). Thus it drives the generated electrons and holes to move in different directions and the photon energies of electrons excited upon LSPR are able to cross the energy junction at the interface. As a result electrons are transferred from Pd NPs to CB of TiO_2 (Lang et al., 2014; Linic et al., 2011). Furthermore with the formation of Schottky junction, it shrinks the recombination of electrons and holes, and prolongs the lifetime of the charge carriers (X. Zhang et al., 2013). Therefore with the complement of this mechanism supported by Pd NPs showed an exemplary photocatalytic performance in shorter duration.

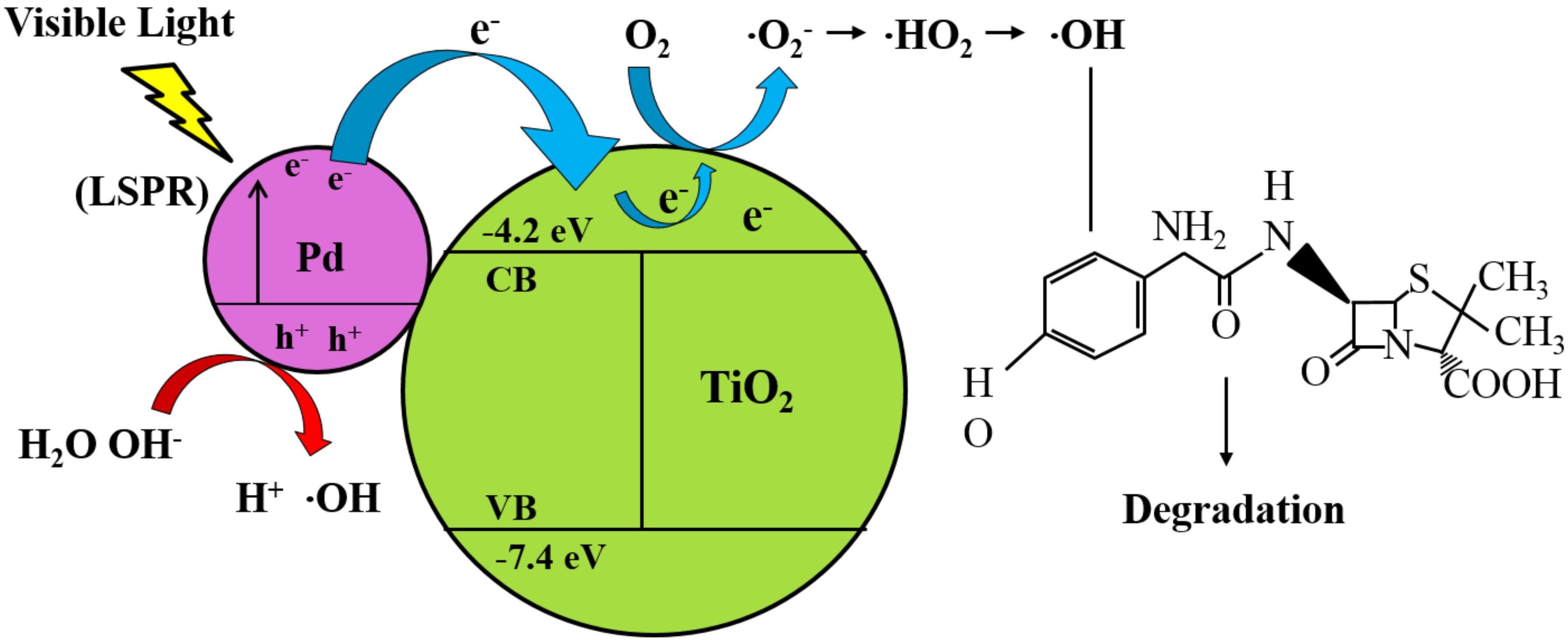

Figure 4.22: Schematic diagram of electron transfer and degradation mechanism of AMX

Meanwhile, in the study on influence of palladium weight percentage (0.5wt%, 1.0wt% and 3.0wt %) on the photocatalytic efficiency, it showed an optimum value at 0.5wt%. According to the optical spectra and photoluminescence analysis the 1.0wt% Pd/TiO_2 was expected to yield better photocatalytic efficiency as compare to the rest. However, the obtained contradictory observance was attributed to the following reasons. During the irradiation of suspension of photocatalyst particles, photon are absorbed and scattered. As observed in the optical spectra similar peak broadening phenomenon was observed for 1.0wt% owing to the scattering of light. Thus it destruct the absorption of visible light due to the shielding effect exhibited by the Pd layers and resulting in low generation of active electrons (Kwak et al., 2009; W. Wang et al., 2012). Therefore, it results in lower photocatalytic degradation efficiency as compare to others though it has the lowest recombination of electron and hole pairs.

Stability of the prepared photocatalyst is significantly important for real time applications. Therefore it was carried out through recycle experiment under identical conditions and shown Figure 4.23. The photocatalytic activity of 0.5wt% Pd/TiO_2 exhibited 92.3% and was able to achieve even after the 3rd run, there by establishing the excellent photostability. The kinetics of the photocatalytic degradation of AMX best fitted to the pseudo first-order reaction kinetics (Figure 4.24). The obtained kinetics parameters are tabulated in Table 4.3. Finally the degree of mineralization of AMX during the photocatalytic degradation was also presented through a TOC analysis and depicted in Figure 4.25. The TOC results well corresponds with the degradation trend analysed through UPLC. Over all the study showed that the adopted Pd noble metal played a key role in enhancing the visible light harvesting and prolonged the life time of charge carriers.

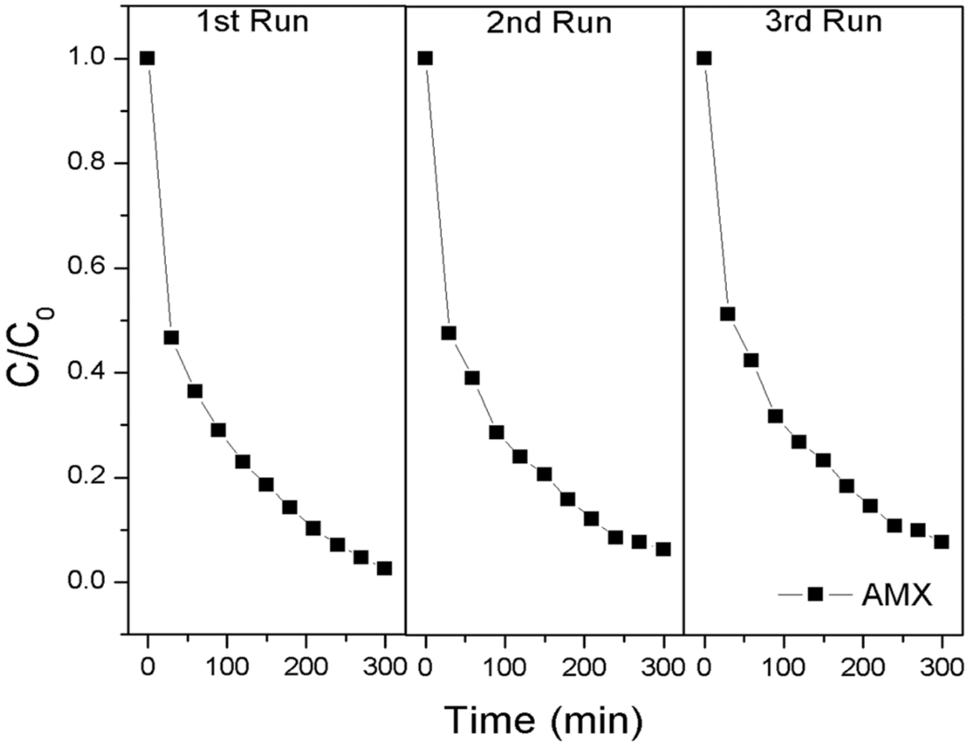

Figure 4.23: Stability analysis of modified TiO_2 with 0.5wt% Pd loading

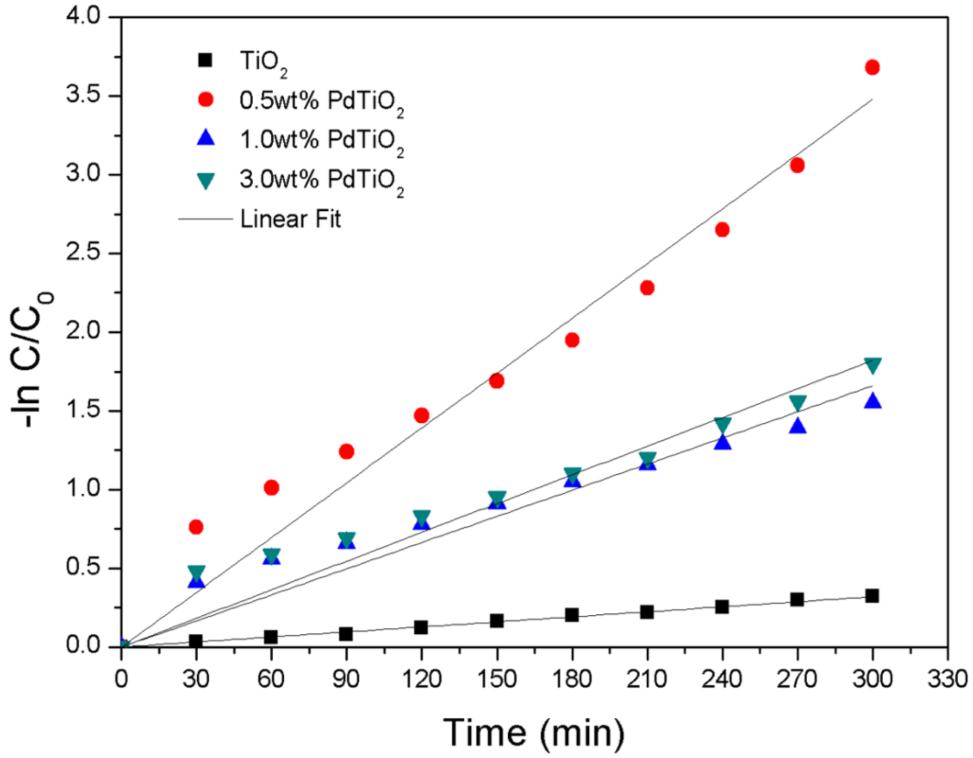

Figure 4.24: The kinetics of AMX degradation by modified TiO_2 with varied Pd loading

Table 4.3: Degradation kinetic parameters obtained from the model for different photocatalysts

	First Order Kinetics			
	TiO_2	0.5wt% Pd/TiO_2	1.0wt% Pd/TiO_2	3.0wt% Pd/TiO_2
R^2	0.9983	0.9901	0.9811	0.9845
k	0.00107	0.01161	0.00553	0.00608

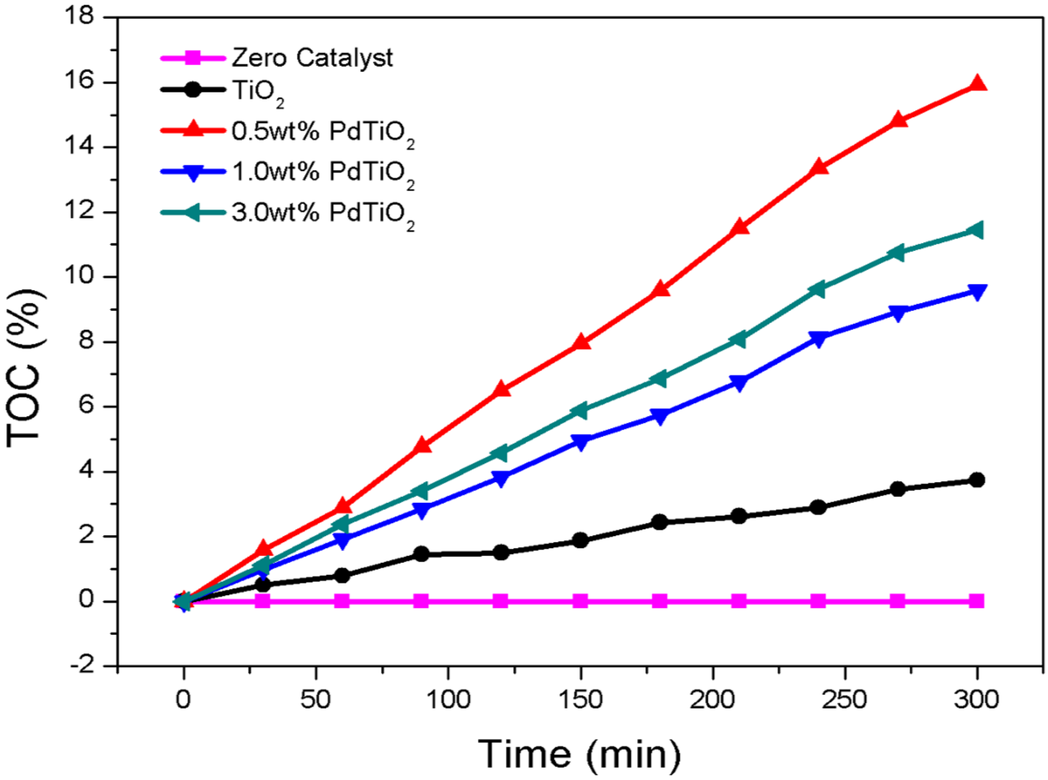

Figure 4.25: TOC analysis for AMX removal

However the study motivated us to expand the search with other noble metal. Hence Ag a well-known noble metal was chosen as a potential visible light enhancer. The Ag was tailored with the TiO_2 through a similar sustainable photodeposition and the obtained inherent materials and photocatalytic characteristics are discussed in the following section.

4.3 Silver Modified TiO_2 for Synergised Visible Light Activity

Figure 4.26 depicts the X-ray diffraction pattern of Ag/TiO_2 with varied Ag loading (0.5wt%, 1.0wt%, 3.0wt% and 5.0wt %) along with pure TiO_2. The anatase phase of the titania and well supported with the JCPDS no 21-1272. The sustainable synthesis of Ag NPs assisted through sun light exhibited diffraction peaks at $2\theta = 38.1°$ (1 1 1), 44.3° (2 0 0), 64.4° (2 2 0) and 77.4° (3 1 1) planes with face centered cubic (FCC) attributed to Ag (JCPDS no 04-0783) with increase in Ag diffraction peaks for increased in Ag loading. However, 0.5wt% loading does not show any peak due to its lower concentration (i.e. below the detection limit of the XRD). The diffraction peaks also confirm the stability of the synthesized silver crystals a significant character that promotes visible light photoexcitation. Overall, the sharp and intense peaks indicate the high crystalline characteristics of all prepared samples. The average crystalline sizes of TiO_2 calculated using Scherrer equations was found to be 17.28 nm where no change was observed after the deposition of Ag NPs indicating perfect surface deposition of Ag NPs. Meanwhile the crystallite size of the Ag particles were calculated to be 7.05 nm, 7.04 nm and 7.38 nm for 1.0wt% Ag/TiO_2, 3.0wt% Ag/TiO_2 and 5.0wt% Ag/TiO_2 respectively.

The phase purity of TiO_2 was confirmed with Raman analysis through four distinct peaks at 145 (E_g), 399 (B_{1g}), 519 ($A_{1g} + B_{1g}$) and 639 cm^{-1} (E_g) and is shown in Figure 4.27 (W. Li & Zeng, 2011).

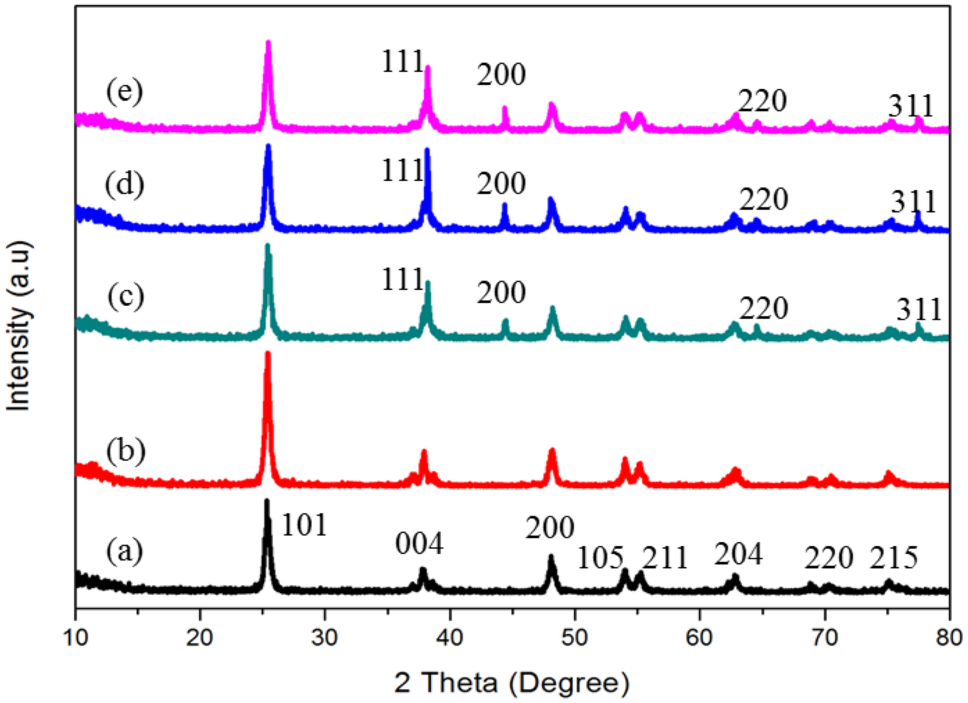

Figure 4.26: X-ray diffraction patterns of (a) TiO_2 (b) 0.5wt% Ag/TiO_2 (c) 1.0wt% Ag/TiO_2 (d) 3.0wt% Ag/TiO_2 (e) 5.0wt% Ag/TiO_2

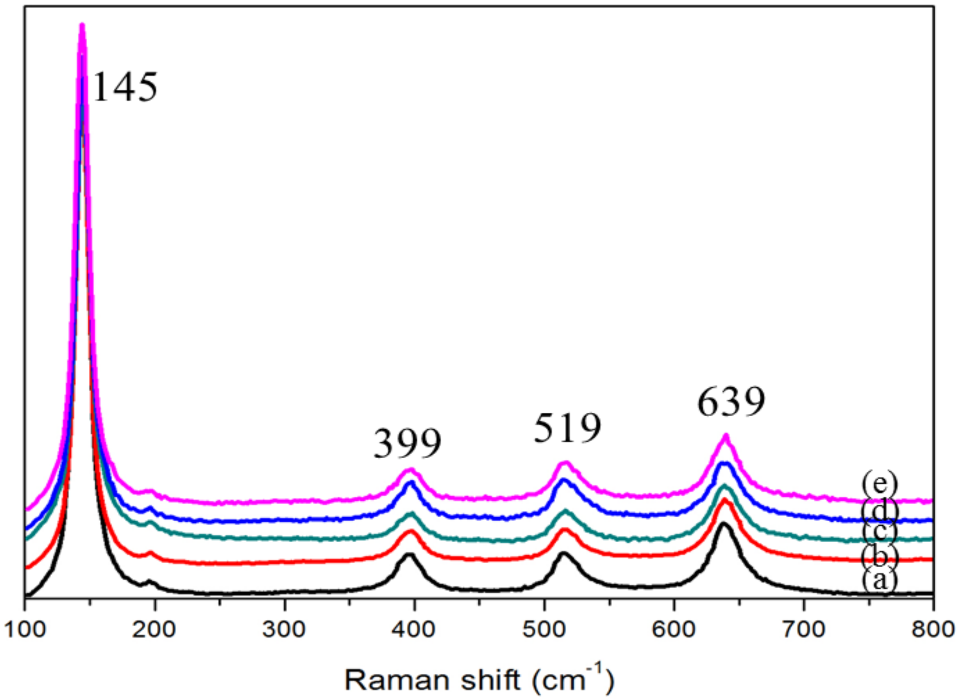

Figure 4.27: Raman spectra of (a) TiO_2 (b) 0.5wt% Ag/TiO_2 (c) 1.0wt% Ag/TiO_2 (d) 3.0wt% Ag/TiO_2 (e) 5.0wt% Ag/TiO_2

The obtained surface structures of the composite is depicted in Figure 4.28 (a-c). It is evident that synthesized Ag NPs are uniform and homogenous and spherical. The inset of Figure 4.28 (c) shows the EDX spectrum of the synthesized Ag/TiO_2 confirming elemental composition of the prepared photocatalyst. The particles size and lattice fringe of the synthesized samples were acquitted through HRTEM analysis and is illustrated in Figure 4.28 (d-f). The average particles size deposited Ag NPs was between 4 and 8 nm. A 0.24 nm and 0.35 nm fringe spacing was observed through the fringe analysis and is attributed to the face centered cubic (FCC) Ag (1 1 1) and TiO_2 (1 0 1) respectively (D. Chen et al., 2013; Z. Chen et al., 2014; Jiang, Zhou, Mi, & Wu, 2012).

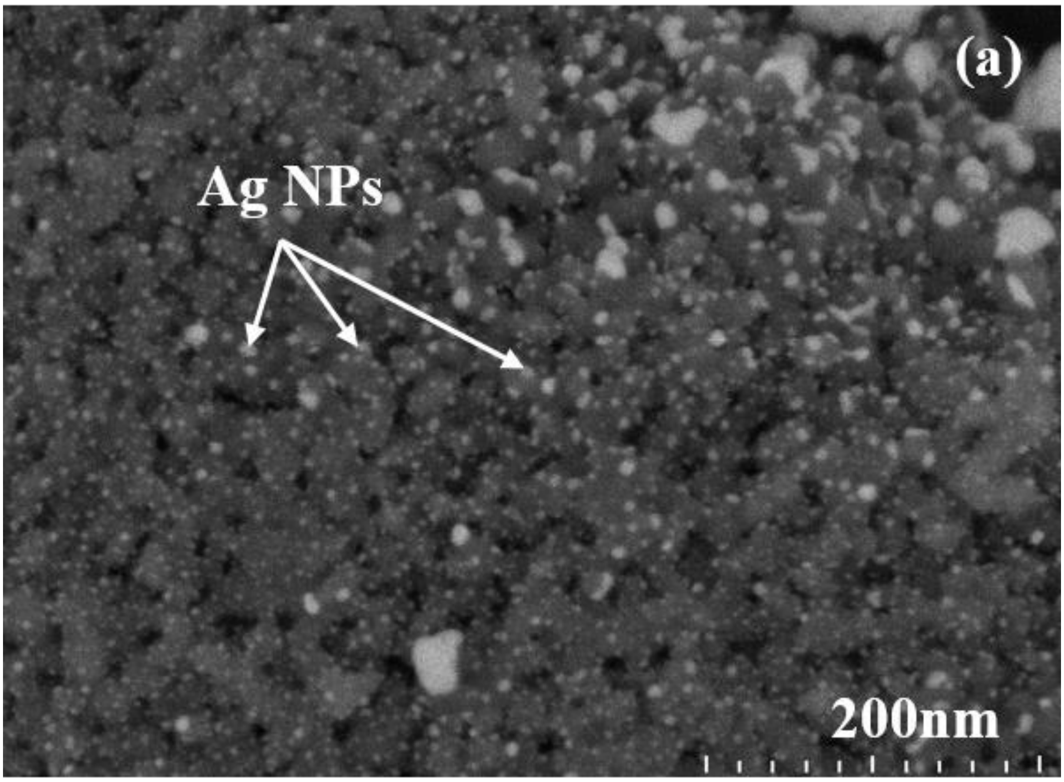

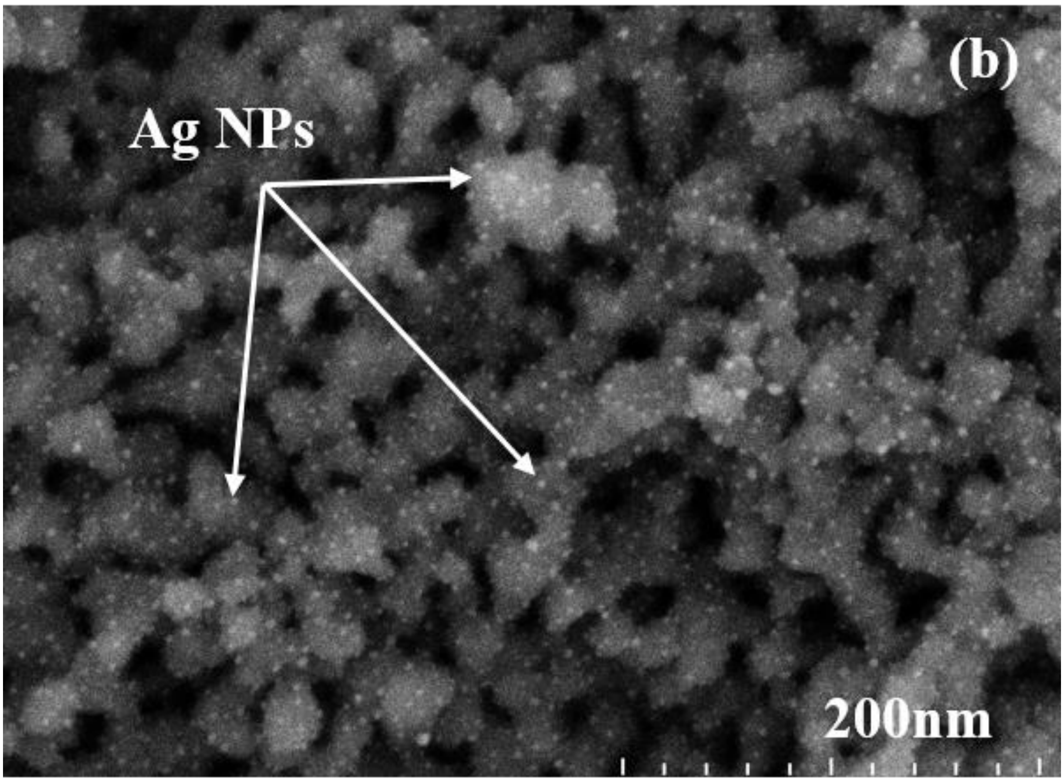
(b)
Ag NPs
200nm

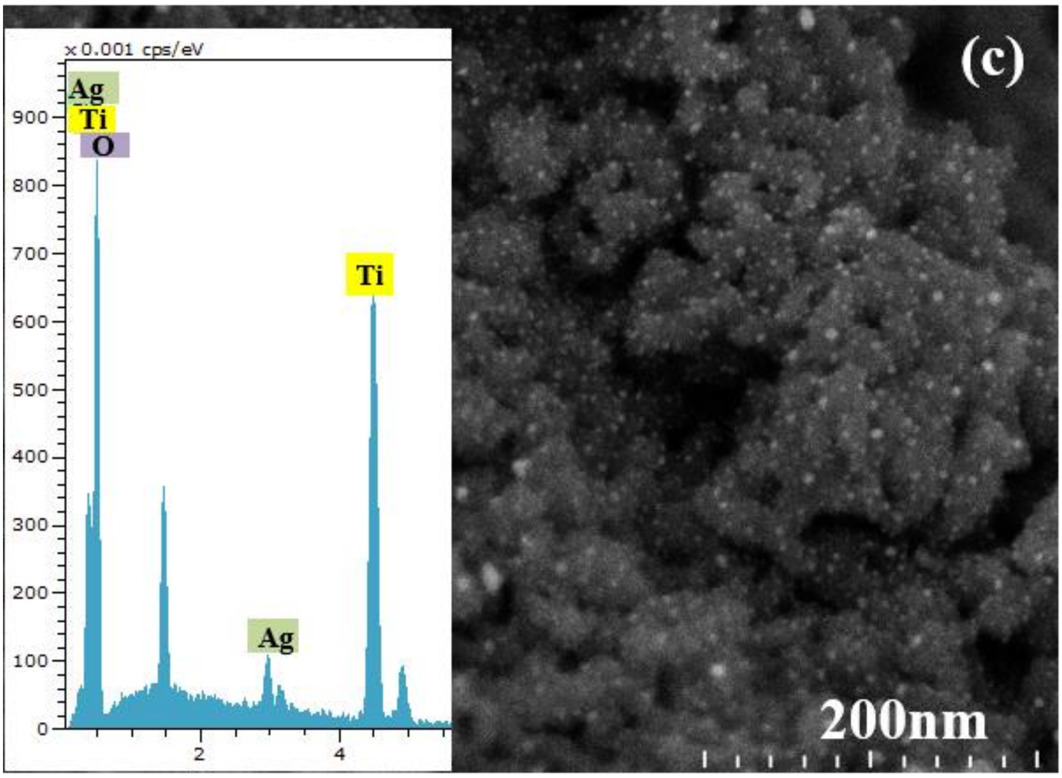
(c)
x 0.001 cps/eV
Ag
Ti
O
Ti
Ag
0
100
200
300
400
500
600
700
800
900
2
4
200nm

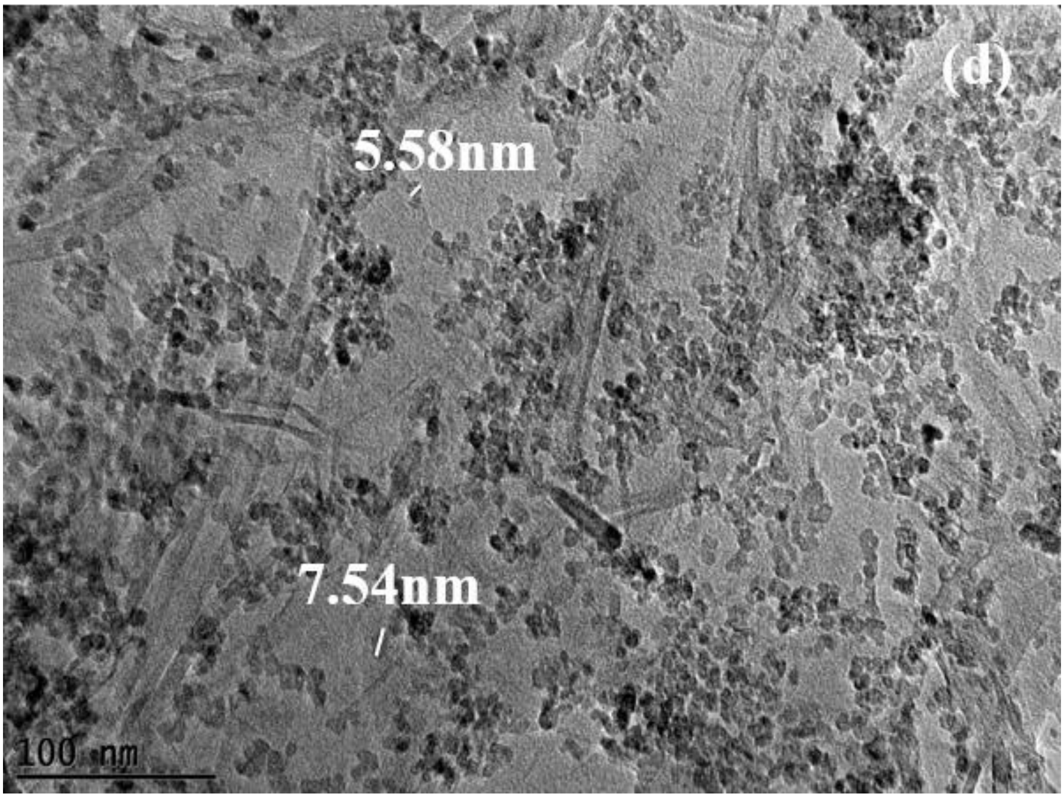
(d)
5.58nm
7.54nm
100 nm

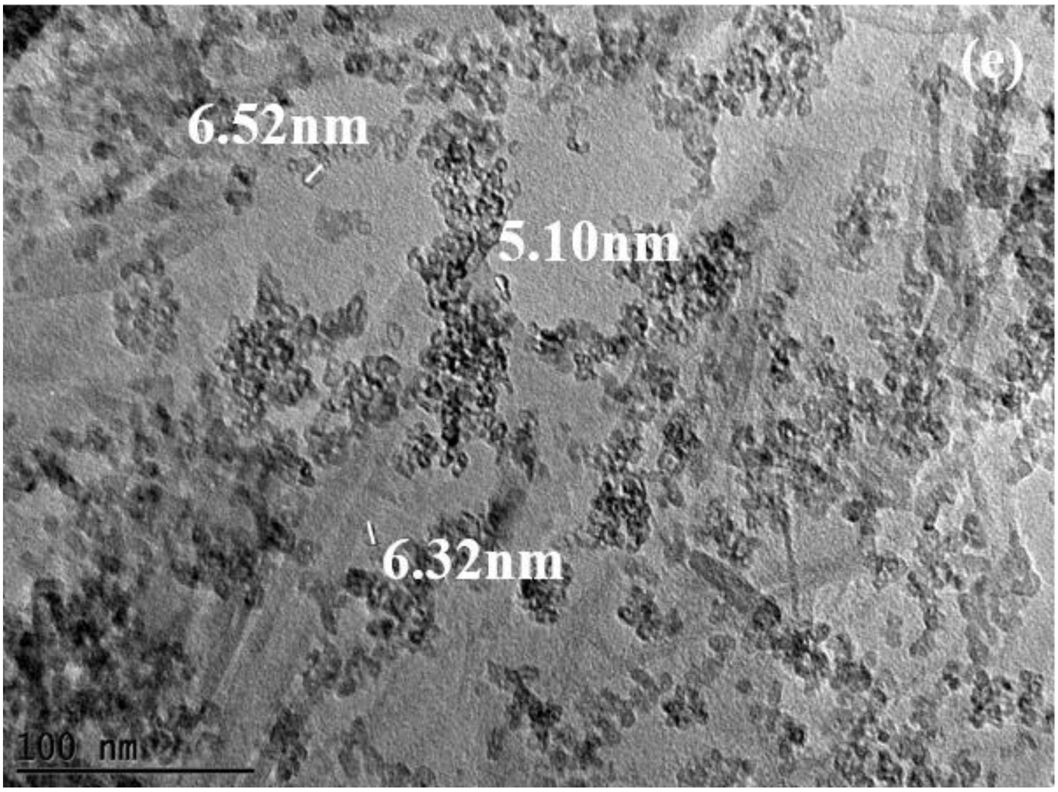
(e)
6.52nm
5.10nm
6.32nm
100 nm

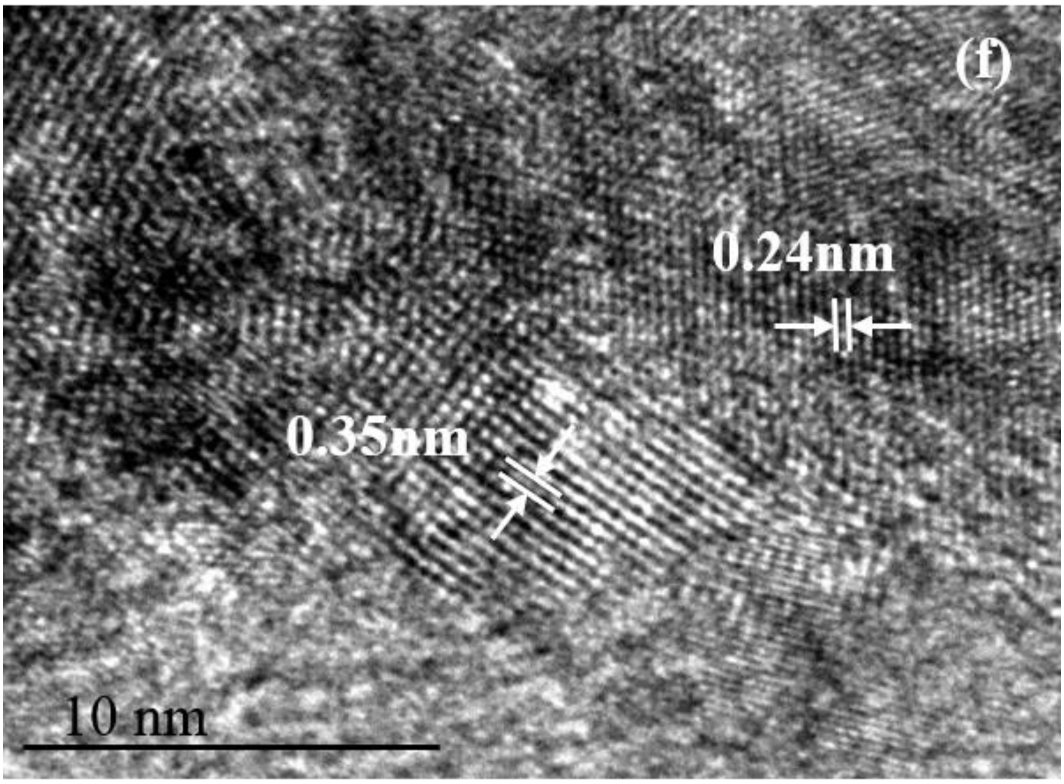

Figure 4.28: FESEM images of (a-c) 3.0wt% Ag/TiO_2. The inset of (c) is the EDX of 3.0wt% Ag/TiO_2 and (d-f) HRTEM images of 3.0wt% Ag/TiO_2

The adsorption-desorption hysteresis of the synthesized samples were presented in Figure 4.29. The samples metaphorised a stepwise adsorption and desorption hysteresis, well described by type IV isotherms based on IUPAC classification with a good mesoporous nature (Pan & Xu, 2013b). This inference was consistent with BJH desorption pore distribution curve and pore diameters (Inset of Figure 4.29 (a) and (b)). A significant reduction in BET surface area (46.6 m^2/g) was reported for 3.0wt% Ag/TiO_2 as compare to (52.2 m^2/g) TiO_2 was due to partial filling of titania pores by Ag NPs.

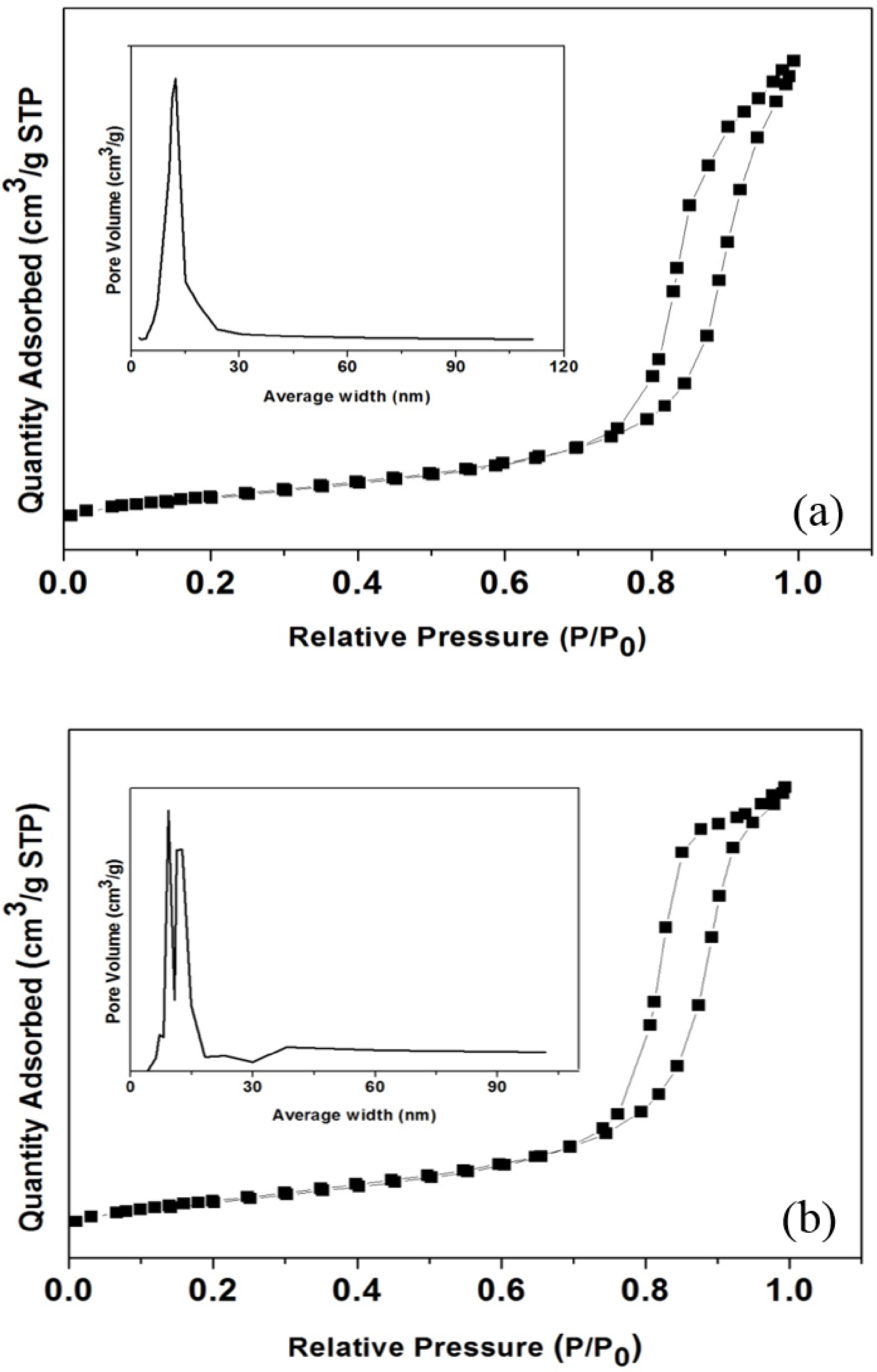

Figure 4.29: Adsorption-desorption isotherm of (a) TiO_2 (b) 3.0wt% Ag/TiO_2 and the inset is the pore size distribution

The chemical composition and oxidation state for the synthesized samples is displayed in Figure 4.30. With the presence of two peaks (Figure 4.30 (a)) at the binding energies of 458.06 and 463.65 eV which corresponded to Ti $2p_{3/2}$ and Ti $2p_{1/2}$ spin-orbital splitting photoelectrons for anatase TiO_2 respectively (Di Li, Haneda, Labhsetwar, Hishita, & Ohashi, 2005; H. Liu, Dong, Li, Su, & Zhu, 2013). This is attributed to the strong presence of Ti^{4+} oxidation state in the synthesized sample (Aziz, Cheng, et al., 2012). The strong existence of Ag NPs can be distinguished through peaks centered at binding energy 367.03 and 373.07 eV corresponding to Ag $3d_{5/2}$ and Ag $3d_{3/2}$ respectively with spin energy separation of 6.04 eV (D. Chen et al., 2013; S. F. Chen et al., 2010; Guin, Manorama, Latha, & Singh, 2007; Pan & Xu, 2013a; Zhao, Kuai, & Geng, 2012). Thereby, prove the predominance existence of the Ag NPs in the metallic form as like Pd NPs (F. Xiao, 2012a).

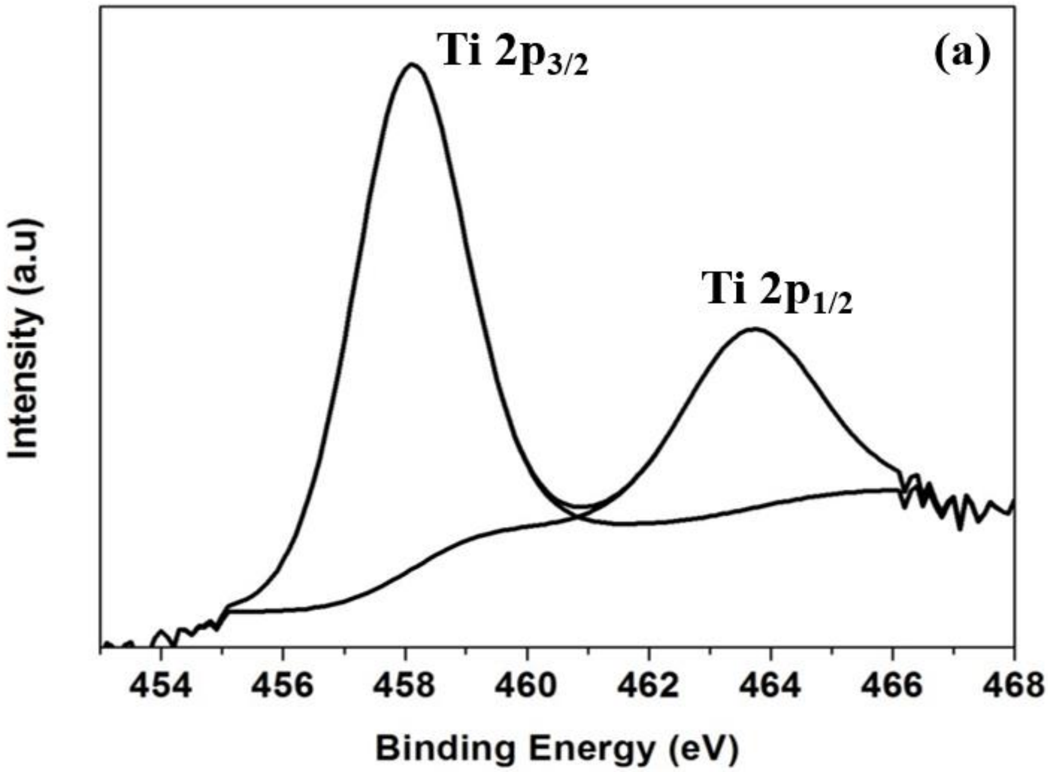

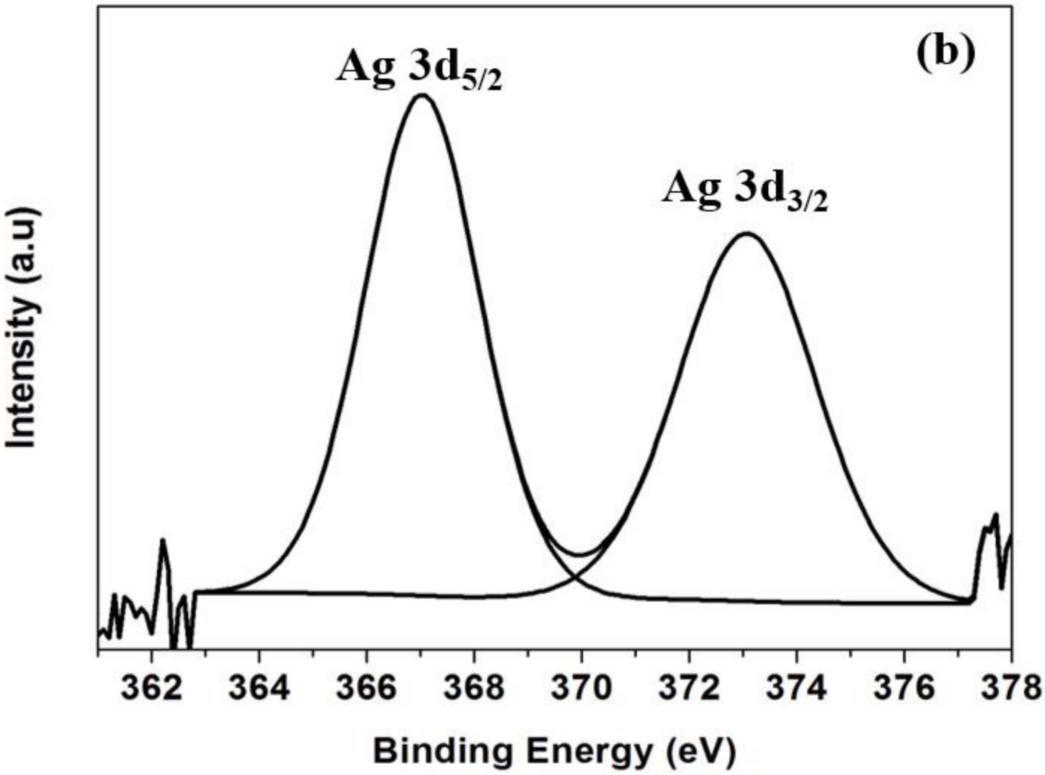

Figure 4.30: Core level XPS spectra of (a) Ti 2p (b) Ag 3d of 3.0wt% Ag/TiO$_2$

The diffuse reflectance spectra (DRS) were used to determine the optical property of the synthesized sample and illustrated in Figure 4.31. The absorbance spectrum of TiO$_2$ was well discussed in the descending sections. The spectrum exhibited a strong and wide absorption peak at 570 nm after the deposition on Ag NPs. This significant change is strongly acknowledged to localized surface plasmon resonance (LPSRs) triggered by Ag NPs (Link & El-Sayed, 1999; Ramchiary & Samdarshi, 2014; Roy, Bandyopadhyaya, & Pal, 2004; Zhao et al., 2012; Zheng et al., 2011). The presence of Ag NPs on the titania surface had drastically created disturbance on dielectric constant of the surrounding matrix and contributed for visible light absorption (Ung, Liz-Marzán, & Mulvaney, 1998). It is also noteworthy that the visible light absorption peaks of the various Ag doping are unchanged, except the intensities due to the different in catalyst loading.

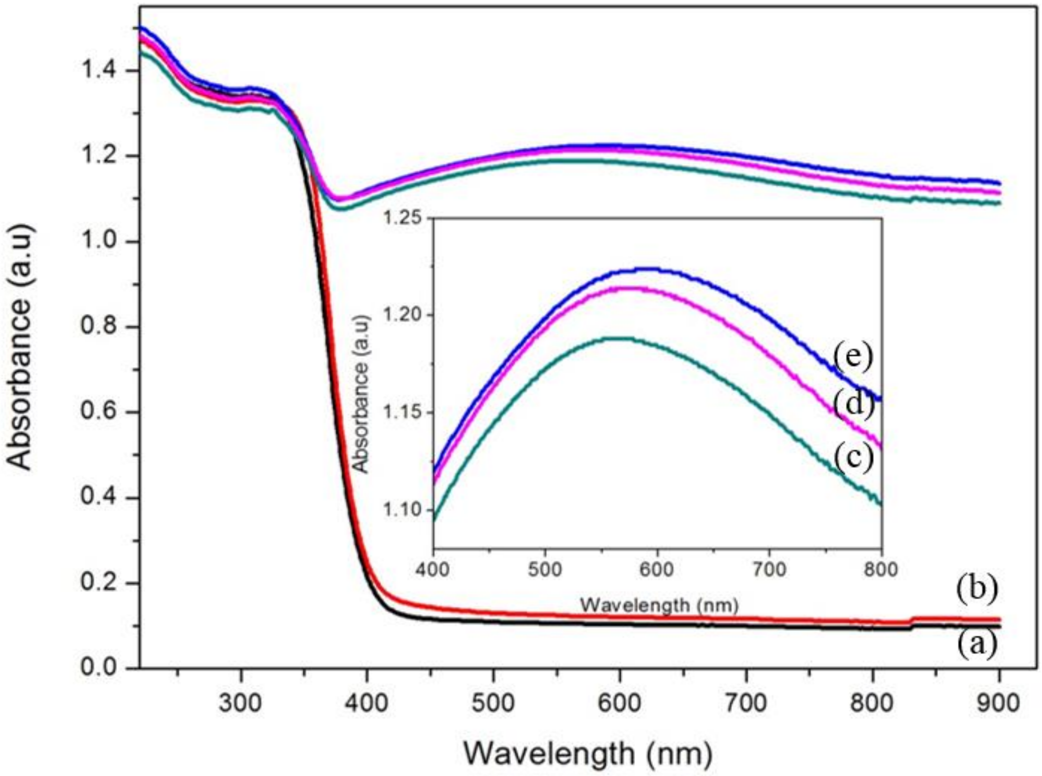

Figure 4.31: UV-visible absorption spectra of (a) TiO_2 (b) 0.5wt% Ag/TiO_2 (c) 1.0wt% Ag/TiO_2 (d) 5.0wt% Ag/TiO_2 (e) 3.0wt% Ag/TiO_2

Figure 4.32 shows the studied PL spectrum in order to evaluate the trapping, separation and migration of the photogenerated charge carriers of the synthesized samples. From the results it is well proven that deposition of Ag NPs onto the surface of TiO_2 contributed for reduction of electron and hole recombination’s. Thus lay bridge for the excess electrons to be transferred from the Ag valence band (VB) to conduction band (CB) of TiO_2 under photoexcitation. The Ag also well contributes for the prolonged lifetime for the charge carriers. However, with the further increase of Ag loading from 3.0 to 5.0wt%, also increased the PL intensity which is due to redundant of Ag NPs that act as a recombination sites for electrons and holes (Z. Liu et al., 2011).

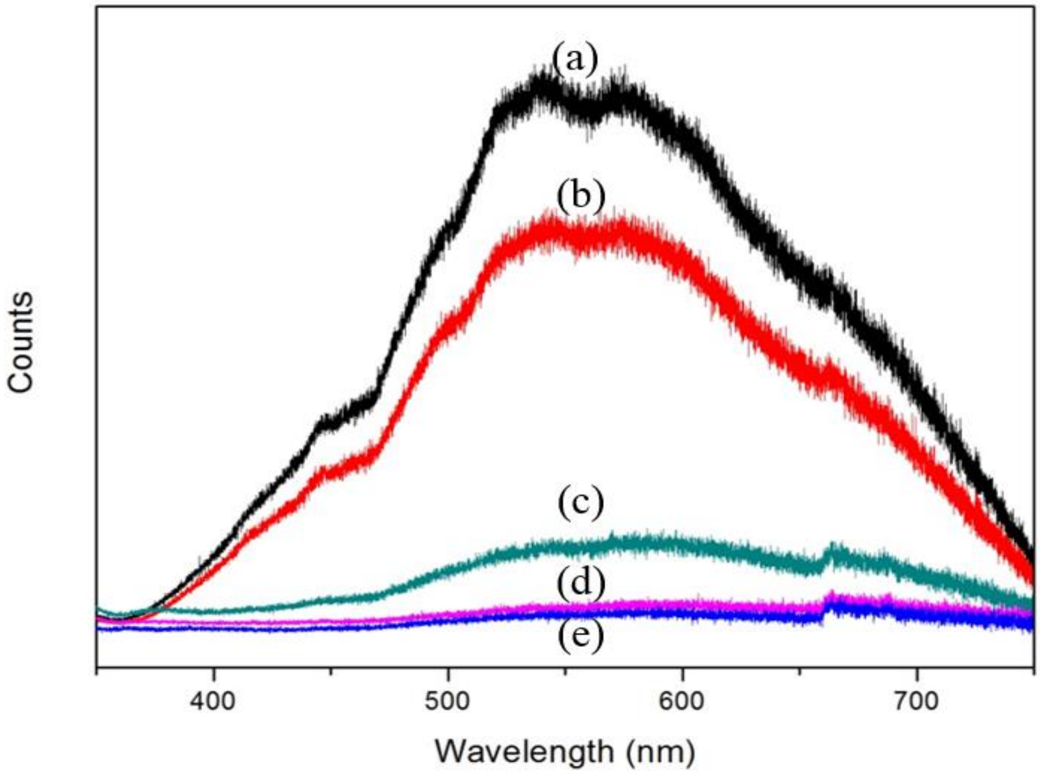

Figure 4.32: Photoluminescence spectra of (a) TiO_2 (b) 0.5wt% Ag/TiO_2 (c) 1.0wt% Ag/TiO_2 (d) 5.0wt% Ag/TiO_2 (e) 3.0wt% Ag/TiO_2

The synthesized Ag deposited photocatalysts with different loading were evaluated for photocatalysis by degrading two different genera of pollutants under the artificial visible light irradiation. The study demonstrated a superior photocatalytic performance for both the pollutants. Figure 4.33 (a) depicted the photocatalytic degradation efficiency of AMX. 3.0wt% Ag/TiO_2 achieved the highest efficiency of 63.48% followed by 61.06%, 57.66%, 28.73% and 27.88% for 5.0wt%, 1.0wt%, 0.5wt% Ag/TiO_2 and TiO_2 respectively. Similar observation (Figure 4.33 (b)) was also inferred for 2, 4-DCP where the highest efficiency was obtained for 3.0wt% Ag/TiO_2 (60.23%) as compare to 5.0wt% Ag/TiO_2 (59.17%), 1.0wt% Ag/TiO_2 (55.99%), 0.5wt% Ag/TiO_2 (15.21%) and TiO_2 (14.14%). Under the absence of photocatalyst, almost negligible degradation was observed for both the EDCs clarifying that they are not of photosensitising category. The deposition of Ag NPs, well acknowledged the visible light driven photoexcitation and this notable improvement was attributed to the unique characteristics of noble metals, i.e., localized surface plasmon resonance (LSPR) which enables Ag NPs to strongly absorb light in the visible spectrum. The charge density is redistributed and thus establishes a strong coulombic restoring force further resulted in oscillation of charge density like a harmonic oscillator in phase with the incident light (Kochuveedu et al., 2013; Lang et al., 2014; Qu & Duan, 2013; Zhou et al., 2012). Thus occurred oscillation distressed the dielectric constant of the surrounding matrix (Ung et al., 1998). The Ag NPs leads to the formation of Schottky barrier at the interface of Ag-TiO_2 and promotes the transport of excited electrons from Ag interface to the TiO_2 due to the strong electric field (Bumajdad & Madkour, 2014; Xiang et al., 2010). This electric field forced both the photogenerated electrons and holes on Ag NPs to isolate each other. These entire phenomenon’s are apparently contributed for the reduction of recombination rate of electron-hole pairs and prolong the lifetime of the charges carriers (Qi, Yu, Liu, & Wong, 2014; Xiang et al., 2010; X. Zhang et al., 2013).

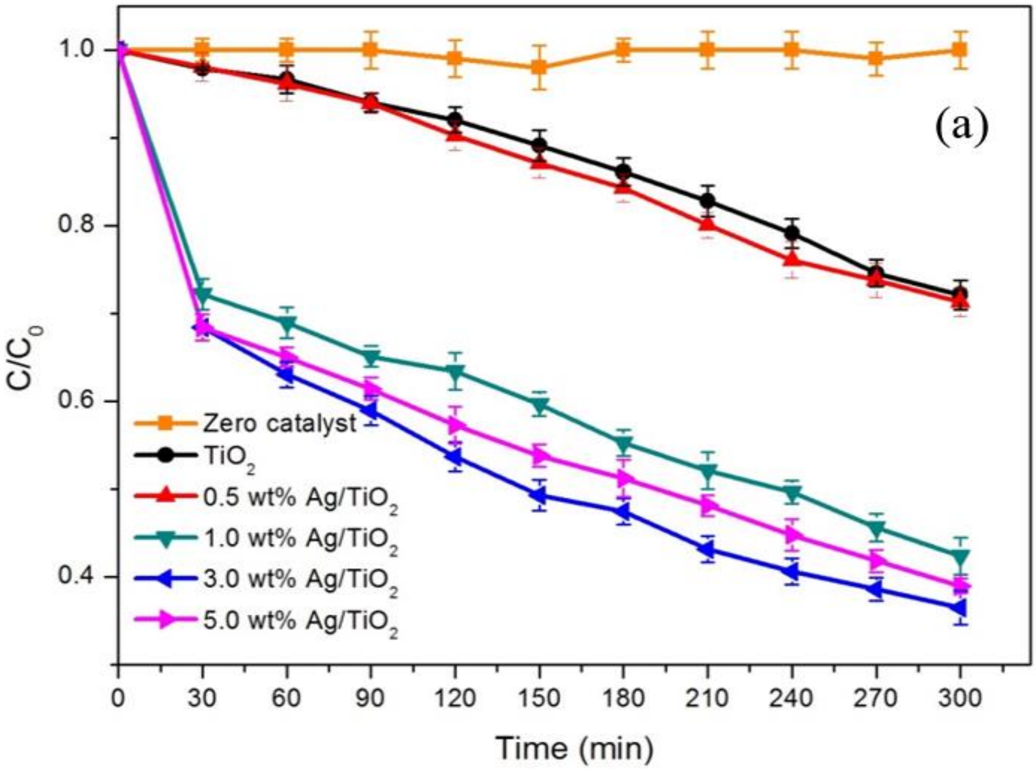

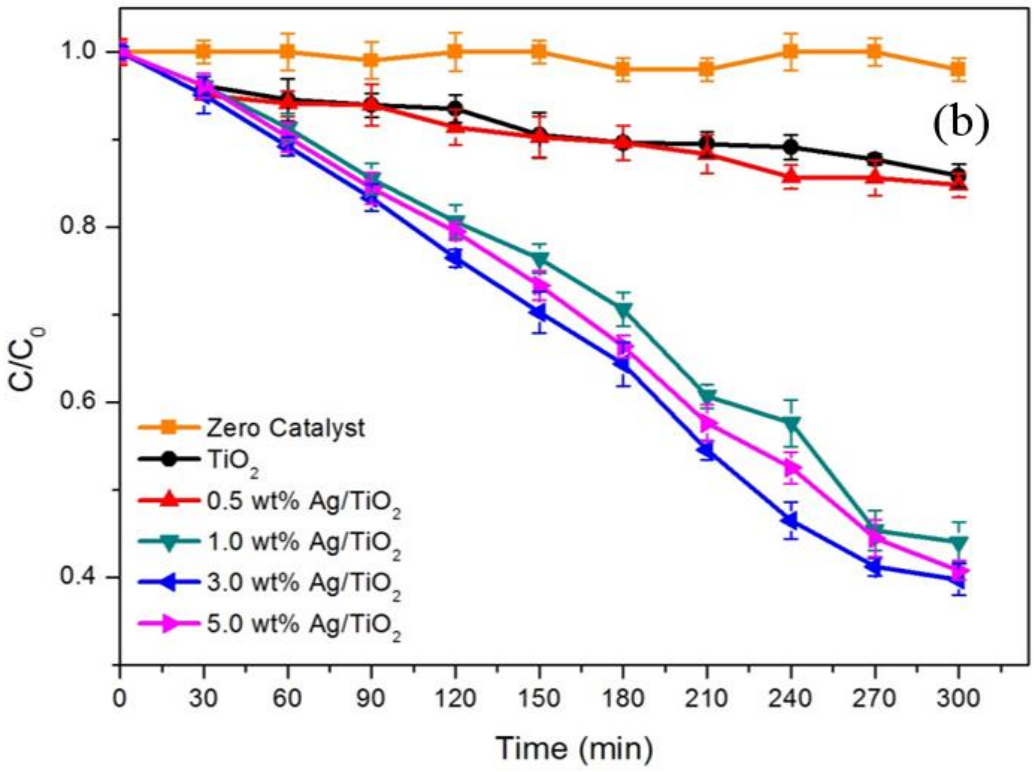

Figure 4.33: Photocatalytic degradation of (a) AMX (b) 2, 4-DCP under artificial visible light irradiation

Figure 4.34 illustrates the degradation mechanism promoted through electron transfer in the photocatalytic activity. When Ag/TiO_2 is irradiated with visible light the electrons lying below the Fermi level (E_f) of Ag NPs gets excited to the surface plasmon states, leaving positive charges (h^+) below the E_f. Thus, with the contact of Ag NPs on the surface of TiO_2, the energetic electrons from Ag excites to the CB of TiO_2. As the CB of TiO_2 is an electron acceptor, it readily accepts the electrons and forms superoxide anion radicals ($^{\bullet}O_2^-$) and followed by the protonation and yields $^{\bullet}HO_2$ radicals. This $^{\bullet}HO_2$ radicals easily combines with the trapped electrons resulting H_2O_2 and finally forming a photodegradation active species $^{\bullet}OH$ radicals. Moreover Schottky barrier was formed at the interface of Ag/TiO_2 because the Fermi level of TiO_2 is higher than that of Ag which will hinder the transfer of electron from the Ag to TiO_2. However, it is evident that electrons are capable to transfer from Ag to TiO_2 due to its strong electron oscillation collectively through SPR excitation. These lead to interband excitation giving sufficient energy to the electrons to overcome the Schottky barrier at the interface of Ag/TiO_2 (Kochuveedu et al., 2013; Wen, Ding, & Shan, 2011; M. Xiao et al., 2013). Thus it triggers the energetic electron to be transferred to the CB of TiO_2 and lead to the enriched formation of $^{\bullet}OH$ radicals thus enhancing the photocatalytic oxidation.

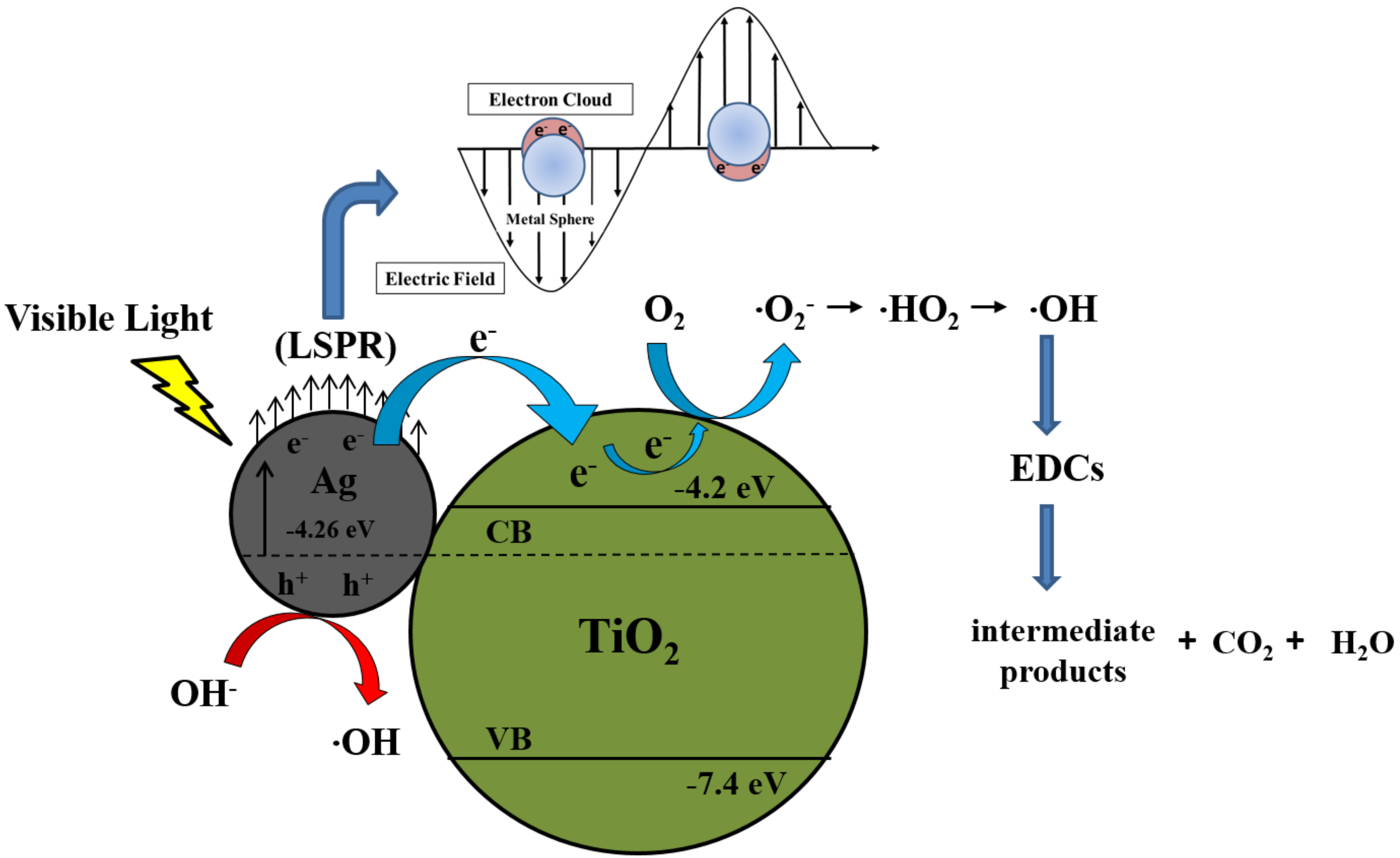

Figure 4.34: Schematic diagram of photocatalysis mechanism Ag/TiO_2 photocatalyst under artificial visible light irradiation

As like Pd the importance of optimal loading was also studied for Ag and correlated with photocatalytic performance. The photocatalyst with low Ag loading (0.5wt% Ag/TiO_2) exhibited a weak performance with only 28.73% for AMX and 15.21% for 2, 4-DCP. This poor performance was due to the low absorption capacity of the photocatalyst in the visible region (D. Chen et al., 2013). On the other hand, high Ag loading (5.0wt% Ag/TiO_2) also resulted in poor performance due to the overlapping of the plasmonic field region. Besides that, it also promoted shielding effect of Ag layer and marginally declined the photocatalytic performance as observed in Pd composite (W. Wang et al., 2012). Therefore the optimal Ag loading content found to be 3.0wt% that delivered the best photocatalytic efficiencies in accordance to LSPR effect and Schottky interface. The photocatalytic degradation of both the AMX and 2, 4-DCP followed the pseudo first-order reaction kinetics as shown in Figure 4.35 and the rate constants (k_1) are summarized in Table 4.4.

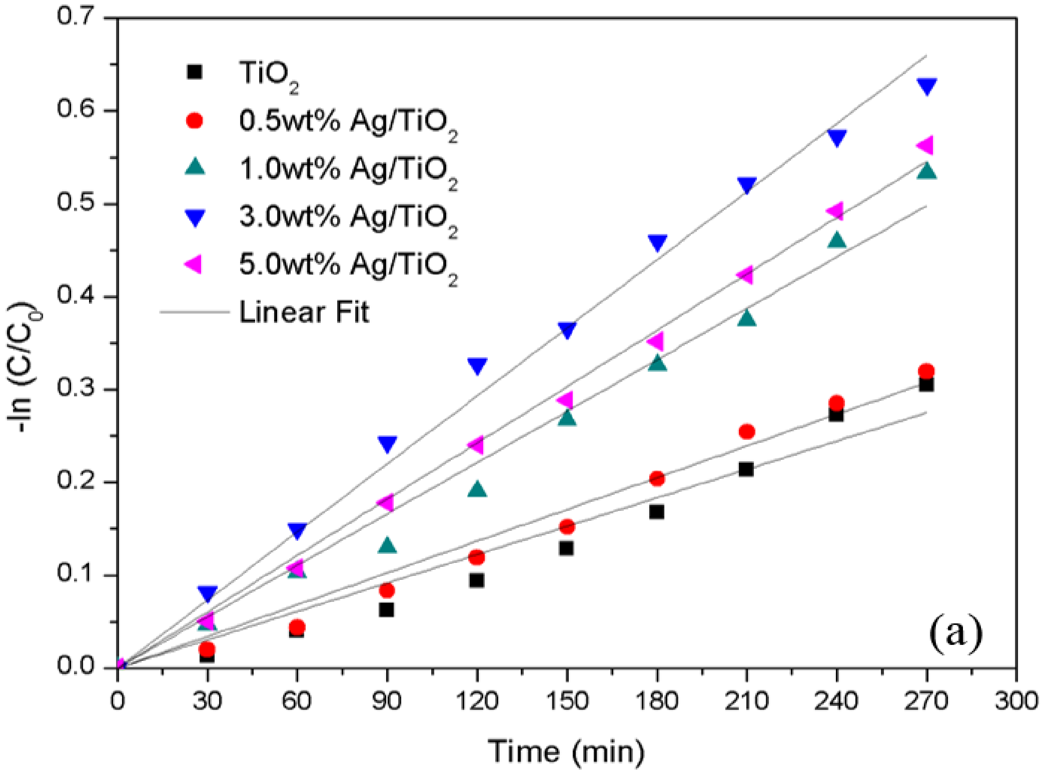

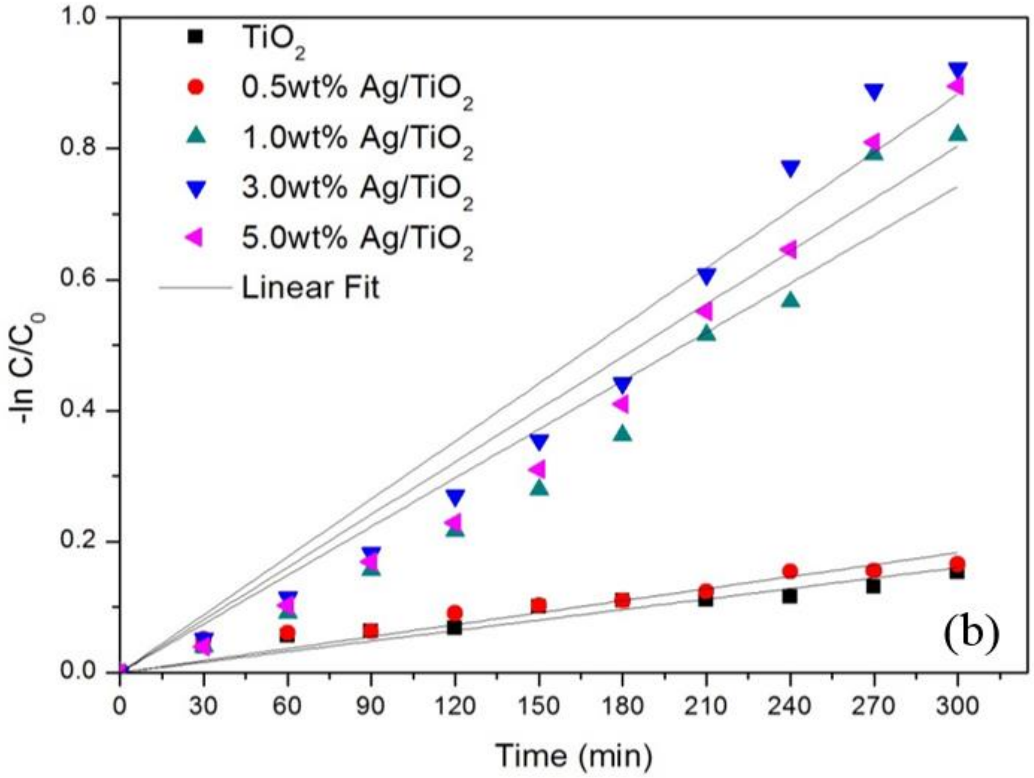

Figure 4.35: The kinetics of (a) AMX and (b) 2, 4-DCP degradation

Table 4.4: The obtained kinetic constants along with the coefficient of regression for AMX and 2, 4-DCP degradation

	First Order Kinetics			
Sample	**AMX**		**2, 4-DCP**	
	K	**R^2**	**k**	**R^2**
TiO_2	0.0009	0.978	0.0005	0.975
0.5wt% Ag/TiO_2	0.0011	0.988	0.0006	0.978
1.0wt% Ag/TiO_2	0.0031	0.959	0.0025	0.973
3.0wt% Ag/TiO_2	0.0039	0.954	0.0029	0.982
5.0wt% Ag/TiO_2	0.0035	0.951	0.0027	0.979

The degree of mineralization presented in Figure 4.36 also well supported the above findings and also well correlated with the liquid chromatography quantification. An efficiency of 51.5% and 43.6% were achieved for mineralization of AMX and 2, 4-DCP by 3.0wt% Ag/TiO_2 respectively. Thus it also proved that the deposition of Ag onto TiO_2 photocatalysts also exhibited a strong oxidation as like palladium under visible light with varied contribution.

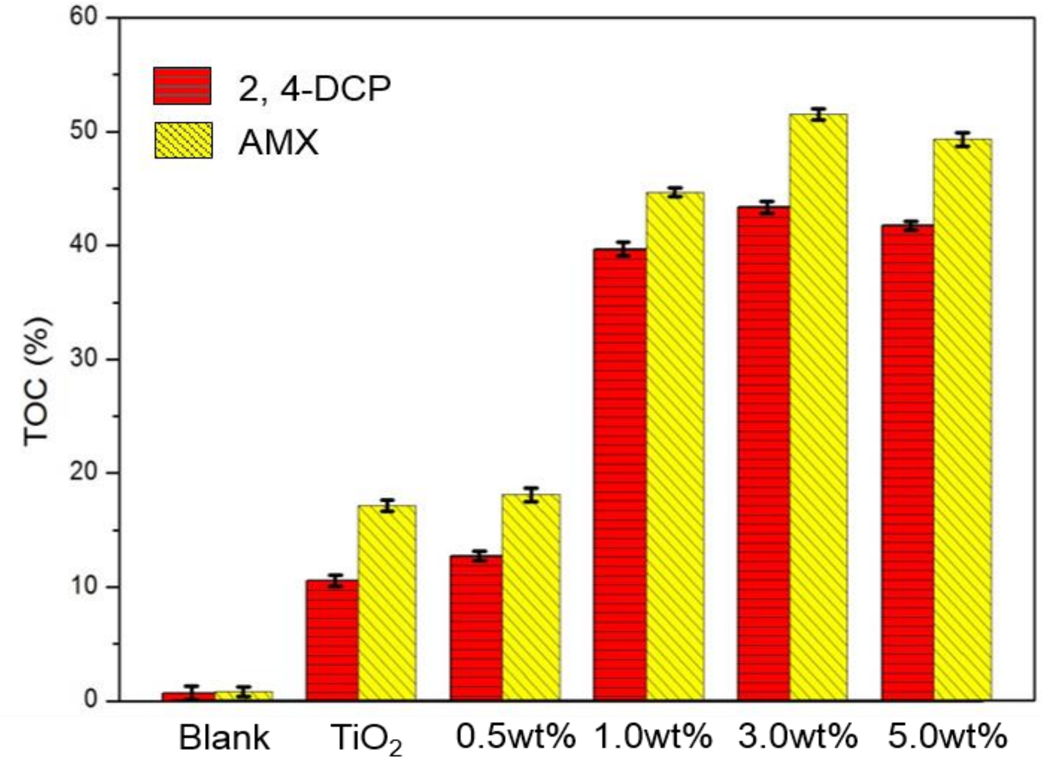

Figure 4.36: TOC analysis of AMX and 2, 4-DCP

Though both the noble metals proved their candidature as a good visible light enhancer along with the suppressing the recombination rate of TiO_2 but the achievement could not be denoted as the superior. Hence the modification of the titania was continued by further incorporating with conducting carbon source. The Ag was chosen as one of the composite from the above study owing to the unique size sensitive nature of palladium. The chosen impurities will notably appraise the visible light enhancement and charge separation through its traditional inherent nature.

4.4 Reduced Graphene Oxide (RGO) Wrapped Ag/TiO_2 Photocatalyst

Figure 4.37 details the XRD spectra of the synergized composite RGO-Ag/TiO_2 along with RGO-TiO_2 composite and the synthesized pristine GO, TiO_2 employed in the composite. The analysis and discussion on TiO_2 was discussed well in the descending section. The synergized composite showed diffraction peaks at 2θ = 38.1°, 44.3°, 64.4°, 77.4° which corresponded to crystal phase (1 1 1), (2 0 0), (2 2 0) and (3 1 1) respectively (JCPDS no. 04-0783). The intense diffraction peaks also confirm the stability of the synthesized silver NPs through sustainable photo deposition. A diffraction peak at 2θ = 10.6° (0 0 2) was observed for GO sample signifying almost complete oxidation of natural graphite into GO through d-spacing expansion from 3.37 to 8.6 Å. This prove the incorporation of oxygen containing group on to the GO sheets (J. Zhang, Xiong, & Zhao, 2011).

Once the reduction of GO is complete no diffraction peak was observed in the composite samples that consists RGO. This was owing to small amount of carbon species in the composites and is beyond the detection limit (W.-S. Wang, Wang, Qu, Lu, & Xu, 2012; Y. Wang et al., 2013a; C. Zeng et al., 2013). Overall, the sharp peaks seen in all sample indicating the high crystalline characteristics. The crystalline grain size of TiO_2 was independent of composites (Ag and RGO).

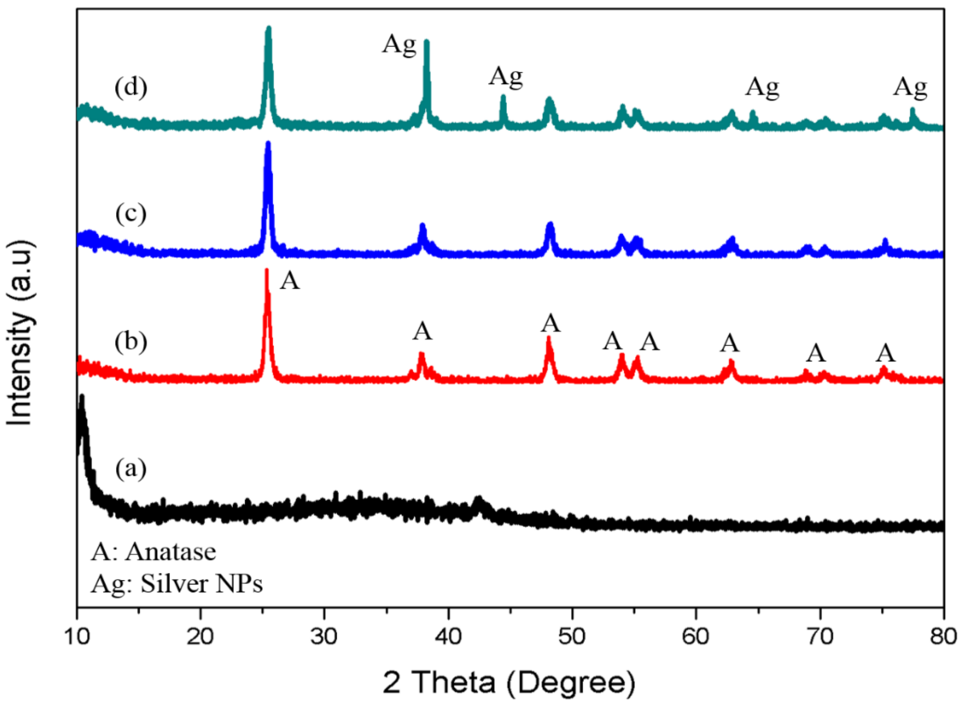

Figure 4.37: XRD patterns of (a) GO, (b) TiO_2, (c) RGO-TiO_2, (d) RGO-Ag/TiO_2

The Raman spectrum shown in Figure 4.38 illustrates the distinct peaks for anatase was observed in this case also. The inset of Figure 4.38 shows the Raman spectrum of GO with two intense peaks at 1351 cm^{-1} (D-band) and 1605 cm^{-1} (G-band). The D-band resembles the disorder band related with structural imperfections created in the reduced graphene oxide during the reduction of GO by hydrothermal process. Meanwhile, the G-band corresponds to the first order scattering of E_{2g} phonon of sp^2 C atoms of graphene (Shah et al., 2013). Therefore, the intensity ratio (I_D/I_G) for GO was 0.78 signifying the presence of large amount of sp^3 domain in the GO sample. The D- and G-band of RGO-TiO_2 and RGO-Ag/TiO_2 were approximately in the same position with GO. However, the I_D/I_G ratio of RGO-TiO_2 (0.95) and RGO-Ag/TiO_2 (0.97) increased from 0.78 for GO, proved the reduction of GO achieved through hydrothermal process. The adopted process was successful whereby some of the oxygenated groups leading to re-establishment of conjugated graphene network are eliminated (Yang, Tian, Wang, &

Fu, 2011). Through the Raman analysis, it could also verify the charge transfer between GO and the hybridized components. This was shown in the G-band of GO having a slight shift of ~ 9 cm^{-1} to a lower frequency at 1596 (RGO-Ag/TiO_2) from 1605 cm^{-1} (GO) confirms the charge transfer between the two hybrid composites where RGO-Ag/TiO_2 acts as an electron donor while GO as an electron acceptor (M. Zhu, Chen, & Liu, 2011).

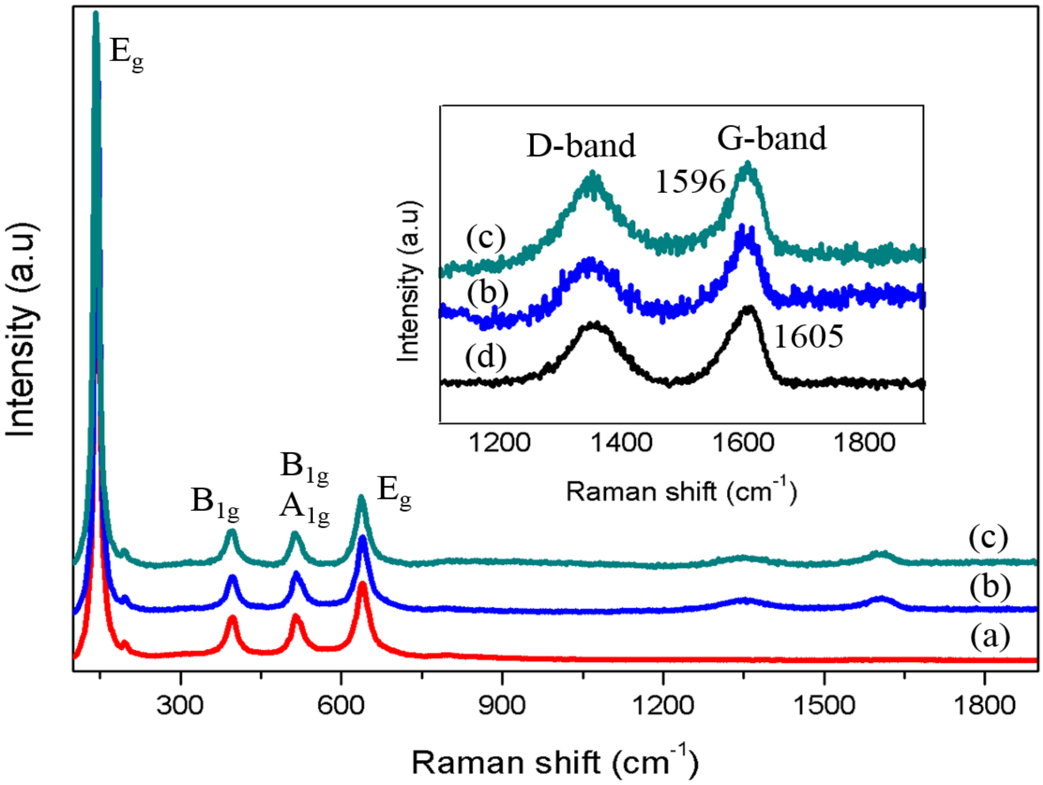

Figure 4.38: Raman spectra of (a) TiO_2, (b) RGO-TiO_2, (c) RGO-Ag/TiO_2 and inset is the (d) GO

The FESEM images (Figure 4.39 (a) and (b)) illustrated the successful wrapping of RGO and Ag NPs with TiO_2. The image (Figure 4.39 (a)) clarifies the uniform distribution of Ag/TiO_2 onto the RGO sheets and (Figure 4.39 (b)) Ag NPs onto the surface of TiO_2 through efficient sustainable photodeposition method. The HRTEM images shows the average particle size of Ag NPs is between 7 and 9 nm (Figure 4.39 (c)) with a lattice fringes spacing of 0.24 nm and 0.35 nm (Figure 4.39 (d)). The observed fringes signifies the presence of Ag NPs (1 1 1) and TiO_2 (1 0 1) respectively (D. Chen et al., 2013; Z. Chen et al., 2014).

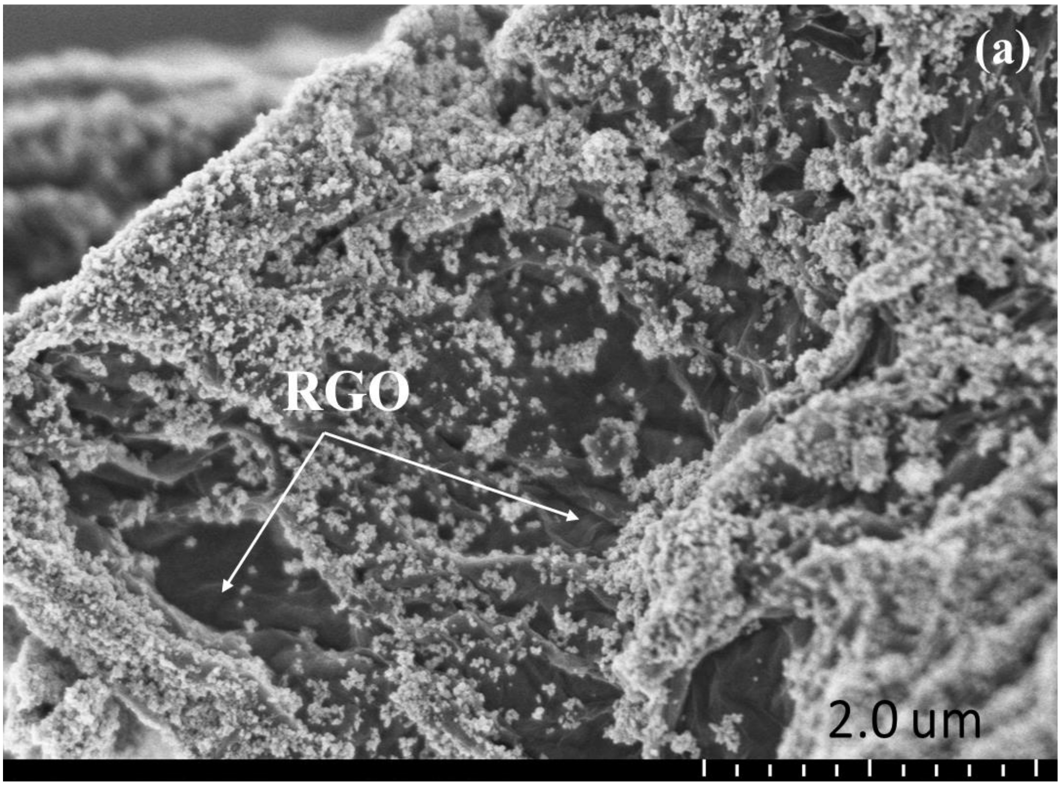

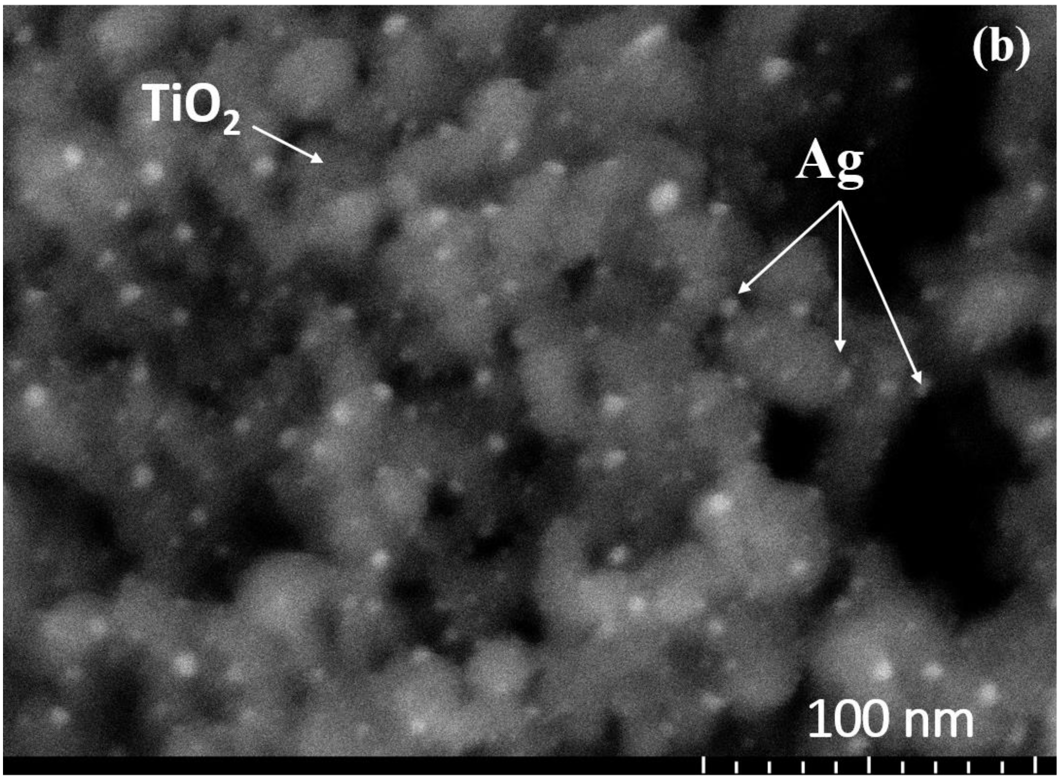

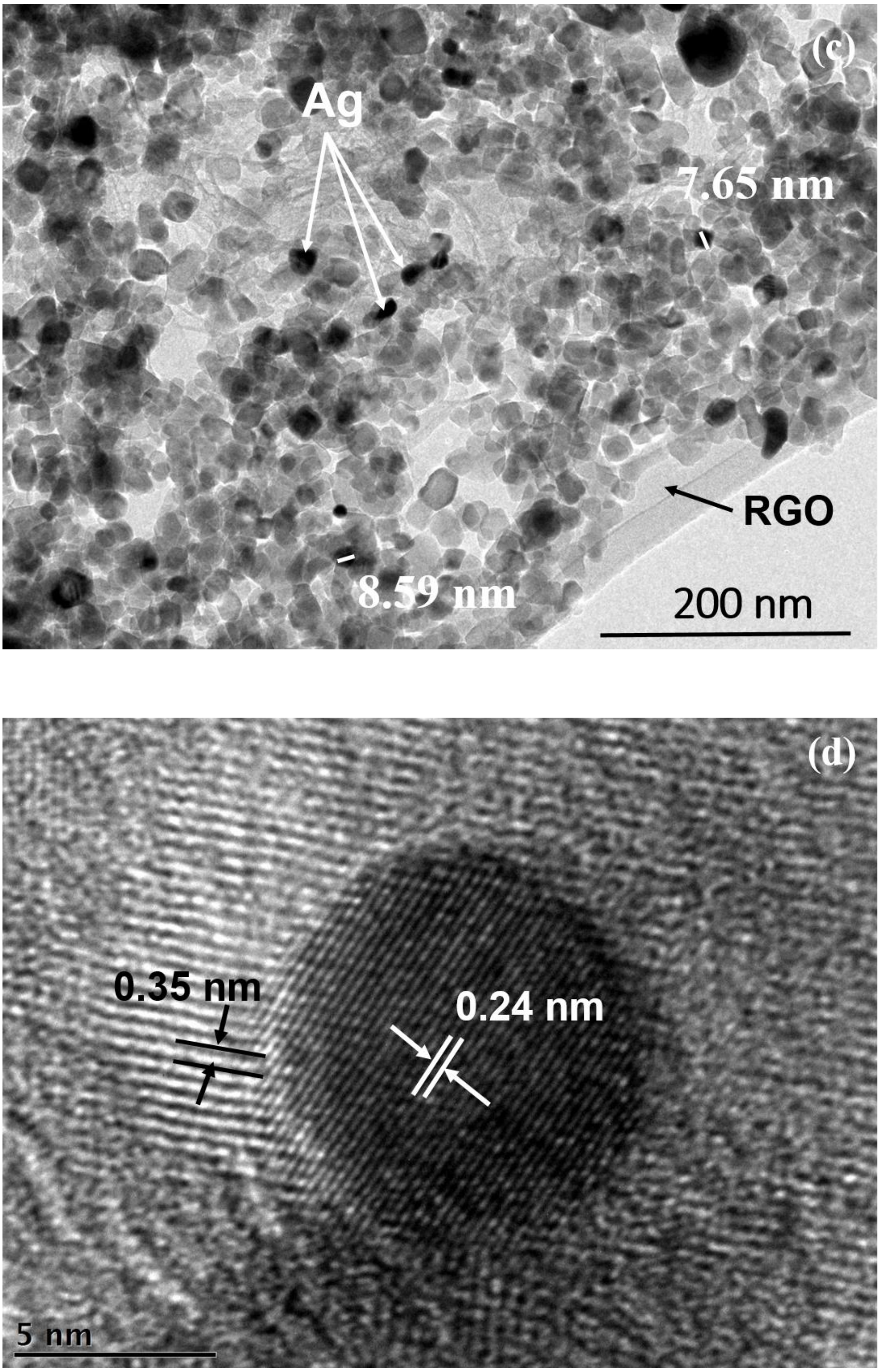

Figure 4.39: FESEM images of the (a-b) RGO-Ag/TiO$_2$ and (c-d) HRTEM images of RGO-Ag/TiO$_2$

The adsorption-desorption hysteresis loop of the synthesized photocatalysts are illustrated in Figure 4.40 (a-c). All the obtained hysteresis well correlated to the type IV isotherms with mesoporous structure. The BET surface area for all the samples was found to be 52.24 m^2/g for TiO_2, 61.47 m^2/g for RGO-TiO_2 and 73.68 m^2/g for RGO-Ag/TiO_2 respectively. The surge in surface area of the synergized composite was contributed by the RGO. It also further shows a well distribution of RGO sheets onto the surface of TiO_2 (Ryu et al., 2015).

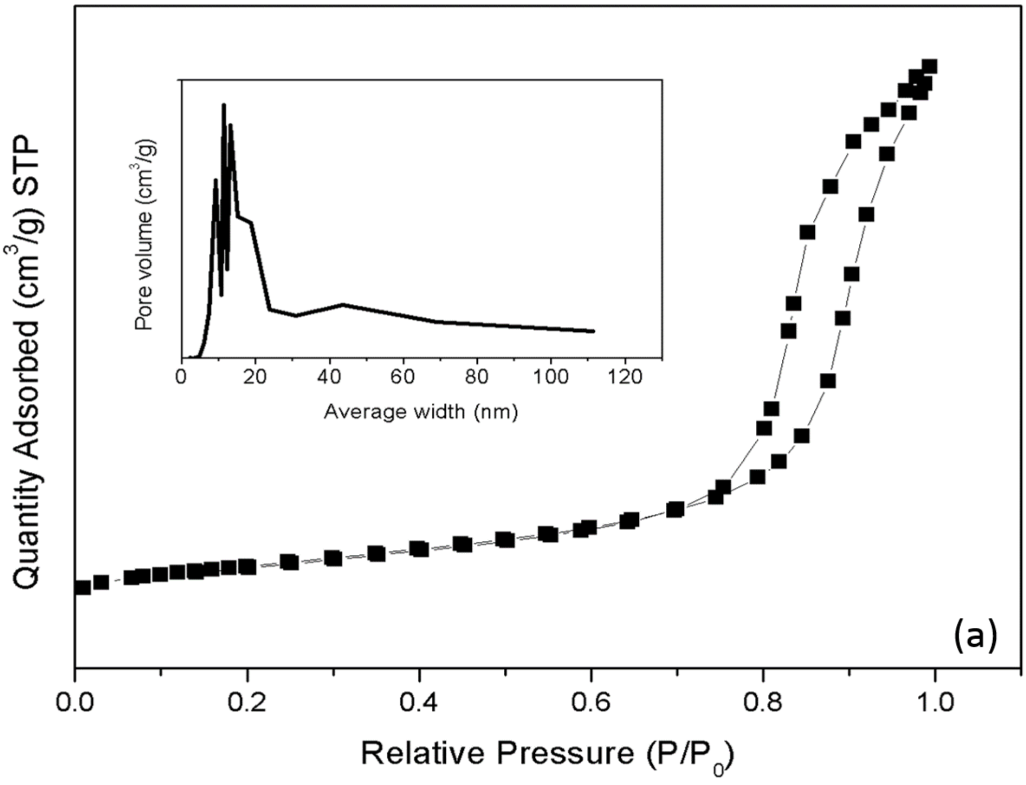

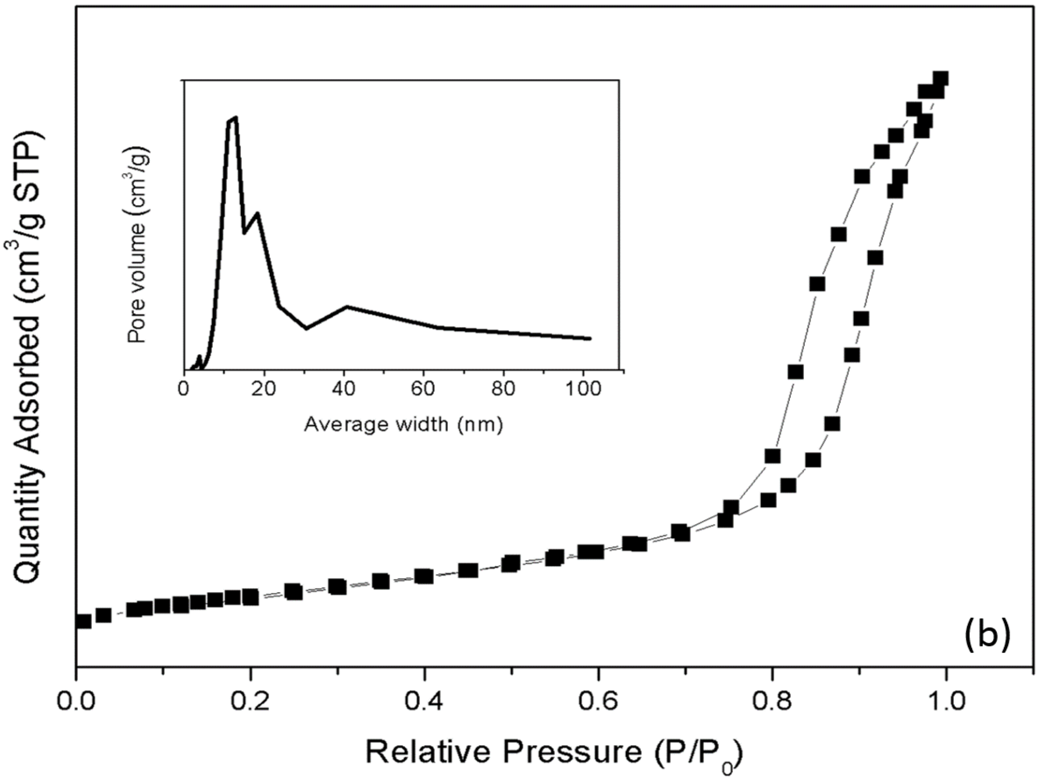

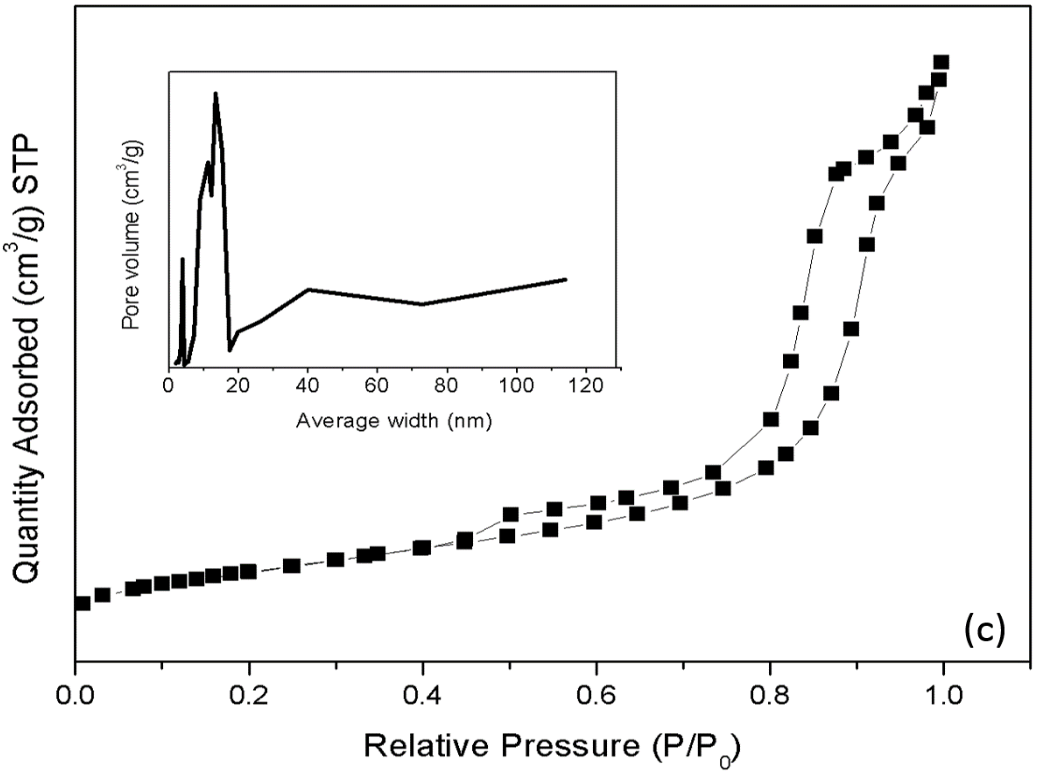

Figure 4.40: Adsorption hysteresis of (a) TiO_2, (b) RGO-TiO_2 and (c) RGO-Ag/TiO_2 and the inset is the pore size distribution

The FTIR spectra of all prepared samples are illustrated in Figure 4.41. The GO displayed several robust absorption peaks corresponding to various oxygen functional groups. The absorption peaks included the wide broad peak at 3400 cm^{-1} which correspond to O-H stretching. The carboxylates C=O stretching occurred at 1730 cm^{-1} while the hydroxyl groups of molecular water bending and C=C stretching indicated the absorption at 1620 cm^{-1}. The carboxyl group, phenolic C-O-H and C-O stretching vibrations in the epoxy was detected at 1375, 1220 and 1045 cm^{-1} respectively (Tan et al., 2013). A distinct and drastic decrease in intensity of absorption peaks was observed at C=O (1750 cm^{-1}), C=C (1620 cm^{-1}), C-O-H (1220 cm^{-1}) and C-O (1045 cm^{-1}) that corresponds to oxygen functional groups contributed by the reduction of GO. Meanwhile, TiO_2 NPs shown wide peaks at 3350 and 1630 cm^{-1} which is ascribed to the O-H group of water, whereas the wide and broad peaks at 500-900 cm^{-1} is to the stretching vibration of Ti-O-Ti and Ti-O-C bonds. (Yueli Liu et al., 2014).

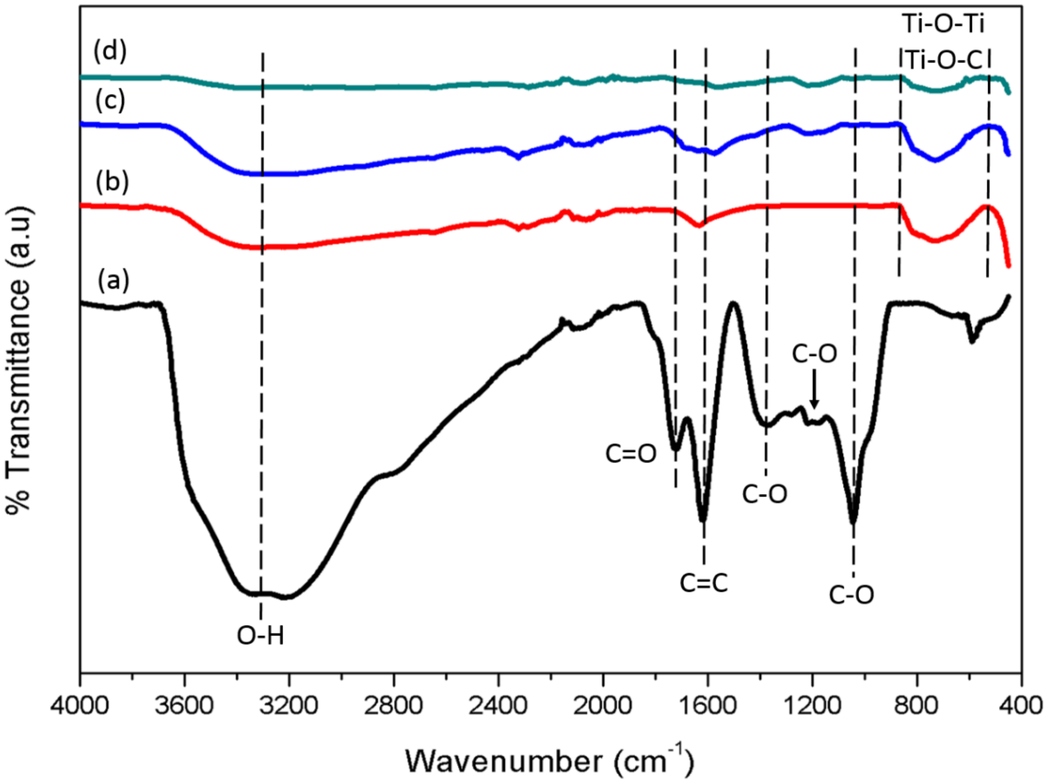

Figure 4.41: Functional group spectra of (a) GO, (b) TiO_2, (c) RGO-TiO_2 and (d) RGO-Ag/TiO_2

The XPS spectra of the prepared samples were presented in Figure 4.42 (a-d). Figure 4.42 (a) shows the C 1s XPS spectrum of GO with generally can be devolved into four peaks at 284.8, 286.6, 287.8 and 289.0 eV and this binding energies corresponds to different functional group of C-C and C-O in hydroxyl or epoxy forms, C=O and COOH respectively (D. Wang, Li, Chen, & Tao, 2012; H. Zhang et al., 2011). After the hydrothermal treatment at 180°C for 6 h, significant decrease of contents C-O and C=O peaks of C 1s observed in the synergized composite sample (RGO-Ag/TiO_2) indicating the substantial removal of oxygen containing groups during the treatment (Figure 4.42 (b)). This significant decrease in the oxygen concentrations shows a remarkable effectiveness in reduction of GO. Figure 4.42 (c) illustrated the Ti core level XPS spectrum where two peaks centered at 459.8 eV (Ti $2p_{3/2}$) and 465.5 eV (Ti $2p_{1/2}$) as seen in our previous studies. The presence of Ag NPs were represented in Figure 4.42 (d) with two peaks centered at 368.6 and 374.6 eV for Ag $3d_{5/2}$ and Ag $3d_{3/2}$ respectively with 6 eV splitting between two peaks.

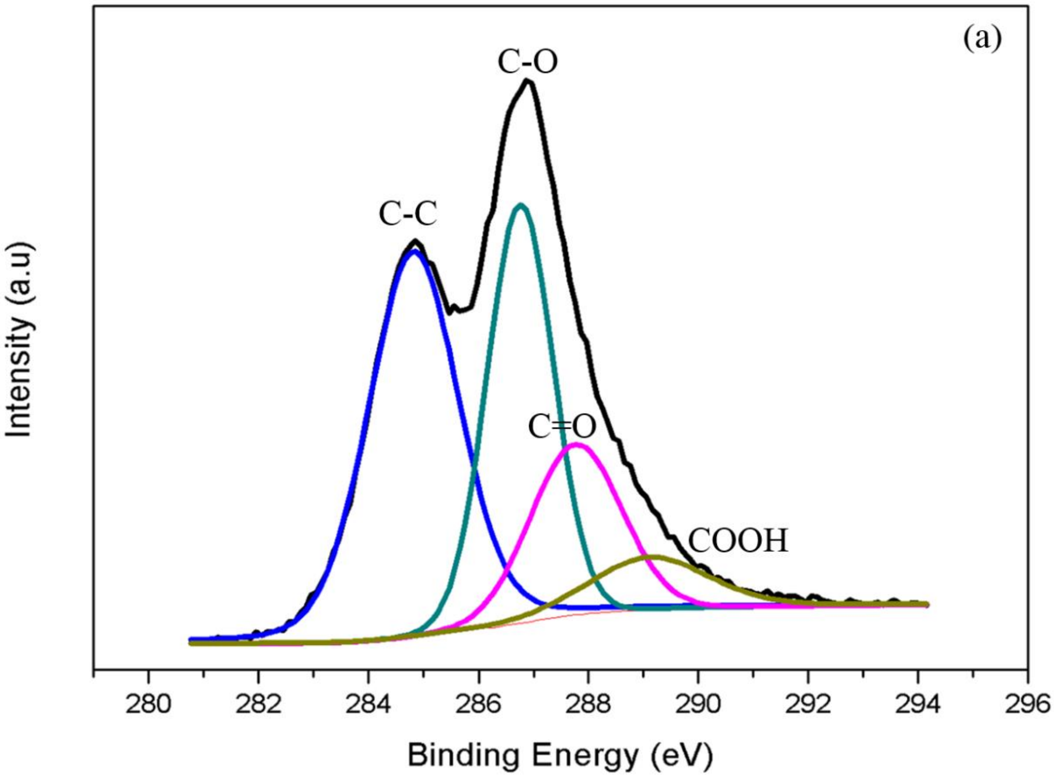

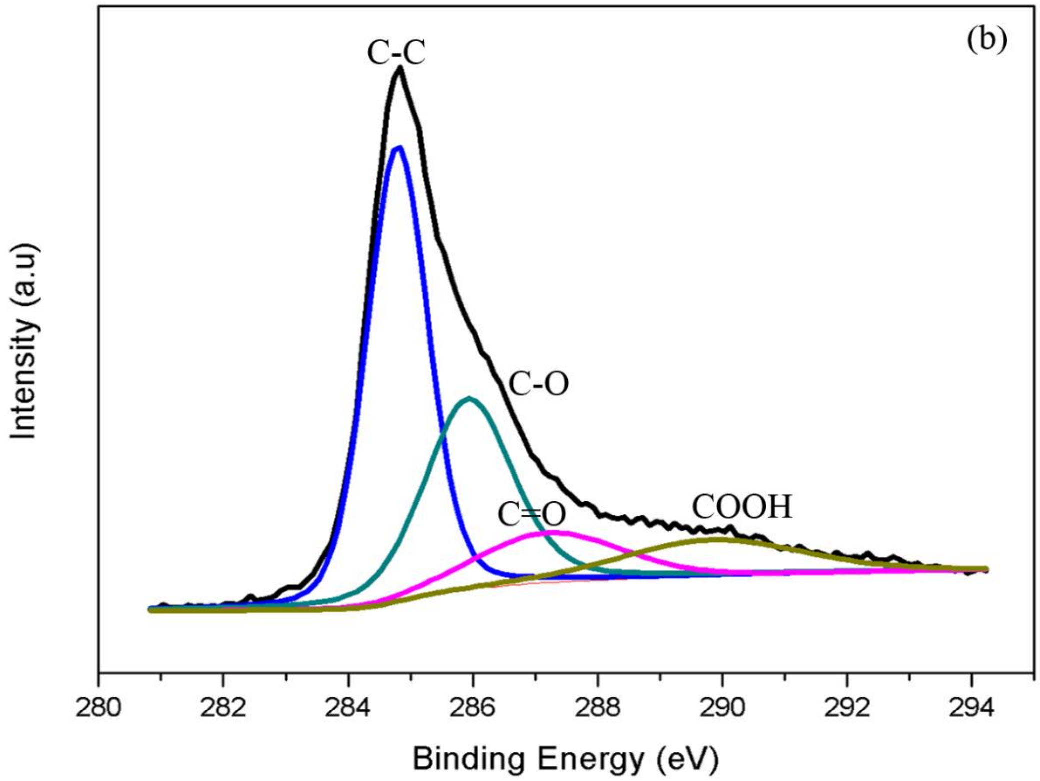
(b)
C-C
C-O
C=O
COOH
Intensity (a.u)
280
282
284
286
288
290
292
294
Binding Energy (eV)

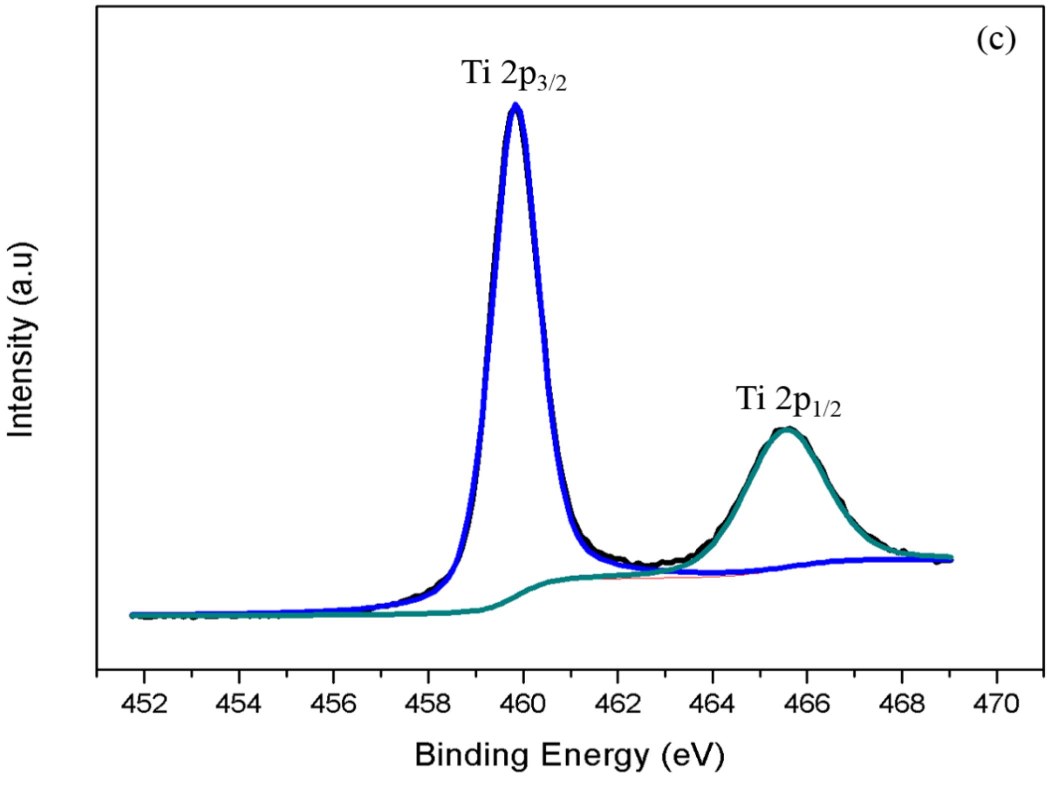
(c)
Ti 2p3/2
Ti 2p1/2
Intensity (a.u)
452
454
456
458
460
462
464
466
468
470
Binding Energy (eV)

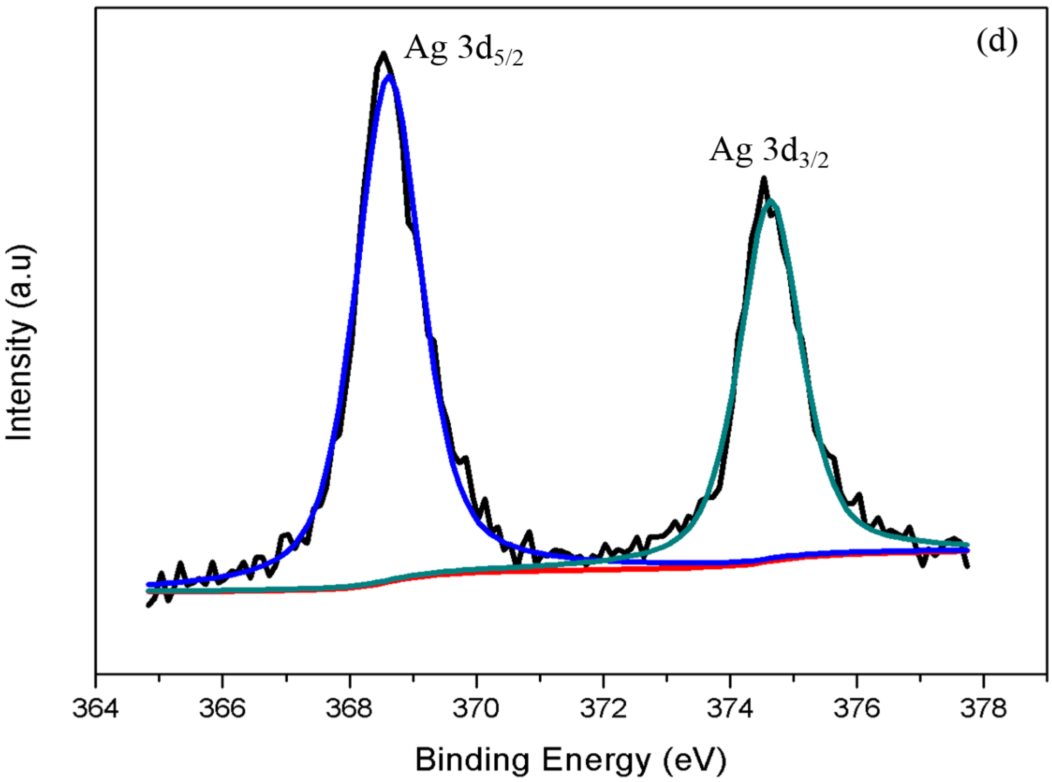

Figure 4.42: Core level XPS spectrum of (a) C 1s of GO, (b) C 1s of RGO-Ag/TiO$_2$, (c) Ti 2p and (d) Ag 3d

In scrutinize the absorption of the synthesized materials, UV-visible absorption spectroscopy analysis was executed and shown in Figure 4.43. A considerable red shift towards visible light region is clearly observed for RGO-TiO$_2$ and RGO-Ag/TiO$_2$ indicating narrow band gap energy with the introduction of RGO. This significant shift ascertain the incorporation of RGO in the composite through Ti-O-C bond (Shah et al., 2013; Yuhao Yang et al., 2014). Further enhancement in the visible light region at ~ 460 nm was noticed after the incorporation of Ag NPs into the composite (RGO-Ag/TiO$_2$) (Shah et al., 2013). The existence of Ag NPs on the surface of TiO$_2$ significantly oscillated the dielectric constant surrounding the matrix leading to the visible light absorption. The Figure 4.44 reveals the calculated band gap energy for the prepared photocatalysts by using Kulbeka-Munk equation. It was found that after the incorporation of RGO the band gap energy of TiO_2 was narrowed to 2.9 eV. The reduction in band gap was attributed to the formation of Ti-O-C bond, where the free electrons on the surface of TiO_2 are bonded with unpaired π-electrons and leading to a shift upwards the valence band edge (Umrao et al., 2014). The observed phenomenon enhanced the RGO-Ag/TiO_2 with a notable visible light performance.

The photoluminescence spectra for the prepared samples were portrayed in Figure 4.45. It is well proven from the analysis that the composite RGO and Ag NPs had drastically reduced the recombination rate of electron-hole pairs. This is attributed to the trapping of the photo-excited electrons by RGO (Shah et al., 2013). A more active separations of electron-hole pairs was observed after the incorporation of Ag NPs. This resulted from the effective electrons transfer from TiO_2 - Ag NPs - RGO. Therefore, it is clear that RGO-Ag/TiO_2 composite exhibited a better photocatalytic performance.

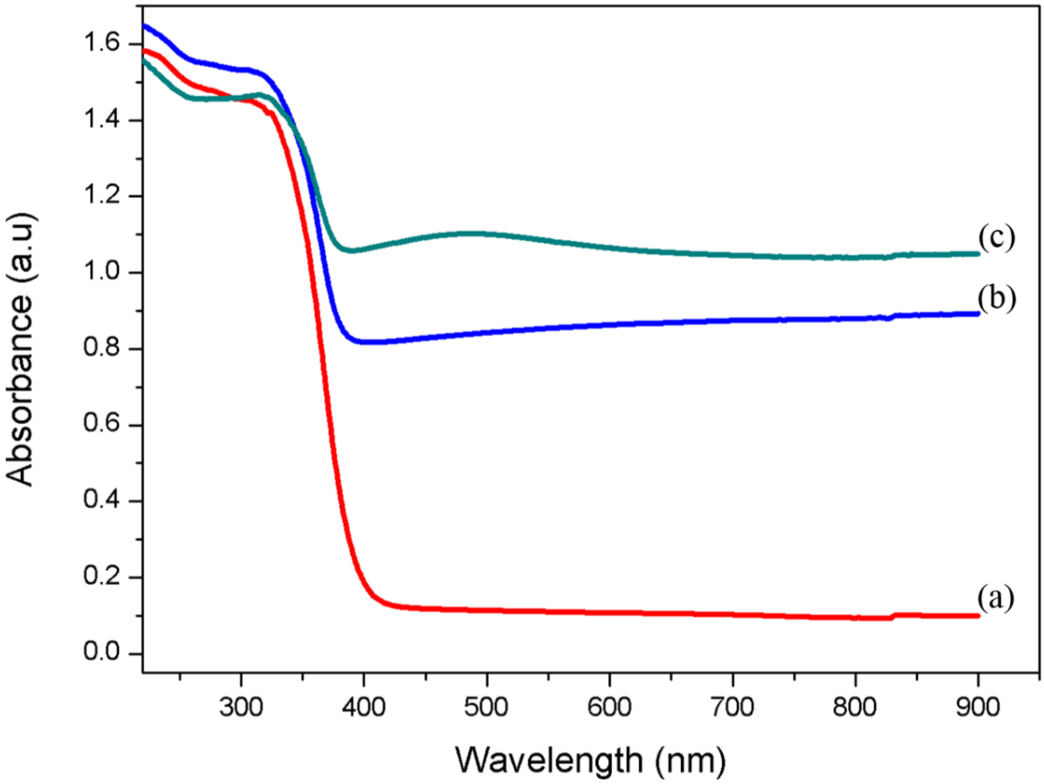

Figure 4.43: UV-vis absorption spectra (a) TiO_2, (b) RGO-TiO_2 and (c) RGO-Ag/TiO_2

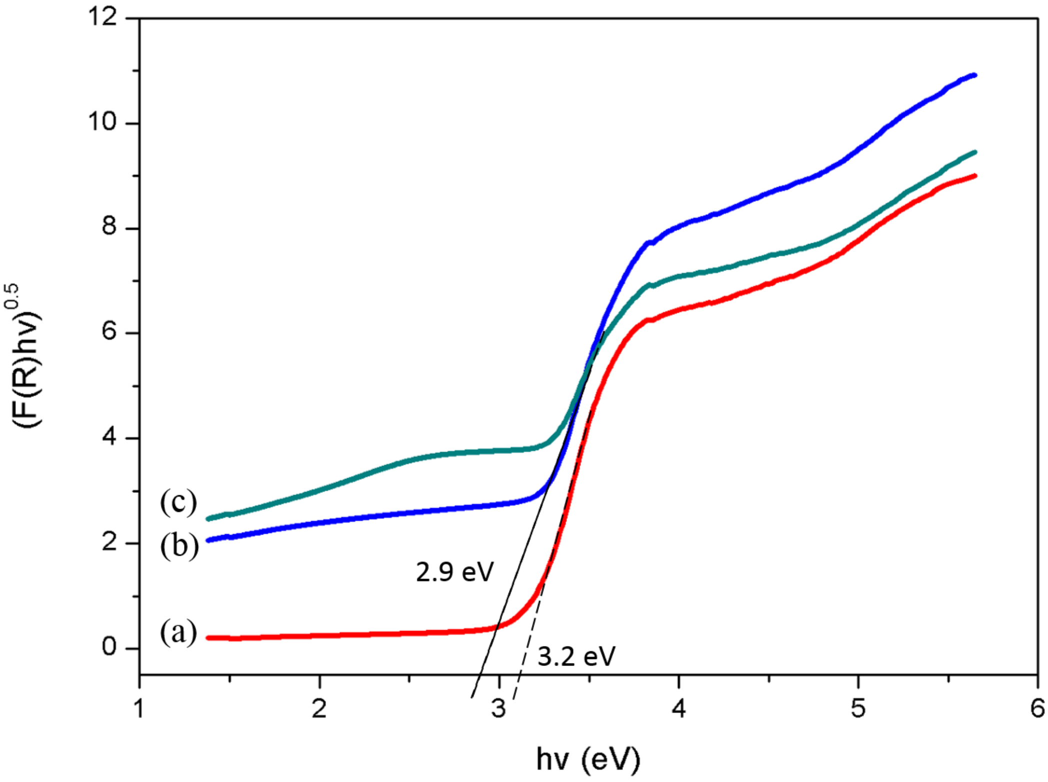

Figure 4.44: Calculated band gap energy of (a) TiO_2, (b) RGO-TiO_2 and (c) RGO-Ag/TiO_2

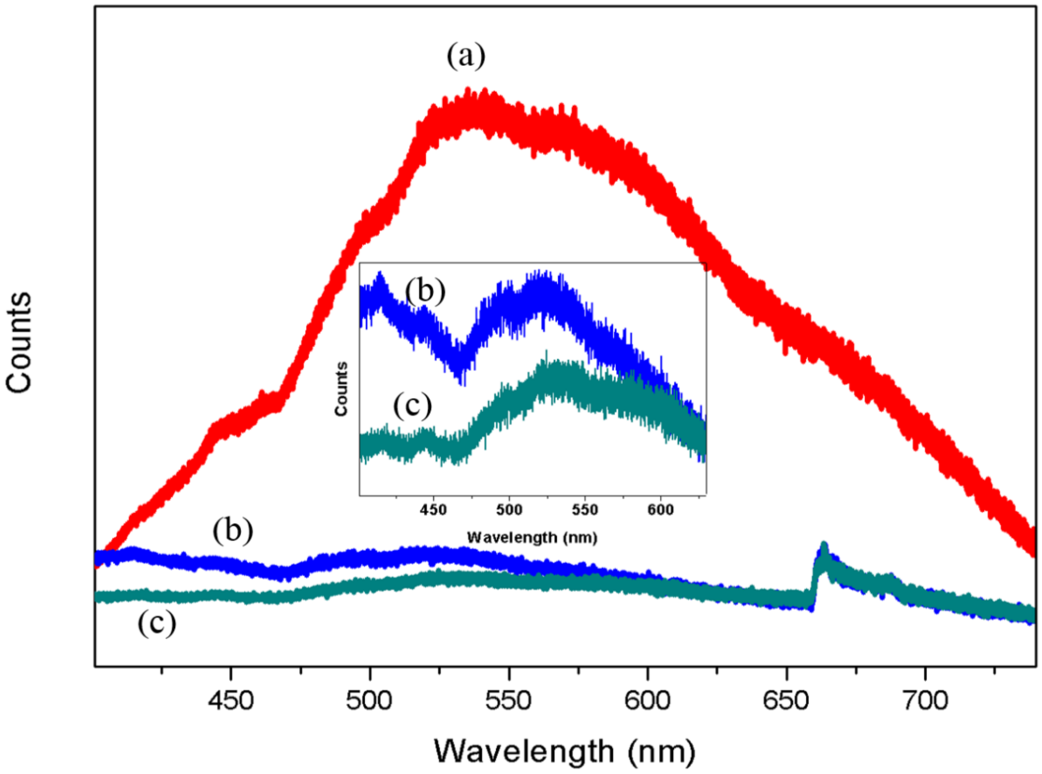

Figure 4.45: Photoluminescence spectra of (a) TiO_2, (b) RGO-TiO_2 and (c) RGO-Ag/TiO_2

Figure 4.46 (a-c) clearly shows the visible light photocatalytic degradation efficiency of the prepared photocatalysts. It was clearly observed that the degradation efficiency followed an order of RGO-Ag/TiO_2 > RGO-TiO_2 > TiO_2. It is evident that BPA is very stable and possesses poor photosensitizing nature where almost nil degradation was observed in the presence of visible light alone. An improved comprehensive degradation was achieved by RGO-TiO_2 for BPA compounds within 6 h. The attained improvement on visibility was attributed to the enhancement of the significant red shift through Ti-O-C bond. The bond formation was appraised by the oxygen sites in the TiO_2 lattice and was substituted by carbon atoms (Dong, Wang, & Wu, 2009). Therefore, when visible light illumination is enabled, the photoexcitation took place in the O-2p orbital to Ti-3d orbital and leaves behind holes at the O-2p state with a very high redox potential (Umrao et al., 2014). This high redox potential catalyse the reaction between holes and H_2O leading to the formation of active $^{\bullet}OH$ radicals. The high redox potential also allows ease transfer of photogenerated electrons from TiO_2 to RGO due to work functions of RGO (4.4 eV) that underlay below the conduction band of TiO_2 (4.2 eV) (Y. Wang et al., 2013). These electrons then react with adsorbed O_2 to form superoxide anion radical ($^{\bullet}O_2^-$). Thus, it prolongs the lifetime of electron and hole pairs (P. Wang et al., 2013; Y. Wang et al., 2013).

A good photodegradation efficiency of 61.9% was observed for the RGO-Ag/TiO_2 than that of RGO-TiO_2 (39.5%) and TiO_2 (22.2%). It is well evident that this greater efficiency was equally attributed to the inclusion of Ag NPs into the composite. The Ag NPs with a characteristic of negative work function (4.26 eV) stimulated the ability to capture the photogenerated electrons of TiO_2. When these NPs get intimated with RGO, it further transfers the electrons to the surface of RGO. Hence it further suppresses the charge recombination and thereby increasing the overall photocatalysis efficiency. Moreover the LSPR phenomenon triggered by the noble metal also well contributed for the visible light enhancement. The presence of visible light excited the Ag surface plasmon and this collective electron oscillation generates high concentration of energetic electrons at its surface. The RGO surface then quickly transports those electrons from Ag surface through extended π-conjugation structure. This movement of electron from Ag to RGO surface prolongs the life span of the charge carriers (Bhunia & Jana, 2014). The excess formation of electrons through Ag also reacts with surface absorbed oxygen forming superoxide anion radical ($^{\bullet}O_2^-$). Where else the holes forms active radicals ($^{\bullet}OH$) by reacting with H_2O molecule. Thus the immense production of $^{\bullet}OH$ radicals triggered through respective mechanism contributed for enhanced suppression of electron-holes recombination. The proposed mechanism for the photocatalytic degradation of poor sensitizing compound under visible light irradiation is illustrated in Figure 4.47.

Meanwhile, a similar experiment was also carry out to evaluate the good photosensitizing compounds namely anionic (Reactive Blue 19-RB19) and cationic (Methylene Blue-MB) dye pollutants. From Figure 4.46 (b) and (c) clearly show the similar photodegradation efficiency trend as BPA compounds. However, both RGO-TiO_2 and RGO-Ag/TiO_2 exhibited a high absorption capacity for MB as compared to RB19 and BPA. This phenomena was mainly due to the strong formation of $\pi - \pi$ stacking interaction between the benzene ring of MB and the surface of RGO (T. Wu et al., 2011). The high degradation efficiency observed in both the dyes was mainly due to the presence of RGO and Ag NPs along with the photosensitizing nature. In most cases the RGO act as an electron sink to facilitate photo generated electrons separation and store the separated electrons (Ping Wang, Zhai, Wang, & Dong, 2011). Moreover, RGO can accumulate electrons injected from the photo generated dyes because of the π-conjugated network that increase the photocatalytic degradation efficiency.

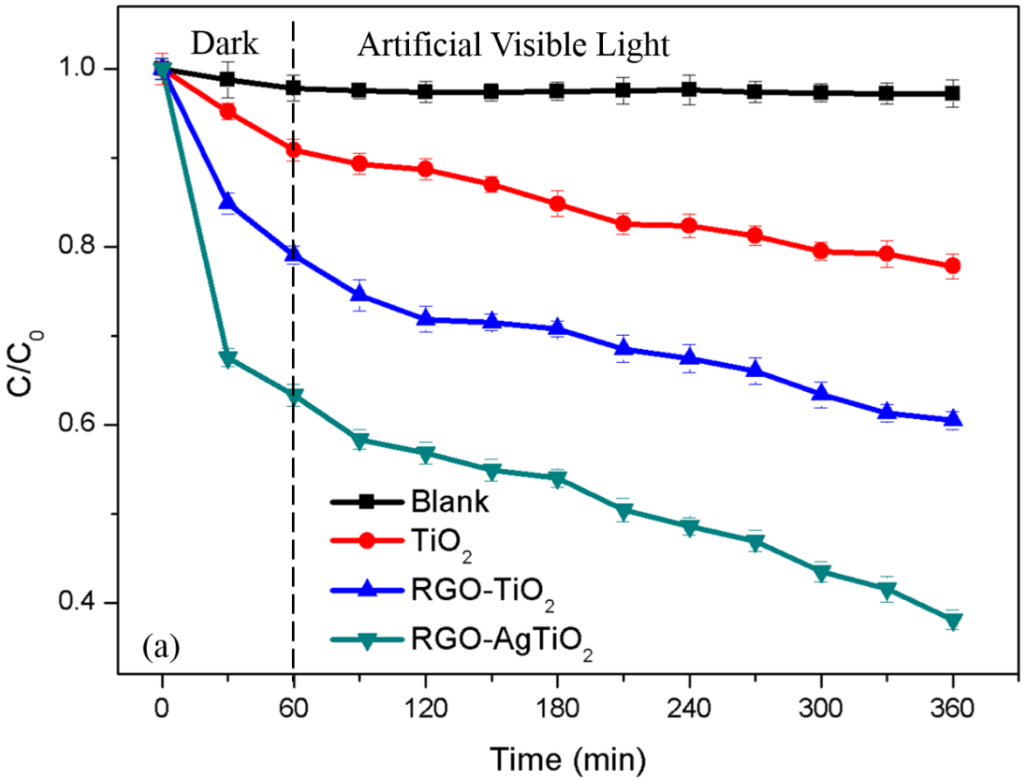
Dark
Artificial Visible Light
C/C$_0$
1.0
0.8
0.6
0.4
0
60
120
180
240
300
360
Time (min)
Blank
TiO$_2$
RGO-TiO$_2$
RGO-AgTiO$_2$
(a)

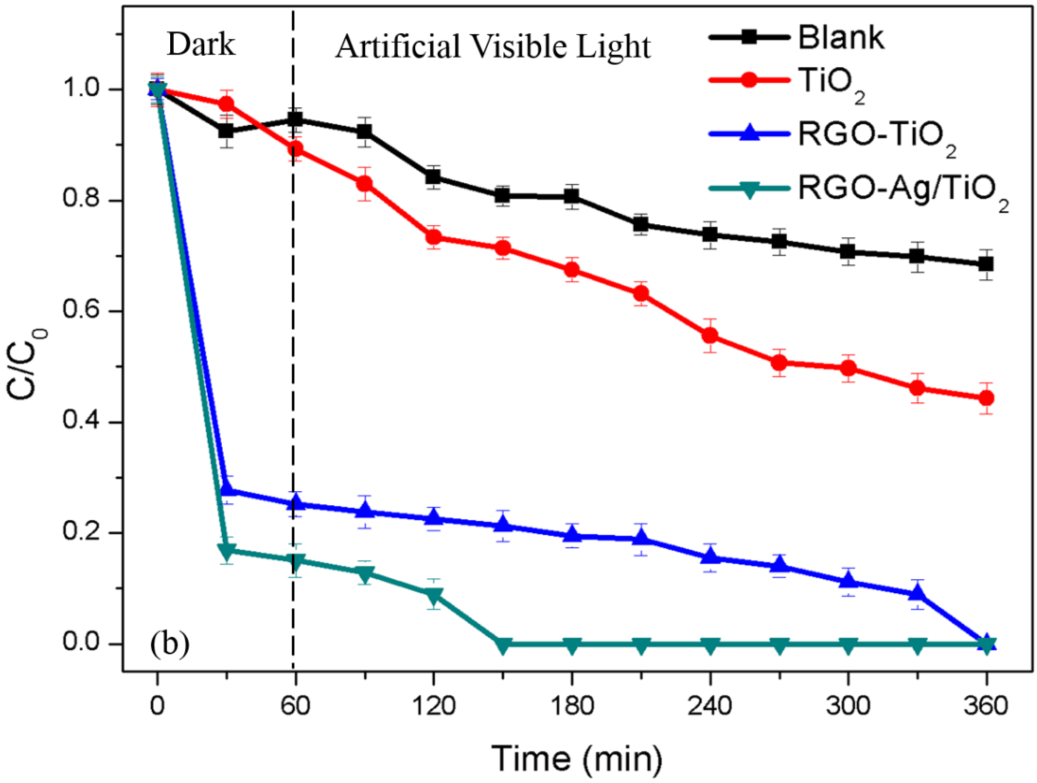
Dark
Artificial Visible Light
Blank
TiO$_2$
RGO-TiO$_2$
RGO-Ag/TiO$_2$
C/C$_0$
1.0
0.8
0.6
0.4
0.2
0.0
0
60
120
180
240
300
360
Time (min)
(b)

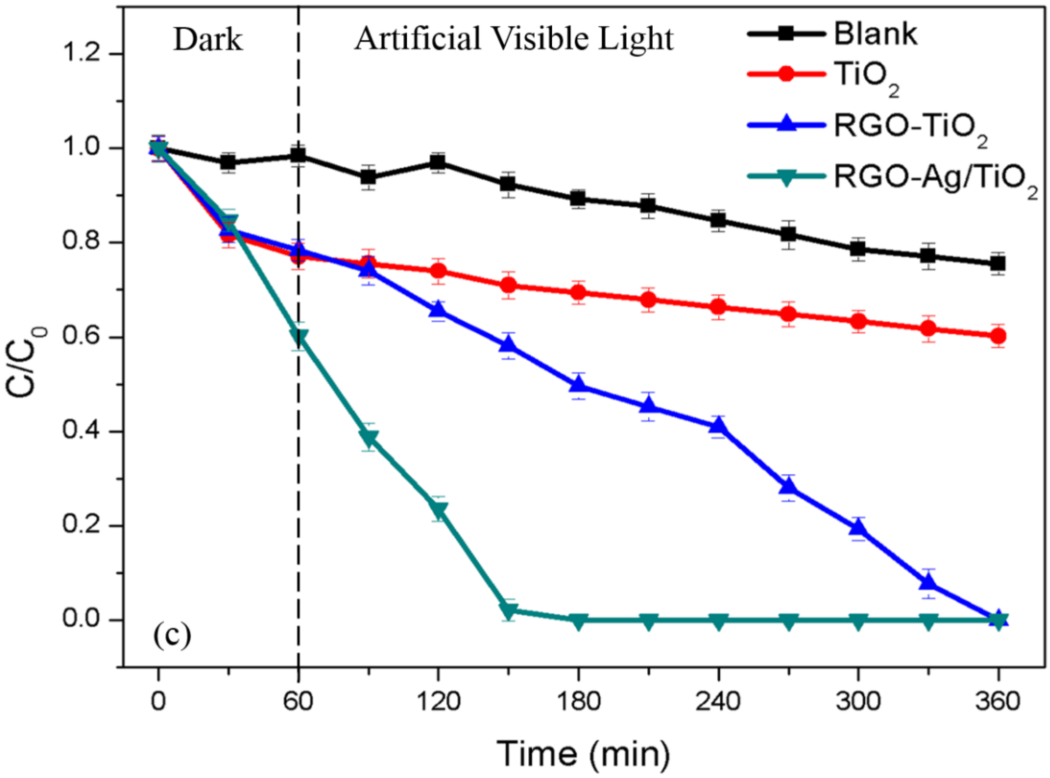

Figure 4.46: Artificial visible light photocatalytic activity of (a) Bisphenol A, (b) Methylene Blue and (c) Reactive Blue 19

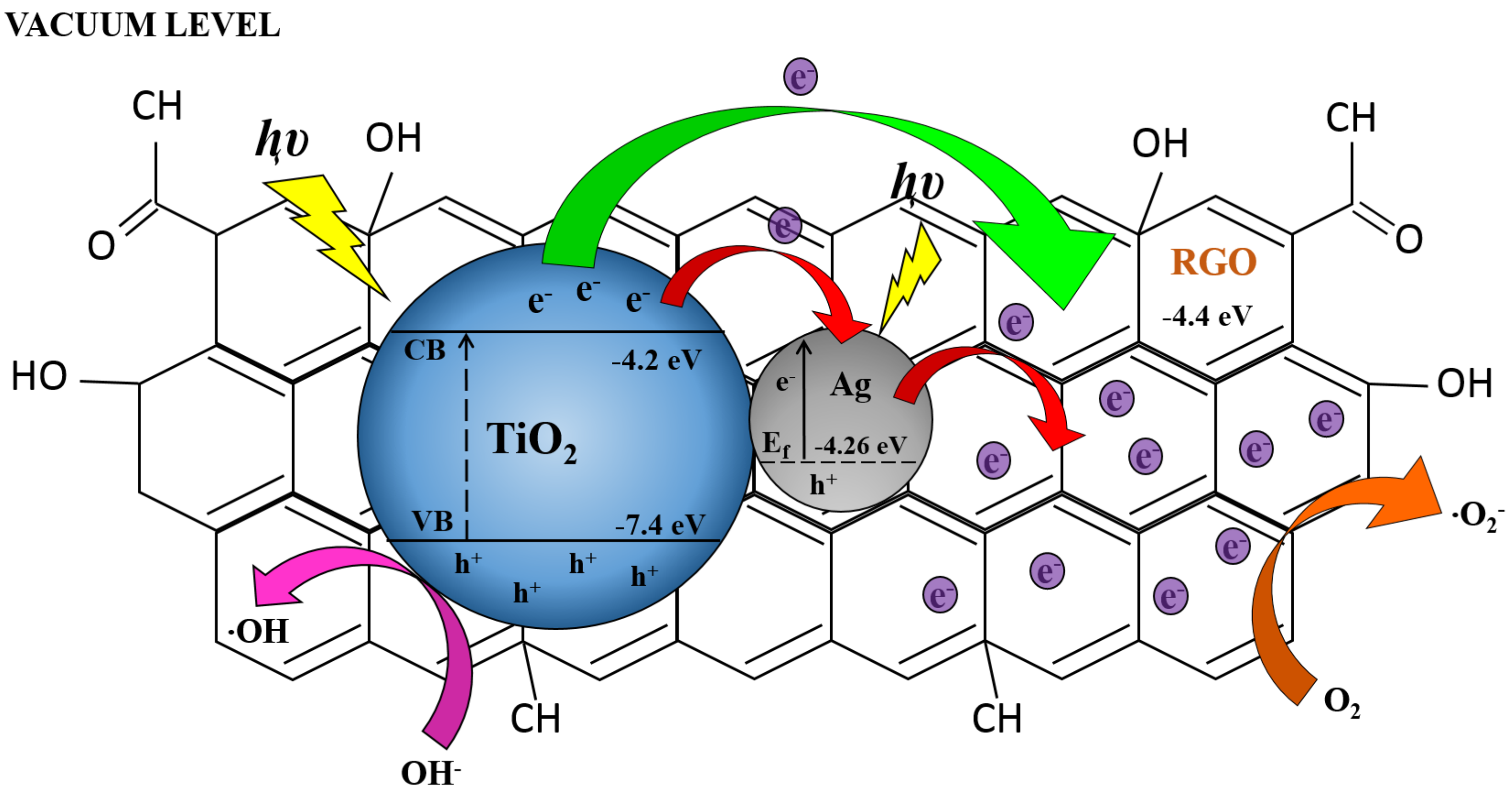

Figure 4.47: Schematic diagram of photocatalysis mechanism of RGO-Ag/TiO_2 photocatalyst under artificial visible light irradiation

Recycle experiments were carried out to evaluate the stability of the prepared photocatalysts. It clearly shows in Figure 4.48 (a-c) that the RGO-Ag/TiO_2 still sustains a high level of degradation efficiency even after three rounds of recycling. An efficiency of 56.3% was able to accomplish after the third run. Similarly complete removal MB and RB19 was achieved as compared to the first run showing with marginal increases in reaction time.

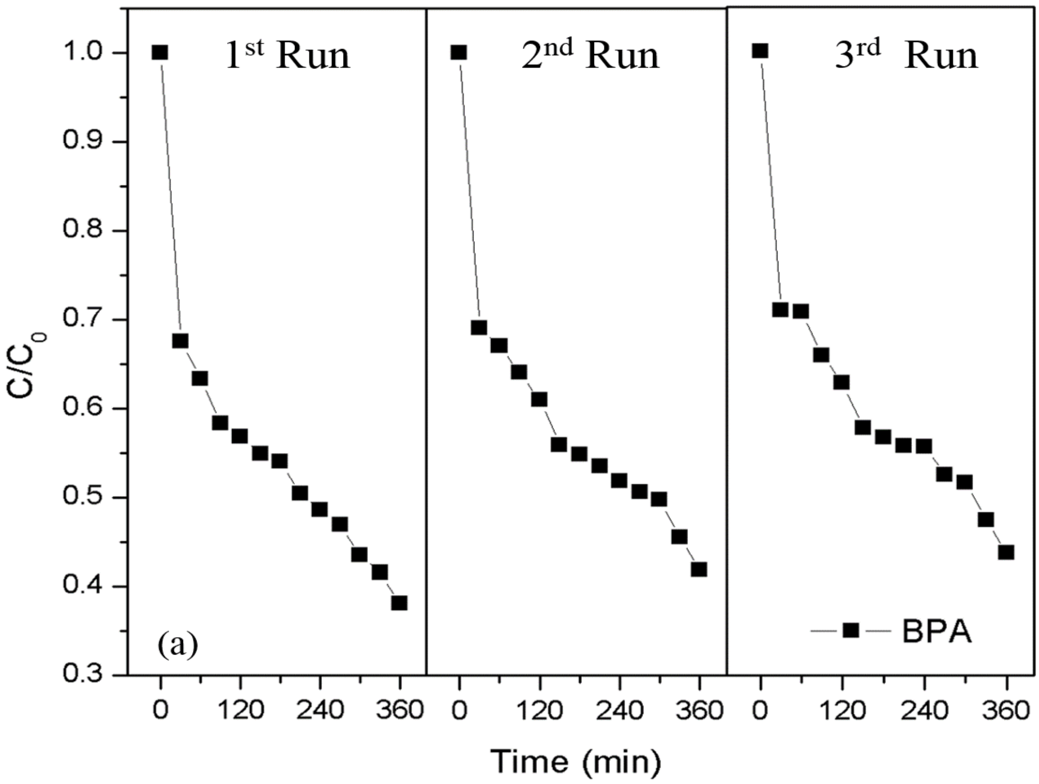

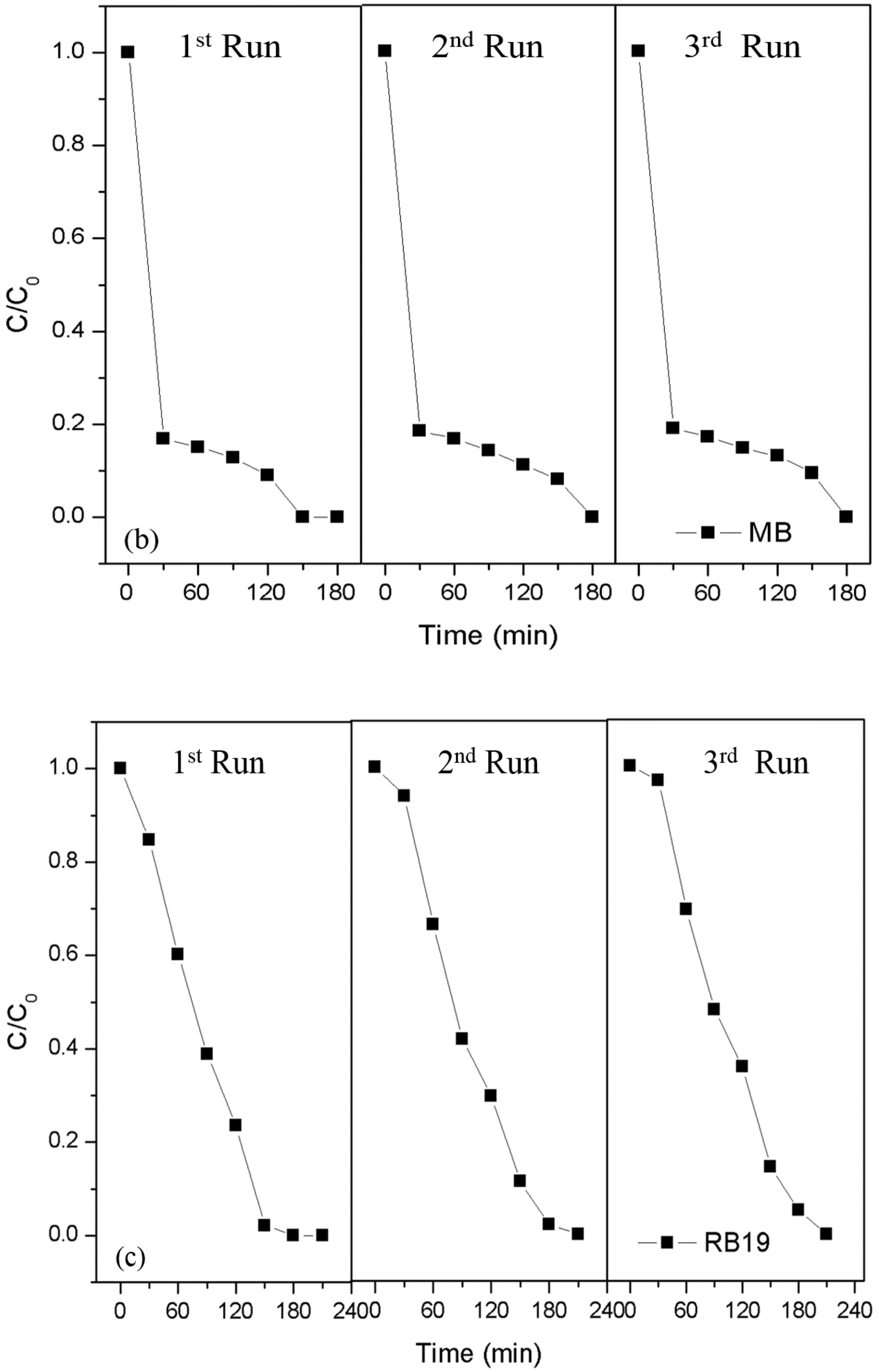

Figure 4.48: Stability analysis of prepared photocatalysts (a) BPA, (b) MB and (c) RB19

The kinetics of degradation best fitted the pseudo first-order reaction kinetics and the results are illustrated in Figure 4.49 (a-c) and the kinetics parameters are tabulated in Table 4.5. The degree of mineralization are depicted in Figure 4.50 (a) and (b).

Table 4.5: Kinetic parameters obtained on various pollutants degradation

	First Order Kinetics					
Sample	**MB**		**RB19**		**BPA**	
	k	**R^2**	**k**	**R^2**	**k**	**R^2**
TiO_2	0.0025	0.9959	0.0008	0.9990	0.0005	0.9949
RGO-TiO_2	0.0031	0.9495	0.0041	0.9701	0.0009	0.9880
RGO-Ag/TiO_2	0.0080	0.9611	0.0154	0.9990	0.0016	0.9936

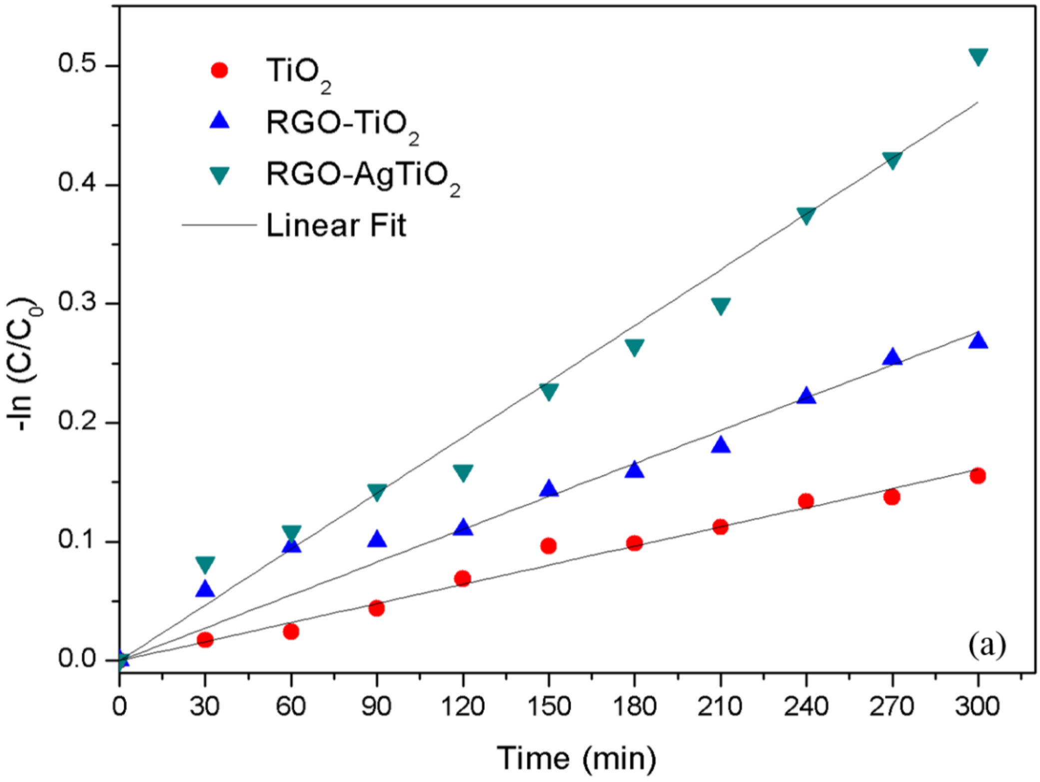

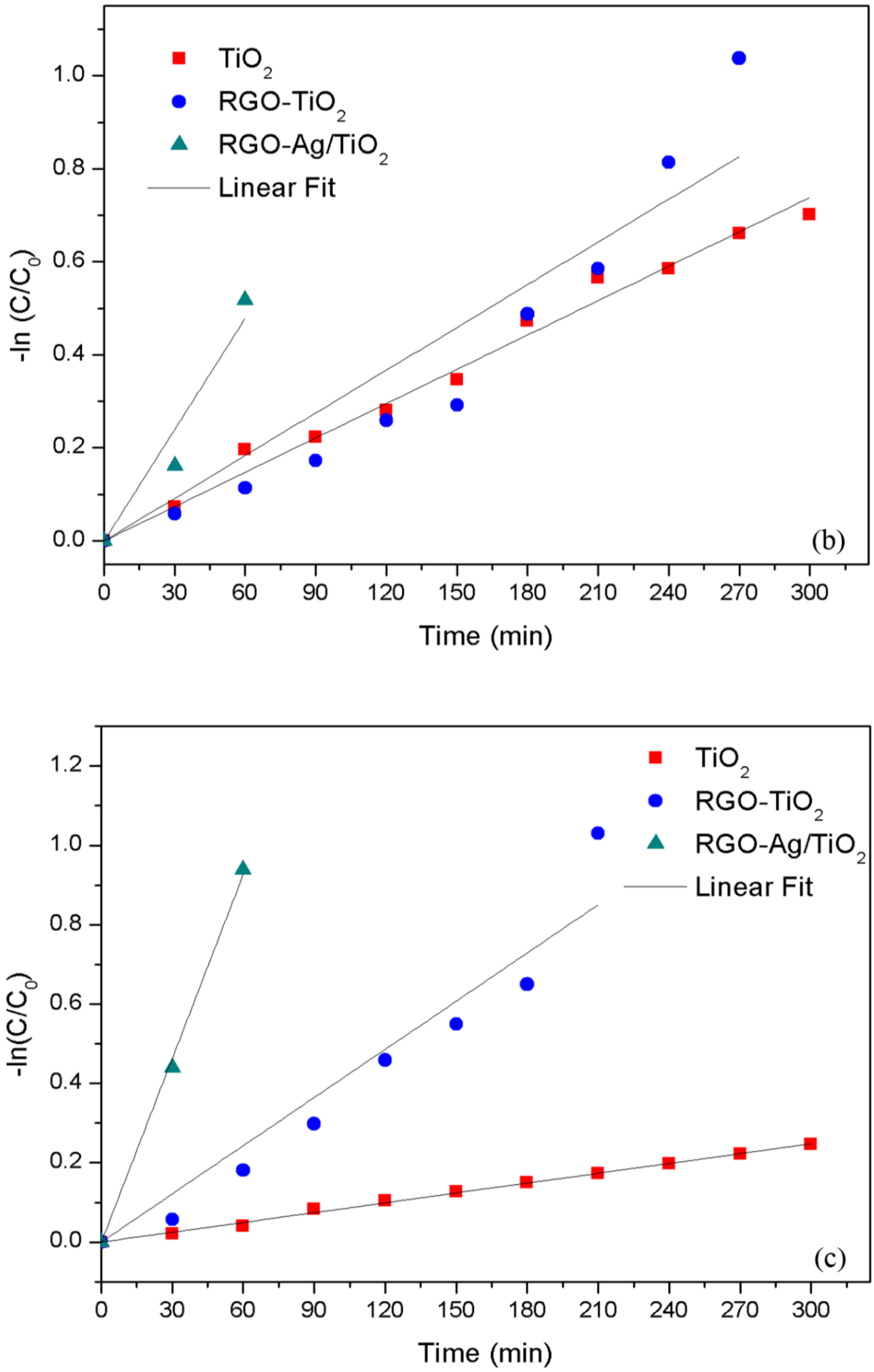

Figure 4.49: The kinetics of (a) BPA, (b) MB and (c) RB19

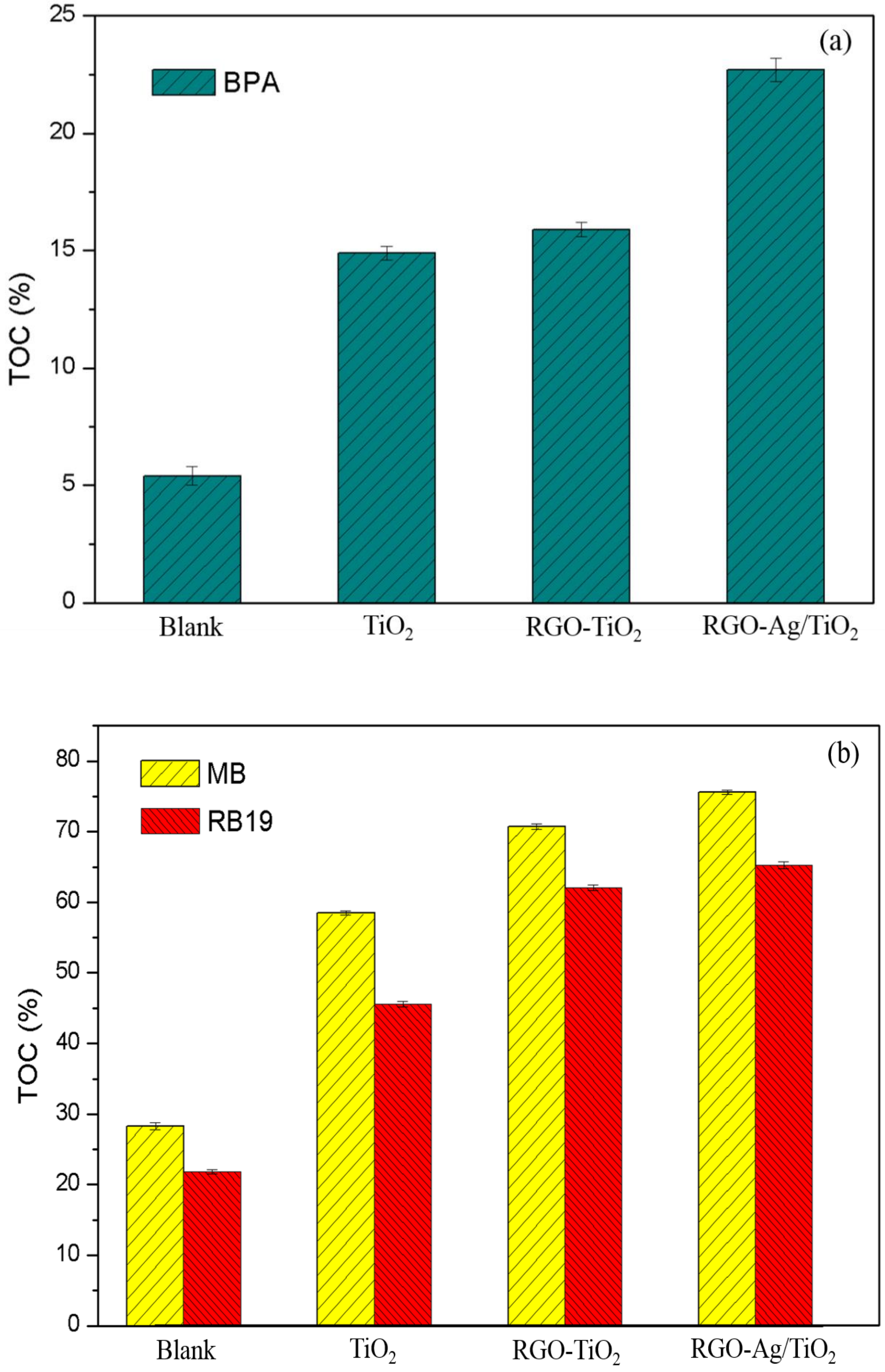

Figure 4.50: TOC removal quantification for (a) BPA and (b) Dyes

The synergisation of the Ag and RGO proved their candidature as a good visible light enhancer and also prolonged the life time of the charge carrier of TiO_2. The photocatalysis with varied pollutant also demonstrated the ability of the synergized composite. However a exploring the potential of a semiconductor carbon compound could of more interest and valued for the visible light enhancement. Hence the study was further extended by choosing one such semiconductor carbon compound, Graphitic Carbon Nitride (g-C_3N_4).

4.5 Graphitic Carbon Nitride Incorporate with Ag/TiO_2 Photocatalyst

The prepared novel (g-C_3N_4)-Ag/TiO_2 composite was analyzed for the phase composition and was presented in Figure 4.51. The presence of two peaks at $2\theta = 13.1°$ and 27.4° are attributed to the interlayer stacking of g-C_3N_4 that indexed as (0 0 1) and (0 0 2) respectively. The presences of Ag NPs are detected with the occurrence and are well supported with JCPDS no 04-0783. It is noted that no typical diffraction peaks of g-C_3N_4 appeared for composites due to the low amount of loading on the surface of the nanocomposite (Y. Chen et al., 2014). Figure 4.52 displayed the Raman spectrum that well correlated with XRD analysis proven the presence of anatase phase of the prepared TiO_2 and the respective peaks are denoted in the figure.

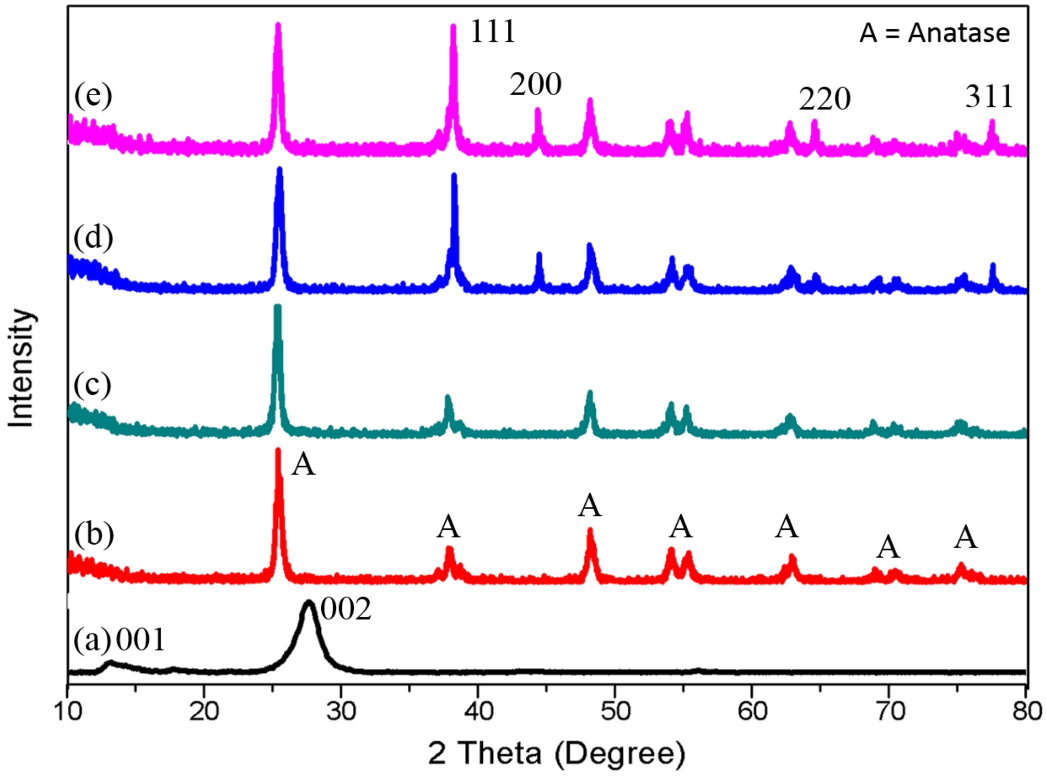

Figure 4.51: XRD pattern of (a) g-C_3N_4, (b) TiO_2, (c) (g-C_3N_4)-TiO_2, (d) Ag/TiO_2 and (e) (g-C_3N_4)-Ag/TiO_2

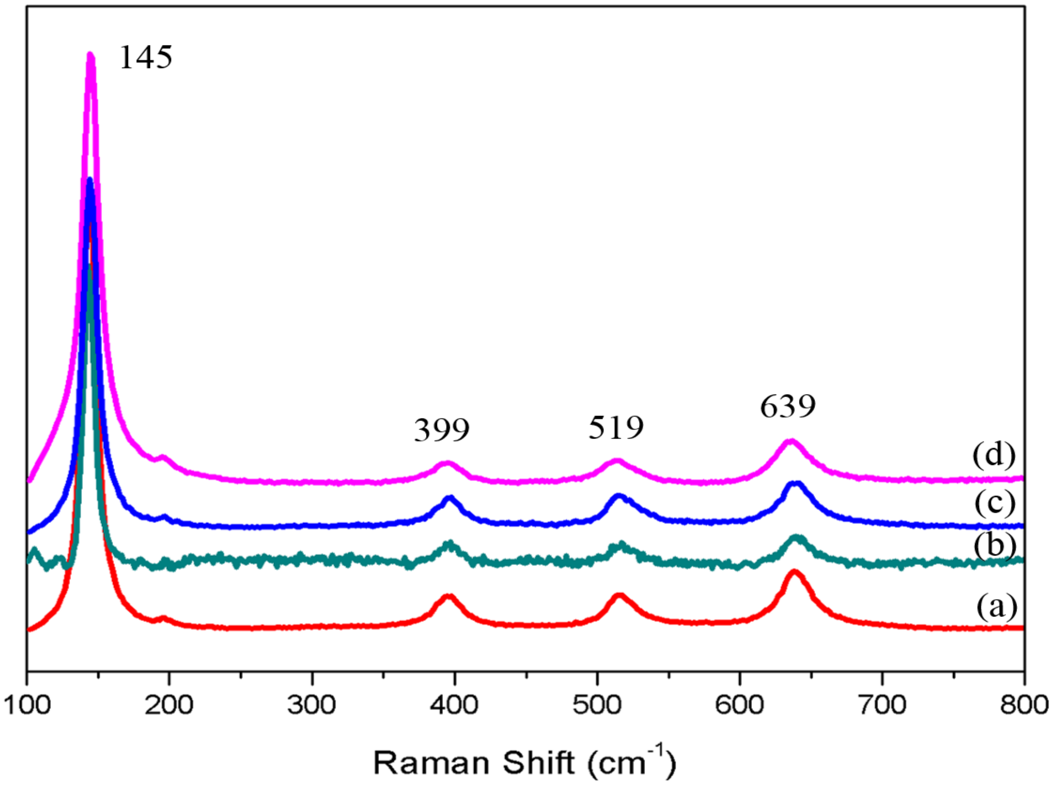

Figure 4.52: Raman spectra of (a) TiO_2, (b) (g-C_3N_4)-TiO_2, (c) Ag/TiO_2 and (d) (g-C_3N_4)-Ag/TiO_2

The morphology of the (g-C_3N_4)-Ag/TiO_2 was illustrated in Figure 4.53 (a-f). It is clearly seen that the g-C_3N_4 is well distributed onto the surface of Ag/TiO_2. The high resolution image of Figure 4.53 (d) clarified more uniform photodeposition of Ag NPs onto the surface of TiO_2 similar to our earlier findings. The average particles size of Ag NPs captured through HRTEM images are in range of 4 – 6 nm. Figure 4.53 (f) depicts the lattice fringes that denotes the presence of Ag NPs (0.24 nm) and TiO_2 (0.35 nm) in the prepared photocatalysts.

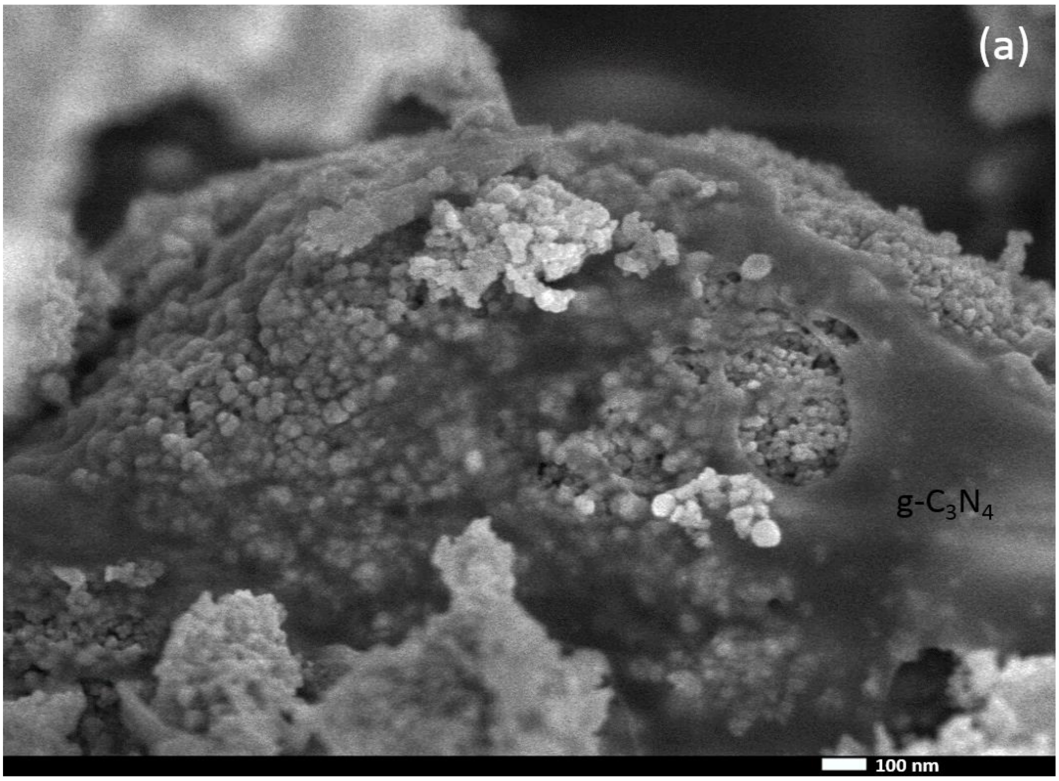

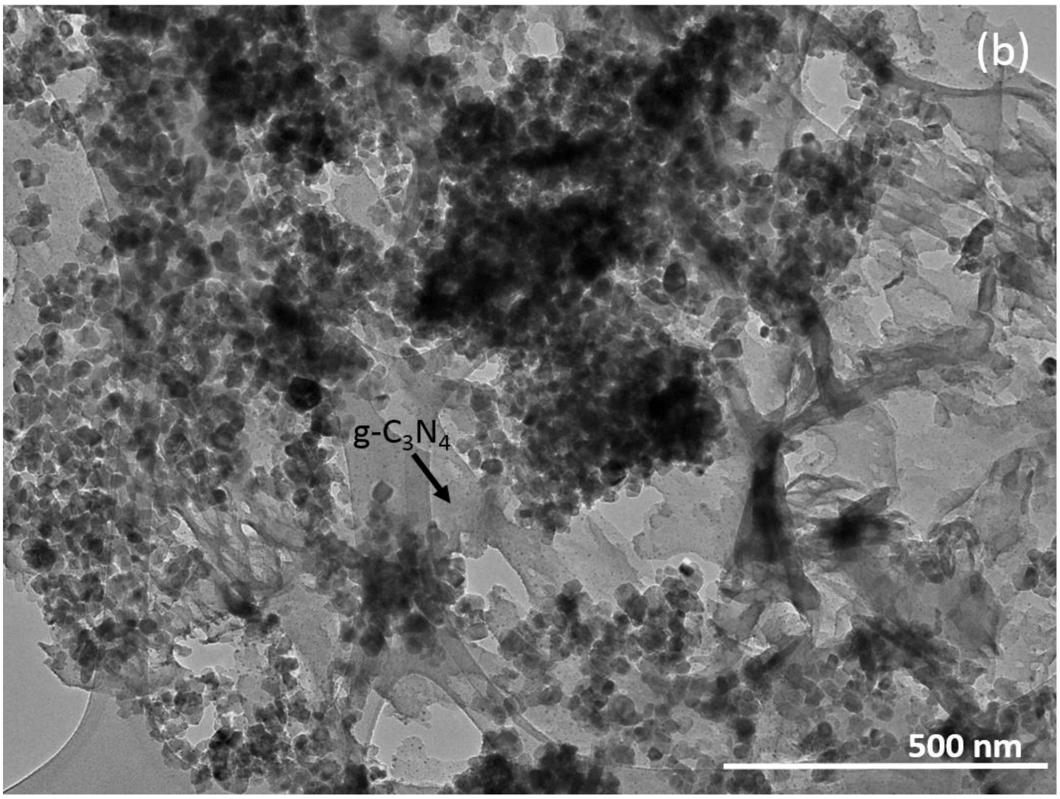
(b)
g-C3N4
500 nm

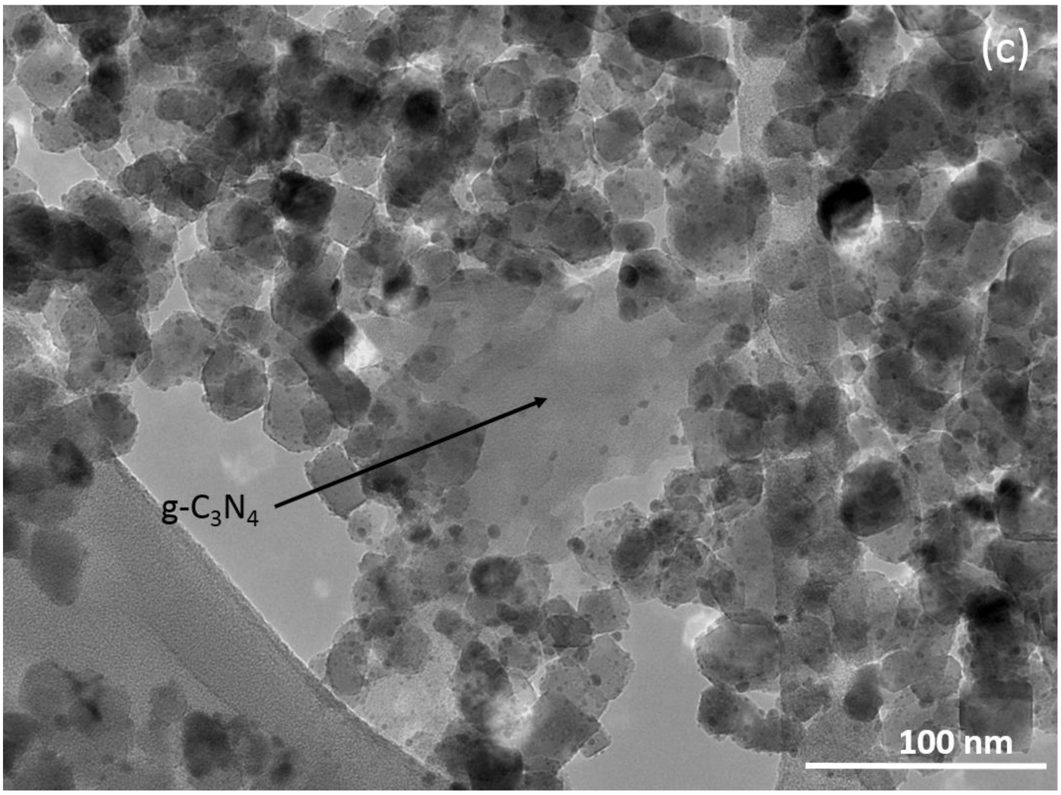
(c)
g-C3N4
100 nm

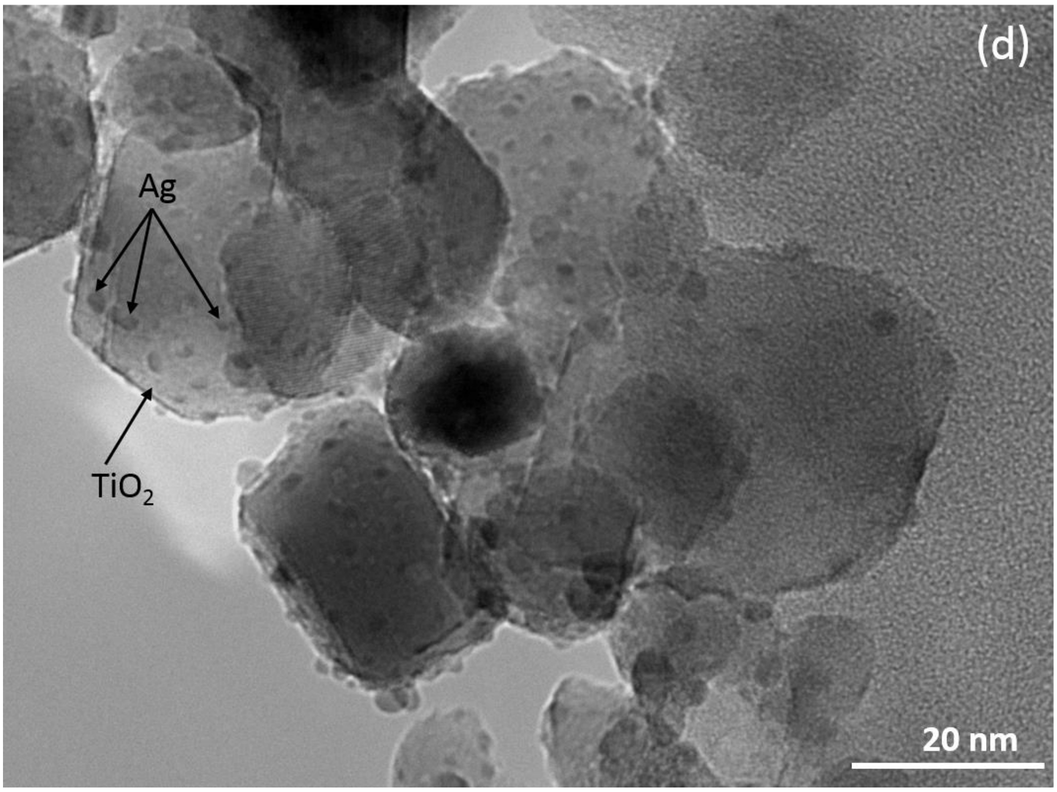
(d)
Ag
TiO2
20 nm

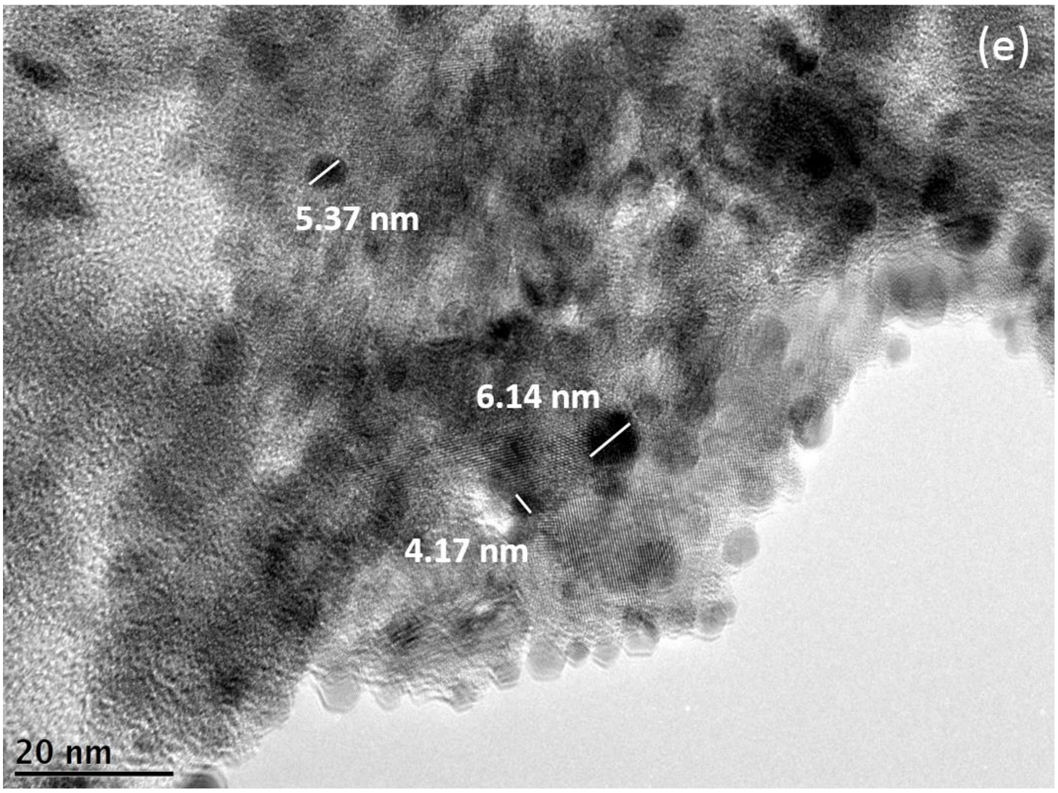
(e)
5.37 nm
6.14 nm
4.17 nm
20 nm

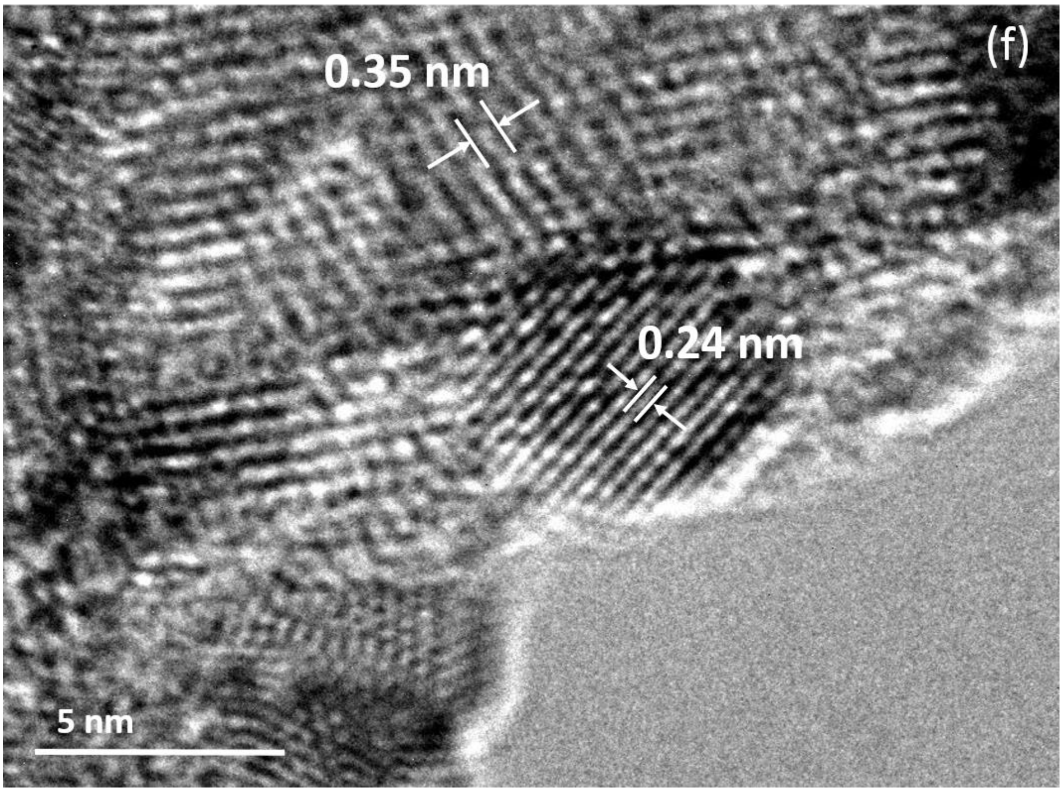

Figure 4.53: (a) FESEM image, (b-f) HRTEM images of (g-C_3N_4)-Ag/TiO_2

The functional group analyses of the prepared nanocomposites are illustrated in Figure 4.54. An intense band recorded at 1641, 1570, and 1410 cm^{-1} was assigned to the stretching vibration modes of aromatic C-N and proved the successful synthesis of g-C_3N_4 (J. Liu et al., 2011). The sharp band at 807 cm^{-1} is attributed to the out-of plane bending vibration characteristic of triazine units (J. Liu et al., 2011; Y. Chen et al., 2014). Meanwhile, the bands at 1320 and 1240 cm^{-1} are resembled to the stretching vibration of connected unit of C-N (-C)-C or C-NH-C. This is also well correlated with the stretching vibration of hydrogen bonding interaction with a broad band in-between 3100-3300 cm^{-1} (J. Liu et al., 2011). Where else a broad band at 3350 cm^{-1} represents the O-H group of water molecule. In addition, the presence of wide absorption band at 500-700 cm^{-1} is ascribed to the Ti-O-Ti bonding (Umrao et al., 2014; Yueli Liu et al., 2014). The Ag/TiO_2 also showed a similar absorption bands as that of TiO_2. The obtained spectrum successfully shown the key characteristic bands for g-C_3N_4 and TiO_2 appeared in the nanocomposites indicating the accomplishment of the synthesis route.

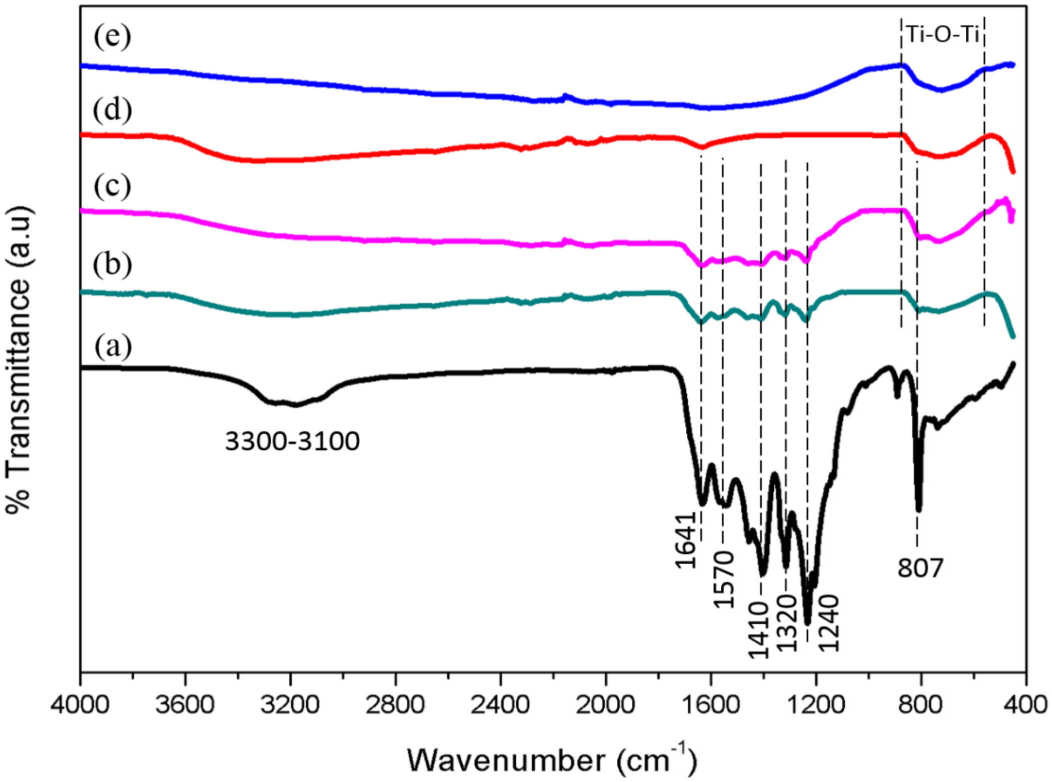

Figure 4.54: FTIR spectra of (a) g-C_3N_4, (b) (g-C_3N_4)-TiO_2, (c) (g-C_3N_4)-Ag/TiO_2, (d) TiO_2 and (e) Ag/TiO_2

Figure 4.55 explicates the X-ray photoelectron spectra that shows the surface chemical composition of each elements for the prepared (g-C_3N_4)-Ag/TiO_2 photocatalyst. The spectrum displayed all the basic elements of the nanocomposite. The C 1s spectrum displayed two distinct peaks located at 284.9 and 288.1 eV. These peaks are attributed to C-C coordination including the adventitious hydrocarbon and the sp^2 hybridized carbon atom existent from g-C_3N_4 nanosheets. While the peak at 288.1 eV is ascribed to N-C=N coordination. The N 1s spectrum displayed three peaks that ascribed to C=N-C at 398.6 eV, N-$(C)_3$ at 399.8 eV and C-N-H at 401.1 eV whereas the O 1s spectrum exhibited two peaks at 530.1 and 531.8 eV corresponds to Ti-O bond and O-H bond respectively. The occurrence of O-H bond was due to the presence of water molecule on the surface of (g-C_3N_4)-Ag/TiO_2. Furthermore, the Ti 2p spectrum also showed two distinct peaks at 458.9 eV (Ti $2p_{3/2}$) and 464.6 eV (Ti $2p_{1/2}$). As usual two typical peaks for Ag 3d was seen at 368.6 eV and 374.6 eV are ascribed to Ag $3d_{3/2}$ and Ag $3d_{5/2}$.

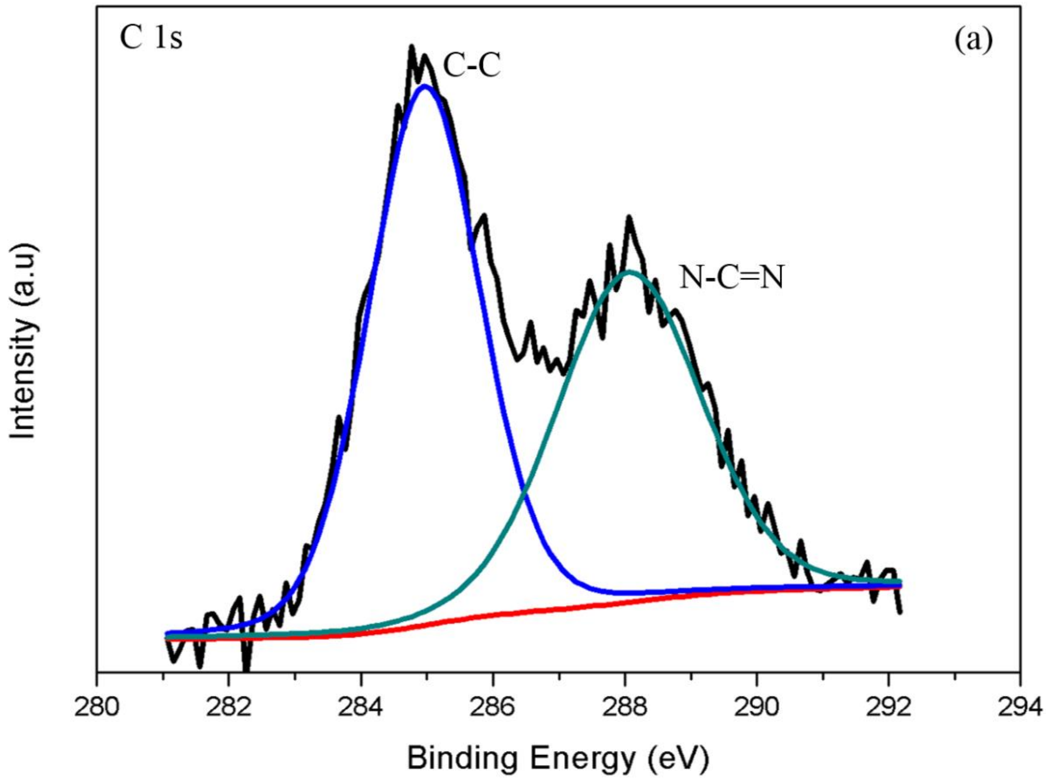

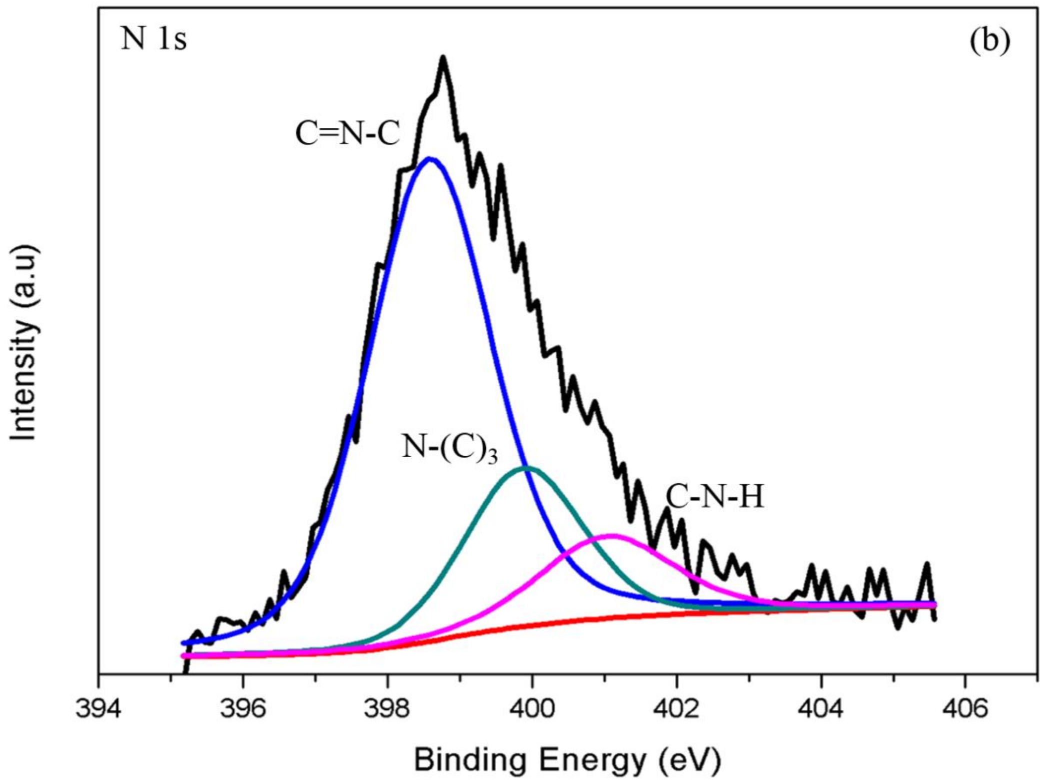
N 1s
(b)
C=N-C
N-(C)₃
C-N-H
Intensity (a.u)
394
396
398
400
402
404
406
Binding Energy (eV)

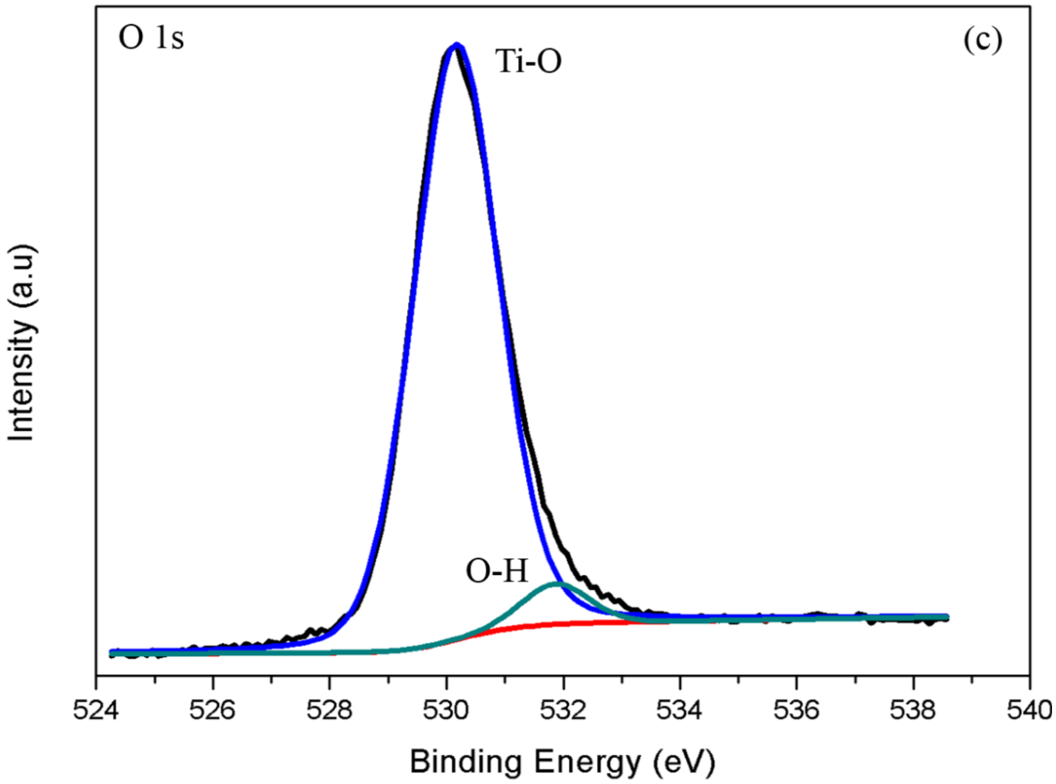
O 1s
(c)
Ti-O
O-H
Intensity (a.u)
524
526
528
530
532
534
536
538
540
Binding Energy (eV)

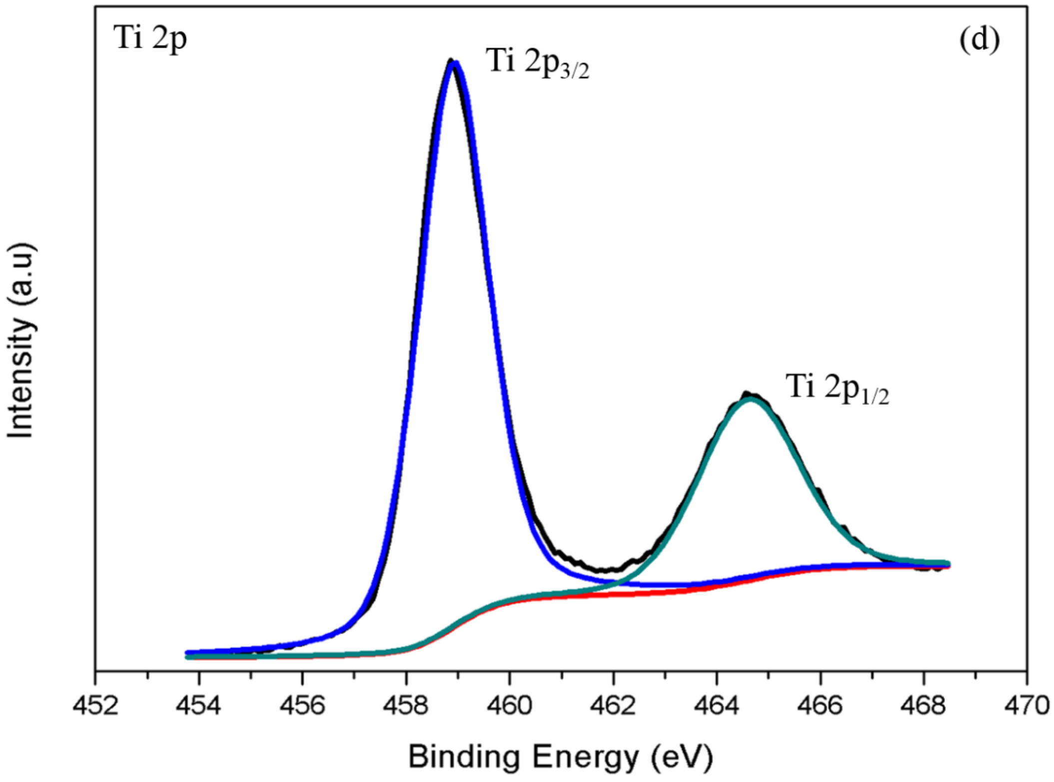

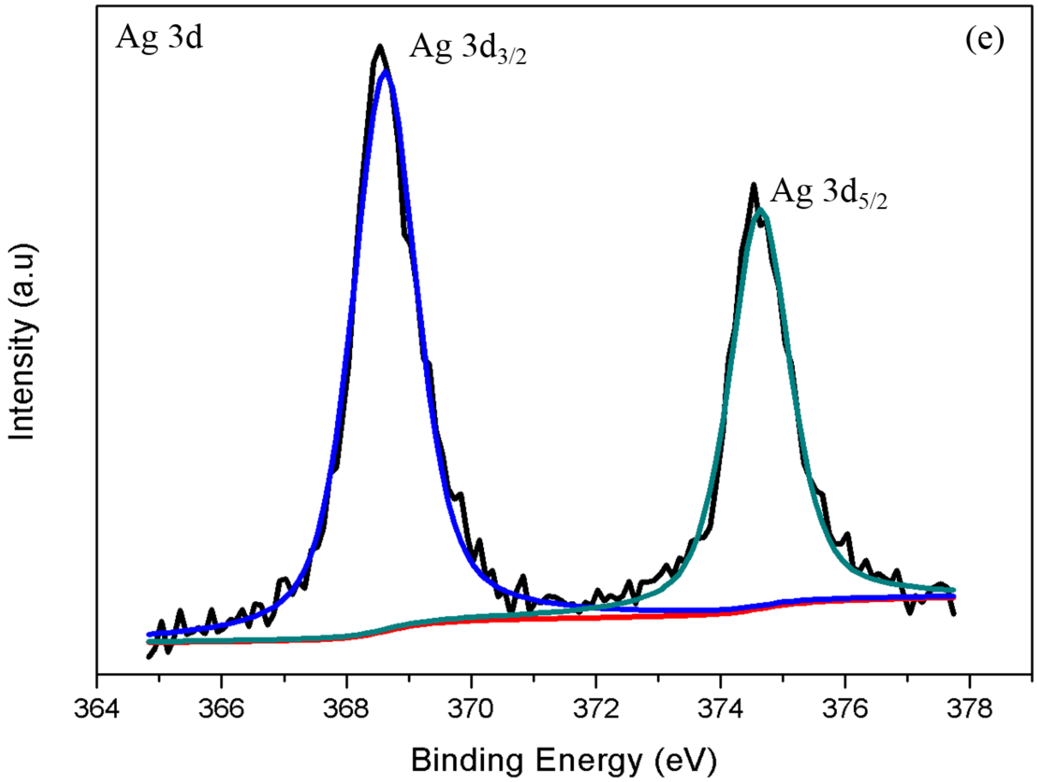

Figure 4.55: X-ray photoelectron spectra of (a) C 1s, (b) N 1s, (c) O 1s, (d) Ti 2p and (e) Ag 3d

The optical properties of the prepared photocatalysts are analysed using UV-vis diffuse reflectance spectroscopy. Figure 4.56 displayed the absorbance spectra of the (g-C_3N_4)-Ag/TiO_2, Ag/TiO_2 and (g-C_3N_4)-TiO_2 nanocomposite, together with those pure TiO_2 and g-C_3N_4. As proven in our previous studies, the absorption edge of pure TiO_2 only occurs at wavelength shorter than 390 nm. However, pure graphitic carbon nitride rises the absorption intensity edge to about 460 nm. Therefore by incorporating g-C_3N_4 onto the surface of TiO_2 drastically increased the absorption intensity in-between 390-460 nm and shifted the absorption edge to 460 nm.

Thus the g-C_3N_4 greatly improved the absorption ability of TiO_2 in the visible light region. In addition the incorporation of noble metal (Ag) onto the surface of TiO_2 also enhanced the absorption ability in the visible spectrum. The absorption curve of ternary composite (g-C_3N_4)-Ag/TiO_2 displayed a distinct shift towards the visible light spectrum as compared to the rest. The band gap energies of the prepared photocatalysts were estimated through Kubelka-Munk equation and the obtained band gap calculation is depicted in Figure 4.57 (a-e). The TiO_2 resulted with well-known band gap energy 3.2 eV where else the g-C_3N_4 with 2.7 eV. The chosen composite very well contributed for tuning of band gap and was narrowed to 3.0, 3.1 and 2.5 eV for (g-C_3N_4)-TiO_2, Ag/TiO_2 and (g-C_3N_4)-Ag/TiO_2 respectively.

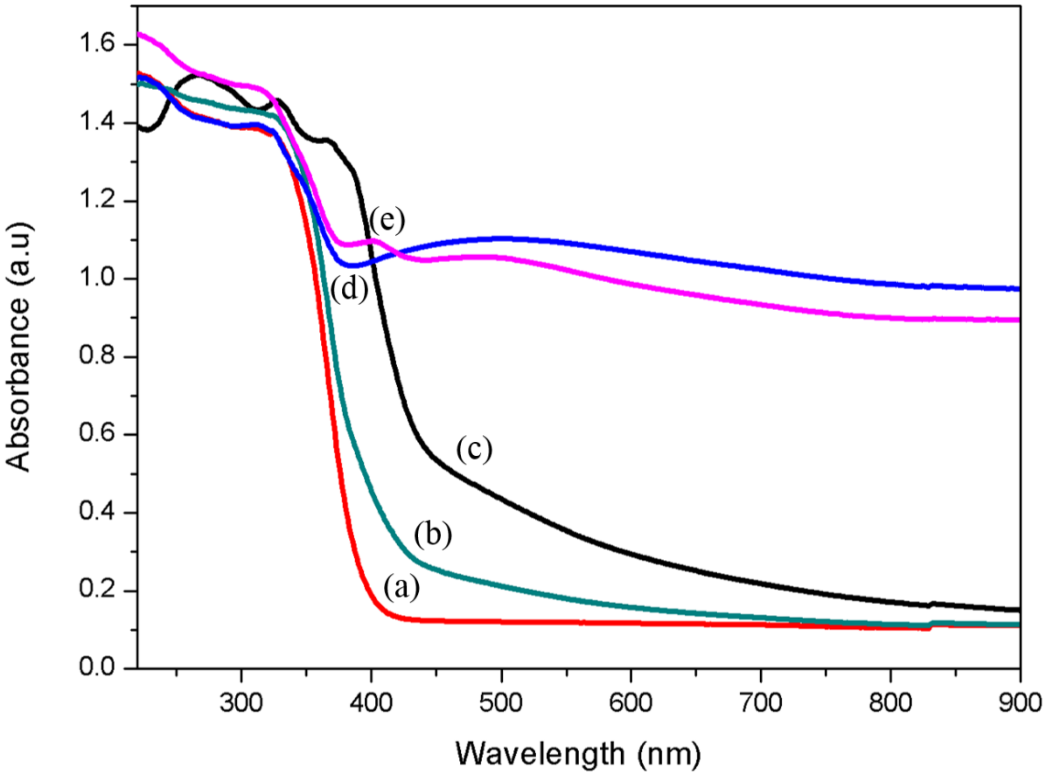

Figure 4.56: UV-vis absorption spectra of (a) TiO_2, (b) (g-C_3N_4)-TiO_2, (c) g-C_3N_4, (d) Ag/TiO_2 and (e) (g-C_3N_4)-Ag/TiO_2

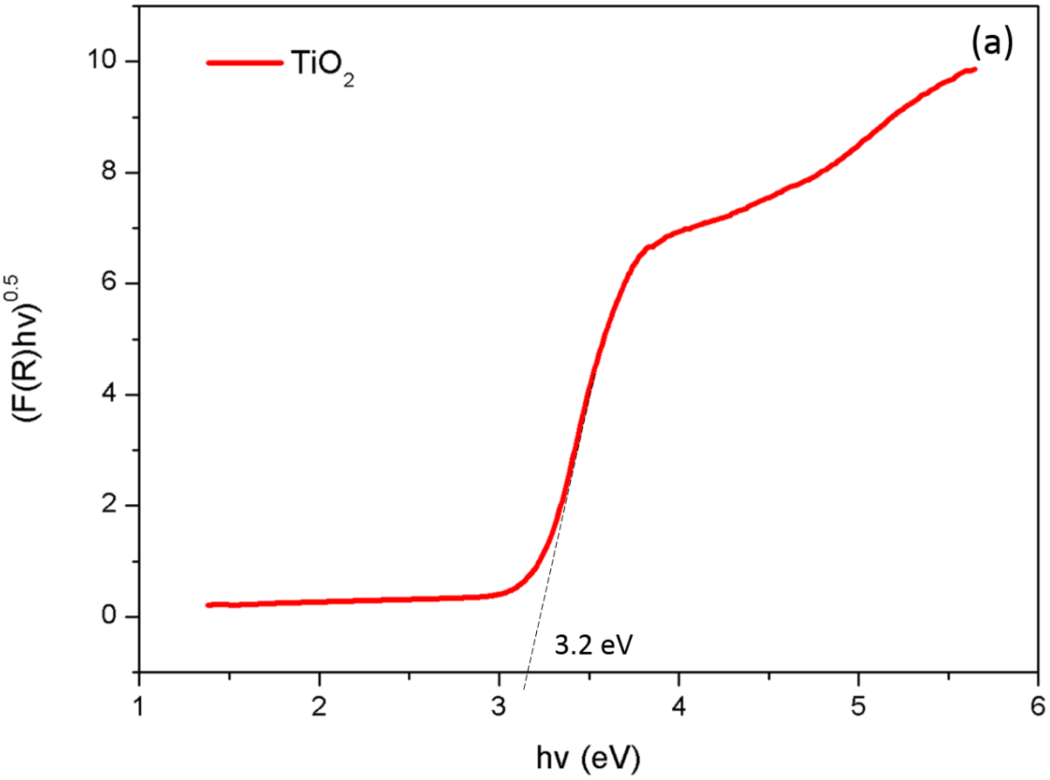

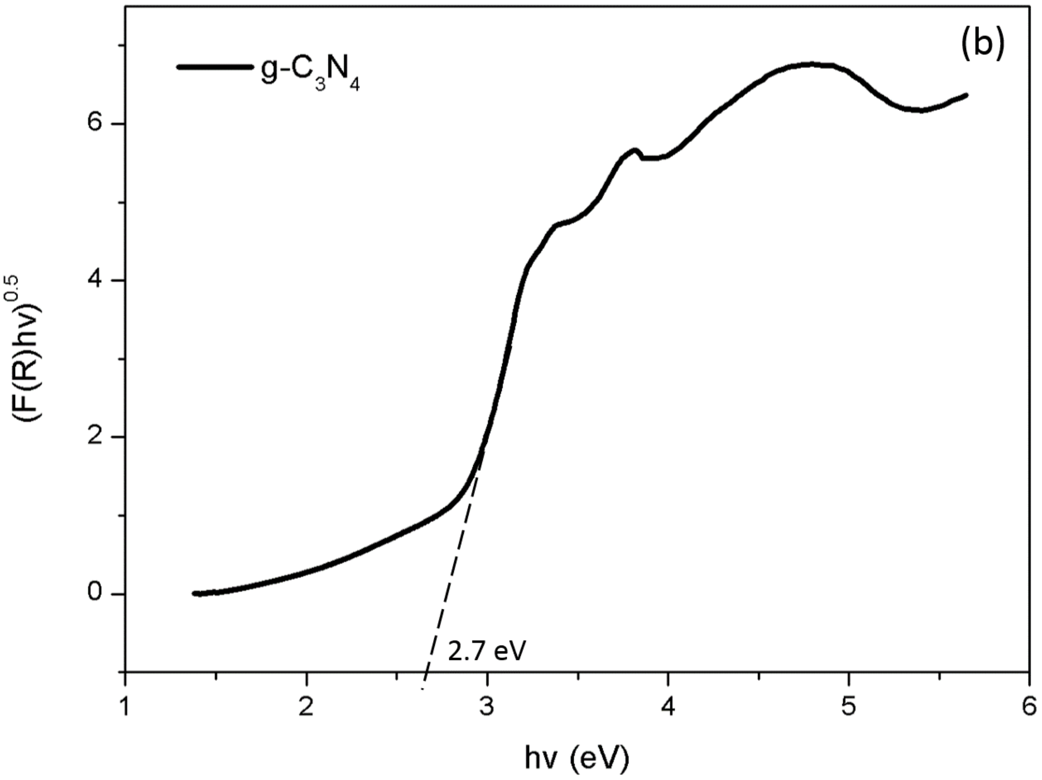
(b)
g-C3N4
(F(R)hv)^0.5
6
4
2
0
2.7 eV
1
2
3
4
5
6
hv (eV)

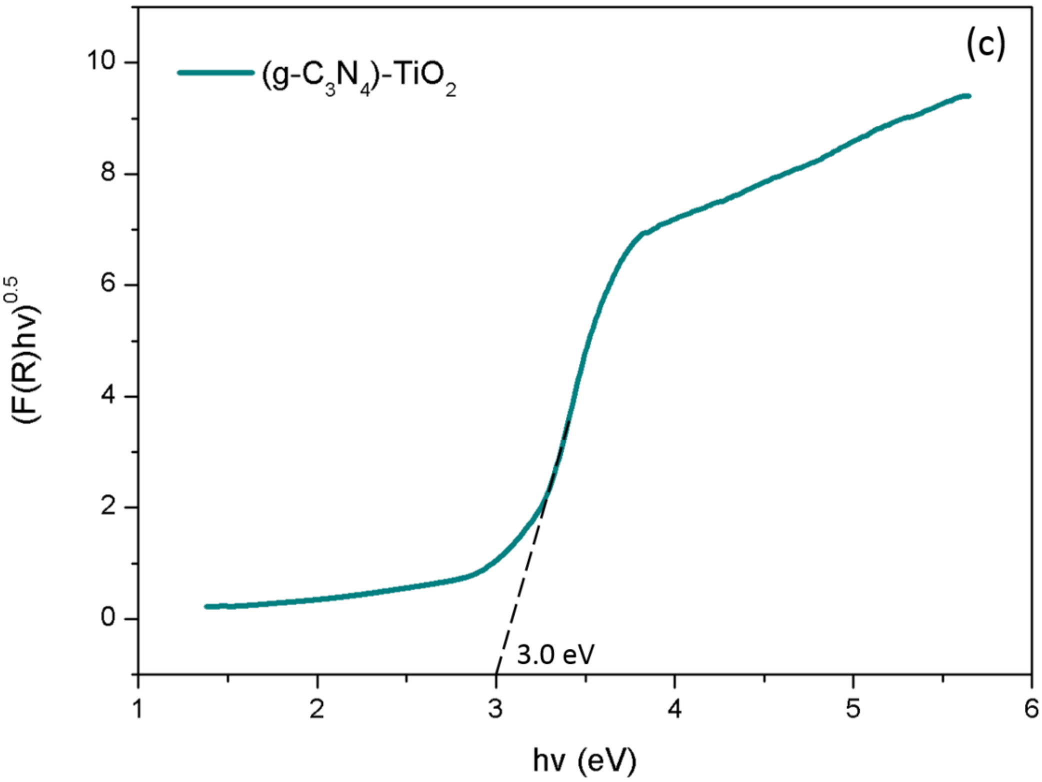
(c)
(g-C3N4)-TiO2
(F(R)hv)^0.5
10
8
6
4
2
0
3.0 eV
1
2
3
4
5
6
hv (eV)

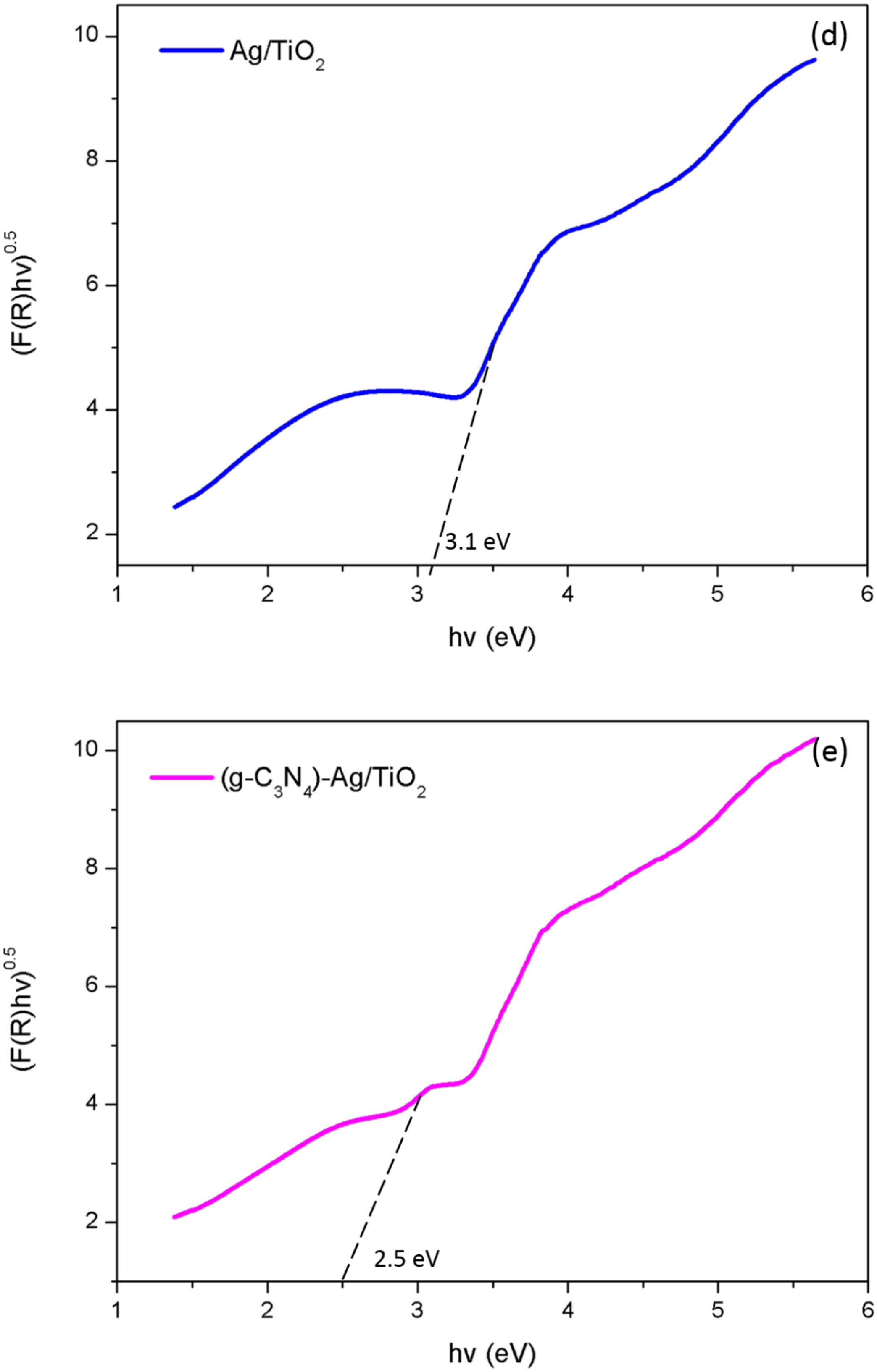

Figure 4.57: Calculated band gap energy of (a) TiO_2, (b) g-C_3N_4, (c) (g-C_3N_4)-TiO_2, (d) Ag/TiO_2 and (e) (g-C_3N_4)-Ag/TiO_2

Figure 4.58, portraits the life time of the charge carries. The g-C_3N_4 demonstrated a rapid recombination of charge carriers as compared to the rest by showing the highest light emission after the absorption of illuminated photons. However the phenomenon drastically reduced after incorporating g-C_3N_4 with TiO_2.The g-C_3N_4 prolonged the lifespan of the electron by allowing the electrons to be transferred from g-C_3N_4 to the conduction band of TiO_2. In comparison, the photoluminescence intensities of Ag/TiO_2 and (g-C_3N_4)-Ag/TiO_2 are lower than that of the pure TiO_2 indicates the good separation of charge carriers in Ag/TiO_2 and (g-C_3N_4)-Ag/TiO_2. The Photoluminescence results clearly demonstrated the formation of heterostructure between (g-C_3N_4) and Ag/TiO_2. The heterojunction allows the electron transferring from g-C_3N_4 to Ag NPs and then finally being transported to the conduction band of TiO_2 for potential redox reactions. Thus formed heterostructure blocked the recombination of electrons and holes and prolonged the lifetime.

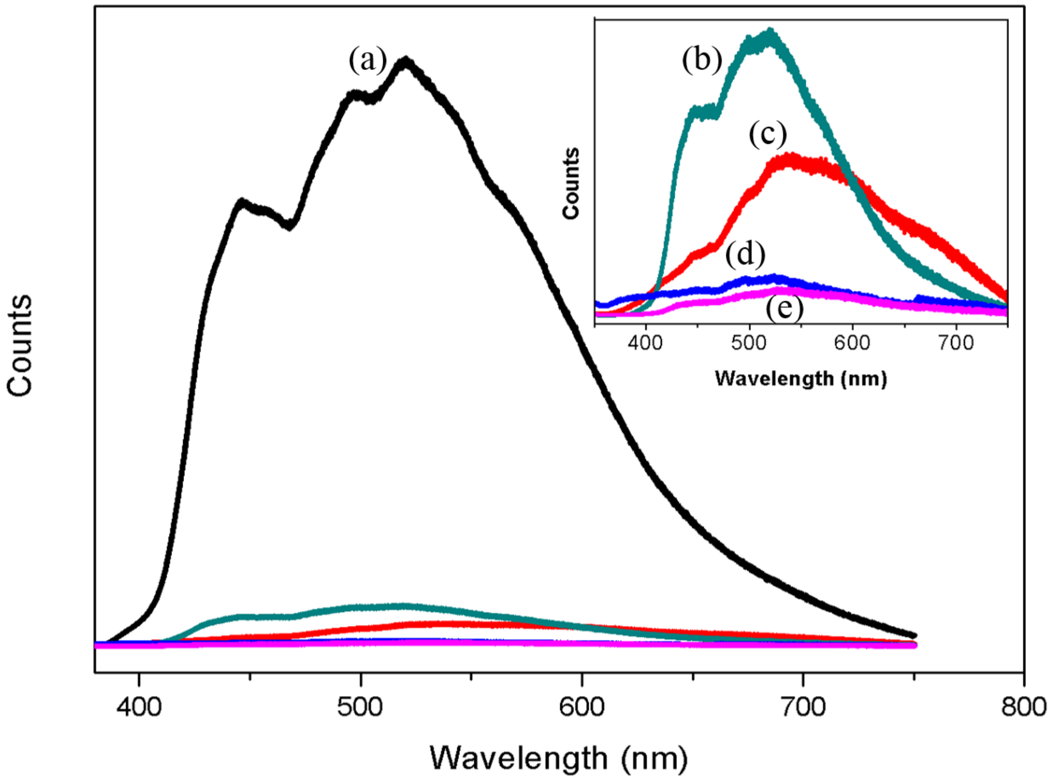

Figure 4.58: Photoluminescence spectra of (a) g-C_3N_4, (b) (g-C_3N_4)-TiO_2, (c) TiO_2, (d) Ag/TiO_2 and (e) (g-C_3N_4)-Ag/TiO_2

The visible light photocatalysis ability was evaluated by adopting AMX and well known endocrine disrupting compound. The photocatalytic degradation profile of the AMX with aid of prepared photocatalysts is illustrated in Figure 4.59. The degradation followed an order of (g-C_3N_4)-Ag/TiO_2 (73.4%) > Ag/TiO_2 (56.2%) > (g-C_3N_4)-TiO_2 (38.9%) > g-C_3N_4 (35.1%) > TiO_2 (22.7%).

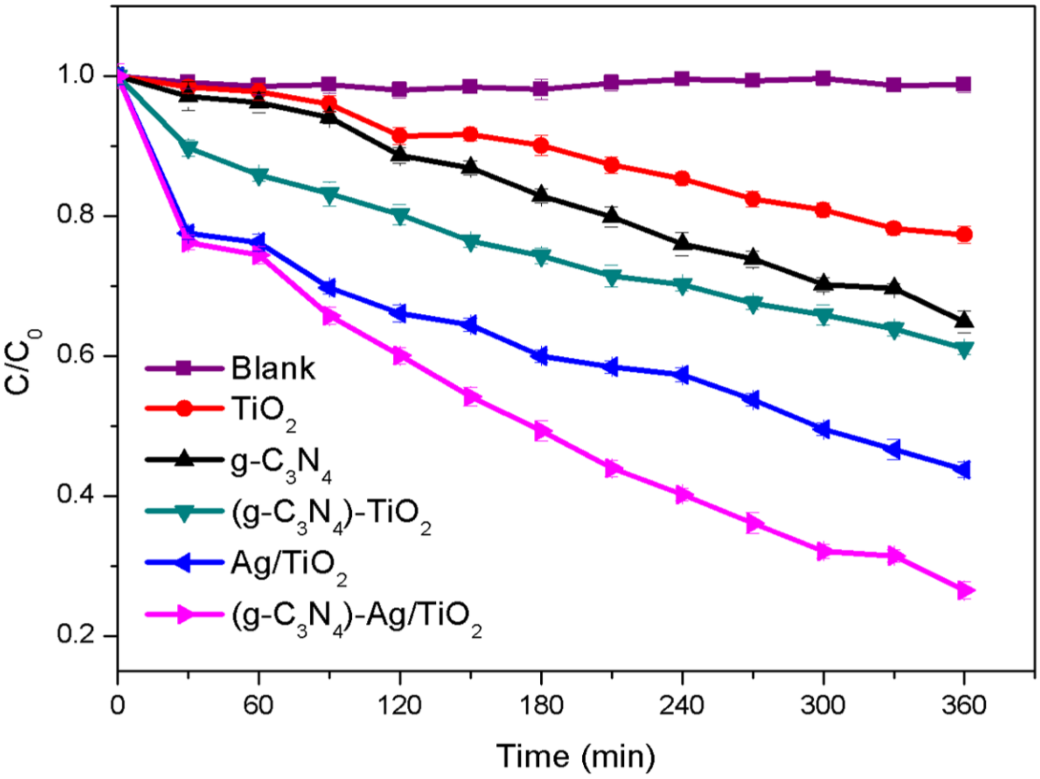

Figure 4.59: Artificial visible light photocatalysis performance of prepared photocatalysts

As expected a poor photodegradation efficiency was exhibited by TiO_2 owing to non-visible light sensitive. While wrapping of g-C_3N_4 with TiO_2 showed an increase in photodegradation efficiency 1.7 times than TiO_2. This was attributed to the characteristics of g-C_3N_4 which stimulated the visible light absorption. Further a remarkable increase of photocatalytic degradation by 3.2 times than TiO_2 was successfully achieved for (g-C_3N_4)-Ag/TiO_2. With further additional of Ag NPs to the (g-C_3N_4)-TiO_2 triggered the visible light absorption characteristics through an intrinsic surface plasmon resonance and also extended the separation time of charge carriers.

From the obtained materials chemistry and photodegradation profile the mechanism behind the prepared ternary photocatalyst is metaphorized in Figure 4.60. The edge potential of CB and VB of a semiconductor can be estimated based on the following equations:

$$E_{VB} = \chi - E^{e} + 0.5\,E_{g} \tag{4.5}$$

$$E_{CB} = E_{VB} - E_{g} \tag{4.6}$$

where E_{VB} and E_{CB} is the valence band and conduction band edge potential respectively, χ is the electronegativity of the semiconductor; E^{e} is the energy of free electrons on the hydrogen scale (about 4.5 eV vs NHE) and E_g is the band gap energy of the semiconductor. The electronegativity of g-C_3N_4 and TiO_2 are 4.64 and 5.81 eV respectively (Y. Chen et al., 2014).

Based on the calculation, the CB and VB edge potential of g-C_3N_4 were at -1.21 and 1.49 eV respectively. Meanwhile for TiO_2, the CB was found to be -0.29 eV and the VB was 2.91 eV. During the visible light illumination, g-C_3N_4 dominates TiO_2 owing to its tendency to absorb visible light and produces electrons and holes. The prevailing negative edge potential of g-C_3N_4 (-1.21 eV) allows the photogenerated electrons to be transferred to the lower negative edge potential of CB of TiO_2 (-0.29 eV). It is well-known that the redox potential of $O_2/{}^{\bullet}O_2^-$ (-0.33 eV) is more negative than the CB of TiO_2 (-0.29 eV) and hence the transferred electrons in the CB of TiO_2 are not favourable to reduce the O_2. Instead, these electrons can reduce O_2 to H_2O_2 (O_2/H_2O_2 is 0.695 eV) and the formed H_2O_2 would further transformed into ${}^{\bullet}OH$ by capturing an electron. Meanwhile, the holes in the VB of g-C_3N_4 can directly oxidise the AMX, but not the OH^- to generate

$^{\bullet}$OH radicals due to lower positive potential of VB of g-C_3N_4 (1.49 eV) against standard redox potential of $^{\bullet}$OH/OH$^-$ (1.99 eV). In the ternary composite the presence of Ag NPs onto the surface of TiO_2 played a key role as an electron-conduction bridge. This enabled a notable electron-holes separation in g-C_3N_4 and also enhanced the electron transfer towards TiO_2 through Schottky barrier between Ag and TiO_2. Therefore the excited electrons from g-C_3N_4 directly migrate to Ag/TiO_2. Thus it retarded the recombination of electron and holes pairs and promoted more promising photodegradation efficiency. The formation of Schottky barrier between Ag and TiO_2 occurs due to the higher Fermi level (E_f) of TiO_2 than Ag. The formation hinders the transfer of electrons from Ag to TiO_2. However, the barrier was shattered and the transfer was possible due to strong electron oscillating on the LSPR excitation and leads to the interband excitation. Thus, it triggers the energetic electron to be transfer to the TiO_2 conduction band. Moreover the LSPR effect of Ag NPs also significantly contributed for the visible light absorption of the ternary. The presence of visible light excites the electrons below the Fermi level of Ag NPs to the surface plasmon states. Thus, this excitation contributed to the high generation of energetic electrons. These electrons migrates to TiO_2 which then reduce the O_2 to H_2O_2 and further transformed into $^{\bullet}$OH radicals. This aggressive formation of electrons contributed to the better photocatalytic performance.

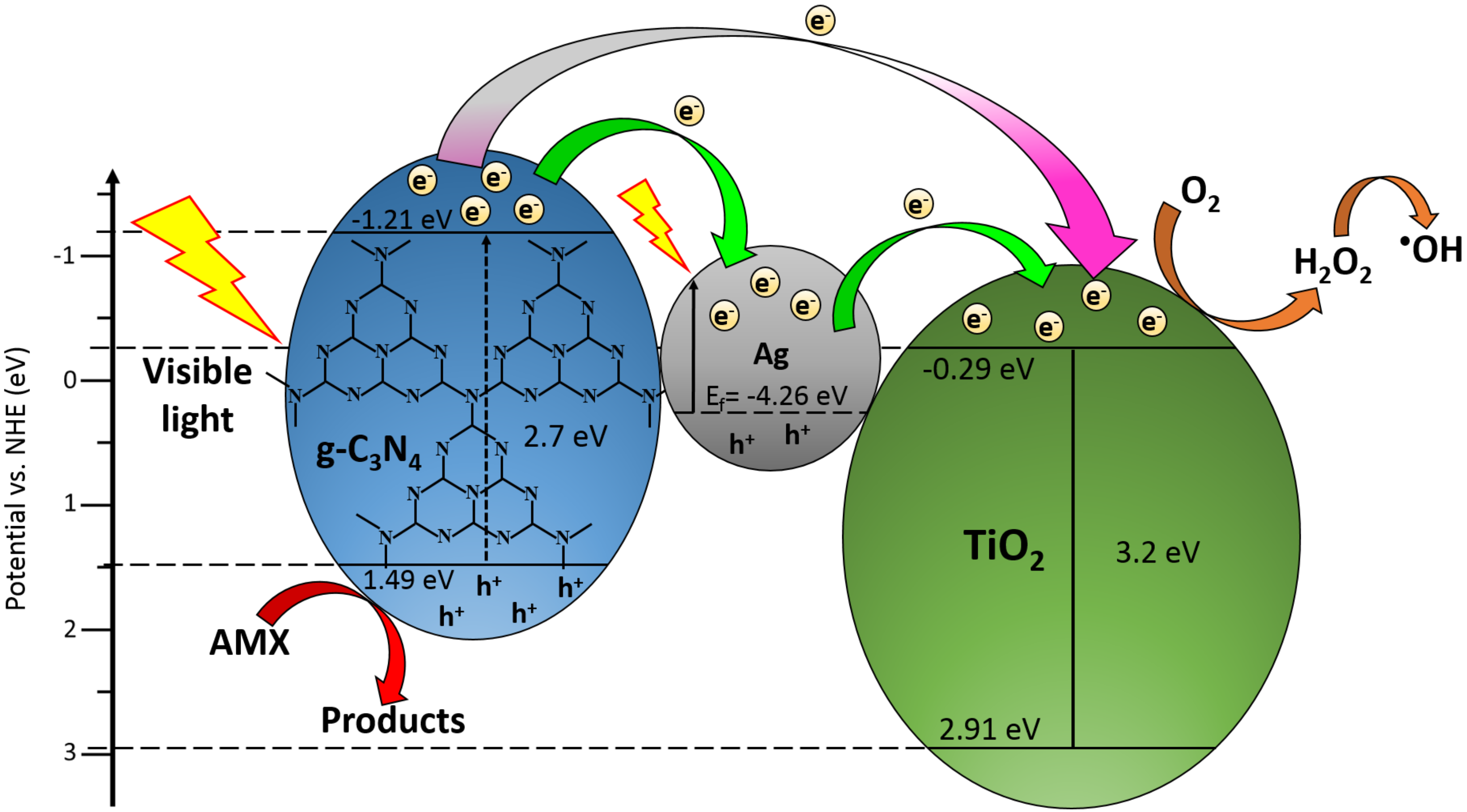

Figure 4.60: Schematic diagram of photocatalytic mechanism of (g-C_3N_4)-Ag/TiO_2

The kinetics of the photocatalytic activities well fitted with pseudo first-order reaction kinetics and the results are depicted in Figure 4.61 and Table 4.6. The recyclability experiments were performed and depicted in Figure 4.62. The photocatalysis of (g-C_3N_4)-Ag/TiO_2 for AMX declined marginally after three cycles. However the photocatalytic efficiency was not much affected.

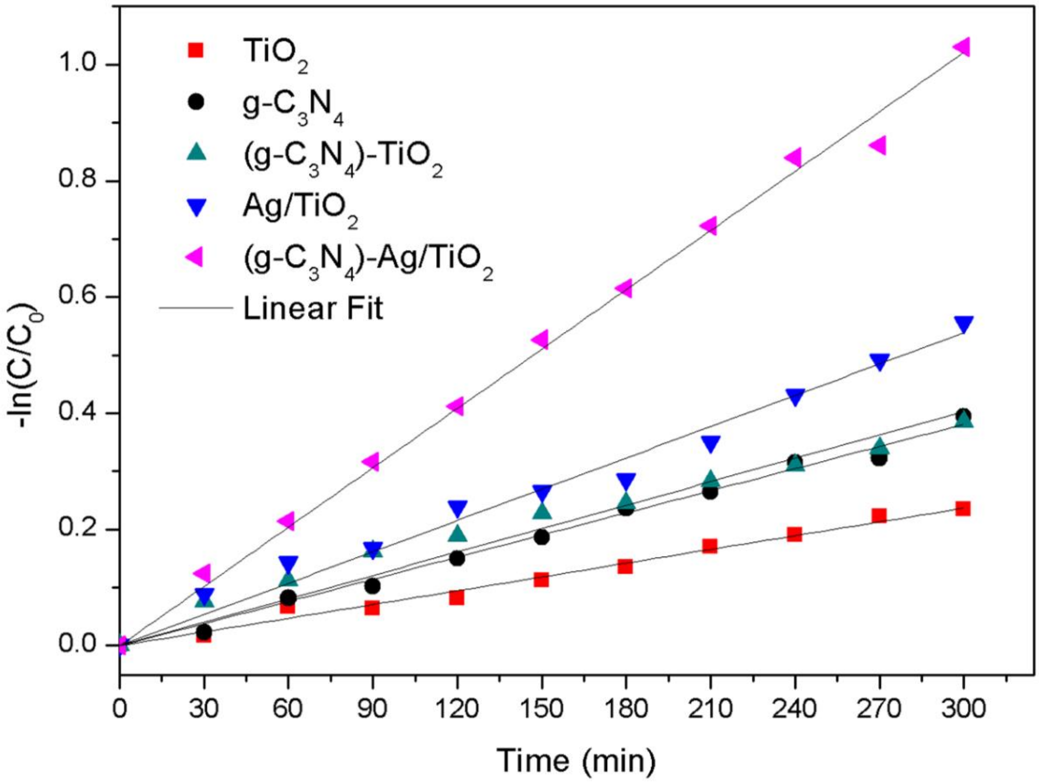

Figure 4.61: The kinetics fitting for AMX degradation

Table 4.6: Obtained kinetic parameters for prepared photocatalysts

	First Order Kinetics				
	TiO_2	**g-C_3N_4**	**(g-C_3N_4)-TiO_2**	**Ag/TiO_2**	**(g-C_3N_4)-Ag/TiO_2**
R^2	0.9958	0.9976	0.9888	0.9946	0.9986
k	0.00078	0.00127	0.00134	0.00180	0.00340

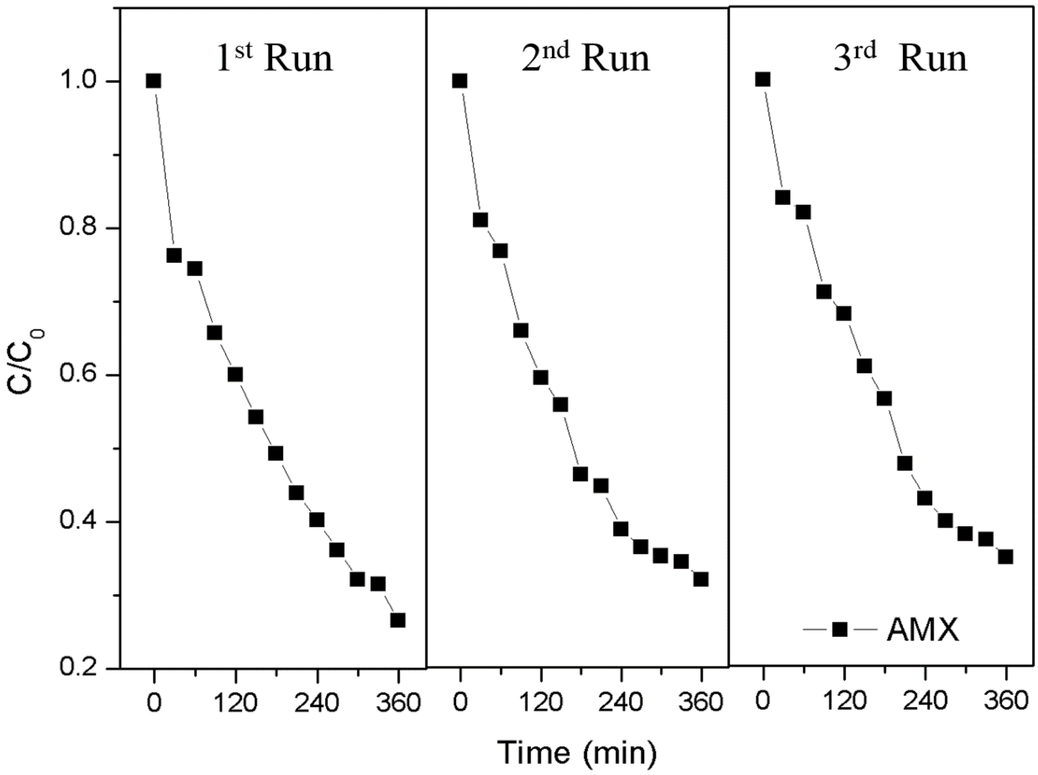

Figure 4.62: Stability analysis of prepared photocatalysts for AMX degradation

Overall entire present thesis showed the contribution of the chosen composites for enhancing the visible light utilization and prolonging the charge carriers of the conventional TiO_2. Also the prepared composite photocatalysts well proved the candidature for visible light photocatalysis.

CHAPTER 5

CONCLUSIONS AND RECOMMENDATIONS

5.1 Conclusions

The foremost aim of the thesis was to modify and tune the band gap of conventional TiO_2 that is readily activated through photons generated by the visible light. The foresaid objective was successfully achieved by synthesizing binary and ternary composite with the aid of noble metal and carbon conducting materials. The conclusions for the adopted objectives of the present thesis are as follows:

- The template TiO_2 was successfully achieved with controlled particles size. The calcination step encouraged the photocatalytic performance and shown comparatively better activity by destructing 2, 4-DCP illuminated under solar irradiation.

- The fabrications of heterogeneous plasmonic photocatalysts (Pd/TiO_2 & Ag/TiO_2) were successfully synthesised through smart, ease and sustainable approach.

- The maximize usage of natural sunlight well supported for the reduction and anchoring of studied noble metals onto the TiO_2 yielding classification photocatalysts called “Plasmonic photocatalysts” with enhanced visible light utilisation.

- The formations of localized surface plasmon resonance and Schottky barrier evidently triggered the enhancement of harvesting visible light and prolonged the lifetime of the charge carriers with an excellent photocatalytic performance.

- The exfoliation of RGO also well promoted the visible light utilisation through stable Ti-O-C bond. It also eased the electron mobilisation that significantly enhance the transport of charge carrier and further extend duration of charge carriers.
- The deployment of Graphitic Carbon Nitride (g-C_3N_4) a unique semiconductor organic compound, drastically surged the visible light absorption intensity, narrowed the band gap energy and shifted the absorption edge to higher wavelength than RGO.
- The proposed photocatalysis mechanisms revealed the unique behaviour expressed by the each element for the visible light enhancement and charge carriers suppression.
- The accomplishment of both noble metals and conducting carbon materials in modified conventional titania contributed for a robust visible light photocatalysis and was well demonstrated through adopted pollutants.

5.2 Recommendations

The following recommendations are to be considered or future research works.

- A scale up study followed by a pilot with the help of a proper reactor could demonstrate real time applications and industrial feasibility.
- The influence of the photons on the degradation could be modelled and simulated by understanding the light interaction on the photocatalyst.

- The quantity of hydroxyl radicals ($^{\bullet}OH$) could be quantitatively analyzed for additional information on the surface reactions that pave a pathway for an efficient modelling.

.

References

Abdelsayed, V., Moussa, S., Hassan, H. M., Aluri, H. S., Collinson, M. M., & El-Shall, M. S. (2010). Photothermal deoxygenation of graphite oxide with laser excitation in solution and graphene-aided increase in water temperature. *The Journal of Physical Chemistry Letters*, *1(19*), 2804-2809.

Ahn, Y. U., Kim, E. J., Kim, H. T., & Hahn, S. H. (2003). Variation of structural and optical properties of sol-gel TiO_2 thin films with catalyst concentration and calcination temperature. *Materials Letters, 57(30)*, 4660-4666.

Akhavan, O., & Ghaderi, E. (2009). Photocatalytic reduction of graphene oxide nanosheets on TiO_2 thin film for photoinactivation of bacteria in solar light irradiation. *The Journal of Physical Chemistry C, 113(47),* 20214-20220.

Almquist, C. B., & Biswas, P. (2002). Role of Synthesis Method and Particle Size of Nanostructured TiO_2 on Its Photoactivity. *Journal of Catalysis, 212(2),* 145-156.

An, C., Peng, S., & Sun, Y. (2010). Facile Synthesis of Sunlight-Driven AgCl: Ag Plasmonic Nanophotocatalyst. *Advanced Materials*, 22(23), 2570-2574.

Anastas, P. T., Kirchhoff, M. M., & Williamson, T. C. (2001). Catalysis as a foundational pillar of green chemistry. *Applied Catalysis A: General, 221(1),* 3-13.

Aziz, A. A., Cheng, C. K., Ibrahim, S., Matheswaran, M., & Saravanan, P. (2012). Visible light improved, photocatalytic activity of magnetically separable titania nanocomposite. *Chemical Engineering Journal, 183,* 349-356.

Aziz, A. A., Puma, G. L., Ibrahim, S., & Saravanan, P. (2013). Preparation, characterisation and solar photoactivity of titania supported strontium ferrite nanocomposite photocatalyst. *Journal of Experimental Nanoscience, 8(3),* 295-310.

Aziz, A. A., Yong, K. S., Ibrahim, S., & Pichiah, S. (2012). Enhanced magnetic separation and photocatalytic activity of nitrogen doped titania photocatalyst supported on strontium ferrite. *Journal of Hazardous Materials, 199*, 143-150.

Bai, H., Li, C., & Shi, G. (2011). Functional composite materials based on chemically converted graphene. *Advanced Materials, 23(9),* 1089-1115.

Barakat, M., Schaeffer, H., Hayes, G., & Ismat-Shah, S. (2005). Photocatalytic degradation of 2-chlorophenol by Co-doped TiO_2 nanoparticles. *Applied Catalysis B: Environmental, 57(1),* 23-30.

Baur, W. (1961). Atomabstande und Bindungswinkel im Brookit, TiO_2. *Acta Crystallographica, 14(3),* 214-216.

Bayarri, B., Gimenez, J., Curco, D., & Esplugas, S. (2005). Photocatalytic degradation of 2, 4-dichlorophenol by TiO_2/UV: Kinetics, actinometries and models. *Catalysis Today, 101(3),* 227-236.

Behnajady, M. A., & Modirshahla, N. (2006). Nonlinear regression analysis of kinetics of the photocatalytic decolorization of an azo dye in aqueous TiO_2 slurry. *Photochemical & Photobiological Sciences, 5(11),* 1078-1081.

Bhunia, S. K., & Jana, N. R. (2014). Reduced Graphene Oxide-Silver Nanoparticle Composite as Visible Light Photocatalyst for Degradation of Colorless Endocrine Disruptors. *ACS Applied Materials & Interfaces, 6(22),* 20085-20092.

Boltasseva, A., & Atwater, H. A. (2011). Low-loss plasmonic metamaterials. *Science, 331*, 290-291.

Bumajdad, A., & Madkour, M. (2014). Understanding the superior photocatalytic activity of noble metals modified titania under UV and visible light irradiation. *Physical Chemistry Chemical Physics, 16(16),* 7146-7158.

Burgeth, G., & Kisch, H. (2002). Photocatalytic and photoelectrochemical properties of titania–chloroplatinate (IV). *Coordination Chemistry Reviews, 230(1),* 41-47.

Carp, O., Huisman, C. L., & Reller, A. (2004). Photoinduced reactivity of titanium dioxide. *Progress in Solid State Chemistry, 32(1),* 33-177.

Chan, C.-C., Chang, C.-C., Hsu, W.-C., Wang, S.-K., & Lin, J. (2009). Photocatalytic activities of Pd-loaded mesoporous TiO_2 thin films. *Chemical Engineering Journal, 152(2),* 492-497.

Chen, D., Chen, Q., Ge, L., Yin, L., Fan, B., Wang, H., . . . Shao, G. (2013). Synthesis and Ag-loading-density-dependent photocatalytic activity of Ag@TiO_2 hybrid nanocrystals. *Applied Surface Science, 284,* 921-929.

Chen, F., Zou, W., Qu, W., & Zhang, J. (2009). Photocatalytic performance of a visible light TiO2 photocatalyst prepared by a surface chemical modification process. *Catalysis Communications, 10(11)*, 1510-1513.

Chen, J., Yao, M., & Wang, X. (2008). Investigation of transition metal ion doping behaviors on TiO_2 nanoparticles. *Journal of Nanoparticle Research, 10(1),* 163-171.

Chen, S. F., Li, J. P., Qian, K., Xu, W. P., Lu, Y., Huang, W. X., & Yu, S. H. (2010). Large scale photochemical synthesis of M@TiO_2 nanocomposites (M= Ag, Pd, Au, Pt) and their optical properties, CO oxidation performance, and antibacterial effect. *Nano Research, 3(4)*, 244-255.

Chen, X., Wu, G., Chen, J., Chen, X., Xie, Z., & Wang, X. (2011). Synthesis of "clean" and well-dispersive Pd nanoparticles with excellent electrocatalytic property on graphene oxide. *Journal of the American Chemical Society, 133(11)*, 3693-3695.

Chen, Y., Huang, W., He, D., Situ, Y., & Huang, H. (2014). Construction of heterostructured g-C_3N_4/Ag/TiO_2 microspheres with enhanced photocatalysis performance under visible-light irradiation. *ACS Applied Materials & Interfaces, 6(16)*, 14405-14414.

Chen, Z., Fang, L., Dong, W., Zheng, F., Shen, M., & Wang, J. (2014). Inverse opal structured Ag/TiO_2 plasmonic photocatalyst prepared by pulsed current deposition and its enhanced visible light photocatalytic activity. *Journal of Materials Chemistry A, 2(3)*, 824-832.

Cheng, H., Huang, B., Wang, P., Wang, Z., Lou, Z., Wang, J., . . . Dai, Y. (2011). In situ ion exchange synthesis of the novel Ag/AgBr/BiOBr hybrid with highly efficient decontamination of pollutants. *Chem. Commun., 47(25),* 7054-7056.

Cheng, H., Ma, J., Zhao, Z., & Qi, L. (1995). Hydrothermal preparation of uniform nanosize rutile and anatase particles. *Chemistry of Materials, 7(4)*, 663-671.

Cheng, H., Wang, W., Huang, B., Wang, Z., Zhan, J., Qin, X., . . . Dai, Y. (2013). Tailoring AgI nanoparticles for the assembly of AgI/BiOI hierarchical hybrids with size-dependent photocatalytic activities. *Journal of Materials Chemistry A, 1(24),* 7131-7136.

Cheng, N., Tian, J., Liu, Q., Ge, C., Qusti, A. H., Asiri, A. M., . . . Sun, X. (2013). Au-nanoparticle-loaded graphitic carbon nitride nanosheets: green photocatalytic synthesis and application toward the degradation of organic pollutants. *ACS Applied Materials & Interfaces, 5(15)*, 6815-6819.

Choi, M., Shin, K.-H., & Jang, J. (2010). Plasmonic photocatalytic system using silver chloride/silver nanostructures under visible light. *Journal of Colloid and Interface Science, 341(1),* 83-87.

Choi, W., Termin, A., & Hoffmann, M. R. (1994). The role of metal ion dopants in quantum-sized TiO_2: correlation between photoreactivity and charge carrier recombination dynamics. *The Journal of Physical Chemistry, 98(51),* 13669-13679.

Chong, M. N., Jin, B., Chow, C. W., & Saint, C. (2010). Recent developments in photocatalytic water treatment technology: a review. *Water Research, 44(10),* 2997-3027.

Christopher, P., Ingram, D. B., & Linic, S. (2010). Enhancing photochemical activity of semiconductor nanoparticles with optically active Ag nanostructures: photochemistry mediated by Ag surface plasmons. *The Journal of Physical Chemistry C, 114(19),* 9173-9177.

Christopher, P., Xin, H., & Linic, S. (2011). Visible-light-enhanced catalytic oxidation reactions on plasmonic silver nanostructures. *Nature Chemistry, 3(6),* 467-472.

Clavero, C. (2014). Plasmon-induced hot-electron generation at nanoparticle/metal-oxide interfaces for photovoltaic and photocatalytic devices. *Nature Photonics, 8(2),* 95-103.

Cromer, D. T., & Herrington, K. (1955). The structures of anatase and rutile. *Journal of the American Chemical Society, 77(18),* 4708-4709.

Cushing, S. K., Li, J., Meng, F., Senty, T. R., Suri, S., Zhi, M., . . . Wu, N. (2012). Photocatalytic activity enhanced by plasmonic resonant energy transfer from metal to semiconductor. *Journal of the American Chemical Society, 134(36),* 15033-15041.

Das, S., & Ghosh, S. (2013). Fabrication of different morphologies of ZnO superstructures in presence of synthesized ethylammonium nitrate (EAN) ionic liquid: synthesis, characterization and analysis. *Dalton Transactions, 42(5),* 1645-1656.

Ding, Z., Lu, G., & Greenfield, P. (2000). Role of the crystallite phase of TiO_2 in heterogeneous photocatalysis for phenol oxidation in water. *The Journal of Physical Chemistry B, 104(19),* 4815-4820.

Djerdj, I., Arčon, D., Jagličić, Z., & Niederberger, M. (2008). Nonaqueous synthesis of metal oxide nanoparticles: short review and doped titanium dioxide as case study for the preparation of transition metal-doped oxide nanoparticles. *Journal of Solid State Chemistry, 181(7),* 1571-1581.

Dolat, D., Quici, N., Kusiak-Nejman, E., Morawski, A., & Li Puma, G. (2012). One-step, hydrothermal synthesis of nitrogen, carbon co-doped titanium dioxide (N, $CTiO_2$) photocatalysts. Effect of alcohol degree and chain length as carbon dopant precursors on photocatalytic activity and catalyst deactivation. *Applied Catalysis B: Environmental, 115,* 81-89.

Dong, F., Wang, H., & Wu, Z. (2009). One-step "green" synthetic approach for mesoporous C-doped titanium dioxide with efficient visible light photocatalytic activity. *The Journal of Physical Chemistry C, 113(38),* 16717-16723.

Doong, R.-A., Chen, C.-H., Maithreepala, R., & Chang, S.-M. (2001). The influence of pH and cadmium sulfide on the photocatalytic degradation of 2-chlorophenol in titanium dioxide suspensions. *Water Research, 35(12),* 2873-2880.

Fu, Y., & Wang, X. (2011). Magnetically separable $ZnFe_2O_4$–graphene catalyst and its high photocatalytic performance under visible light irradiation. *Industrial & Engineering Chemistry Research, 50(12),* 7210-7218.

Fujishima, A., & Honda, K. (1972). Photolysis-decomposition of water at the surface of an irradiated semiconductor. *Nature, 238(5385),* 37-38.

Galian, R., & Pérez-Prieto, J. (2010). Catalytic processes activated by light. *Energy & Environmental Science, 3(10),* 1488-1498.

Gao, X., Jang, J., & Nagase, S. (2009). Hydrazine and thermal reduction of graphene oxide: reaction mechanisms, product structures, and reaction design. *The Journal of Physical Chemistry C, 114(2),* 832-842.

Garcia, M. (2011). Surface plasmons in metallic nanoparticles: fundamentals and applications. *Journal of Physics D: Applied Physics, 44(28),* 283001.

Gomes Silva, C. u., Juárez, R., Marino, T., Molinari, R., & García, H. (2010). Influence of excitation wavelength (UV or visible light) on the photocatalytic activity of titania containing gold nanoparticles for the generation of hydrogen or oxygen from water. *Journal of the American Chemical Society, 133(3),* 595-602.

Grabowska, E., Zaleska, A., Sorgues, S., Kunst, M., Etcheberry, A., Colbeau-Justin, C., & Remita, H. (2013). Modification of titanium (IV) dioxide with small silver nanoparticles: application in photocatalysis. *The Journal of Physical Chemistry C, 117(4),* 1955-1962.

Grätzel, M. (2001). Photoelectrochemical cells. *Nature, 414(6861),* 338-344.

Guin, D., Manorama, S. V., Latha, J. N. L., & Singh, S. (2007). Photoreduction of silver on bare and colloidal TiO_2 nanoparticles/nanotubes: synthesis, characterization, and tested for antibacterial outcome. *The Journal of Physical Chemistry C, 111(36),* 13393-13397.

Han, D., Li, Y., & Jia, W. (2010). Preparation and characterization of molecularly imprinted SiO_2-TiO_2 and photo-catalysis for 2, 4-dichlorophenol. *Advance Material Letter, 1(3),* 188-192.

Han, L., Wang, P., Zhu, C., Zhai, Y., & Dong, S. (2011). Facile solvothermal synthesis of cube-like Ag@AgCl: a highly efficient visible light photocatalyst. *Nanoscale, 3(7),* 2931-2935.

Haruta, M. (2005). Catalysis: gold rush. *Nature, 437(7062),* 1098-1099.

Hench, L. L., & West, J. K. (1990). The sol-gel process. *Chemical Reviews, 90(1),* 33-72.

Hines, M. A., & Guyot-Sionnest, P. (1996). Synthesis and characterization of strongly luminescing ZnS-capped CdSe nanocrystals. *The Journal of Physical Chemistry, 100(2),* 468-471.

Hoffmann, M. R., Martin, S. T., Choi, W., & Bahnemann, D. W. (1995). Environmental applications of semiconductor photocatalysis. *Chemical Reviews, 95(1),* 69-96.

Hou, W., Hung, W. H., Pavaskar, P., Goeppert, A., Aykol, M., & Cronin, S. B. (2011). Photocatalytic conversion of CO_2 to hydrocarbon fuels via plasmon-enhanced absorption and metallic interband transitions. *ACS Catalysis, 1(8),* 929-936.

Hou, W., Liu, Z., Pavaskar, P., Hung, W. H., & Cronin, S. B. (2011). Plasmonic enhancement of photocatalytic decomposition of methyl orange under visible light. *Journal of Catalysis, 277(2),* 149-153.

Hummers Jr, W. S., & Offeman, R. E. (1958). Preparation of graphitic oxide. *Journal of the American Chemical Society, 80(6),* 1339-1339.

Hyun, S. H., & Kang, B. S. (1996). Synthesis of Titania Composite Membranes by the Pressurized Sol-Gel Technique. *Journal of the American Ceramic Society, 79(1),* 279-282.

Ilisz, I., Dombi, A., Mogyorósi, K., Farkas, A., & Dékány, I. (2002). Removal of 2-chlorophenol from water by adsorption combined with TiO_2 photocatalysis. *Applied Catalysis B: Environmental, 39(3),* 247-256.

Ingram, D. B., & Linic, S. (2011). Water splitting on composite plasmonic-metal/semiconductor photoelectrodes: evidence for selective plasmon-induced formation of charge carriers near the semiconductor surface. *Journal of the American Chemical Society, 133(14),* 5202-5205.

Jasuja, K., Linn, J., Melton, S., & Berry, V. (2010). Microwave-reduced uncapped metal nanoparticles on graphene: Tuning catalytic, electrical, and raman properties. *The Journal of Physical Chemistry Letters, 1(12)*, 1853-1860.

Jia, C., Yang, P., & Huang, B. (2014). Uniform Ag/AgCl Necklace-Like Nano-Heterostructures: Fabrication and Highly Efficient Plasmonic Photocatalysis. *ChemCatChem, 6(2),* 611-617.

Jiang, L., Zhou, G., Mi, J., & Wu, Z. (2012). Fabrication of visible-light-driven one-dimensional anatase TiO_2/Ag heterojunction plasmonic photocatalyst. *Catalysis Communications*, *24*, 48-51.

Juang, Z.-Y., Wu, C.-Y., Lu, A.-Y., Su, C.-Y., Leou, K.-C., Chen, F.-R., & Tsai, C.-H. (2010). Graphene synthesis by chemical vapor deposition and transfer by a roll-to-roll process. *Carbon, 48(11),* 3169-3174.

Kale, M. J., Avanesian, T., & Christopher, P. (2014). Direct photocatalysis by plasmonic nanostructures. *ACS Catalysis, 4(1),* 116-128.

Karunakaran, C., & Gomathisankar, P. (2013). Solvothermal Synthesis of CeO_2–TiO_2 Nanocomposite for Visible Light Photocatalytic Detoxification of Cyanide. *ACS Sustainable Chemistry & Engineering, 1(12),* 1555-1563.

Kelly, K. L., Coronado, E., Zhao, L. L., & Schatz, G. C. (2003). The optical properties of metal nanoparticles: the influence of size, shape, and dielectric environment. *The Journal of Physical Chemistry B, 107(3)*, 668-677.

Kermanpur, A., Ghassemali, E., & Salemizadeh, S. (2008). Synthesis and characterisation of microporous titania membranes by dip-coating of anodised alumina substrates using sol–gel method. *Journal of Alloys and Compounds, 461(1)*, 331-335.

Khataee, A., & Kasiri, M. B. (2010). Photocatalytic degradation of organic dyes in the presence of nanostructured titanium dioxide: Influence of the chemical structure of dyes. *Journal of Molecular Catalysis A: Chemical, 328(1)*, 8-26.

Kim, K. S., Zhao, Y., Jang, H., Lee, S. Y., Kim, J. M., Kim, K. S., . . . Hong, B. H. (2009). Large-scale pattern growth of graphene films for stretchable transparent electrodes. *Nature, 457(7230)*, 706-710.

Kim, S., Hwang, S.-J., & Choi, W. (2005). Visible light active platinum-ion-doped TiO_2 photocatalyst. *The Journal of Physical Chemistry B, 109(51)*, 24260-24267.

Kimura, K., Naya, S.-i., Jin-nouchi, Y., & Tada, H. (2012). TiO_2 crystal form-dependence of the Au/TiO_2 plasmon photocatalyst's activity. *The Journal of Physical Chemistry C, 116(12)*, 7111-7117.

Kochuveedu, S. T., Jang, Y. H., & Kim, D. H. (2013). A study on the mechanism for the interaction of light with noble metal-metal oxide semiconductor nanostructures for various photophysical applications. *Chemical Society Reviews, 42(21)*, 8467-8493.

Kominami, H., Tanaka, A., & Hashimoto, K. (2010). Mineralization of organic acids in aqueous suspensions of gold nanoparticles supported on cerium (IV) oxide powder under visible light irradiation. *Chemical Communications, 46(8)*, 1287-1289.

Kominami, H., Tanaka, A., & Hashimoto, K. (2011). Gold nanoparticles supported on cerium (IV) oxide powder for mineralization of organic acids in aqueous suspensions under irradiation of visible light of $\lambda = 530$nm. *Applied Catalysis A: General, 397(1)*, 121-126.

Kowalska, E., Abe, R., & Ohtani, B. (2009). Visible light-induced photocatalytic reaction of gold-modified titanium (IV) oxide particles: action spectrum analysis. *Chemical. Communications.(2)*, 241-243.

Kowalska, E., Rau, S., & Ohtani, B. (2012). Plasmonic titania photocatalysts active under UV and visible-light irradiation: influence of gold amount, size, and shape. *Journal of Nanotechnology, 2012*.

Kumar, K. V., Porkodi, K., & Rocha. (2008). Langmuir–Hinshelwood kinetics–a theoretical study. *Catalysis Communications, 9(1)*, 82-84.

Kumar, S. G., & Devi, L. G. (2011). Review on modified TiO_2 photocatalysis under UV/visible light: selected results and related mechanisms on interfacial charge carrier transfer dynamics. *The Journal of Physical Chemistry A, 115(46),* 13211-13241.

Kwak, B. S., Chae, J., Kim, J., & Kang, M. (2009). Enhanced hydrogen production from methanol/water photo-splitting in TiO_2 including Pd component. *Bulletin Korean Chemical Society, 30(5),* 1047-1053.

Lambert, T. N., Chavez, C. A., Hernandez-Sanchez, B., Lu, P., Bell, N. S., Ambrosini, A., . . . Huber, D. L. (2009). Synthesis and characterization of titania− graphene nanocomposites. *The Journal of Physical Chemistry C, 113(46)*, 19812-19823.

Lang, X., Chen, X., & Zhao, J. (2014). Heterogeneous visible light photocatalysis for selective organic transformations. *Chemical Society Reviews, 43(1)*, 473-486.

Lee, M.-K., & Tu, H.-F. (2008). Au–ZnO and Pt–ZnO films prepared by electrodeposition as photocatalysts. *Journal of The Electrochemical Society, 155(12),* D758-D762.

Lei, J., Chen, Y., Shen, F., Wang, L., Liu, Y., & Zhang, J. (2015). Surface modification of TiO_2 with g-C_3N_4 for enhanced UV and Visible photocatalytic activity. *Journal of Alloys and Compounds, 631*, 328-334.

Leung, D. Y., Fu, X., Wang, C., Ni, M., Leung, M. K., Wang, X., & Fu, X. (2010). Hydrogen Production over Titania-Based Photocatalysts. *ChemSusChem, 3(6),* 681-694.

Li, D., Haneda, H., Labhsetwar, N. K., Hishita, S., & Ohashi, N. (2005). Visible-light-driven photocatalysis on fluorine-doped TiO_2 powders by the creation of surface oxygen vacancies. *Chemical Physics Letters, 401(4)*, 579-584.

Li, D., Müller, M. B., Gilje, S., Kaner, R. B., & Wallace, G. G. (2008). Processable aqueous dispersions of graphene nanosheets. *Nature Nanotechnology, 3(2),* 101-105.

Li, G., Zhang, D., & Jimmy, C. Y. (2009). Thermally stable ordered mesoporous CeO_2/TiO_2 visible-light photocatalysts. *Physical Chemistry Chemical Physics, 11(19),* 3775-3782.

Li, M., Zhang, S., Lv, L., Wang, M., Zhang, W., & Pan, B. (2013). A thermally stable mesoporous ZrO_2–CeO_2–TiO_2 visible light photocatalyst. *Chemical Engineering Journal, 229*, 118-125.

Li Puma, G., & Yue, P. L. (2002). Effect of the radiation wavelength on the rate of photocatalytic oxidation of organic pollutants. Industrial & Engineering *Chemistry Research, 41(23)*, 5594-5600.

Li, W., & Zeng, T. (2011). Preparation of TiO_2 anatase nanocrystals by $TiCl_4$ hydrolysis with additive H_2SO_4. *PloS One, 6(6)*, e21082.

Lin, H., Huang, C., Li, W., Ni, C., Shah, S. I., & Tseng, Y.-H. (2006). Size dependency of nanocrystalline TiO_2 on its optical property and photocatalytic reactivity exemplified by 2-chlorophenol. *Applied Catalysis B: Environmental, 68(1)*, 1-11.

Linic, S., Christopher, P., & Ingram, D. B. (2011). Plasmonic-metal nanostructures for efficient conversion of solar to chemical energy. *Nature Materials, 10(12)*, 911-921.

Link, S., & El-Sayed, M. A. (1999). Spectral properties and relaxation dynamics of surface plasmon electronic oscillations in gold and silver nanodots and nanorods. *The Journal of Physical Chemistry B, 103(40)*, 8410-8426.

Liu, H., Dong, X., Li, G., Su, X., & Zhu, Z. (2013). Synthesis of C, Ag co-modified TiO_2 photocatalyst and its application in waste water purification. *Applied Surface Science, 271*, 276-283.

Liu, J., Tang, J., & Gooding, J. J. (2012). Strategies for chemical modification of graphene and applications of chemically modified graphene. *Journal of Materials Chemistry, 22(25)*, 12435-12452.

Liu, J., Zhang, T., Wang, Z., Dawson, G., & Chen, W. (2011). Simple pyrolysis of urea into graphitic carbon nitride with recyclable adsorption and photocatalytic activity. *Journal of Materials Chemistry, 21(38)*, 14398-14401.

Liu, L., Chen, F., Yang, F., Chen, Y., & Crittenden, J. (2012). Photocatalytic degradation of 2, 4-dichlorophenol using nanoscale Fe/TiO_2. *Chemical Engineering Journal, 181*, 189-195.

Liu, L., Liu, H., Zhao, Y.-P., Wang, Y., Duan, Y., Gao, G., . . . Chen, W. (2008). Directed synthesis of hierarchical nanostructured TiO_2 catalysts and their morphology-dependent photocatalysis for phenol degradation. *Environmental Science & Technology, 42(7),* 2342-2348.

Liu, Y. (2014). Hydrothermal synthesis of TiO_2–RGO composites and their improved photocatalytic activity in visible light. *RSC Advances, 4(68),* 36040-36045.

Liu, Y., Chen, K., Xiong, M., Zhou, P., Peng, Z., Yang, G., . . . Chen, W. (2014). Influence of interface combination of reduced graphene oxide/P25 composites on their visible photocatalytic performance. *RSC Advances, 4(82),* 43760-43765.

Liu, Z., Hou, W., Pavaskar, P., Aykol, M., & Cronin, S. B. (2011). Plasmon resonant enhancement of photocatalytic water splitting under visible illumination. *Nano Letters, 11(3),* 1111-1116.

Lotsch, B. V., & Schnick, W. (2005). Thermal Conversion of Guanylurea Dicyanamide into Graphitic Carbon Nitride via Prototype CN_X Precursors. *Chemistry of Materials, 17(15),* 3976-3982.

Lou, Z., Huang, B., Qin, X., Zhang, X., Wang, Z., Zheng, Z., . . . Dai, Y. (2011). One-step synthesis of AgBr microcrystals with different morphologies by ILs-assisted hydrothermal method. *CrystEngComm, 13(6),* 1789-1793.

Lu, X., Shen, J., Wang, J., Cui, Z., & Xie, J. (2015). Highly efficient visible-light photocatalysts: reduced graphene oxide and C_3N_4 nanosheets loaded with Ag nanoparticles. *RSC Advances, 5,* 15993-15999.

Machado, B. F., & Serp, P. (2012). Graphene-based materials for catalysis. *Catalysis Science & Technology, 2(1),* 54-75.

McAllister, M. J., Li, J.-L., Adamson, D. H., Schniepp, H. C., Abdala, A. A., Liu, J., . . . Prud'homme, R. K. (2007). Single sheet functionalized graphene by oxidation and thermal expansion of graphite. *Chemistry of Materials, 19(18),* 4396-4404.

Mohapatra, S. K., Kondamudi, N., Banerjee, S., & Misra, M. (2008). Functionalization of self-organized TiO_2 nanotubes with Pd nanoparticles for photocatalytic decomposition of dyes under solar light illumination. *Langmuir, 24(19),* 11276-11281.

Molina, R. A., Weinmann, D., & Jalabert, R. A. (2002). Oscillatory size dependence of the surface plasmon linewidth in metallic nanoparticles. *Physical Review B : Condensed Matter and Materials Physics, 65(15),* 155427.

Moores, A., & Goettmann, F. (2006). The plasmon band in noble metal nanoparticles: an introduction to theory and applications. *New Journal of Chemistry, 30(8),* 1121-1132.

Murray, W. A., & Barnes, W. L. (2007). Plasmonic materials. *Advanced Materials, 19(22),* 3771-3782.

Nagaveni, K., Hegde, M., & Madras, G. (2004). Structure and Photocatalytic Activity of Ti_{1-x} $M_xO_{2\pm\delta}$ (M= W, V, Ce, Zr, Fe, and Cu) Synthesized by Solution Combustion Method. *The Journal of Physical Chemistry B, 108(52),* 20204-20212.

Nair, R. G., Tripathi, A., & Samdarshi, S. (2011). Photocatalytic activity of predominantly rutile mixed phase Ag/TiV oxide nanoparticles under visible light irradiation. *Energy, 36(5),* 3342-3347.

Niederberger, M., Bartl, M. H., & Stucky, G. D. (2002). Benzyl alcohol and titanium tetrachloride A versatile reaction system for the nonaqueous and low-temperature preparation of crystalline and luminescent titania nanoparticles. *Chemistry of Materials, 14(10),* 4364-4370.

Niederberger, M., & Garnweitner, G. (2006). Organic reaction pathways in the nonaqueous synthesis of metal oxide nanoparticles. *Chemistry-A European Journal, 12(28),* 7282-7302.

Ong, W.-J., Gui, M. M., Chai, S.-P., & Mohamed, A. R. (2013). Direct growth of carbon nanotubes on Ni/TiO_2 as next generation catalysts for photoreduction of CO_2 to methane by water under visible light irradiation. *RSC Advances, 3(14),* 4505-4509.

Ong, W.-J., Tan, L.-L., Chai, S.-P., Yong, S.-T., & Mohamed, A. R. (2014). Highly reactive {001} facets of TiO_2-based composites: synthesis, formation mechanism and characterization. *Nanoscale, 6(4),* 1946-2008.

Palmisano, G., García-López, E., Marcì, G., Loddo, V., Yurdakal, S., Augugliaro, V., & Palmisano, L. (2010). Advances in selective conversions by heterogeneous photocatalysis. *Chemical Communications, 46(38*), 7074-7089.

Pan, X., & Xu, Y.-J. (2013a). Defect-Mediated Growth of Noble-Metal (Ag, Pt, and Pd) Nanoparticles on TiO_2 with Oxygen Vacancies for Photocatalytic Redox Reactions under Visible Light. *The Journal of Physical Chemistry C, 117(35),* 17996-18005.

Pan, X., & Xu, Y.-J. (2013b). Fast and spontaneous reduction of gold ions over oxygen-vacancy-rich TiO_2: A novel strategy to design defect-based composite photocatalyst. *Applied Catalysis A: General, 459,* 34-40.

Pan, X., Yang, M.-Q., Fu, X., Zhang, N., & Xu, Y.-J. (2013). Defective TiO_2 with oxygen vacancies: synthesis, properties and photocatalytic applications. *Nanoscale, 5(9),* 3601-3614.

Park, S., An, J., Jung, I., Piner, R. D., An, S. J., Li, X., . . . Ruoff, R. S. (2009). Colloidal suspensions of highly reduced graphene oxide in a wide variety of organic solvents. *Nano Letters, 9(4),* 1593-1597.

Parmar, K., Ramasamy, E., Lee, J. W., & Lee, J. S. (2010). A simple method for producing mesoporous anatase TiO_2 nanocrystals with elevated photovoltaic performance. *Scripta Materialia, 62(5),* 223-226.

Peng, T., Hu, C., Hu, X., Zhou, X., & Qu, J. (2012). Enhanced Photodegradation of Toxic Pollutants on Plasmonic Au–Ag–AgI/Al_2O_3 Under Visible Irradiation. *Catalysis Letters, 142(5),* 646-654.

Pupo Nogueira, R. F., & Guimarães, J. R. (2000). Photodegradation of dichloroacetic acid and 2, 4-dichlorophenol by ferrioxalate/H_2O_2. *Water Research, 34(3),* 895-901.

Qi, L., Yu, J., Liu, G., & Wong, P. K. (2014). Synthesis and photocatalytic activity of plasmonic Ag@AgCl composite immobilized on titanate nanowire films. *Catalysis Today, 224*, 193-199.

Qu, Y., & Duan, X. (2013). Progress, challenge and perspective of heterogeneous photocatalysts. *Chemical Society Reviews, 42(7),* 2568-2580.

Ramchiary, A., & Samdarshi, S. (2014). Ag deposited mixed phase titania visible light photocatalyst–Superiority of Ag-titania and mixed phase titania co-junction. *Applied Surface Science, 305*, 33-39.

Ramesha, G. K., & Sampath, S. (2009). Electrochemical reduction of oriented graphene oxide films: an in situ Raman spectroelectrochemical study. *The Journal of Physical Chemistry C, 113(19),* 7985-7989.

Reyes-Coronado, D., Rodriguez-Gattorno, G., Espinosa-Pesqueira, M., Cab, C., De Coss, R., & Oskam, G. (2008). Phase-pure TiO_2 nanoparticles: anatase, brookite and rutile. *Nanotechnology, 19(14),* 145605.

Rodríguez-González, V., Zanella, R., del Angel, G., & Gómez, R. (2008). MTBE visible-light photocatalytic decomposition over Au/TiO_2 and $Au/TiO_2–Al_2O_3$ sol–gel prepared catalysts. *Journal of Molecular Catalysis A: Chemical, 281(1),* 93-98.

Roy, R., Bandyopadhyaya, S., & Pal, A. (2004). Surface plasmon resonance in nanocrystalline silver in a ZnO matrix. *The European Physical Journal B-Condensed Matter and Complex Systems, 39(4),* 491-498.

Ryu, J., Kim, S., Kim, H. I., Jo, E.-H., Kim, Y. K., Kim, M., & Jang, H. D. (2015). Self-assembled TiO_2 agglomerates hybridized with reduced-graphene oxide: A high-performance hybrid photocatalyst for solar energy conversion. *Chemical Engineering Journal, 262,* 409-416.

Samuneva, B., Kozhukharov, V., Trapalis, C., & Kranold, R. (1993). Sol-gel processing of titanium-containing thin coatings. *Journal of Materials Science, 28(9),* 2353-2360.

Sarina, S., Waclawik, E. R., & Zhu, H. (2013). Photocatalysis on supported gold and silver nanoparticles under ultraviolet and visible light irradiation. *Green Chemistry, 15(7),* 1814-1833.

Sclafani, A., & Herrmann, J. (1996). Comparison of the photoelectronic and photocatalytic activities of various anatase and rutile forms of titania in pure liquid organic phases and in aqueous solutions. *The Journal of Physical Chemistry, 100(32),* 13655-13661.

Sério, S., Melo Jorge, M., Maneira, M., & Nunes, Y. (2011). Influence of O_2 partial pressure on the growth of nanostructured anatase phase TiO_2 thin films prepared by DC reactive magnetron sputtering. *Materials Chemistry and Physics, 126(1),* 73-81.

Serpone, N., Lawless, D., Khairutdinov, R., & Pelizzetti, E. (1995). Subnanosecond relaxation dynamics in TiO_2 colloidal Sols (particle sizes Rp= 1.0-13.4 nm). relevance to heterogeneous photocatalysis. *The Journal of Physical Chemistry, 99(45),* 16655-16661.

Serpone, N., & Pelizzetti, E. (1989). Photocatalysis: fundamentals and applications. (p. 113) *Wiley New York.*

Shah, M. S. A. S., Zhang, K., Park, A. R., Kim, K. S., Park, N.-G., Park, J. H., & Yoo, P. J. (2013). Single-step solvothermal synthesis of mesoporous Ag–TiO_2–reduced graphene oxide ternary composites with enhanced photocatalytic activity. *Nanoscale, 5(11),* 5093-5101.

Shin, D. O., Jeong, J.-R., Han, T. H., Koo, C. M., Park, H.-J., Lim, Y. T., & Kim, S. O. (2010). A plasmonic biosensor array by block copolymer lithography. *Journal of Materials Chemistry, 20(34),* 7241-7247.

Sridharan, K., Jang, E., & Park, T. J. (2013). Novel visible light active graphitic C_3N_4–TiO_2 composite photocatalyst: synergistic synthesis, growth and photocatalytic treatment of hazardous pollutants. *Applied Catalysis B: Environmental, 142,* 718-728.

Stahl, S. S. (2005). Palladium-catalyzed oxidation of organic chemicals with O_2. *Science, 309(5742),* 1824-1826.

Stoyanova, A., Sredkova, M., Bachvarova-Nedelcheva, A., Iordanova, R., Dimitriev, Y., Hitkova, H., & Iliev, T. (2010). Nonhydrolytic sol-gel synthesis and antibacterial properties of nanosized TiO_2. *Optoelectronics and Advanced Materials-Rapid Communications, 4,* 12.

Su, K., Ai, Z., & Zhang, L. (2012). Efficient Visible Light-Driven Photocatalytic Degradation of Pentachlorophenol with $Bi_2O_3/TiO_{2-x}B_x$. *The Journal of Physical Chemistry C, 116(32),* 17118-17123.

Su, R., Bechstein, R., Sø, L., Vang, R. T., Sillassen, M., Esbjörnsson, B. r., . . . Besenbacher, F. (2011). How the anatase-to-rutile ratio influences the photoreactivity of TiO_2. *The Journal of Physical Chemistry C, 115(49),* 24287-24292.

Sun, B., Vorontsov, A. V., & Smirniotis, P. G. (2003). Role of platinum deposited on TiO_2 in phenol photocatalytic oxidation. *Langmuir, 19(8),* 3151-3156.

Sun, L., Zhao, Z., Zhou, Y., & Liu, L. (2012). Anatase TiO_2 nanocrystals with exposed {001} facets on graphene sheets via molecular grafting for enhanced photocatalytic activity. *Nanoscale, 4(2),* 613-620.

Sun, S., Wang, W., Zhang, L., Shang, M., & Wang, L. (2009). Ag@C core/shell nanocomposite as a highly efficient plasmonic photocatalyst. *Catalysis Communications, 11(4),* 290-293.

Sung-Suh, H. M., Choi, J. R., Hah, H. J., Koo, S. M., & Bae, Y. C. (2004). Comparison of Ag deposition effects on the photocatalytic activity of nanoparticulate TiO_2 under visible and UV light irradiation. *Journal of Photochemistry and Photobiology A: Chemistry, 163(1),* 37-44.

Suwanchawalit, C., Wongnawa, S., Sriprang, P., & Meanha, P. (2012). Enhancement of the photocatalytic performance of Ag-modified TiO_2 photocatalyst under visible light. *Ceramics International, 38(6),* 5201-5207.

Tan, L.-L., Ong, W.-J., Chai, S.-P., & Mohamed, A. R. (2013). Reduced graphene oxide-TiO_2 nanocomposite as a promising visible-light-active photocatalyst for the conversion of carbon dioxide. *Nanoscale Research Letters, 8(1),* 1-9.

Tanaka, A., Hashimoto, K., & Kominami, H. (2011). Selective photocatalytic oxidation of aromatic alcohols to aldehydes in an aqueous suspension of gold nanoparticles supported on cerium (IV) oxide under irradiation of green light. *Chemical Communications, 47(37),* 10446-10448.

Tang, Y., Jiang, Z., Tay, Q., Deng, J., Lai, Y., Gong, D., . . . Chen, Z. (2012a). Visible-light plasmonic photocatalyst anchored on titanate nanotubes: a novel nanohybrid with synergistic effects of adsorption and degradation. *RSC Advances, 2(25),* 9406-9414.

Tang, Y., Luo, S., Teng, Y., Liu, C., Xu, X., Zhang, X., & Chen, L. (2012b). Efficient removal of herbicide 2, 4-dichlorophenoxyacetic acid from water using Ag/reduced graphene oxide co-decorated TiO_2 nanotube arrays. *Journal of Hazardous Materials, 241*, 323-330.

Thomann, I., Pinaud, B. A., Chen, Z., Clemens, B. M., Jaramillo, T. F., & Brongersma, M. L. (2011). Plasmon enhanced solar-to-fuel energy conversion. *Nano Letters, 11(8)*, 3440-3446.

Thompson, T. L., & Yates, J. T. (2006). Surface science studies of the photoactivation of TiO_2 new photochemical processes. *Chemical Reviews, 106(10)*, 4428-4453.

Tian, J., Liu, S., Zhang, Y., Li, H., Wang, L., Luo, Y., . . . Sun, X. (2012). Environmentally friendly, one-pot synthesis of Ag nanoparticle-decorated reduced graphene oxide composites and their application to photocurrent generation. *Inorganic Chemistry, 51(8)*, 4742-4746.

Tian, J., Zhao, Z., Kumar, A., Boughton, R. I., & Liu, H. (2014). Recent progress in design, synthesis, and applications of one-dimensional TiO_2 nanostructured surface heterostructures: a review. *Chemical Society Reviews, 43(20)*, 6920-6937.

Tompsett, G., Bowmaker, G., Cooney, R., Metson, J., Rodgers, K., & Seakins, J. (1995). The Raman spectrum of brookite, TiO_2 (PBCA, Z= 8). *Journal of Raman Spectroscopy, 26(1)*, 57-62.

Tong, H., Ouyang, S., Bi, Y., Umezawa, N., Oshikiri, M., & Ye, J. (2012). Nano-photocatalytic Materials: Possibilities and Challenges. *Advanced Materials, 24(2)*, 229-251.

Torimoto, T., Horibe, H., Kameyama, T., Okazaki, K.-i., Ikeda, S., Matsumura, M., . . . Ishihara, H. (2011). Plasmon-enhanced photocatalytic activity of cadmium sulfide nanoparticle immobilized on silica-coated gold particles. *The Journal of Physical Chemistry Letters, 2(16)*, 2057-2062.

Tung, V. C., Allen, M. J., Yang, Y., & Kaner, R. B. (2008). High-throughput solution processing of large-scale graphene. *Nature Nanotechnology, 4(1)*, 25-29.

Umrao, S., Abraham, S., Theil, F., Pandey, S., Ciobota, V., Shukla, P. K., . . . Popp, J. (2014). A possible mechanism for the emergence of an additional band gap due to a Ti–O–C bond in the TiO_2–graphene hybrid system for enhanced photodegradation of methylene blue under visible light. *RSC Advances, 4(104)*, 59890-59901.

Ung, T., Liz-Marzán, L. M., & Mulvaney, P. (1998). Controlled method for silica coating of silver colloids. Influence of coating on the rate of chemical reactions. *Langmuir, 14(14)*, 3740-3748.

Valencia, S., Marín, J. M., & Restrepo, G. (2010). Study of the bandgap of synthesized titanium dioxide nanoparticules using the sol-gel method and a hydrothermal treatment. *Open Materials Science Journal, 4(1)*, 9-14.

Vinodgopal, K., Neppolian, B., Lightcap, I. V., Grieser, F., Ashokkumar, M., & Kamat, P. V. (2010). Sonolytic design of graphene− Au nanocomposites. simultaneous and sequential reduction of graphene oxide and Au (III). *The Journal of Physical Chemistry Letters, 1(13)*, 1987-1993.

Vioux, A. (1997). Nonhydrolytic sol-gel routes to oxides. *Chemistry of Materials, 9(11)*, 2292-2299.

Wang, C.-C., & Ying, J. Y. (1999). Sol-gel synthesis and hydrothermal processing of anatase and rutile titania nanocrystals. *Chemistry of Materials, 11(11),* 3113-3120.

Wang, C., & Astruc, D. (2014). Nanogold plasmonic photocatalysis for organic synthesis and clean energy conversion. *Chemical Society Reviews, 43(20),* 7188-7216.

Wang, D.-H., Jia, L., Wu, X.-L., Lu, L.-Q., & Xu, A.-W. (2012). One-step hydrothermal synthesis of N-doped TiO_2/C nanocomposites with high visible light photocatalytic activity. *Nanoscale, 4(2),* 576-584.

Wang, D., Li, X., Chen, J., & Tao, X. (2012). Enhanced photoelectrocatalytic activity of reduced graphene oxide/TiO_2 composite films for dye degradation. *Chemical Engineering Journal, 198,* 547-554.

Wang, F., & Zhang, K. (2011). Reduced graphene oxide–TiO_2 nanocomposite with high photocatalystic activity for the degradation of rhodamine B. *Journal of Molecular Catalysis A: Chemical, 345(1),* 101-107.

Wang, H., Zhang, L., Chen, Z., Hu, J., Li, S., Wang, Z., . . . Wang, X. (2014). Semiconductor heterojunction photocatalysts: design, construction, and photocatalytic performances. *Chemical Society Reviews, 43(15),* 5234-5244.

Wang, P., Huang, B., Dai, Y., & Whangbo, M.-H. (2012). Plasmonic photocatalysts: harvesting visible light with noble metal nanoparticles. *Physical Chemistry Chemical Physics, 14(28),* 9813-9825.

Wang, P., Huang, B., Lou, Z., Zhang, X., Qin, X., Dai, Y., . . . Wang, X. (2010). Synthesis of highly efficient Ag@ AgCl plasmonic photocatalysts with various structures. *Chemistry-A European Journal, 16(2),* 538-544.

Wang, P., Huang, B., Zhang, Q., Zhang, X., Qin, X., Dai, Y., . . . Lou, Z. (2010). Highly efficient visible light plasmonic photocatalyst Ag@Ag (Br, I). *Chemistry-A European Journal, 16(33),* 10042-10047.

Wang, P., Huang, B., Zhang, X., Qin, X., Dai, Y., Wang, Z., & Lou, Z. (2011). Highly Efficient Visible Light Plasmonic Photocatalysts Ag@ Ag (Cl, Br) and Ag@ AgCl-AgI. *ChemCatChem, 3(2),* 360-364.

Wang, P., Huang, B., Zhang, X., Qin, X., Jin, H., Dai, Y., . . . Wang, S. (2009). Highly Efficient Visible-Light Plasmonic Photocatalyst Ag@ AgBr. *Chemistry-A European Journal, 15(8),* 1821-1824.

Wang, P., Tang, Y., Dong, Z., Chen, Z., & Lim, T.-T. (2013). Ag–AgBr/TiO_2/RGO nanocomposite for visible-light photocatalytic degradation of penicillin G. *Journal of Materials Chemistry A, 1(15)*, 4718-4727.

Wang, P., Zhai, Y., Wang, D., & Dong, S. (2011). Synthesis of reduced graphene oxide-anatase TiO_2 nanocomposite and its improved photo-induced charge transfer properties. *Nanoscale, 3(4)*, 1640-1645.

Wang, W.-S., Wang, D.-H., Qu, W.-G., Lu, L.-Q., & Xu, A.-W. (2012). Large ultrathin anatase Ti_{O2} nanosheets with exposed {001} facets on graphene for enhanced visible light photocatalytic activity. *The Journal of Physical Chemistry C, 116(37)*, 19893-19901.

Wang, W., Cheng, B., Yu, J., Liu, G., & Fan, W. (2012). Visible-Light Photocatalytic Activity and Deactivation Mechanism of Ag_3PO_4 Spherical Particles. *Chemistry-An Asian Journal, 7(8)*, 1902-1908.

Wang, Y., Tang, Y., Chen, Y., Li, Y., Liu, X., Luo, S., & Liu, C. (2013a). Reduced graphene oxide-based photocatalysts containing Ag nanoparticles on a TiO_2 nanotube array. *Journal of Materials Science, 48(18)*, 6203-6211.

Wang, Y., Wang, Q., Zhan, X., Wang, F., Safdar, M., & He, J. (2013b). Visible light driven type II heterostructures and their enhanced photocatalysis properties: a review. *Nanoscale, 5(18)*, 8326-8339.

Wang, Z., Huang, B., Dai, Y., Qin, X., Zhang, X., Wang, P., . . . Yu, J. (2009). Highly photocatalytic ZnO/In_2O_3 heteronanostructures synthesized by a coprecipitation method. *The Journal of Physical Chemistry C, 113(11)*, 4612-4617.

Wang, Z., Liu, J., & Chen, W. (2012). Plasmonic Ag/AgBr nanohybrid: synergistic effect of SPR with photographic sensitivity for enhanced photocatalytic activity and stability. *Dalton Transactions, 41(16)*, 4866-4870.

Wang, Z., Liu, Y., Huang, B., Dai, Y., Lou, Z., Wang, G., . . . Qin, X. (2014). Progress on extending the light absorption spectra of photocatalysts. *Physical Chemistry Chemical Physics, 16(7)*, 2758-2774.

Wei, D., Liu, Y., Wang, Y., Zhang, H., Huang, L., & Yu, G. (2009). Synthesis of N-doped graphene by chemical vapor deposition and its electrical properties. *Nano Letters, 9(5)*, 1752-1758.

Wen, Y., Ding, H., & Shan, Y. (2011). Preparation and visible light photocatalytic activity of Ag/TiO_2/graphene nanocomposite. *Nanoscale, 3(10)*, 4411-4417.

White, T. P., & Catchpole, K. R. (2012). Plasmon-enhanced internal photoemission for photovoltaics: Theoretical efficiency limits. *Applied Physics Letters, 101(7)*, 073905.

Wu, J.-J., & Tseng, C.-H. (2006). Photocatalytic properties of nc-Au/ZnO nanorod composites. *Applied Catalysis B: Environmental, 66(1)*, 51-57.

Wu, T., Cai, X., Tan, S., Li, H., Liu, J., & Yang, W. (2011). Adsorption characteristics of acrylonitrile, p-toluenesulfonic acid, 1-naphthalenesulfonic acid and methyl blue on graphene in aqueous solutions. *Chemical Engineering Journal, 173(1)*, 144-149.

Xiang, Q., Yu, J., Cheng, B., & Ong, H. (2010). Microwave-hydrothermal preparation and visible-light photoactivity of plasmonic photocatalyst Ag-TiO_2 nanocomposite hollow spheres. *Chemistry, an Asian journal, 5(6)*, 1466-1474.

Xiang, Q., Yu, J., & Jaroniec, M. (2011). Nitrogen and sulfur co-doped TiO_2 nanosheets with exposed {001} facets: synthesis, characterization and visible-light photocatalytic activity. *Physical Chemistry Chemical Physics, 13(11)*, 4853-4861.

Xiang, Q., Yu, J., & Jaroniec, M. (2012). Graphene-based semiconductor photocatalysts. *Chemical Society Reviews, 41(2)*, 782-796.

Xiang, Q., Yu, J., Wang, W., & Jaroniec, M. (2011). Nitrogen self-doped nanosized TiO_2 sheets with exposed {001} facets for enhanced visible-light photocatalytic activity. *Chemical Communications., 47(24)*, 6906-6908.

Xiao, F. (2012a). Layer-by-Layer Self-Assembly Construction of Highly Ordered Metal-TiO_2 Nanotube Arrays Heterostructures (M/TNTs, M= Au, Ag, Pt) with Tunable Catalytic Activities. *The Journal of Physical Chemistry C, 116(31)*, 16487-16498.

Xiao, F. (2012b). Self-assembly preparation of gold nanoparticles-TiO_2 nanotube arrays binary hybrid nanocomposites for photocatalytic applications. *Journal of Materials Chemistry, 22(16)*, 7819-7830.

Xiao, M., Jiang, R., Wang, F., Fang, C., Wang, J., & Jimmy, C. Y. (2013). Plasmon-enhanced chemical reactions. *Journal of Materials Chemistry A, 1(19)*, 5790-5805.

Xie, Y., Kum, J., Zhao, X., & Cho, S. O. (2011). Enhanced photocatalytic activity of mesoporous SN-codoped TiO_2 loaded with Ag nanoparticles. *Semiconductor Science and Technology, 26(8)*, 085037.

Xiong, Y., Chen, J., Wiley, B., Xia, Y., Yin, Y., & Li, Z.-Y. (2005). Size-dependence of surface plasmon resonance and oxidation for Pd nanocubes synthesized via a seed etching process. *Nano Letters, 5(7)*, 1237-1242.

Xiong, Y., Wiley, B., Chen, J., Li, Z. Y., Yin, Y., & Xia, Y. (2005). Corrosion-Based Synthesis of Single-Crystal Pd Nanoboxes and Nanocages and Their Surface Plasmon Properties. *Angewandte Chemie International Edition, 44(48)*, 7913-7917.

Xu, A.-W., Gao, Y., & Liu, H.-Q. (2002). The Preparation, Characterization, and their Photocatalytic Activities of Rare-Earth-Doped TiO_2 Nanoparticles. *Journal of Catalysis, 207(2)*, 151-157.

Xu, J., Li, Y., Peng, S., Lu, G., & Li, S. (2013). Eosin Y-sensitized graphitic carbon nitride fabricated by heating urea for visible light photocatalytic hydrogen evolution: the effect of the pyrolysis temperature of urea. *Physical Chemistry Chemical Physics, 15(20)*, 7657-7665.

Yan, J., Wu, G., Guan, N., Li, L., Li, Z., & Cao, X. (2013). Understanding the effect of surface/bulk defects on the photocatalytic activity of TiO_2: anatase versus rutile. *Physical Chemistry Chemical Physics, 15(26)*, 10978-10988.

Yan, S., Li, Z., & Zou, Z. (2009). Photodegradation performance of g-C_3N_4 fabricated by directly heating melamine. *Langmuir, 25(17)*, 10397-10401.

Yang, J., Tian, C., Wang, L., & Fu, H. (2011). An effective strategy for small-sized and highly-dispersed palladium nanoparticles supported on graphene with excellent performance for formic acid oxidation. *Journal of Materials Chemistry, 21(10)*, 3384-3390.

Yang, Y., Guo, Y., Liu, F., Yuan, X., Guo, Y., Zhang, S., . . . Huo, M. (2013). Preparation and enhanced visible-light photocatalytic activity of silver deposited graphitic carbon nitride plasmonic photocatalyst. *Applied Catalysis B: Environmental, 142*, 828-837.

Yang, Y., Liu, E., Dai, H., Kang, L., Wu, H., Fan, J., . . . Liu, H. (2014). Photocatalytic activity of Ag–TiO_2-graphene ternary nanocomposites and application in hydrogen evolution by water splitting. *International Journal of Hydrogen Energy, 39(15),* 7664-7671.

Yoshimura, M., & Byrappa, K. (2008). Hydrothermal processing of materials: past, present and future. *Journal of Materials Science, 43(7)*, 2085-2103.

Yu, H., Liu, R., Wang, X., Wang, P., & Yu, J. (2012). Enhanced visible-light photocatalytic activity of Bi_2WO_6 nanoparticles by Ag_2O cocatalyst. *Applied Catalysis B: Environmental, 111*, 326-333.

Yu, J., Qi, L., & Jaroniec, M. (2010). Hydrogen production by photocatalytic water splitting over Pt/TiO_2 nanosheets with exposed (001) facets. *The Journal of Physical Chemistry C, 114(30)*, 13118-13125.

Yu, J., Xiang, Q., & Zhou, M. (2009). Preparation, characterization and visible-light-driven photocatalytic activity of Fe-doped titania nanorods and first-principles study for electronic structures. *Applied Catalysis B: Environmental, 90(3),* 595-602.

Zeng, C., Guo, M., Tian, B., & Zhang, J. (2013). Reduced graphene oxide modified Ag/AgBr with enhanced visible light photocatalytic activity for methyl orange degradation. *Chemical Physics Letters, 575*, 81-85.

Zeng, T., Qiu, Y., Chen, L., & Song, X. (1998). Microstructure and phase evolution of TiO_2 precursors prepared by peptization-hydrolysis method using polycarboxylic acid as peptizing agent. *Materials Chemistry and Physics, 56(2),* 163-170.

Zhai, W., Xue, S., Zhu, A., Luo, Y., & Tian, Y. (2011). Plasmon-Driven Selective Oxidation of Aromatic Alcohols to Aldehydes in Water with Recyclable Pt/TiO_2 Nanocomposites. *ChemCatChem, 3(1)*, 127-130.

Zhang, H., Fan, X., Quan, X., Chen, S., & Yu, H. (2011). Graphene sheets grafted Ag@ AgCl hybrid with enhanced plasmonic photocatalytic activity under visible light. *Environmental Science & Technology, 45(13)*, 5731-5736.

Zhang, J., Chen, X., Takanabe, K., Maeda, K., Domen, K., Epping, J. D., . . . Wang, X. (2010). Synthesis of a carbon nitride structure for visible-light catalysis by copolymerization. *Angewandte Chemie International Edition, 49(2)*, 441-444.

Zhang, J., Xiong, Z., & Zhao, X. (2011). Graphene–metal–oxide composites for the degradation of dyes under visible light irradiation. *Journal of Materials Chemistry, 21(11)*, 3634-3640.

Zhang, L., Jing, D., She, X., Liu, H., Yang, D., Lu, Y., . . . Guo, L. (2014). Heterojunctions in g-C_3N_4/TiO_2 (B) nanofibres with exposed (001) plane and enhanced visible-light photoactivity. *Journal of Materials Chemistry A, 2(7)*, 2071-2078.

Zhang, N., Liu, S., Fu, X., & Xu, Y.-J. (2011). Synthesis of M@TiO_2 (M= Au, Pd, Pt) core–shell nanocomposites with tunable photoreactivity. *The Journal of Physical Chemistry C, 115(18)*, 9136-9145.

Zhang, N., Zhang, Y., & Xu, Y.-J. (2012). Recent progress on graphene-based photocatalysts: current status and future perspectives. *Nanoscale, 4(19)*, 5792-5813.

Zhang, Q., Joo, J.-B., Lu, Z., Dahl, M., Oliveira, D. Q., Ye, M., & Yin, Y. (2011). Self-assembly and photocatalysis of mesoporous TiO_2 nanocrystal clusters. *Nano Research, 4(1)*, 103-114.

Zhang, X., Chen, Y. L., Liu, R.-S., & Tsai, D. P. (2013). Plasmonic photocatalysis. *Reports on Progress in Physics, 76(4)*, 046401.

Zhang, Y., Tang, Z.-R., Fu, X., & Xu, Y.-J. (2011). Engineering the unique 2D mat of graphene to achieve graphene-TiO_2 nanocomposite for photocatalytic selective transformation: what advantage does graphene have over its forebear carbon nanotube? *ACS Nano, 5(9)*, 7426-7435.

Zhao, S., Chen, S., Yu, H., & Quan, X. (2012). g-C_3N_4/TiO_2 hybrid photocatalyst with wide absorption wavelength range and effective photogenerated charge separation. *Separation and Purification Technology, 99*, 50-54.

Zhao, Y., Kuai, L., & Geng, B. (2012). Low-cost and highly efficient composite visible light-driven Ag–AgBr/γ-Al_2O_3 plasmonic photocatalyst for degrading organic pollutants. *Catalysis Science & Technology, 2(6)*, 1269-1274.

Zheng, Z., Huang, B., Qin, X., Zhang, X., Dai, Y., & Whangbo, M.-H. (2011). Facile in situ synthesis of visible-light plasmonic photocatalysts M@TiO_2 (M= Au, Pt, Ag) and evaluation of their photocatalytic oxidation of benzene to phenol. *Journal of Materials Chemistry, 21(25)*, 9079-9087.

Zhou, S., Liu, Y., Li, J., Wang, Y., Jiang, G., Zhao, Z., . . . Wei, Y. (2014). Facile in situ synthesis of graphitic carbon nitride (g-C_3N_4)-N-TiO_2 heterojunction as an efficient photocatalyst for the selective photoreduction of CO_2 to CO. *Applied Catalysis B: Environmental, 158*, 20-29.

Zhou, X., Liu, G., Yu, J., & Fan, W. (2012). Surface plasmon resonance-mediated photocatalysis by noble metal-based composites under visible light. *Journal of Materials Chemistry, 22(40)*, 21337-21354.

Zhu, M., Chen, P., & Liu, M. (2011). Graphene oxide enwrapped Ag/AgX (X= Br, Cl) nanocomposite as a highly efficient visible-light plasmonic photocatalyst. *ACS Nano, 5(6)*, 4529-4536.

Zhu, S., Liang, S., Gu, Q., Xie, L., Wang, J., Ding, Z., & Liu, P. (2012). Effect of Au supported TiO_2 with dominant exposed {001} facets on the visible-light photocatalytic activity. *Applied Catalysis B: Environmental*, *119*, 146-155.

LIST OF PUBLICATIONS AND PAPERS PRESENTED

Papers Published

1. Leong, K. H., Liu, S. L., Sim, L.C., Saravanan, P., Jang, M., & Ibrahim, S. (2015). Surface reconstruction of titania with g-C_3N_4 and Ag for promoting efficient electrons migration and enhanced visible light photocatalysis. *Applied Surface Science* – DOI: 10.1016/j.apsusc.2015.06.184.

2. Leong, K. H., Sim, L. C., Bahnemann, D., Jang, M., Ibrahim, S., & Saravanan, P. (2015). Reduced graphene oxide and Ag wrapped TiO_2 photocatalyst for enhanced visible light photocatalysis. *APL Materials,* 3, 104503.

3. Leong, K. H., Chu, H. Y., Ibrahim, S., & Saravanan, P. (2015). Palladium nanoparticles anchored to anatase TiO_2 for enhanced surface plasmon resonance-stimulated, visible-light-driven photocatalytic activity. *Beilstein Journal of Nanotechnology*, 6, 428-437.

4. Leong, K. H., Gan, B. L., Ibrahim, S., & Saravanan, P. (2014). Synthesis of surface plasmon resonance (SPR) triggered Ag/TiO_2 photocatalyst for degradation of endocrine disturbing compounds. *Applied Surface Science, 319*, 128-135.

5. Leong, K. H., Monash, P., Ibrahim, S., & Saravanan, P. (2014). Solar photocatalytic activity of anatase TiO_2 nanocrystals synthesized by non-hydrolitic sol-gel method. *Solar Energy, 101*, 321-332.

Conference Presentations

1. Leong, K. H., Chu, H. Y., Ibrahim, S., & Saravanan, P. “Palladium nanoparticles anchored to anatase TiO_2 for enhanced surface plasmon resonance-stimulated, visible-light-driven photocatalytic activity” 5th International Conference on Environment. 18-19 August (2015) Penang, Malaysia.
2. Leong, K. H., Gan. B. L., Ibrahim, S., & Saravanan, P. “Synthesis of surface plasmon resonance (SPR) triggered Ag/TiO_2 photocatalyst for degradation of endocrine disturbing compounds” Seminar Kebangsaan Teknologi Makmal Ke-12. 8-11 Februari (2015) Kuala Lumpur, Malaysia.
3. Leong, K. H., Sim. L. C., Ibrahim, S., & Saravanan, P. “Visible light driven reduced graphene oxide enwrapped Ag/TiO_2 photocatalyst” 3rd Water Research Conference. 11-14 Januari (2015) Shenzhen, China.
4. Leong, K. H., Monash, P., Ibrahim, S., & Saravanan, P. “Solar photocatalytic activity of anatase TiO_2 nanocrystals synthesized by non-hydrolitic sol-gel method.” 1st International Conference on Energy Environment and Human Engineering (ICEEHE 2013). 21−23 Dec (2013) Yangon, Myanmar.